DEPARTMENT OF ELECTRICAL ENGINEERING
INDIAN INSTITUTE OF TECHNOLOGY
MADRAS
CHENNAI – 600 036

A-mode ultrasound methods for measurement of arterial structure and functional properties: a window to early vascular ageing

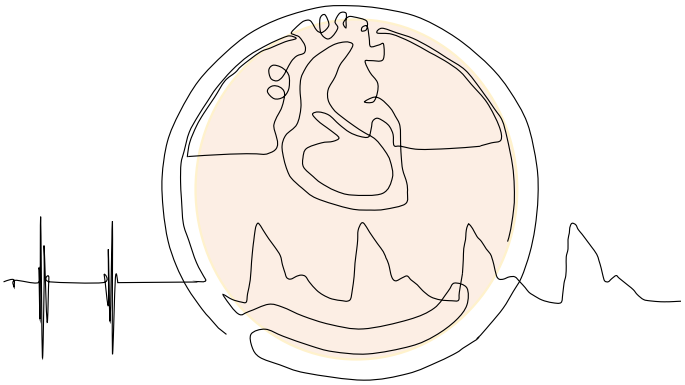

A Thesis

Submitted by

V Raj Kiran

For the award of the degree

Of

DOCTOR OF PHILOSOPHY

March 2023

DEPARTMENT OF ELECTRICAL ENGINEERING
INDIAN INSTITUTE OF TECHNOLOGY
MADRAS
CHENNAI – 600 036

A-mode ultrasound methods for measurement of arterial structure and functional properties: a window to early vascular ageing

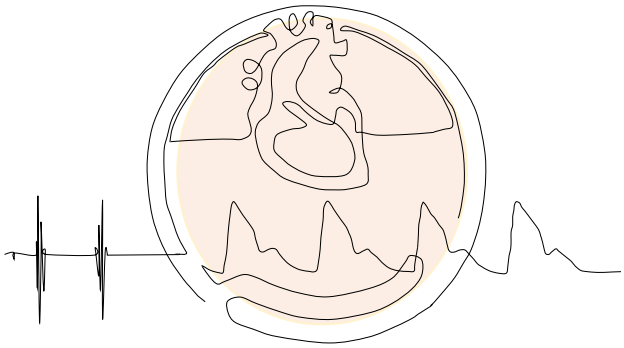

A Thesis

Submitted by

V Raj Kiran

For the award of the degree

Of

DOCTOR OF PHILOSOPHY

March 2023

Being confident of this, that He who began a good work in you will carry it on to completion until the day of Christ Jesus.

- ***Philippians 1:6***

I dedicate this thesis to everyone who have shaped me to what I am today, above all, to my parents, wife, and an irreplaceable teacher Mr. Kamlesh Jha.

THESIS CERTIFICATE

This is to certify that the thesis titled **A-mode ultrasound methods for measurement of arterial structure and functional properties: a window to early vascular ageing** submitted by me to the Indian Institute of Technology, Madras for the award of the degree of **DOCTOR OF PHILOSOPHY,** is a bona fide record of research work carried out by me under the supervision of Dr. Jayaraj Joseph. The contents of this thesis, in full or in parts, have not been submitted to any other Institute or University for the award of any degree or diploma.

Chennai 600 036 **Research Scholar**

Date : Tuesday, 21 March 2023 **Research Guide**

LIST OF PAPERS BASED ON THIS THESIS

REFEREED JOURNALS BASED ON THIS THESIS

1. **Raj, K. V**, Joseph, J., Nabeel, P. M., & Sivaprakasam, M. (2020). Automated measurement of compression-decompression in arterial diameter and wall thickness by image-free ultrasound. Computer Methods and Programs in Biomedicine, 194, 1–12.
2. **Raj, K. V**, Nabeel, P. M., Chandran, D., Sivaprakasam, M., & Joseph, J. (2022). High-frame-rate A-mode ultrasound for calibration-free cuffless carotid pressure: feasibility study using lower body negative pressure intervention. Blood Pressure, 31(1), 1–11.
3. **Raj, K. V**, Nabeel, P. M., & Joseph, J. (2022). Image-Free Fast Ultrasound for Measurement of Local Pulse Wave Velocity: In Vitro Validation and In Vivo Feasibility. IEEE Transactions on Ultrasonics, Ferroelectrics, and Frequency Control, 69(7), 2248–2256.
4. **Raj, K. V**, Nabeel, P. M., Sivaprakasam, M., & Joseph, J. (2022). Time-warping for robust automated arterial wall-recognition and tracking from single-scan-line ultrasound signals. Ultrasonics, 126, 106828.
5. Nabeel, P. M., **Raj, K. V**, & Joseph, J. (2022). Image-free ultrasound for local and regional vascular stiffness assessment: The ARTSENS Plus. Journal of Hypertension, 40(8), 1537–1544.

REFEREED JOURNALS (OTHER)

6. Joseph, J., **Raj, K. V**, Nabeel, P. M., Shah, M. I., Bhaskar, A., Ganesh, C., & Seshadri, S. (2020). ARTSENS® Pen — portable easy-to-use device for carotid stiffness measurement: technology validation and clinical-utility assessment. Biomedical Physics & Engineering Express, 6(2), 1–12.
7. Nabeel, P. M., **Raj, K. V**, Joseph, J., Abhidev, V. V., & Sivaprakasam, M. (2020). Local pulse wave velocity: theory, methods, advancements, and clinical applications. IEEE Reviews in Biomedical Engineering, 13, 74–112.
8. Manoj, R., **Raj, K. V**, Nabeel, P. M., Sivaprakasam, M., & Joseph, J. (2022). Arterial pressure pulse wave separation analysis using a multi-Gaussian decomposition model. Physiological Measurement, 43(5), 1–12.

REFEREED CONFERENCE PUBLICATIONS BASED ON THIS THESIS

1. **Raj, K. V**, Joseph, J., Shah, M. I., & Sivaprakasam, M. (2017). An image-free ultrasound method to estimate artery wall thickness surrogate for screening. IEEE International Symposium on Medical Measurements and Applications (MeMeA), 1–6. Rochester.
2. **Raj, K. V**, Nabeel, P. M., Joseph, J., & Sivaprakasam, M. (2017). Brachial artery stiffness estimation using ARTSENS. 39th Annual International Conference of the IEEE Engineering in Medicine and Biology Society (EMBC), 262–265.
3. **Raj, K. V**, Nabeel, P. M., Joseph, J., & Sivaprakasam, M. (2018). Non-invasive assessment of arterial incremental elastic modulus variations within a cardiac

cycle. 13th Russian-German Conference on Biomedical Engineering (RGC), 108–111.

4. **Raj, K. V**, Nabeel, P. M., Joseph, J., Shah, M. I., & Sivaprakasam, M. (2018). Measurement of Arterial Young's Elastic Modulus using ARTSENS Pen. IEEE International Symposium on Medical Measurements and Applications (MeMeA), 1–6.
5. **Raj, K. V**, Nabeel, P. M., Joseph, J., Shah, M. I., & Sivaprakasam, M. (2018). Evaluation of local pulse wave velocity using an image free ultrasound technique. IEEE International Symposium on Medical Measurements and Applications (MeMeA), 1–6.
6. **Raj, K. V**, Nabeel, P. M., Joseph, J., Venkatramanan, S., Shah, M. I., & Sivaprakasam, M. (2018). An In-Vivo Study on Intra-Day Variations in Vascular Stiffness using ARTSENS Pen. 40th Annual International Conference of the IEEE Engineering in Medicine and Biology Society (EMBC), 4575–4578.
7. **Raj, K. V**, Nabeel, P. M., Joseph, J., & Sivaprakasam, M. (2019). Incorporating Arterial Viscoelastic Modelling for the Assessment of Changes in Pulse Wave Velocity Within a Cardiac Cycle Using Bramwell-Hill Equation. Computing in Cardiology (CinC), 46, 1–4.
8. **Raj, K. V**, Joseph, J., Nabeel, P. M., Frese, H., Sivaprakasam, M., & Shah, M. I. (2019). Analytic phase-based approach for arterial diameter evaluation using a-mode ultrasound frames. IEEE International Symposium on Medical Measurements and Applications (MeMeA), 1–5.

9. **Raj, K. V**, Nabeel, P. M., Joseph, J., & Sivaprakasam, M. (2019). Methodological and measurement concerns of local pulse wave velocity assessment. IEEE International Symposium on Medical Measurements and Applications (MeMeA), 1–6.
10. **Raj, K. V**, Abhidev, V. V., Nabeel, P. M., Joseph, J., Sivaprakasam, M., & Shah, M. I. (2019). Arterial Stiffness in Elastic and Muscular Arteries: Measurement using ARTSENS Pen. IEEE International Symposium on Medical Measurements and Applications (MeMeA), 1–5.
11. **Raj, K. V**, Nabeel, P. M., Joseph, J., Frese, H., & Sivaprakasam, M. (2019). Multimodal Image-Free Ultrasound Technique for Evaluation of Arterial Viscoelastic Properties: A Feasibility Study. 41st Annual International Conference of the IEEE Engineering in Medicine and Biology Society (EMBC), 5034–5037.
12. **Raj, K. V**, Joseph, J., Nabeel, P. M., & Sivaprakasam, M. (2020). A Dynamic Time Warping Method for Improved Arterial Wall-Tracking using A-mode Ultrasound Frames: A Proof-of-Concept. IEEE International Symposium on Medical Measurements and Applications (MeMeA), 1–6. Bari.
13. **Raj, K. V**, Nabeel, P. M., Joseph, J., Chandran, D., & Sivaprakasam, M. (2020). P.41 Measurement of Pressure-dependent Intra-Beat Changes in Carotid Pulse Wave Velocity using Image-Free Fast Ultrasound. Artery Research, 26(Supplement 1), S63.
14. **Raj, K. V**, Nabeel, P. M., Manoj, R., Shah, M. I., & Joseph, J. (2021). Phantom Assessment of an Image - free Ultrasound Technology for Online Local Pulse

Wave Velocity Measurement. 43rd Annual International Conference of the IEEE Engineering in Medicine and Biology Society (EMBC), 5610–5613.

15. **Raj, K. V**, Nabeel, P. M., Sivaprakasam, M., & Joseph, J. (2021). Phantom evaluation of a time warping based automated arterial wall recognition and tracking method. IEEE International Symposium on Medical Measurements and Applications (MeMeA), 1–6.
16. **Raj, K. V**, Nabeel, P. M., Shah, M. I., Sivaprakasam, M., & Joseph, J. (2021). Gaussian-Mixture Modelling of A-Mode Radiofrequency Scans for the Measurement of Arterial Wall Thickness. 43rd Annual International Conference of the IEEE Engineering in Medicine and Biology Society (EMBC), 5598–5601.
17. **Raj, K. V**, Manoj, R., Ishwarya, S., Nabeel, P. M., & Joseph, J. (2022). Operator Variabilities in Carotid Pulse Wave Velocity Measured by an Image-free Ultrasound Device. 44th Annual International Conference of the IEEE Engineering in Medicine & Biology Society (EMBC), 4018-4021.
18. **Raj, K. V**, Manoj, R., Ishwarya, S., Nabeel, P. M., & Joseph, J. (2022). Comparison of Approximated and Actual Bramwell-Hill Equation Implementation for Local Pulse Wave Velocity: Ex-vivo Study. 44th Annual International Conference of the IEEE Engineering in Medicine & Biology Society (EMBC), 3989-3992.

REFEREED CONFERENCE PUBLICATIONS (OTHERS)

1. Joseph, J., Nabeel, P. M., Shah, M. I., **Raj, K. V**, & Sivaprakasam, M. (2018). Live Demonstration of ARTSENS® Pen – An Image-Free Ultrasound Device for Automated Evaluation of Vascular Stiffness. IEEE Sensors, 1.

2. Nabeel, P. M., **Raj, K. V**, Joseph, J., & Sivaprakasam, M. (2018). Non-Invasive Assessment of Local Pulse Wave Velocity as Function of Arterial Pressure. IEEE International Symposium on Medical Measurements and Applications (MeMeA), 1–6.
3. Nabeel, P. M., **Raj, K. V**, Joseph, J., & Sivaprakasam, M. (2018). Local pulse wave velocity and cuffless blood pressure assessment using ARTSENS. 40th Annual International Conference of the IEEE Engineering in Medicine and Biology Society (EMBC), 1. Honolulu.
4. Nabeel, P. M., **Raj, K. V**, Jayaraj, J., & Mohanasankar, S. (2018). Local Evaluation of Variation in Pulse Wave Velocity over the Cardiac Cycle using Single-Element Ultrasound Transducer. 40th Annual International Conference of the IEEE Engineering in Medicine and Biology Society (EMBC), 4560–4563.
5. Joseph, J., **Raj, K. V**, Nabeel, P. M., & Sivaprakasam, M. (2019). Image-free ultrasound technique for calibration-free cuffless blood pressure measurement. 41st Annual International Conference of the IEEE Engineering in Medicine and Biology Society (EMBC), 1. Berlin.
6. Manoj, R., Nabeel, P. M., **Raj, K. V**, Joseph, J., & Sivaprakasam, M. (2019). Cuffless evaluation of arterial pressure waveform using flexible force sensor: a proof of principle. IEEE International Symposium on Medical Measurements and Applications (MeMeA), 1–6.
7. Nabeel, P. M., **Raj, K. V**, Joseph, J., & Sivaprakasam, M. (2019). Determination of Incremental Local Pulse Wave Velocity Using Arterial Diameter Waveform: Mathematical Modeling and Practical Implementation

Theoretical Analysis Modeling of incremental local PWV. Computing in Cardiology (CinC), 46(1), 1–4.

8. Joseph, J., Chandran, D. S., **Raj, K. V**, Abhidev, V. V., & Sivaprakasam, M. (2019). Image-Free Technique for Flow Mediated Dilation Using ARTSENS® Pen. 41st Annual International Conference of the IEEE Engineering in Medicine and Biology Society (EMBC), 5051–5054.
9. Nabeel, P. M., Chilaka, V., **Raj, K. V**, Joseph, J., & Sivaprakasam, M. (2019). Deep Learning for Blood Pressure Estimation: An Approach using Local Measure of Arterial Dual Diameter Waveforms. IEEE International Symposium on Medical Measurements and Applications (MeMeA), 1–6.
10. Chandran, D., Joseph, J., Sen, S., **Raj, K. V**, Nabeel, P. M., & Deepak, K. K. (2020). P.47 Feasibility Evaluation of Imaging-Free Ultrasound Technology to Measure Diameters of Brachial and Radial Arteries for Assessment of Endothelial Function. Artery Research, 26(Supplement 1), S70.
11. Manoj, R., Nabeel, P. M., **Raj, K. V**, Joseph, J., & Sivaprakasam, M. (2020). YI 2.5 Direct Measurement of Stiffness Index β of Superficial Arteries Without Blood Pressure Estimation. Artery Research, 26(Supplement 1), S18.
12. Poojitha, U. P., Ram, K., Nabeel, P. M., **Raj, K. V**, Joseph, J., & Sivaprakasam, M. (2020). Blood Pressure Estimation using Arterial Diameter : Exploring Different Machine Learning Methods. IEEE International Symposium on Medical Measurements and Applications (MeMeA), 1–6. Bari.
13. Manoj, R., **Raj, K. V**, Nabeel, P. M., Joseph, J., & Sivaprakasam, M. (2020). A Bi-modal Probe Integrated with A-mode Ultrasound and Force Sensor for

Single-site Assessment of Arterial Pressure-Diameter Loop. IEEE International Symposium on Medical Measurements and Applications (MeMeA), 1–6. Bari.

14. Nabeel, P. M., Manoj, R., Abhidev, V. V., Joseph, J., **Raj, K. V**, & Mohanasankar, S. (2020). High-Throughput Vascular Screening by ARTSENS Pen During a Medical Camp for Early-Stage Detection of Chronic Kidney Disease. 42nd Annual International Conference of the IEEE Engineering in Medicine and Biology Society (EMBC), 2752–2755. Canada.
15. Manoj, R., Nabeel, P. M., Abhidev, V. V., **Raj, K. V**, Joseph, J., & Sivaprakasam, M. (2020). Demonstration of Pressure-Dependent Inter and Intra-Cycle Variations in Local Pulse Wave Velocity Using Excised Bovine Carotid Artery. 42nd Annual International Conference of the IEEE Engineering in Medicine and Biology Society (EMBC), 2707–2710. Canada.
16. Ramakrishna, P., Nabeel, P. M., **Raj, K. V**, Joseph, J., & Sivaprakasam, M. (2020). Cuffless Blood Pressure Estimation Using Features Extracted from Carotid Dual-Diameter Waveforms. 42nd Annual International Conference of the IEEE Engineering in Medicine and Biology Society (EMBC), 2719–2722. Canada.
17. Nabeel, P. M., **Raj, K. V**, Shah, M. I., Abhidev, V. V., Manoj, R., Sivaprakasam, M., & Joseph, J. (2021). An image-free ultrasound device for simultaneous measurement of local and regional arterial stiffness Indices. IEEE International Symposium on Medical Measurements and Applications (MeMeA), 1–6.
18. Manoj, R., **Raj, K. V**, Nabeel, P. M., Sivaprakasam, M., & Joseph, J. (2021). Multi-gaussian model for estimating stiffness surrogate using arterial diameter

waveform. IEEE International Symposium on Medical Measurements and Applications (MeMeA), 1–6.

19. Manoj, R., **Raj, K. V**, Nabeel, P. M., Sivaprakasam, M., & Joseph, J. (2021). Separation of Forward-Backward Waves in the Arterial System using Multi-Gaussian Approach from Single Pulse Waveform. 43rd Annual International Conference of the IEEE Engineering in Medicine and Biology Society (EMBC), 5547–5550.
20. Nabeel, P. M., **Raj, K. V**, Manoj, R., Abhidev, V. V., Sivaprakasam, M., & Joseph, J. (2021). High-Framerate A-Mode Ultrasound for Vascular Structural Assessments: In-Vivo Validation in a Porcine Model. 43rd Annual International Conference of the IEEE Engineering in Medicine and Biology Society (EMBC), 5602–5605.
21. Manoj, R., **Raj, K. V**, Nabeel, P. M., Sivaprakasam, M., & Joseph, J. (2021). Evaluation of Nonlinear Wave Separation Method to Assess Reflection Transit Time: A Virtual Patient Study. 43rd Annual International Conference of the IEEE Engineering in Medicine and Biology Society (EMBC), 5551–5554.
22. Manoj, R., Nabeel, P. M., **Raj, K. V**, Abhidev, V. V., Sivaprakasam, M., & Joseph, J. (2021). Evaluation of Vascular Pulse Contour Indices over the Physiological Blood Pressure Ranges in an Anesthetized Porcine Model. 43rd Annual International Conference of the IEEE Engineering in Medicine and Biology Society (EMBC), 5594–5597.
23. Navya, R. G, **Raj, K. V**, Nabeel, P. M., Sivaprakasam, M., & Joseph, J. (2022). High Frame-Rate A-Mode Ultrasound System for Jugular Venous Pulse

Tracking: A Feasibility Study. 44th Annual International Conference of the IEEE Engineering in Medicine & Biology Society (EMBC), 4022-4025.

24. Manoj, R., **Raj, K. V**, Nabeel, P. M., Sivaprakasam, M., & Joseph, J. (2022). Evaluation of Pulse Contour Markers using an A-Mode Ultrasound: Association with Carotid Stiffness Markers and Ageing. 44th Annual International Conference of the IEEE Engineering in Medicine & Biology Society (EMBC), 4010-4013.
25. Manoj, R., **Raj, K. V**, Nabeel, P. M., Sivaprakasam, M., & Joseph, J. (2022). Estimation of Characteristic Impedance using Multi-Gaussian Modelled Flow Velocity Waveform: A Virtual Subjects Study. 44th Annual International Conference of the IEEE Engineering in Medicine & Biology Society (EMBC), 2274-2277.
26. Ishwarya, S., Manoj, R., **Raj, K. V**, Nabeel, P. M., & Joseph, J. (2022). Hydrostatic Pressure Compensator for Evaluation of Carotid Stiffness using A-Mode Ultrasound: Design, Characterization, and In-Vivo Validation. IEEE International Symposium on Medical Measurements and Applications (MeMeA), 1–6.
27. Navya, R. G, **Raj, K. V**, Nabeel, P. M., Sivaprakasam, M., & Joseph, J. (2022). Jugular Venous Diameter Measurement Using A-Mode Ultrasound: A Feasibility Study. IEEE International Symposium on Medical Measurements and Applications (MeMeA), 1–6.
28. Manoj, R., **Raj, K. V**, Nabeel, P. M., Sivaprakasam, M., & Joseph, J. (2022). Variation in Pulse Contour Markers on an Anesthetized Porcine During Pressure Perturbation: Association with Local and Regional Stiffness. IEEE

International Symposium on Medical Measurements and Applications (MeMeA), 1–6.

29. Manoj, R., **Raj, K. V**, Nabeel, P. M., Sivaprakasam, M., & Joseph, J. (2022). Assessment of Arterial Reflection Markers using an A-Mode Ultrasound Device. IEEE International Symposium on Medical Measurements and Applications (MeMeA), 1–6.

ACKNOWLEDGEMENTS

As I reach at the cusp of this academic journey, I must acknowledge those who have helped me along the way, beginning with Almighty. As Sir Isaac Newton once said, “I find myself standing on the shoulders of giants who have helped me glimpse new heights of knowledge and achievement”. To these giants, I offer my heartfelt gratitude.

I expressing my utmost appreciation to Dr. Mohanasankar Sivaprakasam, whose discerning eye spotted the potential in me and gave the opportunity to pursue this prestigious doctoral program. I have continually drawn inspiration from his firm insistence on nothing short of excellence. I’m equally grateful to Dr. Jayaraj Joseph, my supervisor, whose exceptional expertise in technology and research acumen have been awe-inspiring. I still remember when I was introduced to the beauty of scientific writing, where his edits transformed my nascent conference paper into an admirable piece. This experience has stirred my appetite for honing this craft. I am deeply indebted to his mentorship and support to navigate the challenges all through my research work.

Further, a heartfelt appreciation also goes out to my doctoral committee members and anonymous reviewers of all my articles, whose insightful feedback and rigorous scrutiny have been instrumental in refining my research. I have utmost respect for the time and efforts they have invested. My sincere endeavor has not been limited to fortifying my aptitude as a researcher alone, but rather, it has been an educational odyssey, that has taught me to be a better mentor and person. All thanks to the distinguished faculty under whom I have taken courses. I am grateful to Dr. Dinu S

Chandran from All India Institute of Medical Sciences, Delhi, for opening his lab to me and helping me understand the medical and physiological aspects of my research.

The orchestration of one's journey depends heavily on the few people and the time you meet them. I am fortunate to have my paths crossed with Mr. Kamlesh Jha, Dr. Ardhendu Saha, and Dr. Sampa das, who catalyzed my interest towards research. I am also thankful to my former co-PhD student and now esteemed doctor, Nabeel, for his invaluable partnership in research. Together, we formed a formidable team, constantly pushing and challenging one another to improve in various aspects of research. This partnership taught me the significance of collaborative work, leveraging each other's unique strengths to achieve success.

Finally, I couldn't have persevered without the moral support of my beloved wife. Surely, she had taken her vows too seriously and partook of my research work by proof reading each and every article with her keen eye for grammar. Despite equating love with time, she generously set aside a significant portion of it for me to indulge into my research problem.

ABSTRACT

KEYWORDS: A-mode ultrasound, central blood pressure, incremental stiffness, intima-media thickness, pulse wave velocity, radio-frequency, ultrafast imaging, vascular aging, wave-reflections.

With respect to preventive and primordial care against cardiovascular diseases, clinical community has been emphasizing the pressing need to assess 'Vascular Ageing' (VA), a continual degradation of vascular structure and function across one's life course. Though, it has been increasingly recognized that measuring the key arterial markers – wall geometry, regional and local stiffness, and central blood pressure (CBP) alongside is pivotal to understanding and monitoring early VA, there is a lack of a single device that features such a measurement of coalescence of markers. From an instrumentation perspective, that implies multiple devices, tedious measurement procedures, the requirement of varied technical expertise, more time, and more cost. Also, there are inherent unsolved technological limitations and challenges associated with measuring a subset of these parameters.

Addressing this gap, in this work, we have developed automated A-mode ultrasound-based methods for multifaceted measurement of the artery's structural and functional properties, catalyzing affordable technology for the comprehensive evaluation of early VA. The first important segment of the work includes development of robust and fully automated methods for assessment of arterial structural properties. The measurement framework involves automated arterial wall recognition, wall motion tracking, and delineation of arterial wall layers' boundaries. As for the framework's first two tasks,

we have developed a dynamic time warping-based method to recognize the arterial walls and track their motion robustly. Further, for the latter task, we have developed an analytic phase-based method that delineates the arterial wall layers from the captured one-dimensional ultrasound frames to measure the instantaneous lumen diameter and a surrogate of wall thickness in real-time. The methods' performance was thoroughly demonstrated via systematic simulations, controlled phantom experiments, and in-vivo human studies (cumulatively on more than 150 volunteers).

The developed automated methods for (i) auto-recognition and tracking of vessel walls, and (ii) diameter and wall thickness measurement were the basis for further work on functional properties assessement. In this regard, we presented the development of fast A-mode ultrasound technology and associated novel methods to measure the functional properties of the arteries in realtime, which include (i) regional stiffness (carotid-femoral pulse wave velocity), (ii) local pulse wave velocity, (iii) its beat-to-beat and intra-beat acute changes, and (iv) CBP. The methods are focused on addressing the crucial methodological considerations in-terms of instrumentation and arterial wave-reflections, which hitherto have limited the reliable measurement of these functional properties in literature. The developed A-mode system and methods were first charecterised by in-silico and in-vitro experiments, to achieve optimal design. The work then thoroughly validates them via controlled in vitro phantom experiments for accuracy and repeatability, and in vivo trials (on more than 250 subjects) for measurement feasibility.

TABLE OF CONTENTS

LIST OF TABLES

LIST OF FIGURES

ABBREVIATIONS

AC	Arterial Compliance
ADC	Analog-to-Digital-Converter
ADL	Augmented Dynamic Lag
AFE	Analog Front End
BA	Bland-Altman
BH	Bramwell-Hill
BMI	Body Mass Index
BP	Blood Pressure
CAVI	Cardio-Ankle Vascular Index
CBP	Central Blood Pressure
cfPWV	Carotid-Femoral Pulse Wave Velocity
CI	Confidence Interval
CoV	Coefficient-of-Variation
CVD	Cardiovascular Diseases
DAQ	Data Acquisition
DBP	Diastolic Blood Pressure
DL	Dynamic Lag
DTW	Dynamic Time Warping
DUT	Device Under Test
ECG	Electrocardiogram
ED	End Diastolic
EF	Endothelial Function
eNOS	Endothelial Nitric Oxide Synthase
EVA	Early Vascular Aging
FMD	Flow-Mediated-Dilation
FN	False Negative
FP	False Positive
FR	Frame Rate

FWTM	Full Width Tenth Maximum
GPU	Graphics Processing Unit
HFR	High Frame Rate
HPF	High Pass Filter
HR	Heart Rate
ICC	Intraclass Correlation Coefficient
IMT	Intima-Media-Thickness
LBNP	Lower Body Negative Pressure Intervention
LFMC	Low-Flow-Mediated-Constriction
LFR	Low Frame-Rate
LI	Lumen-Intima
LM	Levenberg–Marquardt
LoA	Limits of Agreement
LPF	Low-Pass Filter
MA	Media-Adventitia
MAP	Mean Arterial Pressure
MRI	Magnetic Resonance Imaging
NIBP	Noninvasive Blood Pressure
NO	Nitric Oxide
OEM	Original Equipment Manufacturer
PP	Pulse Pressure
PRF	Pulse-Repetition Frequency
PS	Peak-Systole
PTT	Pulse Transit Time
PWV	Pulse Wave Velocity
RF	Radio-Frequency
RMSE	Root-Mean-Square Error
ROI	Region of Interest
SBP	Systolic Blood Pressure
SD	Standard Deviation

sIMT	Surrogate Intima-Media Thickness
SNR	Signal-To-Noise Ratio
SoF	Subset Of Frames
SOI	Segment-Of-Interest
SQ	Signal Quality
SWC	Sliding Window Covariance
TN	True Negative
TP	True Positive
UAP	Unwrapped Analytic Phase
VA	Vascular Aging
WBF	Wall Buffer Function
WT	Wall Thickness

NOTATION

English Symbols

A_D	End diastolic arterial circumference area
A_m, b_m, and c_m	Gaussians model parameters of m^{th} gaussian pulse
$C_{(P)}$	Pressure dependent changes in PWV
D	Inner Lumen diameter
D(N)	Lumen diameter of Nth frame
D(t)	Instantaneous lumen diameter
dA	Instantaneous change in arterial circumference area
DBP_{CAR}	Carotid diastolic pressure
DBP_{FIN}	Finger diastolic pressure
DC	Distensibility
D_D	End-Diastolic diameter
D_F	Diameter close to peak systole
D_{max}	Maximum range of lumen-diameter
D_{min}	Minimum range of lumen-diameter
D_{NW}	Near wall depth
$D_{(P)}$	Pressure dependent lumen diameter
dP	Instantaneous pulse pressure
D_S	Peak Systolic diameter
E	Young's modulus
Ɛ	Error matrix
$\bar{E}(t)$	Over smoothened envelop of echo signal in ROI
$\hat{E}_{CS}(n)$	Modeled envelop of echo signal in ROI
$E_{CS}(n)$	Envelop of echo signal in ROI
E_P	Pressure–strain elastic modulus
E_{pd}	Elastic index
F(t)	Unwrapped analytic phase's first-time derivative subtracted from its mean
f_c	Center frequency of the ultrasound transducer

G_m	Weighted gaussian that modulates m^{th} echo pulse
I(n)	Weighted-impulse train
$\{L_{EV}\}$	Valley locations of the natural logarithm of ROI envelopes
LI_{FW}	Far-wall intima-lumen interface
LI_{NW}	Near-wall intima-lumen interface
Loc_{curr}^{FW}	Locations of far wall in current frame
Loc_{prev}^{FW}	Locations of far wall in preceding frame
Loc_{curr}^{NW}	Locations of near wall in current frame
Loc_{prev}^{NW}	Locations of near wall in preceding frame
L_{SDV_FW}	Set of locations corresponding to the second time-derivative valleys of near wall ROI
L_{SDV_NW}	Set of locations corresponding to the second time-derivative valleys of near wall ROI
MA_{FW}	Far-wall media-adventitia interface
MAP_{CAR}	Carotid mean arterial pressure
MAP_{FIN}	Finger mean arterial pressure
M_{SD}	Second-derivative maxima
P	Transmural pressure
p(n)	Gaussian modulated sinusoidal pulse wavelet
P(t)	Instantaneous pressure
P_ LI_{FW}	Approximate locations of peak intensities for echoes originating from LI_{FW}
P_ MA_{FW}	Approximate locations of peak intensities for echoes originating from MA_{FW}
P_$\bar{E}_{NW}$ and P_$\bar{E}_{FW}$	Locations of peaks in $\bar{E}(t)$
P_LI_{NW}	Approximate locations of peak intensities for echoes originating from LI_{NW}
P_D	End-diastolic pressure
$P_e(t)$	Elastic component of instantaneous pressure
PP_{CAR}	Carotid pulse pressure
P_S	Peak-systolic pressure
$P_v(t)$	Viscous component of instantaneous pressure
$PWV_{(P)}$	Pressure dependent pulse wave velocity

PWV_{BH}	Bramwell-Hill equation-based pulse wave velocity
PWV_D	Pulse wave velocity close to end diastole
PWV_M	Proposed system's pulse wave velocity measurements
PWV_R	Reference pulse wave velocity measurement
PWV_S	Pulse wave velocity close to peak systole
PWV_β	One-point pulse wave velocity
Q	Mass flow rate
r(n)	A-mode echo frame
$r_b(n)$	Blank A-mode frame with an echo at origin
ROI_{FW}	Far wall's region of interest
ROI_{NW}	Near wall's region of interest
S1, S2	Time sequences
SBP_{CAR}	Carotid systolic pressure
SBP_{FIN}	Finger systolic pressure
sIMT(N)	Surrogate intima-media thickness of Nth frame
$s_m(n)$	M^{th} weighted Gaussian modulated sinusoidal pulse in A-mode frame
U	Blood flow velocity
w(n)	White noise
WSA	Wave separation analysis
W_{SC}	Window size for sliding window covariance
Z	Vascular impedance
Z_0	Characteristic impedance

Greek Symbols

η	Viscosity index
β	Stiffness index
Đ	Accumulated error matrix
τ_{NW}	Frame-to-frame shift of near wall
τ_{FW}	Frame-to-frame shift of far wall
τ_m	Delay of mth pusle
θ_m	Phase offset of the mth sinusoid pulse

$\theta(t)$	Instantaneous analytic phase
ψ	Vector containing all Gaussian's model parameters
$\Delta(n)$	Residuals of Levenberg–Marquardt optimization
ΔD	Peak distension
ΔD_M	Measured peak distension
ΔD_R	Reference peak distension
ΔIMT	Intra-cardiac cycle variations of intima-media thickness
ΔPWV	Diastolic-to-systolic change in pulse wave velocity
ΔsIMT	Intra-cardiac cycle variations of surrogate intima-media thickness

CHAPTER 1.

INTRODUCTION

1.1 CARDIOVASCULAR DISEASES AND PREVENTION: WHERE ARE WE?

Cardiovascular diseases (CVD) have grown to be the leading cause of morbidity and mortality in the early twenty-first century, a position it still holds today. Total CVD cases nearly doubled over the last three decades, hitting 523 million in 2019, and likewise, the number of CVD deaths rose gradually from 12.1 million to 18.6 million during this period (Roth et al., 2020). In 2019, an estimated 32 percent of all fatalities worldwide were due to CVDs. Recently, COVID-19 has emphasized the heightened vulnerability that patients with vascular and cardiac risk factors have, with the infection being associated with high mortality in these patients (Crea, 2022). While there is no slowdown but rather a constant increase in CVD cases in third- and second-world countries, it is concerning that CVD rates have begun to re-rise in high-income geographies where they were formerly declining (Roth et al., 2020). Furthermore, premature deaths from CVDs are an alarming element that inhibits healthy and sustainable development in every country worldwide. Heart attacks and strokes account for more than four out of every five CVD deaths, with one-third of these deaths premature in nature (6.2 million between ages 30 – 60 in 2019) (Roth et al., 2020).

These statistics concerning the premature deaths and increased vulnerability of low- and middle-income countries press the need for prevention strategies on multiple fronts, including minimizing the population's exposure to behavioral risk factors and also

facilitating early detection and management at individual level (especially for those that may already be at high risk) (Mendis, 2017). In spite of the efforts to combat it, the current rate of effectiveness in CVD prevention is insufficient to reduce premature mortality by at least a third of what was targeted by 2030 (Mendis, 2017; Roth et al., 2020). It is critical to pay more attention to promoting awareness of cardiovascular health and improved life course for healthy aging. Moreover, the prevention and control strategies do not just need improvement but also should be scalable and affordable, which is the need of the hour. Hitherto, the core of preventive cardiology has been founded on assessing risk factors that predict atherosclerotic events and has been fueled by population-level scoring models derived from traditional risk-factor (Khambhati et al., 2018). However, given the shortcomings of contemporary CVD prevention, the crucial question is whether these traditional scores are adequate?

1.2 PITFALLS OF CONVENTIONAL RISK SCORES

Primordial and primary prevention has been the purpose of years of intense efforts in battling CVDs (Khambhati et al., 2018). Realizing the fact that treatment/interventional decisions are effective when taken into account more than one risk factor, the concept of risk scores has been introduced. Based on these scores, several risk factors are integrated together to predict the risk of CVD (Khambhati et al., 2018). These scores are simple, easy to evaluate, and handy tools for patient education and communication (Lopez-gonzalez et al., 2015). Despite a multitude of scores developed and refined over decades, one sizable limitation is they serve well on a population level rather than for individual or personalized risk prediction and care (Khambhati et al., 2018). They rely on traditional risk factors, which challenges their prediction efficacy for young

individuals who are asymptomatic (devoid of risk factors) but develop CVD (Cooney, Bc, Dudina, Graham, & Bc, 2009). Not only for the younger cohort, but these scores degrade in sensitivity for the older population (Cooney et al., 2009; De Ruijter et al., 2009). For this reason, contemporary strategies recommend the utilization of additional biomarkers, non-traditional risk factors, and selective subclinical atherosclerotic measurements for patients with intermediate or unclear risk (Khambhati et al., 2018; Lloyd-Jones et al., 2019). The solutions in this regard remain still unclear and not validated. The models being population-based, the developed functions potentially underestimate or overestimate risk for different populations – ethnic and social origins, requiring appropriate recalibration (Cooney et al., 2009). Such underestimations also occur from factors such as not adjusting for treatment effects during model generations (Liew, Doust, & Glasziou, 2011). A final universal limitation of these models is their assumption on the effect of risk factors with age; either it is considered constant at differing age or their age-interactions are assumed constant (Cooney et al., 2009). It has been therefore increasingly recognized that for effective individualized prevention and treatment, a paradigm shift is required from only looking at risk factors to considering the damage they cause to the cardiovascular system. More specifically, the focus should be directed to detection of early manifestations of CVD rather than prediction of their risk (Currie & Delles, 2017).

1.3 KNOWLEDGE OF EARLY VASCULAR AGING: A PARADIGM SHIFT

The arterial half of the vasculature is in charge of two critical functions, conducting and buffering (O'Rourke, 2007). As a conduit, it transports nutrients and oxygen to target organs via the blood pumped by the heart. Despite the fact that blood is pumped in a

pulsatile fashion, the peripheral organs are protected by getting a virtually laminar or continuous flow (Nichols, O'Rourke, Vlachopoulos, Hoeks, & Reneman, 2011). This is owing to the heterogeneous construction and complex interplay of the central (large elastic) versus peripheral (muscular resistance) arteries, where the former buffers the blood and complies to the pressure waves generated by the heart. As a result, only arteries with diameters typically greater than 200 μm experience the pulsatile flow as opposed to the arterioles and capillaries (Nichols, O'Rourke, Vlachopoulos, et al., 2011). In addition to the central arteries' buffering function, the difference in their equivalent impedance from peripheral arteries causes arterial wave reflections, which are vital in maintaining the requisite flow dynamics (N. Westerhof & Westerhof, 2012). Due to the ventricular-vascular interplay supported by higher distensibility of central vessels, the wave reflections arrive in the diastolic phase, boosting the diastolic perfusion (O'Rourke, 2007). These hemodynamic facets, which are in synchrony, effectively avoid an increase of pressure in the systolic phase (hypertension) (Van Bortel, Struijker-Boudier, & Safar, 2001). It is these functions that are prey to the risk factors during the course of age, finally leading to CVDs (Currie & Delles, 2017).

Despite the fact that age is a well-known primary risk factor for CVD, its interpretation and definition in the context of cardiovascular health is a passionately debated topic that has remained elusive for years. "Man is as old as his artery" is a famous quotation by Thomas Sydenham (1624–1689) that has been researched rigorously over the years and confirmed by numerous epidemiological and observational studies (Weber & Mayer, 2020). The accumulated evidence suggests that the biological age of blood vessels might differ dramatically from their chronological age, implying that there can be a disparity in the level of damage to vessels among people of the same age (Peter M.

Nilsson, 2008). Aside from the physiological and morphological changes associated with aging that affect cardiovascular function, variances in vascular insults, environment, genetics, and risk factors exposure disrupt the biological-chronological age balance (Bruno et al., 2020; Peter M. Nilsson, 2008). These observations conceived the concept of "Vascular Aging" (VA) and prompted the need to interpret the CV interactions in the light of aging and the pathophysiological states together. On balance, VA is a more refined idea of aging in the context of arterial tree and could be succinctly defined as the cumulative manifestation of stress and wear on the artery, both natural (with age) and pathological. Indeed, with its origin at the fetus stage, VA is a continual process throughout one's life course (Bruno et al., 2020; Peter M. Nilsson, Boutouyrie, & Laurent, 2009). It includes both the arteriosclerotic (dilation and stiffening) and atherosclerotic manifestations and is influenced by several mechanical and biochemical changes such as alterations in the ratio of elastin/collagen, elastin cross-linking, stiffening of smooth muscles, inflammation, and loss of endothelial function (EF) (Boutouyrie, Chowienczyk, Humphrey, & Mitchell, 2021; Rachel E. Climie, Gregory, Denniss, Mynard, & Pepe, 2021).

As stated, the structure and function of the arterial tree normally degrade with age; nevertheless, exposure to accelerators (of damage) – both traditional and sophisticated CV risk factors – leads to premature biological aging, also known as early vascular aging (EVA) (Boutouyrie et al., 2021; P.M. Nilsson, Olsen, & Laurent, 2015). Genetic traits, psychosocial state, lifestyle, stress, and environment further contribute to the elevation of these risk factors (Rachel E. Climie et al., 2021; Peter M. Nilsson, 2008). The VA process appears to be more rapid amongst these susceptible individuals, eventually leading to premature CVD events such as myocardial infarction, coronary

artery disease, stroke, and peripheral arterial diseases (P.M. Nilsson et al., 2015). As a result, it is critical to recognize the involvement of such accelerators in increased CVD risk, even in asymptomatic patients, and to evaluate VA in youth in order to identify individuals who are already at risk from an early age. Children with obesity and blood pressure (BP) were evidenced to have diminished vascular elasticity, and further, it was also demonstrated that improved maintenance of ideal CV health resulted in lower stiffness in adulthood (Aatola et al., 2014; Juonala et al., 2005). Increased stiffness during adolescence predicted the development of hypertension in adulthood, and isolated hypertension at a young age was thought to be benign but was found to increase CV mortality. (Koivistoinen et al., 2018; Yano et al., 2015). Unattended accelerated damage in the elderly can lead to cognitive decline and chronic kidney diseases (Townsend, 2019; Tsao et al., 2016; Waldstein et al., 2008). Therefore, prognostic tools, as such, that can identify early CVD risk by accounting for the damage rather than just risk factors will greatly improve the ability for educated risk stratification, targeted interventions, and individualized care (Currie & Delles, 2017). To accurately assess vascular aging, however, vascular health markers that reliably reflect the onset and progression of early vascular damage must first be recognized.

1.4 UNDERSTANDING STIFFENING: KEY TO IDENTIFYING EVA MARKERS

As mentioned in the earlier section, the conduiting (perfusion) and cushioning (windkessel) functions of the arterial system are the key targets of vascular aging that eventually lead to CVDs. To keep the vascular functions from declining, the molecular, cellular, tissue, and organismal systems work in concert, allowing for a plethora of sophisticated mechanisms and adaptation (Rachel E. Climie et al., 2021; O'Rourke,

2007). These complex interactions between the cellular and structural components of the vessel wall result in vascular stiffening, a process that is natural and continually progresses with age (Zieman, Melenovsky, & Kass, 2005). Hence, understanding stiffness and the mechanisms involved in its development serve as the key to identifying markers of EVA (Weber & Mayer, 2020). It may also be noted that the stiffness progression in arteries across the vasculature is non-uniform, where it is more prominent in the central than the peripheral (Zieman et al., 2005). For this reason, central arterial stiffening has become a credible proxy for VA (Boutouyrie et al., 2021; Bruno et al., 2020). In this section, an overview of the mechanisms of central arterial stiffening (both structural and material) has been presented, thereby pointing to the key markers of EVA.

The constitution of the three layers of the central arteries – intima, media, and adventitia give them their elastic nature (Figure 1.1(a)) (Boutouyrie et al., 2021; Wagenseil & Mecham, 2009). The intimal layer is the inner-most layer exposed to blood flow primarily hosts the endothelial cells. The medial layer is characterized by elastic lamellae arranged concentrically, between which exists smooth muscle cells, collagen, and glycosaminoglycans. Finally, the primary component of the adventitia is collagen. This elastin-rich media is responsible for the elasticity and the windkessel function of the large arteries (Boutouyrie et al., 2021; Wagenseil & Mecham, 2009). As the arteries serve their function using the passive components, there is a complex interaction that exists between endothelial cells in the intimal layer and the smooth muscle cells in the medial layer (Figure 1.1(b)). These combinedly perform mechano-sensing and -regulation for local homeostasis against the stresses experienced by the arterial walls (Humphrey & Schwartz, 2021). There are two primary stresses – (i) shear stress and

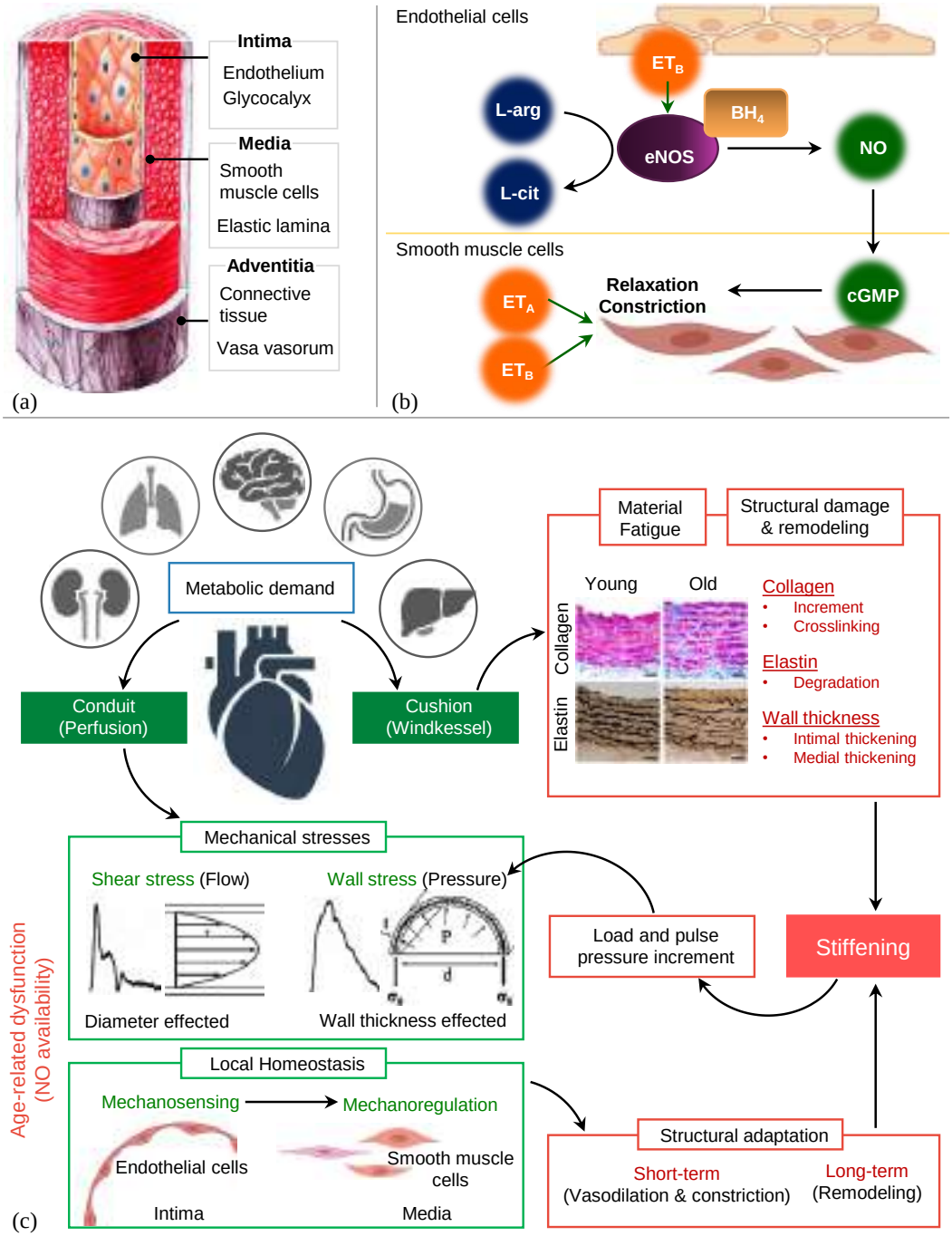

Figure 1.1 (a) Wall composition of central arteries, (b) Cellular mechanotransduction in arterial walls, and (c) Mechanisms of progressive stiffening.

(ii) wall stress. The shear stress is flow-mediated, where due to homeostasis, any change in flow is accommodated by an increase in diameter (vasodilation) by cubic root times (Boutouyrie et al., 2021). Similarly, the wall stress increases as a result of increased

pressure, which requires an increase in wall material or thickness (vasoconstriction) for homeostasis (Boutouyrie et al., 2021). So, the interactions of the intimal and medial layer cells lead to short-term changes in vascular tone and the structure – diameter and wall thickness (Humphrey & Schwartz, 2021).

The endothelium is responsible for producing nitric oxide (NO) for such short-term regulations, which, when impaired, affects the homeostasis, increasing the stresses on the walls and leading the further decline (Marín, Yubero-Serrano, López-Miranda, & Pérez-Jiménez, 2013). Hence loss of EF is considered to be the genesis of stiffening (Verdecchia, Angeli, & Taddei, 2006). As shown in Figure 1.1(b), endothelial nitric oxide synthase (eNOS) oxidizes L-arginine for producing NO, and tetrahydrobiopterin (BH_4) is an essential cofactor for the same (Epstein, Moncada, & Higgs, 1993). The dysfunction progresses with age, reducing the NO availability, and this is multifactorial (Marín et al., 2013) – (i) Deficiency of cofactors and substrates – BH_4 and L-arginine, (Eskurza, Myerburgh, Kahn, & Seals, 2005; Santhanam, Christianson, Nyhan, & Berkowitz, 2008) (ii) enhanced Endothelin (ET-1) pathways, (Thijssen, Rongen, Van Dijk, Smits, & Hopman, 2007) (iii) increased oxidative stress (reactive oxygen species), (Taddei et al., 2001) (iv) increased inflammation pathways, (Csiszar, Wang, Lakatta, & Ungvari, 2008; Rodríguez-Mañas et al., 2009) (v) senescence of progenitor cells (Erusalimsky & Skene, 2009), and (vi) impaired smooth muscle function (Montero, Pierce, Stehouwer, Padilla, & Thijssen, 2015). These age-associated degradations cause a decline in cellular turnover and an increase in senescent cell accumulation (Marín et al., 2013). NO and ET-1 are further responsible for the production rates of extracellular matrix leading to changes in material stiffness (Humphrey, 2008). Phenotypic modulation of smooth muscle cells is another contributing factor that leaves the wall

susceptible to calcification (Vattikuti & Towler, 2004). In conclusion, over the course of time, such cellular level dysfunction leads to structural maladaptation contributing to stiffness (Hahn & Schwartz, 2009; Humphrey & Schwartz, 2021). Not only does dysfunction affect the stiffness, but recent studies have also underlined the vice-versa (Peng, Haldar, Deshpande, Irani, & Kass, 2003).

Following the cellular components, the actual structural components, primarily the proteins elastin and collagen, are responsible for the stiffening process, as shown in Figure 1.1(c). With aging, the balance between elastin and collagen gets deranged. (i) elastin degrades, and (ii) collagen increases, making the arteries progressively stiffer (Zieman et al., 2005). The elastin is majorly produced during the initial postnatal life and diminishes with age-associated fatigue and fracture, giving it a half-life of a few decades (O'Rourke, 2007). Conversely, Collagen is produced as per homeostatic dysregulation and also abnormally due to diabetes and hypertension (Johnson, Baugh, Wilson, & Burns, 2001; C. Xu, Zarins, Pannaraj, Bassiouny, & Glagov, 2000). Collagen cross-linking also adds to this misbalancing process (McNulty, Mahmud, & Feely, 2007). With increased stiffness, the load on the heart increases, leading to an increase in pulse pressure, to which the artery reciprocates with structural adaptation increasing the wall material (Figure 1.1(c)). Therefore, though locally the stresses are regulated, the distensibility is further lost, causing the loss of windkessel function and increasing the load on the heart further. In fact, the pressure and stiffness are strongly tied together in this manner, causing an increase in each other in a vicious cycle (Humphrey, Harrison, Figueroa, Lacolley, & Laurent, 2016). The cross-talk between central and peripheral arteries is also an accompanying factor in the stiffening of central vessels. Hence, even without any external agents or accelerators, the stiffness of the walls, due

to their slow but dynamic structural components, keeps consistently progressing with age. In summary, (i) EF declines, notedly way before the onset of actual stiffening, (ii) wall material responsible for elasticity degrades in the arteries, more prominently in central arteries, (iii) there is a transfer of load-bearing from elastin to collagen, (iv) the pressure that contributes to the load-dependent stiffening increases, and (v) there is slow but constant structural remodeling (maladaptation), all of which are involved in progressive stiffening. Hence focusing the non-invasive measurements on these aspects is the key to identifying EVA syndrome.

The function of the endothelium can be assessed non-invasively by quantifying flow-mediated-dilation (FMD) and low-flow-mediated-constriction (LFMC). Studies show that vascular function decline, measured as FMD%, is strongly associated with age, and the rates/trends vary amongst women and men (Holder et al., 2021). The strong confounding effect of pressure on progressive-stiffening is another important aspect which makes central arterial pressure measurement very relevant. The non-invasive central blood pressure (CBP) measurement has gained much attention in recent years owing to its clinical value above and beyond traditionally measured brachial BP (McEniery, Cockcroft, Roman, Franklin, & Wilkinson, 2014). Discrepancies also exist in CBP values among subjects with identical brachial BP; therefore, the peripheral measures are not always a surrogate of the central ones (H. M. Cheng et al., 2020; Stéphane Laurent, Sharman, & Boutouyrie, 2016). In this regard, CBP independently reflects the actual load on the heart and other target organs, with better implications than the brachial BP (Kollias, Lagou, Zeniodi, Boubouchairopoulou, & Stergiou, 2016; J. E. Sharman & Laurent, 2013; Yamashita, Dohi, Takase, Sugiura, & Ohte, 2014). Stiffness is measured non-invasively as regional pulse wave velocity (PWV) metrics

(example: carotid-femoral pulse wave velocity (cfPWV), brachial-ankle PWV, cardio-ankle vascular Index, etc.) and also, local metrics (such as stiffness-index β, Peterson modulus of elasticity, Young's modulus, distensibility) (Stephane Laurent et al., 2006; Mackenzie, Wilkinson, & Cockcroft, 2002; Segers, Rietzschel, & Chirinos, 2020). The trends of these markers again manifest consistent increments with age (Mattace-Raso et al., 2010; Uejima et al., 2019). Local PWV from target vessels is a new emerging marker that poses relatively greater instrumentation challenges. Finally, geometric measurements are also important, which are performed by ultrasound means as diameter and intima-media-thickness (IMT). These are crucial in furnishing some of the enlisted stiffness markers. With age, the available data clearly demonstrates that both the diameter and IMT increase and also the ratio of IMT to diameter (Engelen, Ferreira, Stehouwer, Boutouyrie, & Laurent, 2013; I. C. L. van den Munckhof et al., 2018; I. van den Munckhof et al., 2012). From the literature, it is clear that there is a multitude of measurements that can be performed non-invasively to gain insight into the EVA. However, a huge discrepancy between the perceived importance and clinical adoption of assessing EVA is also recognized; the question remains why?

1.5 GAPS IN ADOPTION OF VASCULAR AGING ASSESSMENT

It is underwhelming to know that in spite of the clinical community (both researchers and clinicians) recognizing the importance of VA assessment, its adoption has been abysmally low. This gap has been well underlined by European countries, where rigorous efforts were put towards establishing a network – VascAgeNet for refining, harmonizing and promoting the use of VA concepts in clinical practice (Mayer, Climie, Hametner, & Bruno, 2020). One of the primary unmet needs the network aims to

address is affordable and easy-to-use devices that can perform VA measurements (Rachel Emma Climie, Mayer, Bruno, & Hametner, 2020; Mayer et al., 2020). Such devices were deemed necessary to cater to studies and screening at large scale and in resource-constrained settings (more common in middle and low-income countries). In fact, similar opinions resulted from a survey conducted by the network in recent years (Triantafyllou et al., 2022). The deductions from the survey were based on responses submitted by 104 participants (43% clinicians from fields of cardiology, endocrinology, and internal medicine). Though ~62% of responses rated that VA assessment is very important (5/5 score), only ~13% reported that it is clinically being measured. The two largest factors limiting VA clinical assessment were time and cost (as non-refundable tests and expensive equipment).

Clinically, cfPWV, local stiffness indices, ultrasound measurements (IMT), FMD, CBP, and magnetic resonance imaging (MRI)- measurements were recognized as vascular health markers via which VA can be monitored. While there are many heterogenous approaches and markers to assess VA, there is no univocal opinion on which one or combination is the best choice. As the stiffness metrics constitute both the material stiffness (caused purely due to the wall degradation) and structural stiffness (dependent on the geometry), it was deemed relevant to measure them along with the geometry for appropriate interpretations (A. Avolio, 2013). The same applies to measuring the pressure alongside the stiffness to disentangle their inter-dependency (A. Avolio, 2013; Spronck, 2021). There has been evidence that, for seemingly healthy subjects (classified as normotensives based on brachial BP), a diminishing EF is related to elevated central pulse pressure (PP) and stiffness (Verdecchia et al., 2006). Various studies have shown inclusion of markers such as IMT, FMD, ankle-brachial index, etc.,

improved risk prediction and patient classification, especially for the intermediate-risk group (Criqui et al., 2010; Nambi et al., 2010; Yeboah et al., 2012). Evidence also points out that regional and local stiffness markers are not interchangeable and offer different implications on CV health (A. Avolio, 2013; Quinaglia et al., 2018; Segers et al., 2020). Therefore, the notion of measuring a combination of markers may be of superior value as opposed to any single marker. But, from an instrumentation perspective, that implies multiple devices, tedious measurement procedures, the requirement of varied technical expertise, more time, and more cost. In this regard, a single, easy-to-use, affordable tool performing an automated multifaceted assessment of the artery's structural and functional properties would accelerate studies conjoining pulsology and endotheliology and facilitate the development of integrated vascular-age scores (Verdecchia et al., 2006) for CVD risk management.

1.6 OBJECTIVES AND SCOPE OF RESEARCH

On balance, while it has been increasingly recognized that simultaneously measuring the key vascular health markers – wall geometry, regional and local arterial stiffness, and CBP alongside is pivotal to understanding and monitoring EVA, there is a lack of a single device that features such a measurement of coalescence of markers. Independent works have introduced ultrasound-based techniques for measuring a majority (not all the alluded ones) of the enlisted vascular aging markers, which makes it a potential option. These techniques are built around image-based ultrasound systems, employing B-mode, M-mode, M-line, and Doppler-mode scans, typically done with linear array vascular probes containing 128-512 sensing elements. (A detailed review of these methods will be presented in the succeeding chapter). Though the available

ultrasound systems are cheaper than other imaging modalities, the required measurement features are seldom available in affordable entry-level devices. Rather the systems are costly, non-portable, non-field amenable, and demand a trained sonographer. Additionally, for some the markers advanced ultrafast imaging capabilities are required which is not supported by traditional systems in clinics. A-mode systems, scanning single-line one-dimensional frames, are potentially more advantageous: (i) extensively reduce the computational load, (ii) support high-speed ultrasound applications and multimodal sensor integrations, and (iii) by virtue can realize simpler, affordable, and portable technologies. However literature indicates a lack of such robust methods or technologies in this regard.

In summary, inspite of the potential that ultrasound modalities possess, hitherto, there is virtually no system that measures all the listed vital vascular health markers simultaneously. On the other hand, the ultrasound techniques that are introduced for individual markers, are unapplicable or non-robust for A-mode systems (that offer much needed advantages). These fundamental gaps has strongly motivated the research in this thesis. The primary goal of the work is to develop and validate intelligent A-mode ultrasound methods and a device for assessing the structural and functional properties of an artery – lumen diameter, IMT, local and regional PWV, and CBP. The methods were developed not only to perform on par with the existing state-of-the-art but they were also aimed to solve the existing instrumentation challenges pertaining to the measurement of individual parameters. Such specific challenges are listed in Table 1.1 as a preview and are detailly discussed in the next chapter, post presenting a review of the existing literature. The review will also provide an appreciation for the advantages offered by the developed A-mode methods.

Table 1.1 Existing gaps in ultrasound measurement of the enlisted structural and functional properties

Structural properties	Gaps common to geometrical assessment	• Only B-mode or M-line methods exist requiring imaging ultrasound systems. • Features are not existent in entry-level devices. • Non-robust for single-scan line ultrasound frames.
	Auto-recognition of arterial wall location in the ultrasound frames	• Current image-based methods require ultrasound frames with an artery always present and can't differentiate its absence. • Perform poorly if there are hyperechoic regions near to that of arterial walls.
	Auto-tracking of arterial wall location in the ultrasound frames.	• When wall echoes overlap with other structure echoes, the methods can't discriminate between the motions of overlapped sub-echoes. • Accuracy is challenged if artery wall echoes are very near to static or other dynamic ones, resulting errors in tracked distension wave morphology
	Diameter and wall thickness measurement	• Majority are offline image-processing tools. • Existing single scan line methods use only amplitude features and perform poorly. • Even amongst image-based methods, very few track instantaneous IMT.
Functional properties	Regional stiffness (cfPWV)	• Ultrasound techniques are limited and only offer sequential recording of carotid and femoral pulses. • Clinical ultrasound devices don't facilitate multimodality integration
	Local stiffness (carotid PWV)	• Conventional scanners yield extremely poor-resolution pulse waveforms. • Dedicated advanced ultrafast ultrasound systems are required, which are costly and complex. • Even then, majority are offline techniques and limited technologies exist with real-time feedback features.
	Pressure-dependent acute changes in local PWV	• For direct measurement of changes within the cardiac cycle the instrumentation challenges of measuring local PWV apply. • By far, there has been only one group that has performed such direct measurement. • Wave-reflections compromise the accuracy of instantaneous local PWV measurement near peak systole • Indirect measurement of instantaneous local PWV require simultaneous pressure and diameter recordings from single-site, posing instrumentation challenges of sensor fusion and multimodal system integration.
	Central Blood pressure	• Existing methods are calibration-based using peripheral waveforms. • Can't capture the differential response of central BP versus peripheral to physiological/ pharmacological interventions • Only two groups have attempted calibration-free technique, but the systems are again image-based with added cost, complexity, and non-real-time measurements

The specific objectives that were pursued to accomplish the goal of the research are listed below,

- Objectives I: To develop and validate a method for robust recognition and tracking of arterial wall locations from A-scan frames.
- Objective II: To develop and validate an automated A-mode method for evaluation of arterial structural properties – diameter, IMT, and their intra-cardiac cycle changes.
- Objective III: To design and develop a prototype device, a high frame rate (~1 kHz) multimodal system supporting the acquisition of dual-channel A-mode ultrasound and pressure signals. This will also include designing and developing compact probes for sensor fusion.
- Objective IV: To develop and validate A-mode method(s) to measure local PWV and its intra-cardiac variations online using the developed high frame-rate ultrasound prototype device.
- Objective V: To develop and validate a A-mode based method and system for measuring regional stiffness – cfPWV, alongside the local stiffness.
- Objective VI: To develop and validate a method to evaluate CBP in a calibration-free manner using the structural properties and local PWV measured by the high frame rate A-mode system. Subsequently, verify system's reliability to track instantaneous physiological perturbations in CBP.

Figure 1.2 illustrates the dashboard of this research, indicating the key contributions and outcomes of the work.

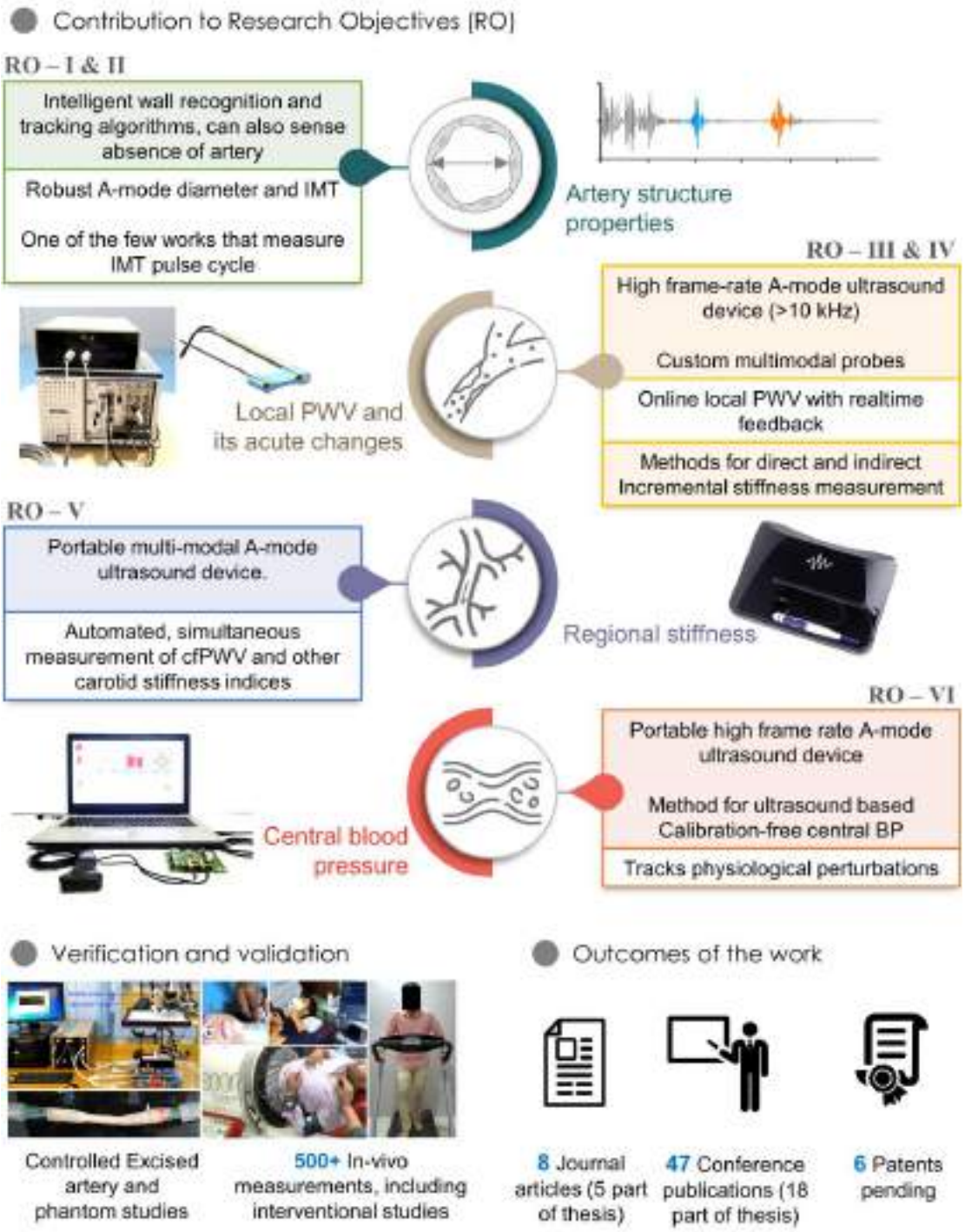

Figure 1.2 Research work dashboard of the thesis: key contributions and outcomes

1.7 ORGANIZATION OF THE THESIS

The thesis is organized into eight chapters, as given below:

Chapter 1 introduces the motivation of the thesis, especially, focusing on the adoption of VA concepts as a paradigm shift in CVD prevention strategies and the associated unmet needs in terms of instrumentation. It further narrates the goal and the specific objectives of this research work.

Chapter 2 reviews the existing literature on state-of-art non-invasive techniques for the measurement of VA markers. In light of that, the chapter presents the identified overall and specific gaps that are addressed in this work.

Chapter 3 presents the work done as part of *objective-I*, a method for arterial wall recognition and tracking from A-scan frames. It starts with a brief theoretical background on dynamic time warping (DTW), a tool on which the working principle of the proposed method relies. Further, the technical aspects and validation of the proposed method are discussed. The material provided in this chapter has been accepted for publication as a peer-reviewed journal paper and also published in a series of conference proceedings.

Chapter 4 presents a method for automated measurement of diameter and wall thickness (WT) using A-scan ultrasound (*objective-II*). The method exploits analytic phase concepts introduced at the beginning of the chapter. The chapter then discusses the method's comprehensive validation via simulations, in-vitro and in-vivo

experiments. The material provided in this chapter has been published as a peer-reviewed journal paper and in a series of conference proceedings.

Chapter 5 presents the design and development of a prototype multi-modal, dual-channel ultrasound system that can perform fast scans (frame rates up to 1 kHz), as per *objective-III*. The chapter further discusses a method for real-time local PWV measurement using this system and its validation (*objective-IV*). The material provided in this chapter has been published as a peer-reviewed journal paper and also in a series of conference proceedings.

Chapter 6 presents the development and validation of an A-mode ultrasound-based measurement of regional arterial stiffness (as cfPWV) exploiting the fast scanning capability of the system disclosed in Chapter 5 (*objective-V*). The material provided in this chapter has been published as a peer-reviewed journal paper.

Chapter 7 presents further work on *objective-IV,* which includes the investigations pertaining to the measurement of acutely pressure-dependent changes in the local stiffness (PWV). The challenges associated with such measurements were solved by employing the device presented in Chapter 5 in conjunction with novel methods proposed in this work. Especially, the chapter demonstrates the measurement of incremental PWV, which was minimally explored and for which direct techniques are not yet proposed. The material provided in this chapter has been published as a peer-reviewed journal paper and also in a series of conference proceedings.

Chapter 8 presents the ability of the device proposed in chapter 5 to measure CBP (*objective-VI*). The pertaining mathematical models were developed earlier by our group, but a unimodal system to implement the models was lacking, constraining the usability factor. However, the work presented in this chapter addresses that and demonstrates real-time beat-to-beat CBP measurements, even under hemodynamic perturbations via lower body negative pressure intervention (LBNP). The material provided in this chapter has been published as a peer-reviewed journal paper.

Chapter 9 Concludes the thesis, presenting an outlook.

CHAPTER 2.

MEASUREMENT OF VASCULAR AGEING MARKERS: STATE-OF-ART AND CHALLENGES

In Chapter 1, the current challenges associated with adopting VA assessment in clinical settings were briefly highlighted, which was the motivation of this work. Ultrasound based methods have been actively researched to measure various VA markers, and that suggests the potential of this modality to serve as a single device for a multi-faceted measurement. The instrumentation solutions this work offers in this regard are as-well based on ultrasound, more specifically A-scan. Therefore, this chapter briefly introduces the role of ultrasound in VA assessment, few fundamental concepts of biomedical ultrasound imaging, and then reviews the literature concerning the measurement methods of the various VA markers. Though not limited to, the review would majorly focus on the ultrasound-based approaches and the gaps in the state-of-the-art pertaining to each marker's measurement. It would provide deeper insights into what has still to be solved as well as an appreciation for the goals of this research.

This chapter is partially adapted from the post-print version of:

Raj, K. V., Joseph, J., Nabeel, P. M., & Sivaprakasam, M. (2020). Automated measurement of compression-decompression in arterial diameter and wall thickness by image-free ultrasound. Computer Methods and Programs in Biomedicine, 194, 1–12.

Raj, K. V., Nabeel, P. M., Sivaprakasam, M., & Joseph, J. (2022). Time-warping for robust automated arterial wall-recognition and tracking from single-scan-line ultrasound signals. Ultrasonics, 126, 106828.

Raj, K. V, Nabeel, P. M., Chandran, D., Sivaprakasam, M., & Joseph, J. (2022). High-frame-rate A-mode ultrasound for calibration-free cuffless carotid pressure: feasibility study using lower body negative pressure intervention. Blood Pressure, 31(1), 1–11.

Raj, K. V, Nabeel, P. M., & Joseph, J. (2022). Image-Free Fast Ultrasound for Measurement of Local Pulse Wave Velocity: In Vitro Validation and In Vivo Feasibility. IEEE Transactions on Ultrasonics, Ferroelectrics, and Frequency Control, 69(7), 2248–2256.

Joseph, J., **Raj, K. V**, Nabeel, P. M., Shah, M. I., Bhaskar, A., Ganesh, C., & Seshadri, S. (2020). ARTSENS Pen — portable easy-to-use device for carotid stiffness measurement: technology validation and clinical-utility assessment. Biomedical Physics & Engineering Express, 6(2), 1–12

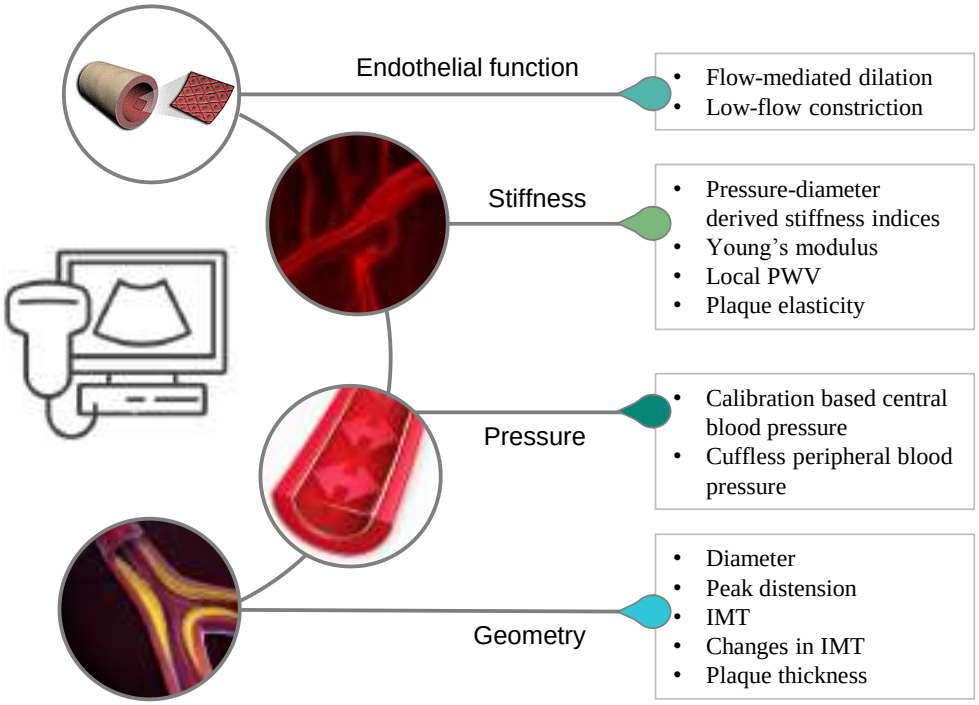

Figure 2.1 Vascular aging measures where ultrasound modalities and methods were demonstrated in literature

2.1 ULTRASOUND FOR VASCULAR AGEING

Ultrasound-based measures play an important role in CV health care, and had been demonstrated to measure several paramters that reflect vascular aging (as shown in Figure 2.1). They offer non-invasive means to perform, primarily, doppler flow and vascular structure measurements. Because they are less expensive and more widely available than other imaging modalities, they have been popularly part of epidemiological and interventional studies as an indicator for atherosclerotic diseases. Vascular ultrasound has been extensively researched over the last two decades for measuring the health of arteries via several dynamic properties, which are among the prominent VA markers (Jurasic, Lovrencic-Huzjan, Bedekovic, & Demarin, 2007; Reneman, Meinders, & Hoeks, 2005; Roman et al., 2006). It enables the measurement of the vessel's local elasticity (derived from the relationship between pressure and

structure), reactivity, and functional properties (Jurasic et al., 2007; Reneman et al., 2005; Roman et al., 2006). Plaque elasticity can be measured using specialized ultrasound modes, such as strain and shear wave imaging (Mahmood, Ewertsen, Carlsen, & Nielsen, 2016; Sigrist, Liau, Kaffas, Chammas, & Willmann, 2017). Advanced systems offering high temporal resolution (via. ultrafast scanning) were devised to measure the local PWV as well (Apostolakis, Nandlall, & Konofagou, 2016; Nagaoka et al., 2015). In recent years, its scope has also extended to the measurement of central and cuffless BP (Rastegar, GholamHosseini, & Lowe, 2019; Seo, Pietrangelo, Lee, & Sodini, 2015; C. Wang et al., 2018). The following portion of this section presents general insights into the fundamentals of ultrasound. Such background is intended to provide the readers a continuity while going through the literature review on the state-of-art techniques to measure various VA markers.

2.1.1 General introduction to clinical ultrasound

Ultrasound refers to the high-frequency acoustic waves (mechanical; >20 kHz) that are propagated through a medium; more specifically, transmitted and received by an ultrasound transducer. In clinics, the commonly available diagnostic ultrasound scanners have operating frequencies of 2 – 18 MHz. Diagnostic ultrasonography is a popular imaging technique that allows visualization of subcutaneous structures and measurement of blood flow while offering the advantages of being harmless, easy to use, and not requiring specialized installation (Carovac, Smajlovic, & Junuzovic, 2011). The imaging technique leverages the differences in absorption and reflection abilities among various tissue interfaces for mapping their locations. Reflection-based imaging is more widely used where short ultrasound pulses (few cycles) are transmitted to the

body, and the echoes reflecting from each tissue interface (discontinuities in acoustic impedance) are captured as a time function so that the time-of-flight yields the depth information. The pulses are periodically transmitted and received, giving the technique a name called pulse-echo operation. There are some key terminologies associated with reflection-based imaging that may be relevant for briefing.

a) Center-frequency: The excitation frequency of the transducer, which also determines the frequency of the transmitted pulses.
b) Scan-line: In pulse-echo operation, a transducer element is excited to transmit an ultrasound pulse and obtain information of a single line along the axis in which it propagates, which is termed a scan line.
c) Scan-depth: Once the transducer emits the pulse, it's configured and kept to receiving mode for a particular time period. Within this period, the maximum depth from which the reflected echoes could be captured is called scan-depth.
d) Radio-frequency (RF) frame: A single frame containing echoes' information from the origin of the transmit pulse to the scan depth. This is a one-dimensional signal resulting from a transducer element.
e) Pulse-repetition frequency: As a single transducer is pulsed at regular intervals of time, the frequency of those excitations is called pulse-repetition frequency (PRF). This frequency is translated to the scan-rate or frame-rate (FR).
f) Echo-sampling rate: For the acquisition of RF signals to the digital domain, the scanners sample them at a designated rate (typically 30 – 50 MHz).
g) Axial resolution: The smallest separation distance required between two echogenic structures along the scan axis to resolve them as distinct structures. Typically, this depends on the spatial length of the transmit pulse.

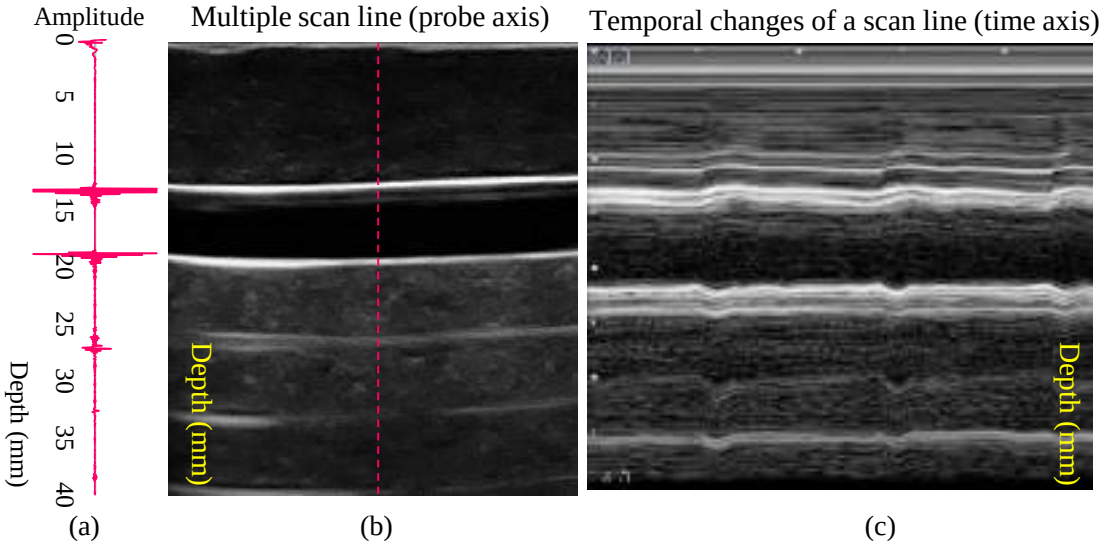

Figure 2.2 Example (a) A-scan frame, (b) B-mode frame, and (c) M-mode scan resulting from imaging a dynamic blood vessel phantom.

h) Lateral resolution. This applies to only two-dimensional scans where an array of ultrasound transducer elements is sequentially excited, yielding information from multiple lines. In this case, the lateral resolution is the separation distance between the structures along the array axis over which they can be resolved.

In the ultrasound scanners, reflection-based imaging is performed in four modes, each differing in the level and packaging of the information – (i) A-mode, (ii) B-mode, (iii) M-mode, and (iv) Doppler-mode. *A-mode* is the simplest of scan types where only a single element ultrasound transducer performs the imaging through the body. This results in a single line of RF signal as a function of depth, with echoes originating from all the tissue interfaces along the scan axis. An example A-scan signal frame imaging the dynamic vessel phantom is shown in Figure 2.2(a). Hence the name A-mode or 'amplitude-mode' where the scan provides a one-dimensional signal with echoes of varying amplitudes (dictated by the echogenicity of an interface) along the depth. *B-mode* imaging results from scanning multi-lines (M-line) employing an ultrasound

probe with an array of transducer elements. The information is then a scan of two-dimensional plane, with one axis representing the scan axis and the other array axis, in Figure 2.2(b). Unlike A-mode, where the frame is the actual signal, in B-mode, the information from multiple A-lines is used to construct a gray scale image. The amplitudes along each line are now represented as pixels with an intensity value mapped to a gray level (256 levels coded using 8 bits). *M-mode* or motion-mode is animated sequences of a particular line in a B-mode frame. Since each echo, according to its amplitude, is assigned a brightness level, the rapid sequence in M-mode exhibits the motion of echoes as shifts in the bright portions. This allows investigation of the echoes' time-dynamics (Figure 2.2(c)). Finally, *Doppler* mode allows the determination of the scatters' velocities, more specifically present in the blood. In this mode, the frequency shifts in the received echo signals are analyzed, which are directly proportional to the scatter velocity.

2.2 MEASUREMENT OF ARTERIAL STRUCTURE

Lumen diameter, wall thickness (as IMT), and plaque thickness are the commonly measured properties of the arterial wall geometry. As per guideline recommendations, these measurements using an image-based ultrasound are performed by scanning the artery in the longitudinal axis. A typical image (B-mode) of the artery, such as carotid, exhibits a double line pattern for the proximal / near wall (NW) and distal / far wall (FW). Pignoli et al. were the first to characterize this pattern and define the source of the various echoes corresponding to the arterial wall structure in the B-mode image (Pignoli, Tremoli, Poli, Oreste, & Paoletti, 1986). The adventitia and intima layers of the arterial walls, in contrast to the tunica media, are highly echogenic, producing the

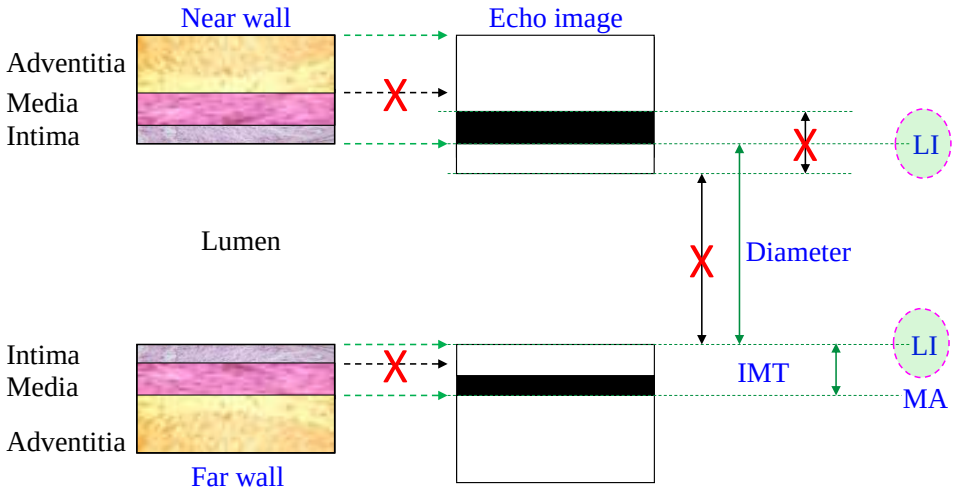

LI : Lumen-Intima Interface; MA : Media-Adventitia Interface

Figure 2.3 Source of the double-line echo pattern of walls in an ultrasound scan of artery. The anatomical interfaces that can be confidently mapped from the echo pattern are also depicted and thereby, illustrating valid measurement of IMT and diameter

bright echoes that form the double line pattern (Figure 2.3). Of note, the thickness of these echoes does not represent any anatomical feature. Instead, their leading edges define the anatomical location of the structures or interfaces they have originated from (Pignoli et al., 1986; Wikstrand, 2007). In practice, this intrinsic double-line pattern of the arterial walls is used to segment the lumen-intima (LI) and media-adventitia (MA) interfaces of the respective walls for the measurement of the WT and diameter. The interfaces of the arterial wall layers that are identifiable on a B-mode image are labeled in Figure 2.3 (Wikstrand, 2007).

It may be noted that the LI interfaces are identifiable for the NW and the FW, whereas the MA interface is only identifiable for the FW. Therefore, a valid measurement of the wall thickness, as defined by IMT, is performed on the FW by measuring the distance between the anatomical locations of the LI and MA interfaces (Touboul et al., 2012; Wikstrand, 2007). Likewise, the lumen diameter measurements are performed between

the locations of LI interfaces (leading edges on the LI echoes) of the walls (Wikstrand, 2007). Manual methods require an expert with sufficient experience to delineate the LI and MA interfaces. The results being subjective to the operator, are likely to suffer substantial inter- and intra-operator variability (Loizou, Pattichis, Nicolaides, & Pantziaris, 2009; Peters & Bots, 2013). For this reason, either computerized semi-automated or automated methods are required, with the latter more preferred. The framework of a fully automated method precludes automated recognition of artery in an ultrasound frame, and tracking it, in-case measurements are required in multiple frames, and auto-gating a region of interest (ROI) to perform segmentation of interfaces within it, as opposed to the full frame.

2.2.1 Computerized artery wall identification and motion-tracking

As seen, since ultrasound provides an easy means to access the dynamic properties of the arteries, it is imperative the measurements are fully automated. One of the fundamental steps in this regard is to computerize the segmentation procedure for the arterial walls. Computerized segmentation of arterial walls from the ultrasound frames assures the measurement is accurate, minimally variable, and convenient (Eigenbrodt et al., 2007; Kumar et al., 2018; Wikstrand, 2007). Structure recognition is the first step in the segmentation process, which is a high-level operation that requires intelligence and is normally performed by experienced operators (Udupa et al., 2006). Because arteries are mobile structures, recognizing them also entails tracking their movement in each scan frame, which adds to the difficulty. The automation of the two tasks – artery wall recognition and motion tracking – is critical for real-time vascular property assessment and other online screening avenues in cardiovascular diagnostics.

A few attempts to automate the process of arterial-wall recognition have been made so far, with the majority of them relying on B-mode imaging data. Fan et al. presented an approach based on local variance analysis (Fan, Santago, Jiang, & Herrington, 2000), which assumes that the artery is horizontally oriented on the image. Another robust approach was developed by Sifakis et al. (Sifakis & Golemati, 2014). Molinari et al. proposed and analyzed three methods: one based on low-pass filtering, thresholding, and local variance analysis, the other on feature extraction, fitting, and classification, and the third on derivative Gaussian edge analysis (Delsanto et al., 2007; Molinari, Meiburger, et al., 2012; Molinari, Zeng, & Suri, 2010b). The most recent of these methods, derivative Gaussian edge analysis, had higher accuracy and a lower processing overhead (Molinari, Meiburger, et al., 2012). Other image processing and transformation approaches, such as spokes-ellipse (D. C. Wang et al., 2009), Hough transform-based (Golemati, Stoitsis, Sifakis, Balkizas, & Nikita, 2007), and External regions of extremum level (EREL) (Faraji, Cheng, Naudin, & Basu, 2018), are again applicable only to images. The use of deep learning networks to detect wall regions is also discussed in the literature (Azzopardi, Camilleri, & Hicks, 2020; Park, Seo, Choi, & Lee, 2022; Yang, Faraji, & Basu, 2019). These have proven to be particularly useful for intravascular ultrasound imaging (Faraji et al., 2018; Yang et al., 2019), which is more prone to substantial image artifacts. Hoeks et al. pioneered work on M-line RF signal processing techniques in this area (A. P.G. Hoeks, Brands, Smeets, & Reneman, 1990; Arnold P.G. Hoeks et al., 1997). Attempts were undertaken in the later decade to automate the complete framework that makes up the tasks of recognition and tracking (Brands, Hoeks, Willigers, Willekes, & Reneman, 1999; Arnold P.G. Hoeks et al., 1997; Kanai & Koiwa, 2000; Rossi, Brands, & Hoeks, 2008). Rossi et al. (Rossi et al.,

2008) developed a method for extracting M-lines directly from B-mode images and performing real-time vessel wall recognition.

One pronounced limitation with the reported wall recognition methods is their inherent assumption that the frames being processed consist of the artery walls and it is the operator's task to discern the presence or absence of the walls while recording the ultrasound frame sequences. Automation is this regard and a feedback to the operator regarding the status of vessels presence in the frame would help realize real-time completely operator independent measurement framework. Such may be necessary if the device is being operated by any general practitioners or in settings as primary healthcare centres or field where expert sonographers may not be available. Further, the recognition and tracking methods mentioned above are all based on utilizing the amplitude or intensity profile characteristics of the echoic artery walls and anechoic lumen. Their robustness is challenged if the desired wall echo is overlapping with an adjacent hyperechoic echo (example: initial saturation region of the walls) or in close proximity to static or dynamic echoes, with introduction of uncertainties in the measurement of parameters (such as local PWV) that require accurate diameter waveform morphology. Finally, existing methods work best with image-based scans rather than for single-line A-scans.

2.2.2 Diameter and wall thickness measurement

A large section of approaches for automated diameter and IMT measurement is applicable to B-mode images, and relatively fewer works are based on RF signal processing. Multiple articles have reviewed several automated and semi-automated techniques that employ segmentation on B-mode ultrasound images to evaluate the

diameter and IMT articles (Kumar et al., 2018; Loizou, 2014; Molinari, Zeng, & Suri, 2010a). Early methods introduced for computerized segmentation of artery layers date back to the late 80's (Pignoli et al., 1986; Touboul et al., 1992). Since then, methods have been evolving, even until recent years, and the current automated ones are able to provide highly accurate measurements (~10 μm error) on par with the manual. The techniques can be categorized to edge- and gradient-based (Faita et al., 2008; Molinari, Pattichis, et al., 2012; Selzer, Mack, Lee, Kwong-Fu, & Hodis, 2001), local statistics-based (Delsanto et al., 2007), gradient-based (Freire et al., 2009; Stein et al., 2005), dynamic programming (D. C. Cheng, Schmidt-Trucksäss, Liu, & Liu, 2010; Liang, Wendelhag, Wikstrand, & Gustavsson, 2000; Wendelhag, Liang, Gustavsson, & Wikstrand, 1997; Zahnd, Orkisz, Sérusclat, Moulin, & Vray, 2014), snake-based (D. chuan Cheng, Schmidt-Trucksäss, Cheng, & Burkhardt, 2002; Loizou et al., 2012; Loizou, Pattichis, Pantziaris, Tyllis, & Nicolaides, 2007), Hough-transformation (Golemati et al., 2007; X. Xu, Zhou, Cheng, Song, & Li, 2012), Nagakami distribution (Destrempes, Meunier, Giroux, Soulez, & Cloutier, 2009), active contours (Bastida-Jumilla et al., 2013; Gutierrez et al., 2002; Santhiyakumari, Rajendran, Madheswaran, & Suresh, 2011), model-based (Ilea, Duffy, Kavanagh, Stanton, & Whelan, 2013; Rossi, Brands, & Hoeks, 2010) and machine learning (Menchón-Lara, Bastida-Jumilla, Morales-Sánchez, & Sancho-Gómez, 2014; Shi et al., 2019; W. Xu et al., 2022).

Each method is subject to its own challenges, which include (i) robustness to speckle noise, (ii) sensitivity to initial contouring and seed points, (iii) dependency on ultrasound scan settings, (iv) requiring manual post-correction, and (v) applicability to a limited number of frames (Kumar et al., 2018; Loizou, 2014; Molinari et al., 2010a). A very important aspect coveted in recent applications is segmentation from videos

(frame sequences). Such is useful for measuring dynamic properties of arterial walls, which make use of continuous waveforms (changes within each cardiac cycle) as opposed to a single value (Bianchini et al., 2010; Boutouyrie et al., 2001; Pascaner et al., 2015; Polak, Meisner, Pencina, Wolf, & D'Agostino, 2012; Selzer et al., 2001; Zahnd et al., 2017a). There are only a few video processing techniques, all of which have been introduced in the last decade (Bianchini et al., 2010; D. C. Cheng et al., 2010; Ilea et al., 2013; Loizou et al., 2012; Zahnd et al., 2017b). Since the alluded methods are applicable to images, they accompany the cost and scalability constraints associated with B-mode imagers when compared to the A-mode systems. Only a few of the listed methods are completely automated without requiring any manual intervention and the systems fully integrated with such tools are scarcer. It may be remembered that offline processing comes with a vulnerability of scan recordings being under-qualitied. Also, such automated online methods may be required to track the intra-cardiac cycle changes in the wall structural parameter and provide phase annotated values.

Contrary to using B-mode images, Hoeks et al. pioneered work on the methods that employed M-line processing (A. P.G. Hoeks et al., 1990). The developments in the M-line processing method, in the later decade, provided solutions for tracking the arterial walls, simultaneous measurement of diameter and WT that was even automated and real-time (Brands, Hoeks, Ledoux, & Reneman, 1997; Brands et al., 1999; Arnold P.G. Hoeks et al., 1997; Willekes et al., 1999). However, the advanced features as those and several other automated tools for performing simultaneous measurements of arterial diameter, wall thickness, and their intracardiac cycle changes are not augmented to the entry-level devices and are inherently expensive. There is virtually any method that is robust of A-scans in the literature.

2.3 MEASUREMENT OF REGIONAL AND LOCAL STIFFNESS

PWV, which is a measure of the propagation speed of blood pulse across the arterial trajectory, is a popular metric of stiffness. It is a structural stiffness metric and is directly related to Young's modulus of elasticity (the material stiffness metric) by the Moens and Korteweg (M-K) equation (Nichols, O'Rourke, Vlachopoulos, et al., 2011). cfPWV is the current guideline-recommended gold-standard estimate of arterial stiffness, and it represents the PWV of the aortic trunk (Wilkinson et al., 2010). This parameter represents the global stiffness of the vasculature as a whole (regional measurement) rather than providing target-specific localized information. There are several commercially available devices, such as SphygmoCor, Complior, PulsePen, etc., that are used to measure cfPWV employing applanation tonometry (Chirinos, Segers, Hughes, & Townsend, 2019). In these devices blood pulses are measured from carotid and femoral artery sites, for which the tonometer is used either at carotid or both the sites. There are single-site regional PWV measuring devices as well, such as Arteriograph and Mobil-O-Graph (Nabeel, Raj, Joseph, Abhidev, & Sivaprakasam, 2020). In some studies, the regional PWV was also measured between other trajectories, e.g., brachial-to-ankle and heart-to-ankle, with the help of bladder-type pressure cuffs (Chirinos et al., 2019). Such systems are aimed at substituting the use of a tonometer that requires technical expertise to achieve high fidelity signals for PWV measurement. These devices, both tonometry and non-tonometry based are incapable of measuring local stiffness measurements. A few of them purport to measure CBP, but their accuracy and clinical value are limited. There are rarely any studies that have reported use of ultrasound for the measurement of regional PWV. This primarily is constrained by non-

integrability of multimodal recording features to the existing image-based ultrasound systems, which is needed to acquire the pulse pair.

There exist local stiffness metrics, typically measured from superficial central artery like carotid employing ultrasound imaging. The measures include pressure–strain elastic modulus (E_P), arterial compliance (AC), and stiffness index (β), all of which require diameter and pressure information from the same site (Mackenzie et al., 2002; Segers et al., 2020). Often, they are calculated using carotid diameters and brachial pressures, given the challenges associated with measuring central pressure from the carotid artery. Ultrasound echo-tracking modalities like ALOKA eTracking and Esaote ArtLab are commercially available B-mode ultrasound devices that can measure these enlisted local stiffness metrics (Carerj, Nipote, & Zimbalatti, 2005; Palombo et al., 2012). For these measurements, the scan rate requirement from the ultrasound instrument is low (< 70 Hz), which makes them feasible to measure with traditional ultrasound. In the recent decade, local PWV has gained the attention of researchers and clinicians in the cardio-vascular domain. It is the measure of PWV from a single arterial site or across a small segment of the target arteries. In our recent review, we have summarized more than 35 clinical studies that underline the clinical relevance of local PWV (Nabeel et al., 2020). It potentially sheds light on localized abnormalities in elasticity, pathophysiological implications, and therapeutic effects on individual target arteries. In addition to the paradigm shift it brought on the way arterial stiffness is viewed and adopted clinically, it has also fueled advancements in several alleys such as in-stent restenosis detection, fetal hemodynamics monitoring, central and cuffless BP assessment, etc. (Nabeel et al., 2020).

Methods for evaluating local PWV can be broadly enlisted into two categories – (i) indirect evaluation based on bio-mechanical expressions and (ii) direct measurement based on the blood pulse transit features. The methods in the first category, such as PD, PU, ln(D)U, $\sum^2$PU, $\sum^2$PR, D^2P, QA techniques, require a distinct pair of physiological signals for local PWV evaluation (Borlotti, Li, Parker, & Khir, 2014; Nabeel et al., 2020; Segers, Swillens, Taelman, & Vierendeels, 2014). These distinct combinations are drawn from two of the following signals – transmural pressure (P), blood flow velocity (U), mass/volume flow rate (Q), and inner lumen diameter (D) that is simultaneously recorded from a single arterial site. Apart from the pressure, the rest signals are non-invasively measurable (though in a sequential manner) using an ultrasound system. However, reliable non-invasive pressure signal recording from the target site is challenging for the respective methods. Additionally, a majority of these approaches are based on the assumption that the pulse waveforms are free from the reflections in the early systolic phase of the cardiac cycle. On this note, there has been a conflict of opinions on the reliability of the majority of these methods (Borlotti et al., 2014; Segers et al., 2014). The second category methods, on the other hand, require identical blood pulse signals from two or multiple local locations of an arterial segment, from which the information regarding the inter-pulse time delay is directly measured for local PWV evaluation. Although these methods appear deceivingly straightforward, the accuracy is sensitive to several factors that affect the characteristic features of the recorded blood pulses' morphology (Nabeel et al., 2020). Further, it is crucial to select an appropriate sensing modality, else corruption due to tissue transit delays, microcirculation, motion artifacts, etc., may factor in, especially for skin surface pulse detectors (Nabeel et al., 2020).

While imaging modalities such as ultrasound are mandatory to implement the ‘category–(i)’ methods non-invasively, they have also been actively employed for ‘category–(ii)’ methods. In this regard, ultrasound systems provide a direct measure of arterial blood pulse in the form of instantaneous lumen diameter or blood flow parameters, the morphology of which is not corrupted by the tissue between the transducer and artery. Also, they have easy access to the deeper vessels. There are, however, instrumentation and methodological considerations associated with ‘category–(ii)’ methods that impose a challenge for image-based systems. The transit features such as time delay that is to be measured between the blood pulses are in the order of just ~5–25 ms, considering measurement segments are smaller than 100 mm. Therefore, to record blood pulse signals with a high temporal resolution, provision for fast imaging with scan rates way higher than that supported by typical clinical ultrasound systems is required. State-of-the-art techniques use M-line with reduced scan lines (Hermeling, Reesink, Reneman, & Hoeks, 2007; J M Meinders, Kornet, Brands, & Hoeks, 2001), plane wave imaging (Bercoff, 2011; C. Huang, Ren, & Luo, 2014; Luo, Li, & Konofagou, 2012), multiline transmission (Bercoff, 2011), compounding (Nagaoka et al., 2015; Nauleau, Apostolakis, McGarry, & Konofagou, 2018), ECG gated-acquisition (Pernot, Fujikura, Fung-Kee-Fung, & Konofagou, 2007), etc. for improved scan rates up to few hundreds or thousands of hertz.

These cutting-edge imaging systems pose stringent hardware requirements built around field programmable gate arrays and graphics processing units with high computational power (Bercoff, 2011). Nevertheless, they only perform offline or non-real-time PWV evaluation, otherwise with only sophisticated and expensive processors. These complex

systems are non-scalable and ill-suited for out-of-clinic field applications, especially in resource constraint settings with a scarcity of specialized operators and experts.

2.4 PRESSURE DEPENDENCY OF STIFFNESS

As seen in section 1.4, structural stiffness such as PWV is dependent on pressure. In this regard, it is relevant to understand that this dependency exists in two ways: (i) stiffness is affected by acute changes in pressure and also, due to (ii) long term phenomenon of hypertension resulting from actual re-modelling (Bortolotto et al., 1999; Stéphane Laurent & Boutouyrie, 2015). Meaning, an increase in stiffness during the instant of measurement need not necessarily imply that wall material is stiffer (due to degradation), rather it could also be due the non-linear elastic nature of the artery (Alberto Avolio, 2013). Further, it also underlines that the interpretation of similar PWV values in two individuals can entirely differ. The pressure-stiffness dependency has, therefore, drawn the attention of several researchers and led the efforts toward measuring pressure-standardized stiffness measurements (Giudici, Khir, Reesink, Delhaas, & Spronck, 2021; Humphrey et al., 2016; Spronck et al., 2015). One of those first attempts introduced cardio-ankle vascular index (CAVI), a stiffness parameter that was claimed to be pressure-independent, modeled based on the exponential relationship between pressure and diameter (Shirai, Utino, Otsuka, & Takata, 2006). A decade post-CAVI, a refined parameter $CAVI_0$ was proposed to overcome its residual pressure dependency (Spronck et al., 2017). The correction was made to the stiffness index formula for this standardizing the DBP with a reference pressure of 100 mmHg. A cold pressor based interventional investigation corroborated the analytical analysis

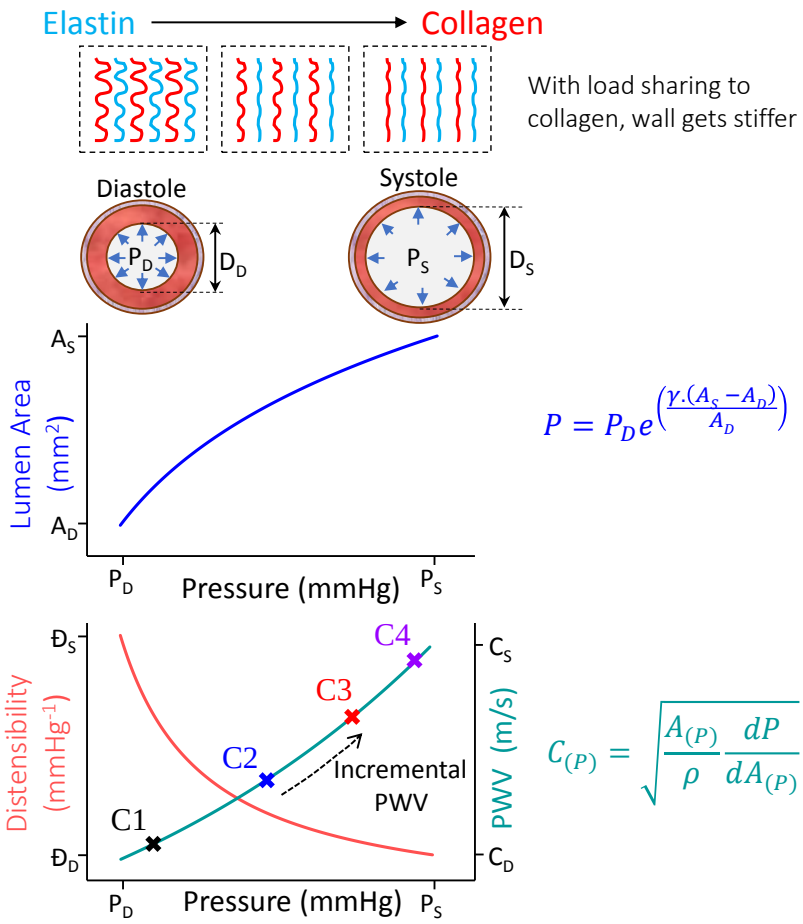

Figure 2.4 Depiction of hyper-elastic nature of artery due to transfer of load-bearing from elastin to collagen. Consequently, the elasticity of artery acutely diminishes with increase in pressure within each cardiac cycle, correspondingly leading to PWV increment.

pertaining to CAVI and $CAVI_0$, where it was demonstrated that the latter didn't change during the entire test, even when the pressure perturbed (Mestanik et al., 2020).

Arterial walls are hyper-elastic in nature, suggesting that their stress-strain relationship is not linear, resulting in an increase of Young's modulus with the circumferential stress (Alberto Avolio, 2013; Shadwick, 1999). As the load bearing is transferred from elastin to collagen with distending artery, the artery wall is stiffer at higher pressures (Figure 2.4). This is termed as incremental stiffness of the artery, where the wall material is stiffer at higher pressures (translating to higher stress). It is known that PWV is directly

related to Young's modulus; hence it is also higher at elevated pressures (Segers et al., 2020), as illustrated in the last row of Figure 2.4. Though with increased pressure (from diastolic P_D to systolic P_S value), the diameter stretches (from diastolic D_D to systolic D_S value) and wall thickness decreases reducing the PWV, the dependence of Young's modulus is stronger, causing it to effectively increase. Hence, PWV within a cardiac cycle is not constant as well but increases from end-diastole (ED) to peak-systole (PS). Additionally, any temporary perturbations in BP consequently perturb the PWV. Measuring such pressure-dependent changes in PWV provides a direct experimental means for pressure-standardization across individuals (Spronck, 2021). But the measurement of instantaneous PWV (C(P)) changes, especially within each cardiac cycle, is challenging. In fact, the non-invasive measurement of incremental PWV has attracted the interest of investigators only in recent years, and its clinical importance is still emerging. Only a few studies have estimated the incremental PWV using theoretical means, and fewer have directly measured it (An, Li, Shi, Ge, & Li, 2022; Hermeling et al., 2012; X. Li et al., 2017; Mirault et al., 2015; Nabeel, Joseph, Karthik, Sivaprakasam, & Chenniappan, 2018; Yin et al., 2021). These studies have demonstrated the pathological significance of measuring both the systolic and diastolic PWVs in diagnosing Ehlers–Danlos syndrome (Mirault et al., 2015), increased left ventricular mass index (Hermeling et al., 2012), hypertension and cardiovascular risks (X. Li et al., 2017), and microangiopathy in patients with type 2 diabetes mellitus (An et al., 2022). Our group has also developed mathematical models for calibration-free CBP evaluation using measured diastolic-to-systolic changes in local PWV (Nabeel et al., 2018), which emphasizes the scope of this measure above and beyond local PWV from a single fiducial point.

Bramwell-Hill (BH) equation relates the PWV to changes in BP and arterial diameter, fundamentally the slope of the P-D curve (Bramwell & Hill, 1922; Segers et al., 2014). Therefore, to evaluate incremental PWV approaches in literature have measured the slope changes in P-D from the diastolic-to-systolic phase. It requires measurement of high-fidelity diameter and pressure waveforms ideally from the same arterial site in a simultaneous fashion. State of the art techniques use B-mode or M-mode ultrasound modalities for estimation of arterial diameter waveforms (Jan M. Meinders & Hoeks, 2004a). Local pressure waveforms are typically obtained using applanation tonometric transducers. However, simultaneous acquisition of diameter and pressure waveforms using such modalities are prone to practical limitations due to the design form factor of the probes. Further, the waveforms can be subject to inherent phase delays due to (i) the acquisition of the desired waveforms from two distinct arterial sites separated by a significant distance and (ii) the lack of time synchronization and dissimilar frequency characteristics between the acquisition modules of pressure and diameter waveforms (Arnold P.G. Hoeks, Willigers, & Reneman, 2000). Also, due to viscoelastic nature of the artery a hysteresis may exist between pressure and diameter, which requires compensation (Bia et al., 2005). There have been approaches to model the pressure using the diameter waveform and brachial pressures, instead of directly measuring it (Jan M. Meinders & Hoeks, 2004a). However, the pressure modeling in those works involved a simple single-exponential P-D relationship, which may not be adequate (Hermeling et al., 2010). Direct assessment of incremental PWV is possible by measuring instantaneous pulse transit features within the cardiac cycle. Specialized ultrafast ultrasound technologies were reported for such measurements (An et al., 2022). Arterial wave reflections, primarily arriving during early systolic phase, are a

noted concern for performing direct measurement of incremental PWV (Hermeling, Reesink, Reneman, & Hoeks, 2008). As alluded earlier, the sophisticated nature of such instruments, and lack of real-time local PWV, still are gaps that are unmet. Realtime measurements are also mandatory for reliable tracking of beat-to-beat variations in PWV that may have induced from perturbations in pressure.

2.5 CENTRAL BLOOD PRESSURE MEASUREMENT

Existing non-invasive CBP measuring devices, both cuff-based and cuffless, are calibration-based methods that make use of brachial BP and/or peripheral waveforms to derive the CBP measures (H. M. Cheng et al., 2020; McEniery et al., 2014). There are few ultrasound-based techniques proposed for cuffless measurement of central pressure, all of which are yet to be translated to clinical practice (Jaffe, Zubajlo, Daniel, & Anthony, 2022; Nabeel et al., 2018; Seo et al., 2015; C. Wang et al., 2018; Zakrzewski & Anthony, 2018; Zakrzewski, Huang, Zubajlo, & Anthony, 2018). While a majority of them are calibration based a few operate without the need for calibration. The available calibration / transfer-function approaches are discussed later as this section follows. Calibration-free based approaches are believed to provide more reliable and physiologically relevant information, over and beyond the brachial BP. A force-coupled ultrasound method was proposed as one of the calibration-free techniques which records the deformation of artery via imaging in proportion to the subjected hold-down force and estimated the transmural pressure (Jaffe et al., 2022; Zakrzewski & Anthony, 2018; Zakrzewski et al., 2018). Our group has proposed a multimodal ultrasound system to measure the local hemodynamics – PWV and diameter, and calculate the CBP (Nabeel et al., 2018). A similar approach with different mathematical

models was introduced another group for calibration-free BP (Giudici, Palombo, et al., 2021). These the major studies on the calibration-free approach.

There are several commercial devices as well, a majority of which make use of applanation tonometric principles (Papaioannou et al., 2016). The tonometer probe tip hosts a pressure transducer that senses the skin surface pressure pulses originating from a superficial artery, provided the artery is applanated with a hold-down pressure. In various approaches, tonometric waveforms are recorded from different arterial sites, carotid, brachial, and radial being the most common and processed (H. Miyashita, 2012). Based on the recording site, the processing principles include direct substitution, general or adaptive transfer functions, pressure pulse analysis, N-point moving average, and blind system identification (Gao et al., 2016; H. Miyashita, 2012). Simple/direct substitution is a method where the carotid tonometric pulses are assumed to be a proxy of the aortic pulses and are calibrated to diastolic blood pressure (DBP) and mean arterial pressure (MAP) from the brachial artery, which scales the systolic blood pressure (SBP). The underlying rationale is that DBP and MAP can be assumed constant throughout the arterial tree in the absence of hydrostatic offset. Tonometry provides optimal pulse quality when there is a supporting structure against which the artery could be applanated. Hence morphological corruptions and bias are excessively subject to the operator's skill and the feasibility on patients. This limitation makes the carotid artery a difficult site, and there have been studies that recommend against carotid tonometry (O'Rourke, 2016). Similar DBP-MAP calibration approaches were then applied to diameter pulses acquired from the carotid artery using ultrasound means. A patch-based ultrasound was developed to apply this method in a practical manner, yielding continuous CBP measurements (C. Wang et al., 2018).

Transfer-function-based approaches measure the pressure pulse from the radial artery, which is translated to CBP measurements, and such use generalized or adaptive functions (Gao et al., 2016; H. Miyashita, 2012; Xiao, Qasem, Butlin, & Avolio, 2017; Xing et al., 2019; Yao et al., 2018). For the generation of transfer function models, different studies have used both invasive and non-invasive reference pressures (H. M. Cheng et al., 2020; H. M. Cheng, Lang, Tufanaru, & Pearson, 2013). The last category of methods uses morphology features from radial pulse waveforms directly to yield the CBP estimates. Another popular category of methods that have been employed for estimating peripheral BP, but could also be potentially adapted for CBP, is the use of models that scale PTT or PWV to the BP values (Ding et al., 2017; Douniama, Sauter, & Couronne, 2009; Patzak, Mendoza, Gesche, & Konermann, 2015; Rastegar et al., 2019; Yao et al., 2018; Yousefian et al., 2019). An ultrasound based technique was recently proposed in this regard that measures carotid PWV to yield calibration-based CBP (Seo et al., 2015). A common challenge associated with all these enlisted non-invasive approaches is their inherent dependence on peripheral pressure measurements. Their model accuracy and/or the errors of peripheral BP measurements compromise the accuracy (Kayrak et al., 2010; Stéphane Laurent et al., 2016). Machine learning approaches purport to provide a calibration-free BP as they may not require recording surrogate pressures at the time of measurement (Rastegar et al., 2019; Xiao et al., 2017; Xing et al., 2019). However, they do use prior BP information as ground truth for training the architectures on large data sets that contain inherent trends. Such approaches should be less useful for clinical applications as they would fail to provide reliable measurements unless they have been thoroughly trained for diverse populations and pathophysiological cases (Rastegar et al., 2019). Recent evidence has shown that

interventions such as pharmacological and hemodynamic modulations amplify the discrepancies between the central and peripheral pressures (H. M. Cheng et al., 2013), which poses a further challenge to aforesaid methods. Heart rate dependency of pulse pressure amplification is another major factor that causes ambiguities. A pacing study has demonstrated such dependencies very clearly (Wilkinson et al., 2002).

2.6 SUMMARY OF RESEARCH GAPS IDENTIFIED FROM THE LITERATURE SURVEY

A universal gap identified from the surveyed literature is the lack of a single device that is able to perform multifaceted measurements of the vascular aging marker that were deemed important for compressive assessment of vascular health status and monitoring of EVA. Further, the available independent devices are individually costly, resulting in a non-affordable equipment setup if multifaceted measurement is desired. Also, multiple devices require differing technical expertise, hence demanding dedicated operators. This has made such facilities non-scalable, non-amenable to the field, and has inadvertently affected their availability to resource-constrained settings (including low- and middle-income countries). As stated towards the beginning of the chapter (section 2.1), ultrasound-based techniques have been popular for measuring a majority of the enlisted vascular aging markers; though not all. Although the available ultrasound systems are cheaper than other imaging modalities, the required measurement features are seldom available in affordable entry-level devices. The automated B-mode image-processing tools for wall structure and local stiffness measurements come as specialized software packages, and markers like local PWV, and CBP can only be measured with advanced ultrasound systems offering high scan-rates or multimodal features. Such high scan-rate systems, because of their reliance on image construction and processing,

require processors with high power and are limited when it concerns real-time assessment. The same applies to even traditional scanners, where the offered software tools support offline processing, otherwise are high-end integrated systems, as B-mode data is two dimensional, involving higher computational overhead. Integrating other sensing modalities with B-mode scanners is not straight-forward given the larger form-factor of the probe, limited hardware provision and difficulties in acquisition synchronization. Those provisions are required for the measurement of regional PWV and also for standardizing arterial stiffness measurements against BP. In summary, even if the feasibility of using image-based (B-mode) ultrasound for the measurement of various VA markers (except for regional stiffness) has been demonstrated in the literature, the gaps in measuring all markers with the same device, limited availability of fully automated and online/real-time assessment features, and affordability still exist. Considering the gaps pertaining to image-based scanners, A-mode methods if robust, can provide several advantages over them: (i) extensively reduce the computational load, (ii) facilitate online measurement, (iii) support high-speed ultrasound applications and multimodal sensor integrations, and (iv) allow the development of simpler, affordable, and portable A-mode ultrasound technologies. However, as seen from the reviewed literature (presented in this chapter), A-mode based instrumental solutions are abysmally low. In-addition to the instrumentation challenges, there are also methodological limitations pertaining to the measurement of individual markers which were listed throughout the review presented in this Chapter that needs to be addressed.

CHAPTER 3.

AUTOMATED METHODS FOR ROBUST ARTERIAL WALL-RECOGNITION AND TRACKING FROM A-MODE ULTRASOUND FRAMES

As alluded in Chapter 2 (Section 2.2.1), the automated frame work for ultrasound based vascular measurements require computerized arterial wall recognition and motion-tracking tasks as pre-requisite. In this context, the current ultrasound approaches for these tasks are suited for image-based B-mode or M-mode scans but not applicable or adequately robust for single-line image-free scans. Therefore, in this chapter, we introduce a novel dynamic time-warping based technique to recognize, locate and continuously tracks the arterial wall echoes within A-mode frames. It combinedly analyses the time-variant effects of tissue dynamics on the phase and the amplitude profile of echoes to evaluate the arterial wall dynamics from the A-mode scans. The method constitutes independent algorithms for recognition and motion-tracking, which are detailed in here. Its performance was assessed based systematic simulations, controlled in-vitro experiments, and in-vivo trials. Pertinent study methodology, results and key observations are also summarized in this chapter, followed by conclusion.

This chapter is partially adapted from the post-print version of:

Raj, K. V., Nabeel, P. M., Sivaprakasam, M., & Joseph, J. (2022). Time-warping for robust automated arterial wall-recognition and tracking from single-scan-line ultrasound signals. Ultrasonics, 126, 106828.

Raj, K. V., Joseph, J., Nabeel, P. M., & Sivaprakasam, M. (2020). A Dynamic Time Warping Method for Improved Arterial Wall-Tracking using A-mode Ultrasound Frames : A Proof-of-Concept. IEEE Symposium on Medical Measurements and Applications (MeMeA), 1–6. Bari.

Raj, K. V., Nabeel, P. M., Sivaprakasam, M., & Joseph, J. (2021). Phantom evaluation of a time warping based automated arterial wall recognition and tracking method. IEEE International Symposium on Medical Measurements and Applications (MeMeA),

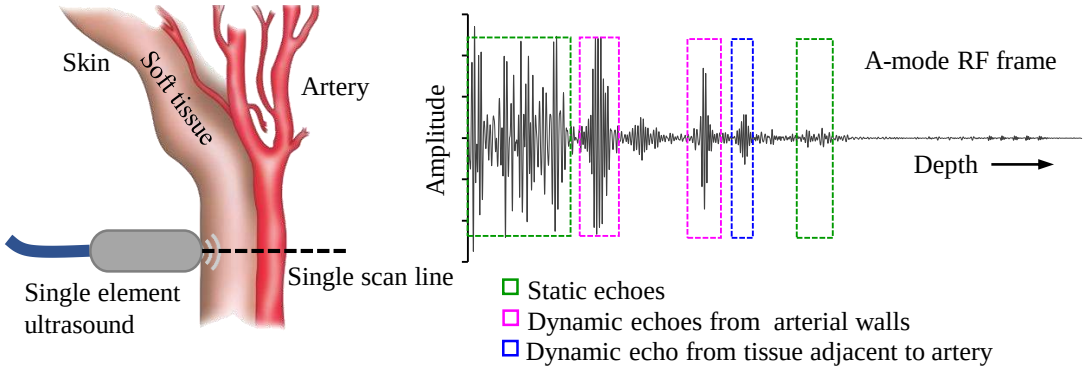

Figure 3.1 A sample RF frame obtained using such a single element ultrasound transducer, with labelled static and dynamic echoes.

3.1 THEORETICAL BACKGROUND

3.1.1 A-mode ultrasound scan of artery

An A-mode ultrasound scan of an artery produces a one-dimensional RF frame (shown in Figure 3.1) made up of multiple individual echoes that can be divided into three groups. These are: (i) Static echoes that do not possess any phase change when observed in consecutive frames. The tissue-gel interface and other stationary tissue structures are the most common sources of these echoes. (ii) Dynamic echoes from the NW and FW of the artery. Because the artery is comprised of three layers: intima, media, and adventitia, and the media being hypo-echogenic, each wall produces an echo signal that is constituted of two gaussian modulated sinusoidal pulses (distinct or overlapping). The vessel's thickness dictates the extension of the composite echoes of the NW and FW. The lumen region between the NW and FW is hypoechogenic in nature, devoid of any echoes, therefore yields a characteristic space between them (lumen, representing the inner diameter of the scanned vessel). The characteristics – the spacing between the wall echoes, the width of each wall echo, and the expected depth of the NW – are all dependent on the artery being scanned and are found in the literature (Zhu, Yuan, Yang,

& Yeo, 2015). Due to the expansion and relaxation of the artery, these two echoes move in opposing directions. In addition, the tracing of their motion has a charectristic morphology. (iii) Dynamic echoes from other mobile structures such as tissue close to arterial walls and, on exceptional cases, an extra vessel such as a jugular vein proximal to the carotid artery. However, in other circumstances, such as when jugular echoes are present, the traced wall motion becomes a distinguishing feature when compared to the artery's motion. These definitions serve as the foundation for automating the detection and tracking of artery wall locations in A-mode frames.

3.1.2 General introduction to DTW

DTW (Müller, 2007) is mathematical tool that provides the similarity between any two finite temporal series. It accomplishes this by applying nonlinear time-warping operations (shrinking, stretching, and shifting) on segments of one of the sequences in order to match the other, and then computing a similarity metric. It's widely used in pattern matching, speech recognition at different speeds, gesture and analysis, and time series clustering (Hachaj & Piekarczyk, 2019; Izakian, Pedrycz, & Jamal, 2015; Müller, 2007). The scope of this tool also extends to analysis of biomedical signals, such as feature extraction of brain data (Karamzadeh, Medvedev, Azari, Gandjbakhche, & Najafizadeh, 2013), cardiac arrhythmia detection (Raghavendra, Bera, Bopardikar, & Narayanan, 2011), electromyography based handwriting recognition (G. Huang, Zhang, Zheng, & Zhu, 2010), and even non-invasive assessment of BP (Pielmus, Klum, Tigges, Orglmeister, & Urban, 2020). The DTW operations can also calculate the shifts required in each sample of one sequence to align the two sequences being compared.

3.1.3 Concept of DTW for wall-recognition and tracking

As narrated in Section 3.1.1, the echo signals in RF frames acquired from a target vascular site contain information about the position and dynamics of the artery walls. The method described here is a time-domain approach that use the DTW concept to extract the locations and motion of artery walls from scanned echo signals. DTW was used to compare any two successive one-dimensional RF frames and generate a time-variant signal known as the 'dynamic lag (DL) waveform.' This waveform depicts the shift in individual RF frames caused by the mobility of various tissue structures along the scan line, and hence aids in the recognition of wall echoes. As a result, the procedure is completely automated and may be applied to raw RF data acquired from even a single channel (A-mode).

3.1.4 Estimation of dynamic lag waveform

This section explains how to evaluate the DL waveform, which is required to implement the proposed approach. The DL illustrates the relative shifts suffered in various regions of sequences when the consecutive two frames are treated as two sequences S_1 and S_2. The misalignment between S_1 and S_2 (comprising of N samples each) was initially quantified. An 'error matrix' $\mathcal{E}$ was generated by comparing each sample in S_1 with H neighboring samples on either side of the corresponding index in S_2. For $h \in [-H, H]$ and $n \in [1, N]$, $\mathcal{E}(h, n)$ was evaluated as,

$$\mathcal{E}(h, n) = \begin{cases} |S_1(n) - S_2(n + h)| \; ; \; N \geq n + h \geq 1 \\ |S_1(n) - S_2(1)| \; ; \; n + h < 1 \\ |S_1(n) - S_2(N)| \; ; \; n + h > N \end{cases} . \qquad (3.1)$$

In any n^{th} column of Ɛ, the vertical index h corresponding to the minimum valued element (i.e., the error) represents the manner in which n^{th} element in S_1 has shifted in S_2. Therefore, the vertical indices lying on the path that traverses from columns 1 to N of Ɛ, accumulating the minimum sum of errors, yield the DL waveform that aligns S_1 and S_2. The minima of Ɛ for the columns corresponding to the dynamic echo regions are located at non-zero h, signifying a non-zero lag. To efficiently trace an optimal path incurring the minimum sum of errors, dynamic programming was used where Ɛ matrix is transformed to an accumulated error matrix Đ. The commonly adopted method for the evaluation of Đ is to progressively accumulate errors by searching for the local minimum errors, following:

$$Đ(h, n) = \begin{cases} Ɛ(h, n) \ ; \ n = 1 \\ Ɛ(h, n) + \min \begin{Bmatrix} D(h - 1, n - 1), \\ D(h, n - 1), \\ D(h + 1, n - 1) \end{Bmatrix} ; \ n = [2, N] \ . \end{cases} \tag{3.2}$$

Now, the optimal path can therefore be easily traced by identifying the minimum valued elements in each column of Đ, while traversing reverse from N^{th} to the 1^{st}. The DL waveform herein can be constructed by evaluating all the vertical indices 'h' that correspond to the minimum valued elements along the traced optimal path, using:

$$DL(N) = \arg\min Đ(h, N), \forall h \tag{3.3}$$

$$DL(n) = \arg\min Đ(h, n), \tag{3.4}$$

$$\text{for, } h \in [DL(n+1)+1, DL(n+1), DL(n+1)-1]$$

$$\text{and } n = N - 1, N - 2, \ldots 1.$$

It may be noted that the samples of wall echoes (about 0.3 to 2 mm) have comparable shifts, and then the shift abruptly transitions from wall echoes to nearby ones. As a result, the proposed method employs a modified Đ evaluation procedure that is more suited for the signals in this study and results in a smoother DL waveform. The horizontal axis of Ɛ was decimated by a factor 'd', and Đ was populated for columns m = {1, 1+d, 1+2d, 1+3d, ..., N}. While populating any m^{th} column of Đ, the local minimum errors were searched from all the possible sub-paths between the corresponding m^{th} column element in Ɛ and its $(m - 1)^{th}$ column elements. As the column indices of Ɛ corresponding to 'm' and '(m – 1)' were separated by factor 'd', this resulted in a maximum of (2d + 1) possible sub-paths per element, from which local minimum errors were searched for accumulation. Upon generation of Đ, a coarsely sampled DL waveform was evaluated and resampled to ensure N elements by adopting a cubic spline interpolation method.

3.2 PROPOSED DTW-BASED ALGORITHMS

This section describes the automated framework for arterial wall recognition and motion tracking methods, the schematics of which are presented in Figure 3.2.

3.2.1 Wall-recognition

Figure 3.3 depicts the important phases and accompanying intermediate signals of the wall recognition method. Two successive example A-mode RF frames are shown in Figure 3.3(a) as input to the method. The frames contain (i) static echoes from non-

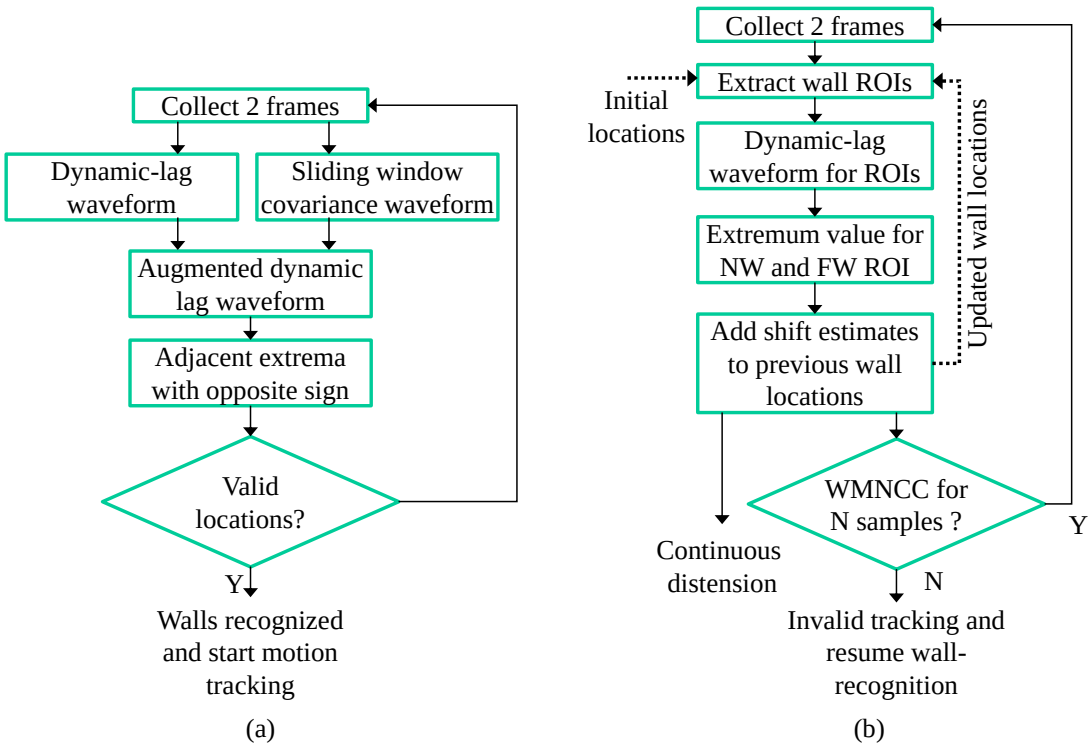

Figure 3.2 Flowcharts illustrating the automated (a) wall recognition and (b) tracking.

moving tissues (inset – V) and a transducer saturation region (close to the transducer-skin interface), (ii) dynamic echoes from arterial walls (inset – II and III), and (iii) other dynamic echoes from tissue adjacent to the walls (inset – I and IV). The Ɛ and Ð matrices for the sample frames are shown in Figure 3.3(b) and (c), respectively. As illustrated in Figure 3.3(d), the static echo areas of RF frames have a flat zero amplitude, whereas the dynamic echo sections have a nonzero amplitude in the DL waveform. The sign of the non-zero amplitude indicated the direction of the shift; a positive sign indicates that the echo in S_2 has shifted away from the origin (to the right) relative to its location in S_1, whereas a negative value suggests a shift toward the origin. The DL waveform clearly contains additional noise, particularly in the parts corresponding to the RF frame, when echoes are absent but noise is present.

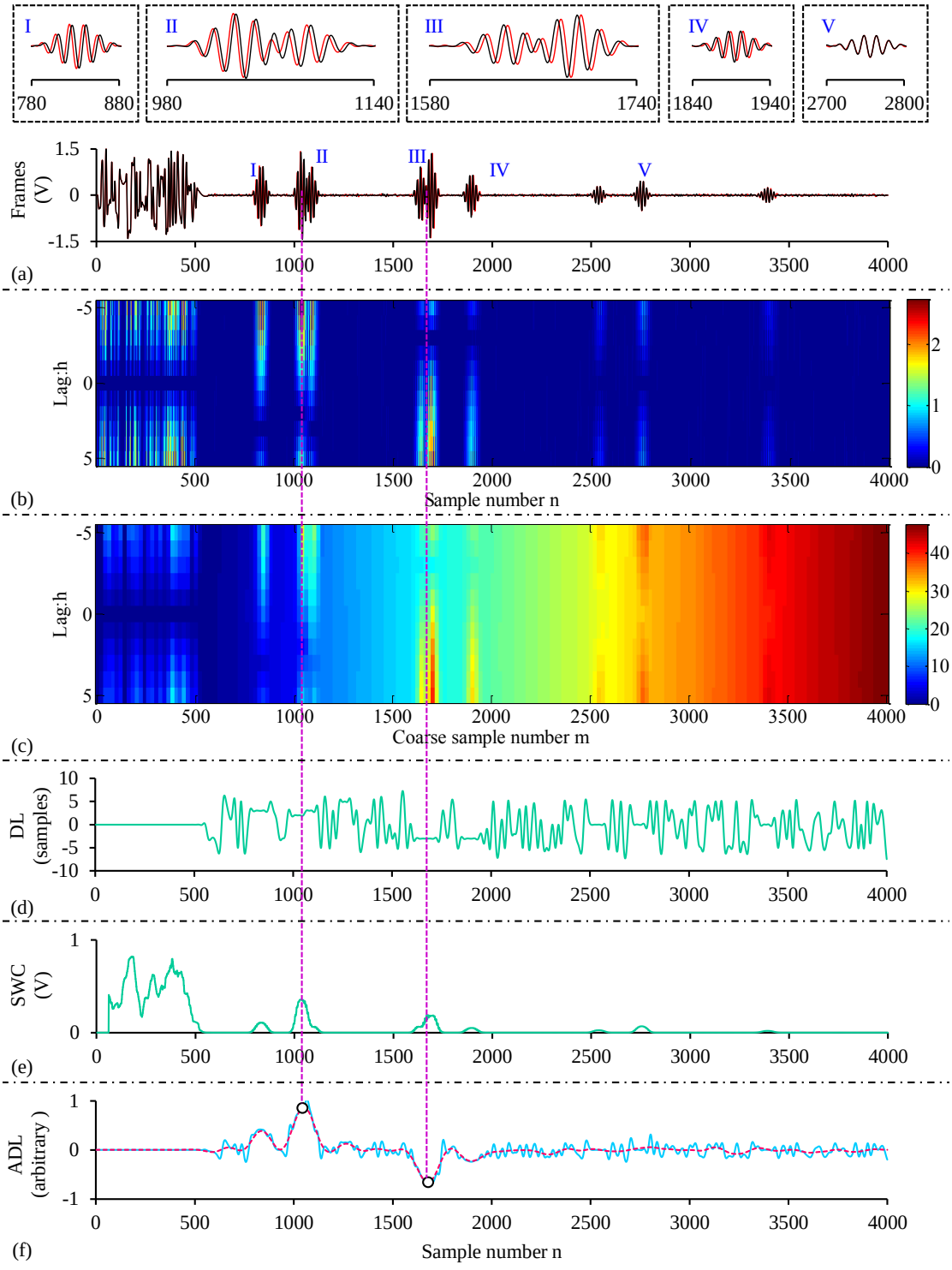

Figure 3.3 Various stages of the arterial wall recognition method and the associated intermediate signals (a) Depicting various type of echoes (static and dynamic) from two successive frames, (b) alignment error matrix and (c) accumulated error matrix for the two frames, (d) the estimated dynamic lag waveform, and (e) sliding window covariance waveform that is augmented over (d) to obtain (f) augmented dynamic lag waveform.

As a result, in (3.5), an augmentation technique was presented that used a sliding window covariance (SWC) waveform to selectively attenuate noise and generate an augmented DL waveform (ADL).

$$\mathrm{ADL(n)} = \mathrm{DL(n)} * \mathrm{SWC\ (n)} \tag{3.5}$$

For any pair of frames S_1 and S_2, the SWC was constructed by iteratively running a window of width W_{SC} over the frames and finding the covariance of the windowed portions as given below.

$$\begin{gathered}\mathrm{SWC(n)} = \frac{\sum_{k=n-\left\lfloor \frac{W_{sc}}{2} \right\rfloor}^{k=n+\left\lfloor \frac{W_{sc}}{2} \right\rfloor} F_1(k)\, F_2(k)}{W_{sc}}; \\ \text{for } \left\lfloor \frac{W_{SC}}{2} \right\rfloor < n < N - \left\lfloor \frac{W_{SC}}{2} \right\rfloor; \\ \text{and } 0, \text{ for all other n}\end{gathered} \tag{3.6}$$

Due to the fact that noise has small covariance, the SWC waveform, as shown in Figure 3.3(e), yields a magnitude near to zero for the noise regions of the frame. It functions as a pseudo-envelope with significant peaks for the rest of the echoed portions. Figure 3.3(f) shows the ADL waveform and its smoothened counterpart created with a moving average filter (20 samples window). Smoothing the ADL waveform results in the appearance of prominent extrema at the locations of the dynamic echoes.

The identification of arterial wall echoes was performed by locating the two extrema of interest (at depths P_1 and P_2) in the smoothened ADL waveform that are subject to the following constraints:

$$P_2 > P_1 \text{ and } ADL|P_1 * ADL|P_2 < 0, \quad (3.7)$$

$$D_{min} < P_2 - P_1 < D_{max}, \quad (3.8)$$

$$\text{and } P_1 > D_{NW}. \quad (3.9)$$

Here, D_{min} and D_{max} are the typically expected minimum and maximum range of lumen-diameters for a target artery and D_{NW} is the least expected depth of the near wall. These are the approximate anatomical norms, which differ amongst arteries. The locations of the generated extrema P_1 and P_2 were then designated as NW and FW, respectively. It may be remembered that the method flags an artery-present (or detected) status and locates the NW and FW, if and only if a single unique pair of extrema satisfies the conditions (3.7) – (3.9). While at least two frames are required for the wall recognition method, a subset of frames (SoF) may be considered for re-enforced recognition, such as SoF = 2, 4, 6, 8, and 10. In such cases, the artery is considered to be detected if the method flags the presence of the arterial walls echoes in at least SoF/2 frames. As a result, such a strategy clusters the detections from multiple frame pairs, increasing their robustness. The locations of NW and FW. As shown in Figure 3.2, these initial identified locations of NW and FW serve as input to the wall motion tracking stage.

3.2.2 Wall-motion tracking

Following wall recognition, a pair of windows with appropriate length to contain the wall echoes were locked on the most recent frame, their centres corresponding to the obtained NW and FW locations. For continuous tracking, only the echoes within the relevant windowed ROI needs to be processed in following frames. Both wall ROIs account for around a tenth of the whole frame. As a result, analysing these instead of

the complete frame reduces the computing load during the tracking stage by at least tenfold. The ROI of both the NW and FW were taken from the latest and preceding frames with each new frame. The DL waveform was then constructed separately for the extracted ROIs of NW and FW. The exact frame-to-frame shift in NW and FW echoes was determined by the extremum amplitude of the corresponding DL waveforms. The updated locations of the walls, $\mathrm{Loc}_{\mathrm{curr}}^{\mathrm{NW}}$ and $\mathrm{Loc}_{\mathrm{curr}}^{\mathrm{FW}}$, were calculated using the frame-to-frame shifts, τ_{NW} and τ_{FW}.

$$\mathrm{Loc}_{\mathrm{curr}}^{\mathrm{NW}} = \tau_{\mathrm{NW}} + \mathrm{Loc}_{\mathrm{prev}}^{\mathrm{NW}}, \tag{3.10}$$

$$\mathrm{Loc}_{\mathrm{curr}}^{\mathrm{FW}} = \tau_{\mathrm{FW}} + \mathrm{Loc}_{\mathrm{prev}}^{\mathrm{FW}}, \tag{3.11}$$

Here, $\mathrm{Loc}_{\mathrm{prev}}^{\mathrm{NW}}$ and $\mathrm{Loc}_{\mathrm{prev}}^{\mathrm{FW}}$ are the previous locations of the walls. As a result, the positions of the widows were updated automatically, allowing continuous monitoring of the artery walls without the need for external/manual input or supervision. Note that, the continuous distension of artery is evaluated as $\mathrm{Loc}_{\mathrm{curr}}^{\mathrm{FW}} - \mathrm{Loc}_{\mathrm{curr}}^{\mathrm{NW}}$.

Since the DL waveform represents the dynamic shifts within each ROI, it provides robust means to discriminate between the motion of several echoes in those ROIs. Physically, the arterial walls are likely to suffer the maximum instantaneous displacement compared to the other neighboring tissue structures under the direct impact of the transmural pressure. This becomes the rationale to select the ROIs' DL waveform's extrema as the incurred shift in wall echoes. While the wall motions were being tracked continually, periodic checks were made to ensure that no inaccurate echoes were being tracked. The FW and NW motion phases were examined during

these checks to discover if they were negatively connected. The checks were also done to evaluate if the distension contour that resulted matched the typical arterial wall dynamics. We previously established the need for such a real-time verification approach in an allied work from our group to avoid misdetections in the presence of other possible moving structures such as the jugular vein (Sahani, Shah, Joseph, & Sivaprakasam, 2016). If any of these checks fail, the method is reverted from tracking to wall-recognition to re-identify actual arterial echoes.

3.3 SIMULATION STUDY

The algorithms were rigorously tested using simulated trials before being deployed on a device for measurements. The elaborate challenging scenarios that were simulated to test the performance of wall identification and motion-tracking methods, as well as the corresponding results, are discussed in this section. The specific goals of this simulation study are to (i) assess the sensitivity and specificity of the wall recognition method in detecting the presence or absence of the artery in a variety of emulated cases, (ii) establish the accuracy of the method to determine the locations of the walls within the frame, and (iii) finally, assess the accuracy of the motion tracking method to trace the continuous dynamics of the walls.

3.3.1 Simulation testbed

The requisite RF frames were generated using a simulation testbed based on set parameters such the number of echoes, their positions and amplitudes, and the frames' overall signal-to-noise ratio (SNR). The RF frame is generated by convolving a Gaussian modulated sinusoidal pulse wavelet p(n) with a weighted-impulse train h(n)

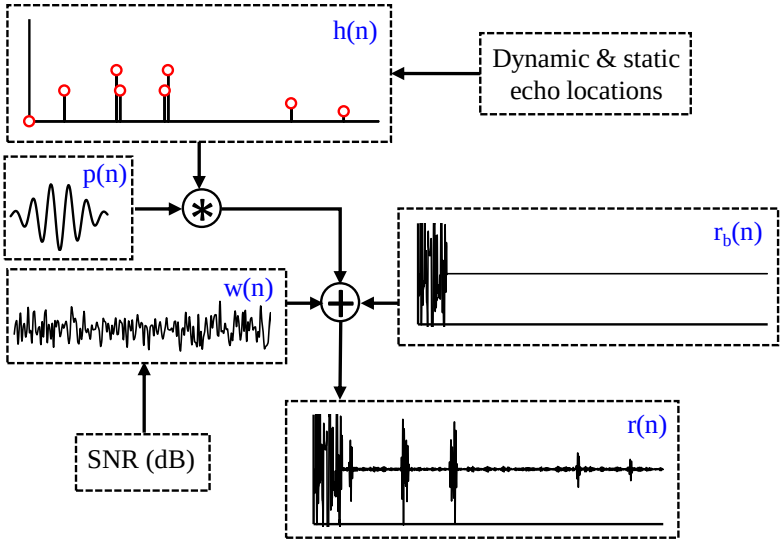

Figure 3.4 Schematic of simulation test-bed.

as shown in the testbed schematic Figure 3.4. Here, h(n) represents the tissue scattering function, with configurable impulse locations and amplitudes. To yield a realistic condition, a blank frame with an echo at origin $r_b(n)$ was added to the convoluted output, simulating transducer saturation region (near the skin-gel interface). To vary the SNR, the frame was subsequently treated with additive white noise w(n). It was calculated as the logarithmic ratio of smallest of the two wall echo amplitudes to noise amplitude (from the region where there are no echoes). As a result, the testbed created the frame r(n) with a designated SNR that included both static and dynamic echoes, given as $r(n) = p(n) \circledast I(n) + w(n) + r_b(n)$. Now the desired simulation category was generated by the amplitudes and locations of impulses in h(n).

3.3.2 Simulations to assess wall-recognition

The artery wall-recognition method was tested on both negative and positive class RF frames, treating it as a classification and localization problem. Negative class frames were either blank or merely static echoes with no artery walls. For both the negative

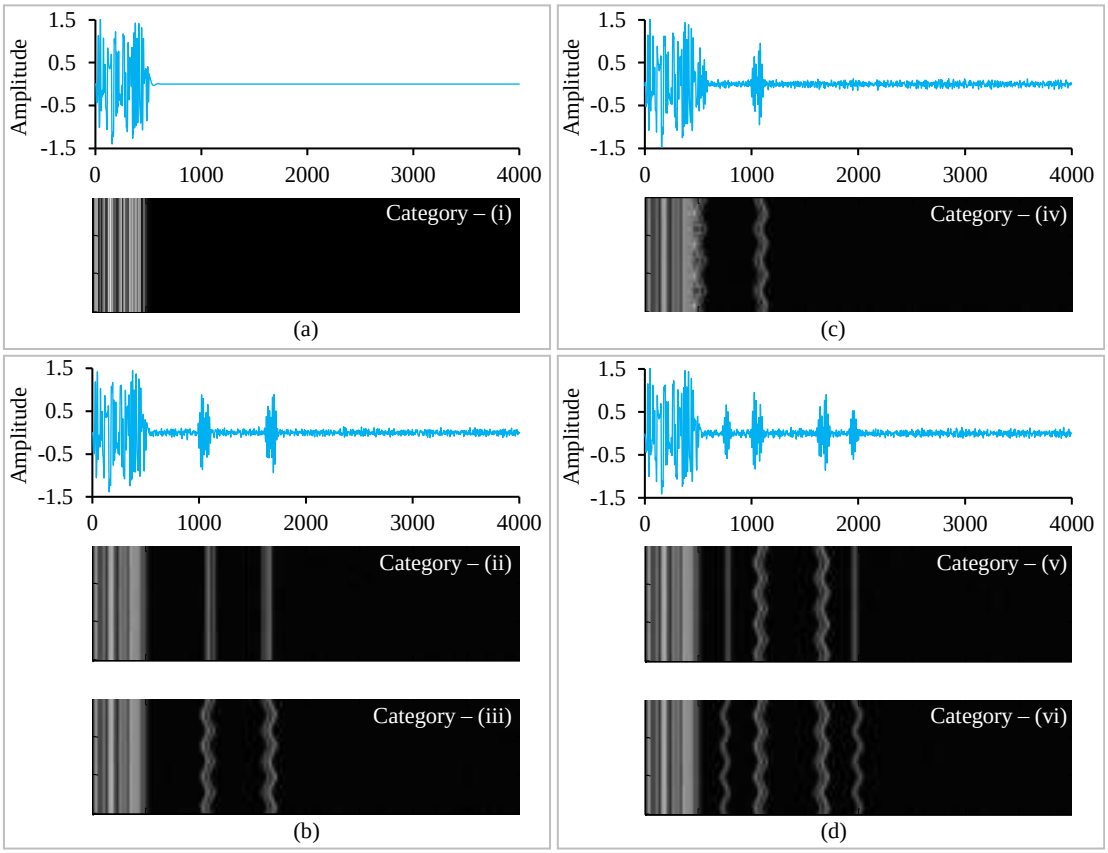

Figure 3.5 Various category of simulations with different number of echoes within the frames to assess wall-recognition method. Also, M-mode images are shown to depict motion of the echoes over 150 frames

and positive class frames, a total of six categories were defined. In contrast, the positive class consisted of the signature echoes of artery walls. These categories of both classes are depicted in Figure 3.5(a) – (d), along with their respective sample M-mode images (stacking 150 consecutive A-mode frames). Table 3.1 lists the descriptions of these categories. For each category, the frames SNR was changed from -5 to 20 dB, and 150 frames were generated for each setting. For these frame sets, the method's performance was assessed using the simulated wall locations as the ground truth. Initially, the wall motion periodicity was set to 1.3 Hz. It was also changed from 0.3 to 3 Hz to assess how a wide range of physiological heart rates affected the performance.

Table 3.1 Simulation study categories for assessing the proposed methods

Name	Frame class	Description
Simulation categories for wall recognition method assessment		
Category-(i)	Negative	Blank frames with saturation region echo
Category-(ii)	Negative	Frames with additional static echoes
Category-(iii)	Positive	Frames with only arterial wall echoes
Category-(iv)	Positive	Frames with only arterial wall echoes with near wall overlapping saturation echo region
Category-(v)	Positive	Frames with wall echoes and adjacent static echoes
Category-(vi)	Positive	Frames with wall echoes and adjacent dynamic echoes moving in the direction of the respective walls
Simulation categories for wall motion tracking method assessment		
Category-(a)	Positive	Wall region of interests have additional static echoes immediately adjacent to the walls
Category-(b)	Positive	Wall region of interests have additional slow-moving echoes immediately adjacent to the walls

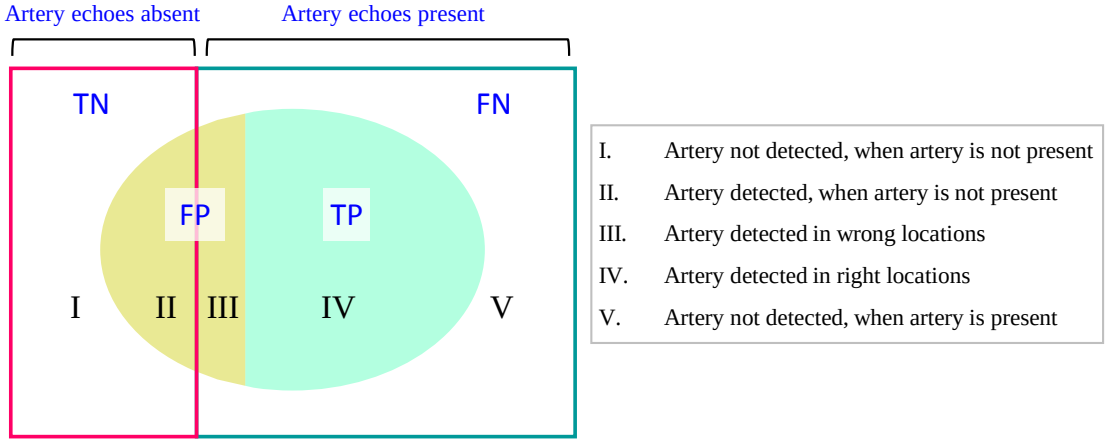

Figure 3.6 Venn-diagram categorizing the wall-recognition outcomes.

For evaluation, the recognized artery wall locations were deemed correct only when their deviation from the ground truth locations was within 1 mm, a criterion that was used in similar studies (Molinari, Meiburger, et al., 2012; Rossi et al., 2008).

Based on this, Figure 3.6 shows a venn-diagram categorizing of the wall-recognition outcomes into true negative (TN), false positive (FP), true positive (TP), and false

negative (FN). The method was classified as TN if it does not detect the artery walls in a negative class frame; FP if it detects in a negative class frame or at inaccurate locations in a positive class frame; TP if it detects at the correct locations in a positive class frame; and FN if it does not detect in a positive class frame. The artery is considered recognized if the method recognizes the arterial wall echoes in at least SoF/2 frames, as explained earlier (sub-section 3.2.1). Only when the recognized artery wall positions were within 1 mm of the ground truth locations were they deemed accurate, a criterion that had previously been applied in similar research (Molinari, Meiburger, et al., 2012; Rossi et al., 2008). Three metrics were evaluated to quantify the performance of the wall recognition method. 'Recall' or sensitivity was evaluated as a ratio of all correct recognitions to the potentially possible recognitions, i.e., 100*TP/(TP+FN). 'Precision' or positive predictive value was evaluated as the ratio of correct recognitions to the total recognitions made by the method, i.e., 100*TP/(TP+FP). Finally, specificity was evaluated as the ratio of all the correct to the total predictions concerning the absence of artery, i.e.100*(TN/TN+FP).

3.3.3 Simulations to assess wall-motion tracking

To investigate the robustness of the wall-tracking method, in particular, we chose to place the additional echoes very close to the wall echoes so that they were contained in the extracted wall ROIs. Table 3.1 shows the nature of the additional echoes within the wall ROIs. Initially, for Category-(b), the wall echoes were moved by ±10 samples whereas the additional echoes were moved by ±7 samples in phase their adjacent wall. In here, the method's ability to track the exact shift of the walls compared to the traditional cross-correlation approach. Then the periodicity of the motion was set to 1.3

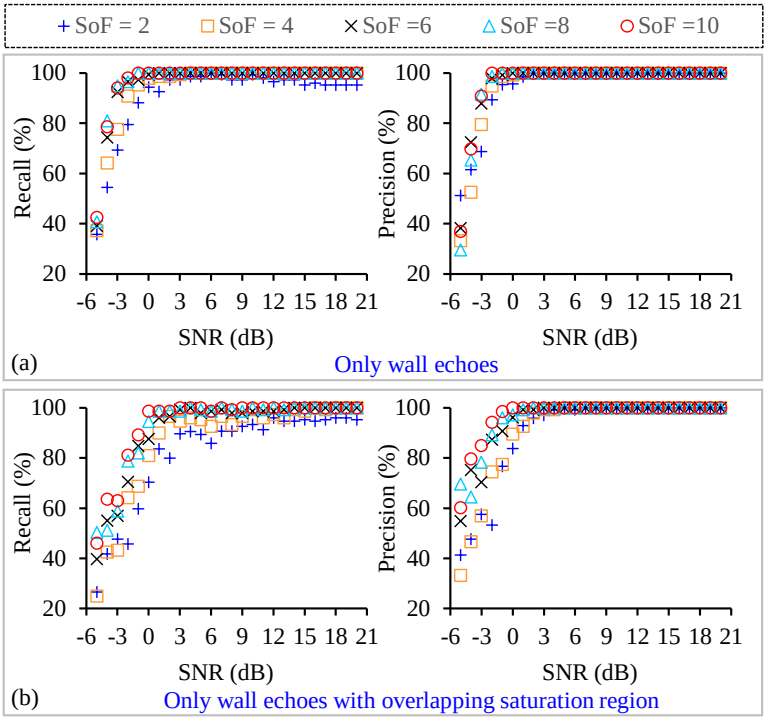

Figure 3.7 Performance taking various SoF – for the positive class frames with only wall echoes

Hz, and the walls were displaced in a sinusoidal fashion with a peak amplitude of 0.5 mm from their initial resting positions. The peak of sinusoid motion of the slow-moving echo for Category-(b) was correspondingly kept as 0.3 mm. The method's tracking capabilities was then examined for both of the categories – (a) and (b) by adjusting the SNR and heart rate. The absolute difference (%) between the tracked and simulated location shifts and the root-mean-square error (RMSE) were used to measure accuracy.

3.3.4 Results from simulation study

3.3.4.1 Performance of wall-recognition method on positive class frames.

Figure 3.7 and Figure 3.8 shows the recall and precision calculated for the positive class frames, with only wall echoes and with alongside additional echoes, respectively, Category – (iii) to (vi) (Table 3.1) shown in Figure 3.5(b) – (d). The method was applied

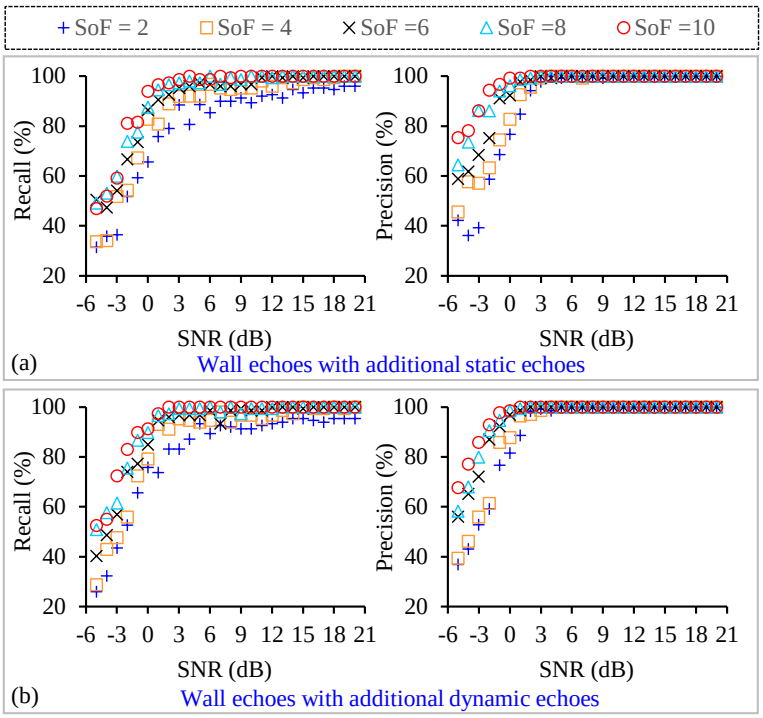

Figure 3.8 Performance taking various SoF – for the positive class frames with additional echoes alongside wall echoes

by taking SoF as 2, 4, 6, 8, and 10 for each frame set with respective SNR configuration. More than 80% recall and 85% precision were yielded for all the SoF cases with a frame SNR ≥ 2 dB. The recall improved to more than 90% with a precision of 100% for all the frames with higher SNRs (> 10 dB). For such high SNRs, the recall yielded for SoF ≥ 6 was as high as 98% to 100%.

3.3.4.2 Performance of wall-recognition method on negative class frames.

Cent percent specificity was observed while applying the wall-recognition method on 150 blank frames with only a saturation echo. Further, the specificity was evaluated Category – (ii) simulations varying the SNR levels for different SoFs. The performance of wall-recognition method for these varying parameters is illustrated in Figure 3.9(a).

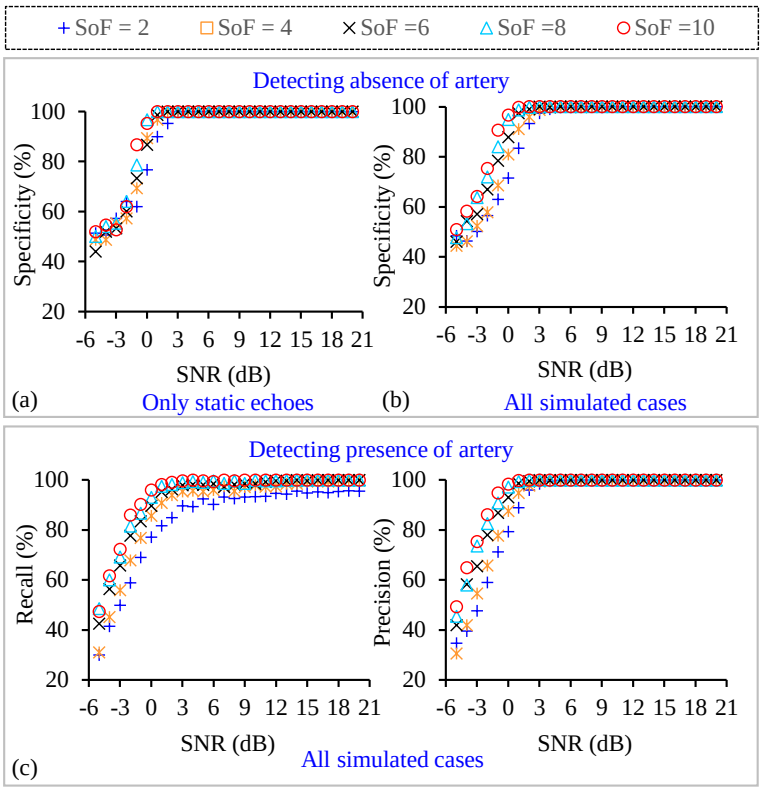

Figure 3.9 Performance taking various SoF – deduce artery's absence (a) when only static echoes are present, (b) overall simulations, (c) deduce artery's presence over all the categories.

For positive SNRs (> 0 dB) the specificity quantified for the SoF cases was greater than 90%, and it further improved to 100% for frames with even moderate SNRs (> 3 dB).

3.3.4.3 Overall wall-recognition method's performance

All the simulated cases alluded in the above subsections were combinedly analysed, where the TN, FP, TP, and FN detections of the respective categories were cumulatively used to evaluate the recall, precision, and specificity. These overall results, as illustrated in Figure 3.9(b) and (c) were comparable to the results yielded from individual categories, further corroborating the above-alluded outcomes. For all the SNR ≥ 5 dB, the recall was consistently greater than 90%, the precision and specificity were 100%,

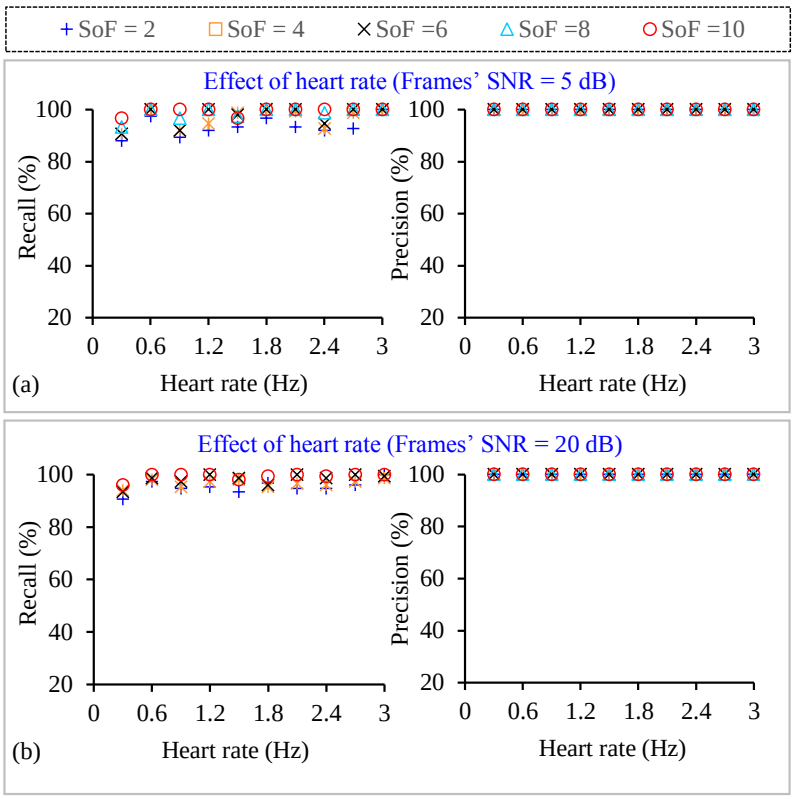

Figure 3.10 Effect of heart rate on performance wall-recognition at (a) low SNR of 5 dB and (b) high SNR of 20 dB.

irrespective of the SoF chosen. For these high SNR frames, the recall was greater than 98% for SoF $\geq$ 6. Only for SNR $\leq$ 0 dB, these performance indices reduced < 80%.

3.3.4.4 Effect of heart rate on wall recognition method's performance

Figure 3.10(a) and (b) show the performance results for various the wall motion periodicities between the extremities of physiological heart rate, specifically for poor SNR (5 dB) and high (20 dB), respectively. At SNR = 5 dB, the mean values of recall across all the heart rates were 93 ± 4%, 96 ± 4%, 97 ± 4%, 98 ± 2% and 99 ± 1% for SoFs 2, 4, 6, 8 and 10, respectively. These were comparable to that from 20 dB SNR frames, which were respectively 95 ± 3%, 96 ± 2%, 98 ± 2%, 98 ± 2%, and 99 ± 1%.

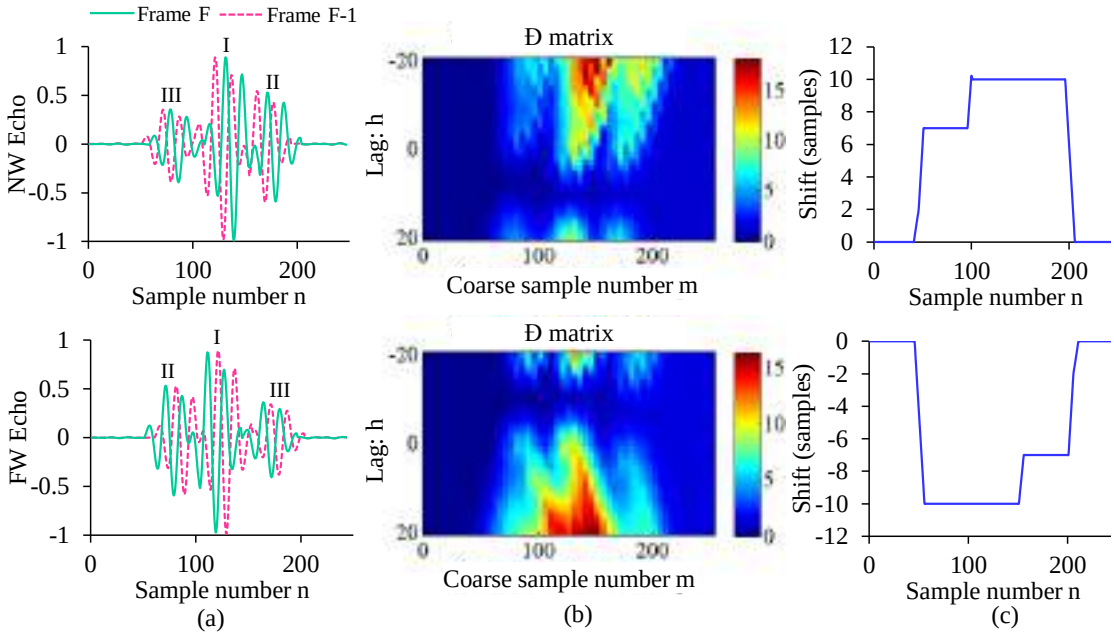

Figure 3.11 (a) NW and FW ROIs extracted from two consecutive RF frames for the first simulation experiment of wall tracking method. (b) A colormap of the accumulated error matrix for the respective walls and (c) the corresponding shift waveforms employing backtracking.

3.3.4.5 Wall-tracking method's performance

Example A-mode frame from pilot simulation experiment is shown in Figure 3.11(a), where the ROIs comprised of three sets of echoes for each NW and FW. In the figure, echoes I and II correspond to the adventitia and intima interfaces respectively and III is the additional dynamic echo with relatively smaller displacement then walls (10 versus 7 samples). The accumulated error matrix in Figure 3.11(b) evidently shows a minimum value (dark blue) for column indices corresponding the actual lags or shifts. The shift waveform yielded by backtracking the Đ matrix is illustrated in Figure 3.11(c). It may be observed that for the portions corresponding to the wall echoes the evaluated shift is ±10 samples (Figure 3.11(c)). For the same ROIs the cross-correlation technique underestimated the shift by 2 samples. Such underestimations over frame-to-frame

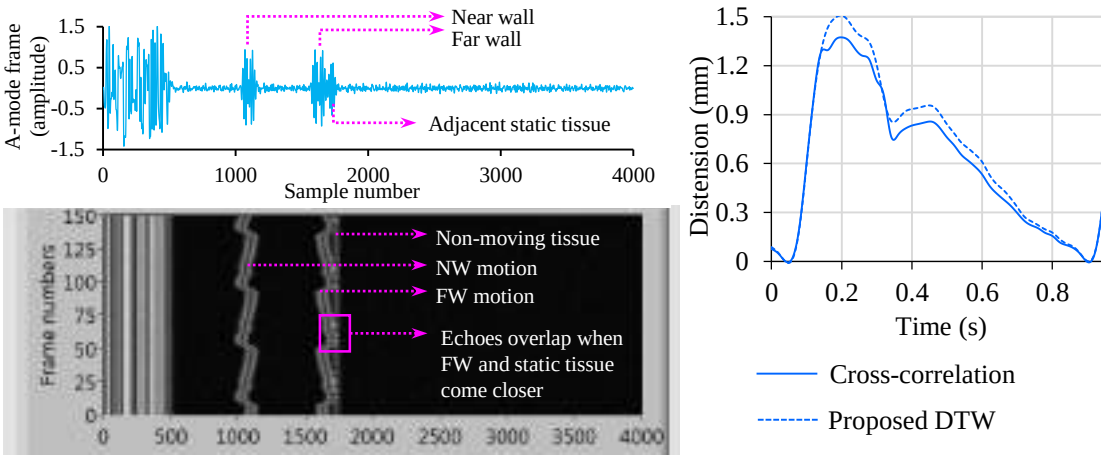

(a) (b)

Figure 3.12 (a) Simulated frame which an additional echo adjacent to only far-wall (FW), (b) M-mode diagram of the simulation represent 150 consecutive frames, over which the FW is corrupted only during late systolic phase. (c) comprision of tracked arterial distension cycle between proposed and cross-correlation methods.

cumulatively have a potential influence on tracked distension morphology. An example shown in Figure 3.12(a), is a sample simulated frame with a pair of echoes for each wall and an additional echo adjacent to the far wall. A total of 150 frames were obtained where the walls were shifted by inputting a characteristic motion pulse and the additional echo was kept constant. Particularly, the frames emulated the scenario where the far wall echo overlaps the additional static echo in its vicinity during late systolic phases. In Figure 3.12(b), the first plot shows the distention estimated (relative to the minimum diameter) by the cross-correlation method (solid line) and by the proposed DTW method (dashed line). It may be noted that the towards late systolic phase, cross-correlation method started to under-estimate the distension due to the overlapping of far wall and neighboring static echoes. The peak distension (ΔD) was underestimated by 0.14 mm (~9% error). Additionally, the morphology also can be seen altered. In fact, the cross-correlation based distension cycle resembles a Type–B waveform, whereas the input pulse was actually a Type–C. DTW method didn't manifest such corruptions.

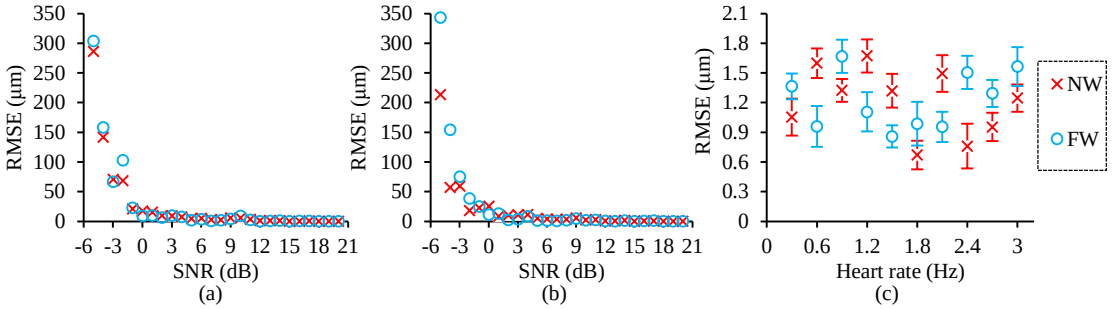

Figure 3.13 Performance wall tracking and different SNR, illustrating RMSE resulted when wall ROIs consisted (a) static echoes, and (b) slow moving dynamic echoes, proximal to the wall echoes. (c) RMSE in tracking NW and FW for different heart rates, while frame SNR was varied from 5 dB to 20 dB.

Figure 3.13(a) and (b) illustrate the RMSEs of the tracked wall locations for the two simulation cases: Category (a) and (b) from Table 3.1, with wall ROIs consisting of static echoes and slow-moving dynamic echoes, respectively. For both cases, the RMSE was smaller than 10 µm for all the frames with SNR > 0 dB. It was reduced below 2 µm for frames with higher SNRs (> 5 dB). Further, RMSEs were evaluated for various heart rates, and the performance for above-moderate SNRs (5 dB to 20 dB) is summarized in Figure 3.13(c). Irrespective of heart rate, RMSE of the tracked NW and FW locations were smaller than 2 µm, and absolute errors were smaller than 3%, supporting the above outcomes.

3.4 IN-VITRO STUDY

Following extensive simulation testing to determine the method's performance, an in-vitro study was conducted to determine the method's applicability to actual RF signals acquired. More precisely, the objective was to demonstrate the method's performance by comparing it to conventional B-mode measurements. This, however, would require simultaneous recording of RF signals and B-mode image sequences, and, preferably,

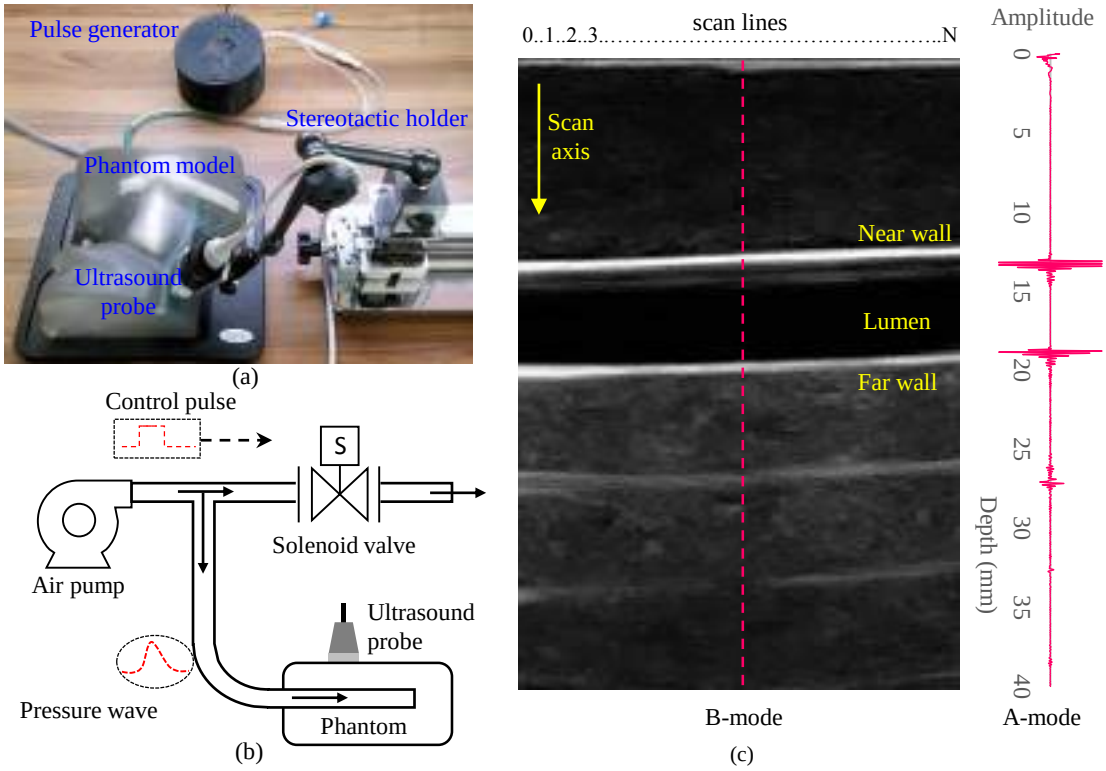

Figure 3.14 (a) Flow-phantom experimental setup and placement of ultrasound probe. (b) Schematic of the flow-phantom. (c) A sample of extracted one-dimensional RF frame and the B-mode image that are acquired simultaneously from the same imaging system.

the source of data is from the same target scan region. To accomplish this, we have developed an experimental setup, the details of which along with the experimental procedure will be explained in the following subsection.

3.4.1 Experimental setup

Figure 3.14(a) depicts the experimental setup, including the phantom and ultrasound probe placement. The study was conducted using a commercially available phantom model (BPIJ500-C – CAE Blue Phantom, Canada). The model was an anatomical model of a human neck, constituting two elastic vessels filled with blood mimicking fluid. A custom pneumatic pulse generator was developed on an embedded

platform, which facilitated the configuration of the amplitude and frequency of the pulsations. The flow-pulse generation setup is depicted schematically in Figure 3.14(b). By periodically opening and shutting a solenoid valve while keeping a miniature air pump operating, the pulse-generator produced continuous pressure pulses. Because the phantom's vessel was closed from the other end, the pump caused the pneumatic pressure in the vessel to rise whenever the solenoid valve was closed. When the valve was opened, it operated as a vent for both the air pumped by the active pump and the previously accumulated air column in the vessel (when the valve was closed). As a result, the air pressure pulse caused a flow pulse in the vessel, causing it to distend and relax. The amplitude and frequency of the pressure pulses, and thus the flow pulses generated during the operation, were governed by the valve's on and off duration and the pump's speed. The arterial pulsations, in particular, have a distinctive morphology, with the ascending slope being significantly greater in magnitude than the descending slope. Therefore, this aspect was simulated by keeping the off-time of the valve smaller than the on-time.

3.4.2 Data acquisition and analysis

The data was collected using a research-grade imaging ultrasound machine (Ultrasonix SonixTouch Q+, BK Medical®, United States). The system was equipped with a linear array transducer, operating at 10 MHz. The data was collected and saved in two formats: (i) post-beam-formed RF signal frames in binary file format, and (ii) cine-loops of B-mode images in .avi format (image resolution = 1729 × 1537 pixels). A single scan line from the middle of each RF frame (containing of multiple scan lines) was extracted and stored into a separate file that served as the stack of A-mode data frames. Figure 3.14(c)

shows an example single scan-line RF frame and the associated B-mode image. The imaging was performed for a scan depth of 40 mm, with frames captured at a rate of 40 Hz and RF signals sampled at a frequency of 40 MHz.

The proposed recognition and tracking method was applied to the single scan line RF data obtained and stored, using LabVIEW-2015 software (National Instruments Co., Austin, Texas, United States). The saved video graphic B-mode cine loops were analyzed on a commercial image-processing software application, Carotid Studio (Cardiovascular Suite 3, Quipu, Italy), as a reference. The Carotid Studio tool performs a semi-automated wall recognition in which a rectangular window spanning the vessel's two walls must be manually placed. This was done by a skilled operator who reviewed the B-mode image sequences and positioned the window on a good quality image, after which the automated tracking for the subsequent images started. The expert also manually annotated the wall locations for comparison of the proposed method's wall recognition performance. Because the RF signal frames and B-mode cine-loops originated from the same scans, the proposed method's wall recognition and tracking results could be directly compared to the B-mode reference.

3.4.3 Results from in-vitro study

The frames were of high quality with SNR $\geq$ 20 dB, and the method could detect the vessel walls in more than 98% of the frames, and for ~100% of those detections, the method localized the vessel walls correctly. This demonstrated the method's robust recognition capabilities, especially to the added noise. Typically, with standard ultrasound devices, the SNRs greater than 20 dB are easily achievable for the RF frames. However, practical factors such as ultrasound coupling, angulation of

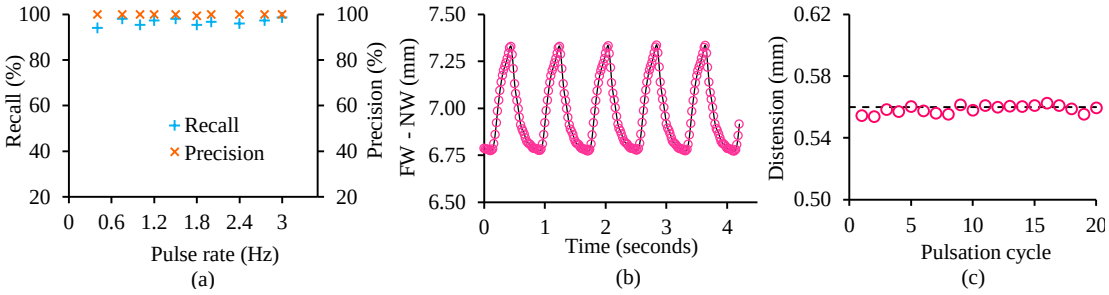

Figure 3.15 (a) Performance of the recognition method over different distension pulse rates, for frames with SNR ≥ 7 dB. (b) A sample of tracked difference between FW and NW locations for multiple pulsation cycles. (c) Sample of beat-to-beat distension, indicating measurement precision.

transducer, ultrasound settings, and operator-dependent variabilities may result in the deterioration of SNR (< 20 dB). The influence of heart rate on the method's wall recognition ability was tested by varying the pulsation rate of the phantom from 0.4 to 3 Hz in a systematic manner. During this, the frame SNR was configured as 10 dB. As shown in Figure 3.15(a), the performance was consistent across all the configured pulsation rates with appreciable recall > 95% and percision 99% - 100%. This further corroborates the wall recognition method's robustness.

As indicative of tracked ability, a sample waveform constructed as the difference of FW and NW dynamic locations is shown in Figure 3.15(b). It may be observed that the waveform manifested a repeatable quasiperiodic locus. A sample of estimated beat-to-beat peak distension for 20 pulsation cycles is shown in Figure 3.15(c). The tracked waveforms measured for the other flow configurations as well exhibited high fidelity, yielding repeatable beat-to-beat distension with a variability smaller than 0.5 %.

The accuracy of the distension measurements performed by the tracking method was further assessed. The regression and Bland-Alman (BA) analyses results are shown in

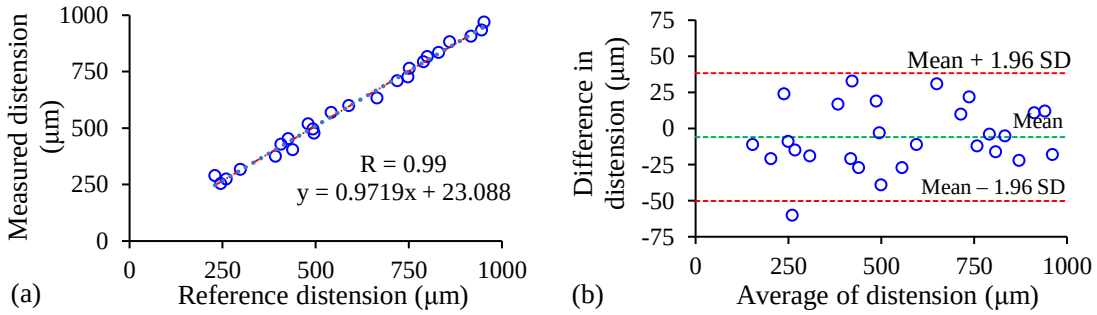

Figure 3.16 (a) Regression plot illustrating the association between the distension measured by the proposed tracking method and the reference B-mode measurements. (b) Bland-Altman analysis demonstrating the agreement between the measured and the reference distension values.

Figure 3.16(a) and (b), respectively. The distension measurements by the proposed method manifested a strong and significant correlation ($p < 0.05$ and $r = 0.99$) with the reference measurements performed by the B-mode image analysis tool. The BA plot didn't manifest any trend, and a bias of -6 µm was observed that was statistically insignificant ($p = 0.17$). The proposed method's versus reference measurements agree within limits-of-agreement (LoA) - 50 µm and 39 µm. They were accurate, yielding an RMSE of 22 µm.

3.5 IN-VIVO STUDY

After the method was tested on RF frames recording from a conventional B-mode scanner in-vitro, it was deployed to ARTSENS®, an in-house developed A-mode based device. The device was used to finally evaluate the feasiblity of performing measurements on human subjects.

3.5.1 Participants and protocol

An in-vivo validation investigation was performed on 21 healthy volunteers (average age = 26 ± 7 years) who had no history of cardiovascular disease. It was done on the

premises of our research and development center (Healthcare Technology Innovation Center, IIT Madras, Chennai, India), with participants recruited opportunistically from among our staff. The internal review committee accepted the study protocols. The study protocols followed the committee's recommendations and adhered to the Declaration of Helsinki's principles. Each subject provided written informed consent. The average height, weight, and body mass index (BMI) were 171 ± 10 cm, 72.4 ± 13.2 kg, and 23.9 ± 4.1 kg/m2, respectively. Likewise, the subjects' SBP, DBP and HR were 112 ± 13 mmHg, 72 ± 8 mmHg, and 69 ± 6 bpm, respectively.

A single operator (with more than three years of experience) collected the raw RF data for all of the recruited individuals using our clinically validated image-free ultrasound equipment (Joseph et al., 2020). The recordings were made from the left common carotid artery with patients sitting. A-mode frames were acquired at a rate of 40 Hz for a length of approximately thirty cardiac cycles. To evaluate the method's performance, a subset (150 frames, approximately comprising 4-5 cardiac cycles) without artery wall echoes and another with artery wall echoes were separated from each subject's recording. The expert determined the reference wall echo locations in these separated frames by manual inspection and annotation on a post-analysis software. The software displayed the first frame along with four cursors, two to annotate the boundaries of each wall, and a play button. The expert dragged the cursors on the frame so as to surround the echoes of NW and FW (a pair for each). The center of the window enclosing each wall designated its location. After manually placing the cursors in the first frame, the play button enabled tracking these locations for subsequent frames with a cross-correlation technique (Joseph, Radhakrishnan, Kusmakar, Thrivikraman, & Sivaprakasam, 2015). These locations were used for evaluating the performance of the

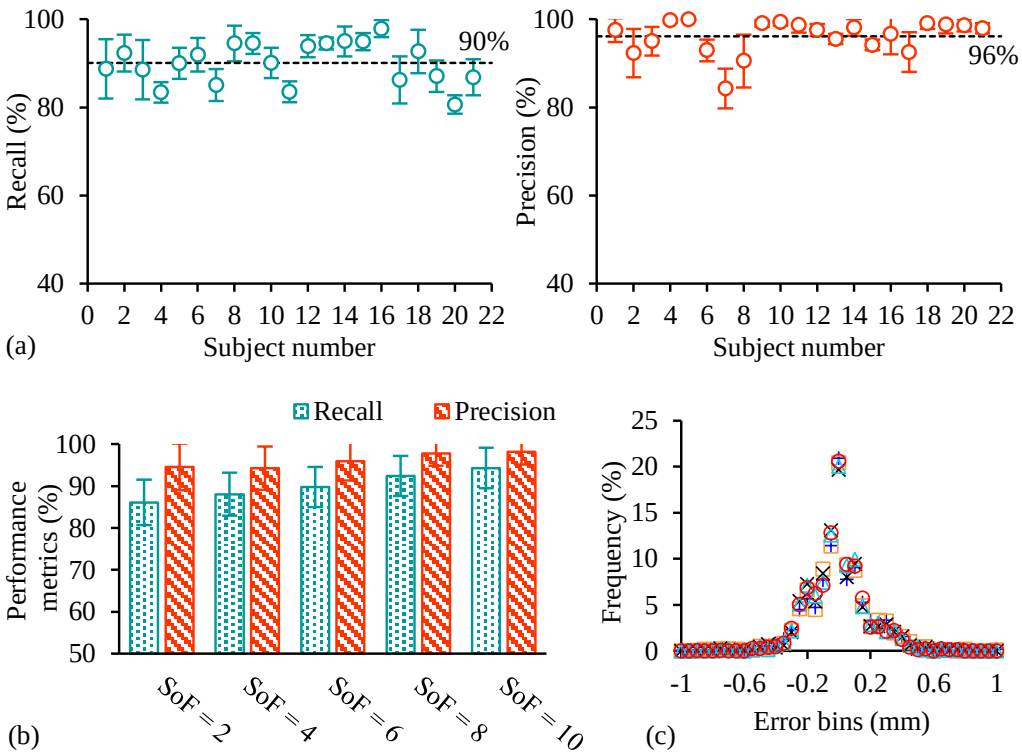

Figure 3.17 In-vivo performance of wall-recognition on positive class frames, (a) for individual subjects, averaged for all SoF and (b) taking different SoF. (c) Frequency distribution of localization errors.

proposed wall recognition method. Further, a clinical-grade B-mode scanner (Ultrasonix SonixTouch Q+, BK Medical®, United States) was employed to compare and evaluate the proposed method's tracking efficiency. The reference distensions were measured using cine-loops recorded in video format (.avi, with an image resolution of 1729 ×1537 pixels) and processed offline using the Carotid Studio analysis package (Cardiovascular Suite 3, Quipu, Italy). Another operator (skilled sonographer) performed all the B-mode data collection.

3.5.2 Results from in-vivo study

Positive and negative class frames were successfully recorded from all the subjects. On analyzing the wall recognition method's performance on the negative class frames,

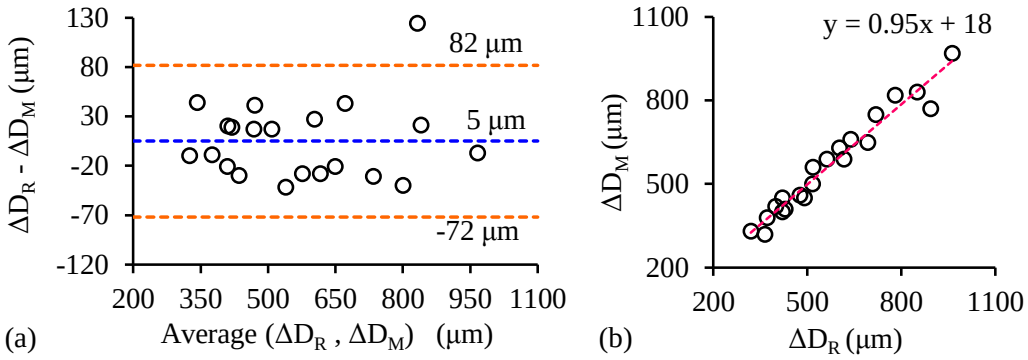

Figure 3.18 (a) Bland-Altman and (b) regression analysis of distension measurements performed by the proposed method and B-mode reference.

a specificity ranging from 98% to 100% was achieved for all the subjects. Averaging the recall and precision for all the SoF cases, the results from individual subjects are plotted in Figure 3.17(a). For each subject, along with the mean, the standard deviation (SD) bars are indicated in the figure (Figure 3.17(a)), and also, the group-average means are indicated with a dashed line (in black). The minimum, mean, and maximum recall for the subject pool were 81%, 90%, and 98%, with precisions of 84%, 96%, and 100%, respectively. Further, the recall and precision resulted by analyzing the positive class frames of all the subjects taking various SoF are shown in Figure 3.17(b). For all the TP detections, the localization errors were computed against the ground truth NW and FW locations, and their frequency distributions are illustrated in Figure 3.17(c). The errors were normally distributed, and the localization errors of walls were limited to ± 0.25 mm for more than 80% of the population. Similar to simulation performance, the percentage of absolute tracking errors obtained was smaller than 3%. Figure 3.18 depicts the BA and regression analyses carried out on the distension ΔD_M given by the proposed method versus the distension ΔD_R obtained from the reference system. An insignificant bias of 5 µm ($p = 0.28$) was observed between the measured and reference values. The lower and upper LoA were -72 µm and 82 µm, respectively. The correlation

coefficient (R) between ΔD_M and ΔD_R values was 0.97 ($p < 0.001$), with regression line's m = 0.95 and c = 18 μm. The measurement error was (1.08 ± 3.65) %, RMSE = 38 μm.

3.6 DISCUSSION

In this work, we have introduced a method to auto-recognize and auto-track the locations of arterial walls from the acquired raw RF signals. While the method is readily applicable to M-line signals acquired using conventional scanners, it also provides sufficient robustness for direct application to A-mode data recorded using single channel or image-free devices. The techniques available in the literature to recognize the arterial wall locations are either by M-line processing or image-processing. These exploit characteristic features such as intensity peaks and patterns of the walls or the lumen region that embodies a wide anechoic well (Delsanto et al., 2007; Fan et al., 2000; Golemati et al., 2007; Arnold P.G. Hoeks et al., 1997; Molinari, Meiburger, et al., 2012; Molinari et al., 2010b; Rossi et al., 2008; Sifakis & Golemati, 2014; D. C. Wang et al., 2009). In addition to these fundamental characteristics, the proposed method investigates the time-variant impacts of tissue dynamics on the phase of various echoes in the RF signal. The method's DL waveform reveals the locations of dynamic echoes, while the SWC waveform accentuates strong echo intensity peaks and suppresses the effect of white noise. Therefore, combinedly these waveforms allowed robust recognition of the prominent dynamic echoes that corresponded to the arterial walls. This has been demonstrated in our simulation and in-vivo studies.

The extensive categories that were developed, specifically incorporating both negative and positive class frames, are the strength of the presented simulation study for wall-recognition. To our knowledge, the majority of works on artery wall recognition algorithms have only assessed their performance for positive class frames (Delsanto et al., 2007; Fan et al., 2000; Golemati et al., 2007; Arnold P.G. Hoeks et al., 1997; Molinari, Meiburger, et al., 2012; Molinari et al., 2010b; Rossi et al., 2008; Sifakis & Golemati, 2014; D. C. Wang et al., 2009). The underlying assumption is that the examinations are always carried out by a specialist or a sonographer who is trained to determine whether or not an artery exists in an image. In this context, our study focuses on adding a layer of intelligence to the approach, allowing it to distinguish between frames with and without artery echoes. As a result of this provision, the technology is amenable to general operators during field research or practitioners at various levels of the healthcare chain. The method successfully judged and notified the lack of artery walls in all of the blank frames as well as frames with static echoes (for SNR > 3 dB) in real-time, as demonstrated by the specificity for simulation Categories (i) and (ii) (in Figure 3.5). The method showed its efficiency even during Category-(ii), where the static echoes were kept in a way to misleadingly mimic the arterial walls and lumen but devoid of any motion. The proposed method's ability to distinguish between dynamic and static echoes online is a major strength. The specificity only decreased by 10% for frames with extremely low positive SNR (0 – 3 dB). Similarly, the wall-recognition approach performed appreciably for all of the positive class frame categories.

It should be emphasized that a high precision only indicates that the locations of the walls were correct in the majority of the frames where the artery was detected; it does not indicate how frequently those detections occurred. It is 'recall' that quantifies the

sensitivity of the method, indicating the percentage of detections relative to the total potentially possible detections. Therefore, a high recall and precision are warranted, which implies detection rate was high, and those detections were majorly correct. The results for the overall and individual categories (Figure 3.7 – Figure 3.9) were statistically similar ($p = 0.57$). A high recall (97 - 100%), as well as precision (99 - 100%), were achieved with optimal and practically rational simulation settings of SNR and SoF. These findings suggest that the method's recognition ability is unaffected by other static and in-phase dynamic structures in the vicinity of artery walls. In some instances, wrong echoes may be identified and tracked when additional out-of-phase moving echoes are present in frames (for example, the jugular vein when targeting the common carotid artery). However, as stated earlier, the method was equipped to check the motion pattern and re-detect in case of an anomaly. A strong performance, particularly in Category – (iv) (refer Figure 3.7 (b)), was encouraging because it indicated that the method was inherently immune to any hyperechoic regions adjacent to artery walls; in some cases, it even shadowed the wall echo peaks. It also shows that the method may be used for highly superficial arteries (such as the radial, tibial, and dorsalis pedis arteries) that are close to the transducer's saturation band, which may especially corrupt their NW echo.

It was anticipated that by utilizing a subset of frames greater than two for decision making, the chance of detection would improve, hence enhancing performance. The efficiency of such clustering schemes was previously demonstrated in mutliple works (Rossi et al., 2008; Sifakis & Golemati, 2014). The detection-results can be clustered across the width for multiple scan-lines within in a frame, as well as across time for multiple frames, which improves detection ability. Because our work was designed to

support even single-line A-mode scans, we effectively clustered detections across time. The obtained results showed that increased SoF improved performance, substantiating this claim (Figure 3.7 – Figure 3.9, and Figure 3.17 (b)). This improvement was more relevant for recall than precision, as the latter had already reached 99 percent for frames with SNR $\geq$ 5 dB, regardless of the considered SoF. For such low SNR frames, the recall improved from 90% (with no clustering) to above 98% with detections clustered for six frames and above. It's also worth noting that the average time it takes to process a cluster of 10 frames for artery wall detection was less than 20 ms, indicating that the execution was real-time even with clustering. When tested at varied heart rates, these performance outcomes were consistent, and they were equally remarkable for low SNR frames. This demonstrated the method's robustness towards the noise that may corrupt the frames in practical settings during actual recordings.

In-vivo results corroborated the simulation study results where the group-average recall, precision, and specificity for all SoF cases exceeded 85%, 90%, and 98%, respectively. The group-average recall and precision were found to be greater than 94 percent and 98 percent, respectively, when the SoF was increased ($\geq$6). It's also pertinent to mention that measurements on a few subjects (n = 4) with heavy breathing during the procedure and for whom one of the walls echoes had a reduced intensity indicated decreased performance (recall 85% and precision 90%). In such subjects, a stronger echo in the vicinity of walls that suffered pseudo tissue motion was at times misinterpreted for walls. The clustering of detections was relevant for these cases, which supported improved performance (recall > 90% and precision > 95% with clustering 6 frames and above). On balance, the wall recognition method exhibited acceptable performance, on par with existing B-mode methods (Delsanto et al., 2007;

Fan et al., 2000; Golemati et al., 2007; Arnold P.G. Hoeks et al., 1997; Molinari, Meiburger, et al., 2012; Molinari et al., 2010b; Rossi et al., 2008; Sifakis & Golemati, 2014; D. C. Wang et al., 2009).

Likewise, the proposed wall-tracking method has demonstrated excellent accuracy (error < 3%) both for simulations, measurement on phantom and human subjects. The method proved robust against additional echoes present in the selected wall ROIs for tracking purposes, as expected. Most of the popular commercial scanners with a provision to auto-track arterial walls employ cross-correlation-based methods (S I Rabben, Baerum, Sørhus, & Torp, 2002; Reneman & Hoeks, 2000). These approaches, as well as the others (Arndt, Klauske, & Mersch, 1968; de Jong, Arts, Hoeks, & Reneman, 1990; A. P.G. Hoeks et al., 1990; Hokanson, Mozersky, Sumner, & Strandness Jr, 1972; S I Rabben et al., 2002), estimate an averaged form of shift for the full wall ROI. The existence of a static echo and/or a slow-moving echo in the ROI causes the wall shifts to be underestimated (Section 3.4.3). When this underestimate is accumulated frame by frame, the true morphology of the distension waveform is corrupted. With emerging vascular diagnostic practices, new applications have been conceived that require accurate morphology or contour of the distension waveforms waveforms (Bia et al., 2005; Nabeel, Raj, Joseph, Abhidev, & Sivaprakasam, 2019; Tang, Lee, Chuang, & Huang, 2020). These applications include ultrasound-based measurement of incremental elasticity of arteries, PWV, viscoelasticity, etc. (Bia et al., 2005; Nabeel et al., 2019). The proposed method demonstrated its ability to distinguish between the various echoes moving at different velocities. Therefore, it estimates more precise frame-to-frame shifts occurred in the NW and FW echoes, enabling sufficient robustness for A-mode signals. It also supports real-time evaluation of high-resolution

dynamic wall properties as the tracking time for each frame was smaller than 5 ms. Such real time methods with a runtime feedback increase the success-rate of the measurements performed (Flore et al., 2015). The applications mentioned above are concerned with the method's ability to track. Other recent advanced applications include strain elastography, shear wave elastography, longitudinal kinetics of walls, and power spectral analysis-based mechanical property evaluation, all of which could benefit from a real-time A-mode based wall-recognition method like the one proposed in this paper (Bazan, Ramos, Balay, & Negreira, 2018; Golemati & Cokkinos, 2022).

The advantages of RF-processing approaches over B-mode methods have already been emphasized in the literature (S I Rabben et al., 2002; Reneman & Hoeks, 2000; Zahnd et al., 2015). In addition to these advantages discussed earlier, reliable implementation of the proposed method to single-channel A-mode scans inherently reduce the processing complexity and facilitates the development of simpler, affordable, and modern A-mode technologies. With the advent of several new cardiovascular measurements (Bia et al., 2005; F. Li et al., 2016; Nabeel et al., 2019), B-mode scanners may not be suitable for all the applications given their limited speed and larger form-factor of the probe that limits sensor fusion (Arnold P.G. Hoeks et al., 2000; Nabeel et al., 2019). For such applications, robust and efficient A-mode or limited M-line methods featuring high frame rates are ideal, as they can provide high-resolution waveforms while also enabling the integration of multimodal systems. In addition, our group and others have attempted to reliably delineate the arterial wall layer-interfaces (intima-lumen and media-adventitia) using RF signals rather than B-mode images (Arnold P.G. Hoeks et al., 1997; V. K. Raj, Joseph, Nabeel, & Sivaprakasam, 2020; Willekes et al., 1999). A unification of such delineation methods with the proposed

arterial wall recognition and tracking methods yields a complete automated framework for reliable wall-segmentation using A-mode scans.

3.7 LIMITATIONS AND FUTURE WORK

This pilot study's in-vivo assessment was limited to healthy volunteers, which validated the method's functionality. Clinical validation studies in healthy and diseased populations, particularly those with arterial plaques, are now being undertaken. In the present technique, the algorithm resumes the wall recognition phase once it notices any different out-of-phase echoes, such as those from the jugular vein, so eliminating erroneous tracking. However, efforts are in progress to develop techniques to recognize and track the artery walls despite such additional misleading out-of-phase moving echoes. To distinguish between the two pairs of wall echoes, such techniques would include enforcing anatomical constraints.

3.8 CONCLUSION

This chapter presented the DTW based arterial wall recognition and motion-tracking methods which can be applied directly to M-line RF signals and are adequately robust for A-mode RF frames. The detailed simulations, in-vitro experiments, and in-vivo trials on 21 subjects have established the methods' performance. The detection rate and correctness of detection of the wall recognition algorithm were both sufficiently high (> 90%). Using a clustering scheme across a subset of successive frames, in particular, produced performance figures that were on par to the best of existing image-based techniques. Further, excellent frame-to-frame tracking accuracy (absolute error < 3%, RMSE < 2 μm) was demonstrated. Image-free measurements of peak arterial distension

agreed with the image-based ones, within an error of 1.08 ± 3.65 % and RMSE of 38 μm. The method discerned the presence/absence of arterial walls in A-mode frames, robustly localized, and tracked them even when they were proximal to hyperechoic regions or slow-moving tissue structures. These were novel highlights of the methods proposed, where works in literature are typically challenged with such scenarios. This was the first goal of this research, based on which the subsequent work was built. Unification of artery wall layer delineation techniques with the proposed methods facilitates a complete image-free framework for measuring arterial wall dynamics and the development of reliable A-mode devices.

CHAPTER 4.

AUTOMATED MEASUREMENT OF DIAMETER AND WALL THICKNESS USING A-SCAN ULTRASOUND

Signal processing methods to robustly evaluate arterial structural properties from A-mode signals are virtually non-existent, especially for wall thickness. As mentioned in section 2.2, an automated framework for measuring artery anatomy with ultrasound entails computerized recognition of the walls in the ultrasound frames and then delineation of their distinct layers using an appropriate segmentation technique. The first objective was covered in Chapter 3, which presented a unique method for recognizing and tracking artery walls from A-mode ultrasound frames. In this chapter we introduce two novel A-mode methods for delineating the arterial wall layers for the measurement of the structural properties, diameter, a surrogate IMT (sIMT) and their pulsatile component within each cardiac cycle. The initially proposed method was based on Gaussian mixture modelling, which exhibited methodological limitations. A better approach based on the analytic phase of echoes was then developed. Simulations, phantom tests, and in-vivo trials were used to validate the method's performance.

This chapter is partially adapted from the post-print version of:

Raj, K. V., Joseph, J., Nabeel, P. M., & Sivaprakasam, M. (2020). Automated measurement of compression-decompression in arterial diameter and wall thickness by image-free ultrasound. Computer Methods and Programs in Biomedicine, 194, 1–12.

Raj, K. V., Joseph, J., Shah, M. I., & Sivaprakasam, M. (2017). An image-free ultrasound method to estimate artery wall thickness surrogate for screening. IEEE International Symposium on Medical Measurements and Applications (MeMeA), 1–6. Rochester.

Raj, K. V., Joseph, J., Nabeel, P. M., Frese, H., Sivaprakasam, M., & Shah, M. I. (2019). Analytic phase based approach for arterial diameter evaluation using A-mode ultrasound frames. IEEE International Symposium on Medical Measurements and Applications (MeMeA), 1–5.

Raj, K. V., Nabeel, P. M., Shah, M. I., Sivaprakasam, M., & Joseph, J. (2021). Gaussian-Mixture Modelling of A-Mode Radiofrequency Scans for the Measurement of Arterial Wall Thickness. 43rd Annual International Conference of the IEEE Engineering in Medicine and Biology Society (EMBC), 5598–5601.

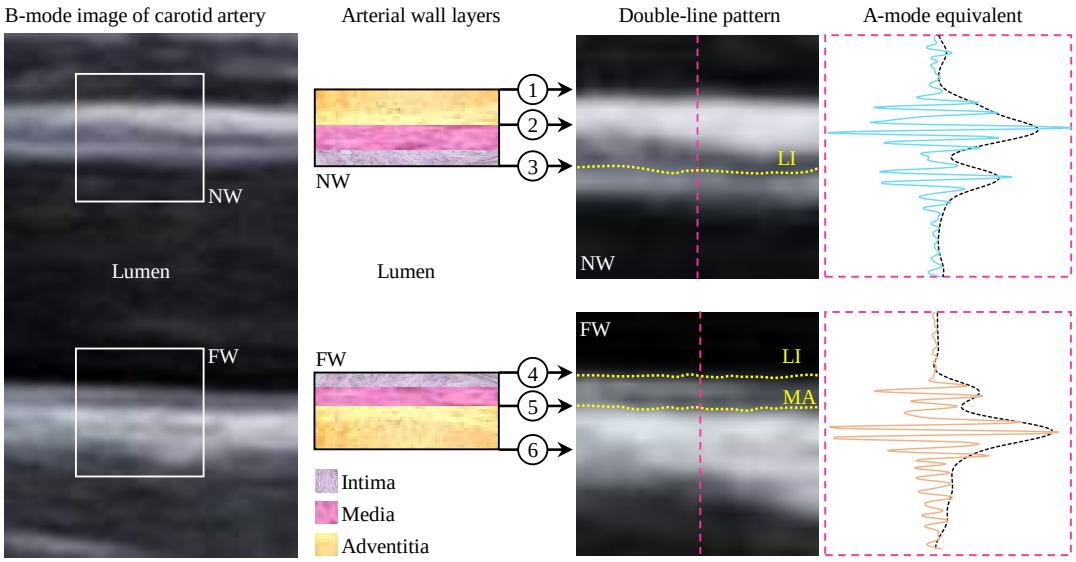

Figure 4.1 A-mode echoes corresponding to the near and far walls, obtained from a single RF-line of the 2D B-mode data are depicted. Wall layer interfaces 1, 3, 4, and 5 are identifiable on a B-mode image and these correspond to the leading edges of intimal and adventitial A-mode echoes.

4.1 THEORETICAL BACKGROUND

This section outlines the necessary concepts for understanding what delineation means in the context of A-mode wall echoes, as well as the basic theory behind the approaches that were introduced.

4.1.1 A-mode arterial wall echo features

A typical carotid artery echo pattern is shown in Figure. 1, and the interfaces of the arterial wall layers that can be seen on a B-mode image (Pignoli et al., 1986; Wikstrand, 2007) are also labelled. In the last column of Figure 4.1, A-mode echoes corresponding to the NW and FW, obtained from an RF-line of the 2D B-mode data, are shown. This A-mode analogue of the B-mode double line pattern depicted in the figure is used in the proposed method (Figure 4.1). Each wall consists of two virtually Gaussian modulated sinusoidal echoes originating from the LI and MA interfaces of the walls, as

seen in the A-mode version. To accomplish the delineation and measurement of D and sIMT, the methods proposed in this chapter rely on defining the leading and trailing boundaries of these two echoes.

4.1.2 Gaussian modelling representation of RF frame

A-mode frames consist of raw RF echoes, and those can be approximately represented by a model as a sum of weighted and shifted Gaussian modulated sinusoidal pulses (Demirli & Saniie, 2001). Each pulse originates at an anatomical location of a new tissue interface. Assuming there are 'M' such interfaces, the A-mode frame r(n) can be expressed as

$$r(n) = \sum_{m=1}^{M} s_m(n) + w(n) \tag{4.1}$$

Where w(n) is the white noise and $s_m(n)$ is the m^{th} weighted Gaussian modulated sinusoidal pulse,

$$s_m(n) = G_m \cos(2\pi f_c(n - \tau_m) + \theta_m). \tag{4.2}$$

Here, G_m represents the weighted gaussian that modulates m^{th} echo pulse, the amplitude of which depends on the echogenicity of the respective tissue structure, τ is the delay of the pulse as a result of scatterer-to-skin-surface distance, f_c is the center frequency of the ultrasound transducer, and θ_m is the phase offset of the mth sinusoid pulse. Now, an envelop constructed on this A-mode frame, therefore, can be modeled by a mixture

of ‘M’ Gaussians that modulate the sinusoidal pulses. From equation (4.1), G_m, i.e., any m^{th} gaussian is given as,

$$G_m(n) = A_m e^{-0.5*\left(\frac{n-b_m}{c_m}\right)^2}, \tag{4.3}$$

where A_m is the amplitude, b_m is the location of the peak, and c_m is the standard deviation of the respective m^{th} gaussian. Such a construct of the A-mode RF frame allows the identification of boundaries of each reflected echo that constitutes the frame.

4.1.3 Analytic phase characteristic of RF frame

Given that each echo in the RF frame may be approximated by a gaussian modulated sine wave, the analytic phase characteristics of an A-mode frame are also worth noting. This characteristic is able to indicate the points where two echoes meet.

For a signal x(t) and its Hilbert transform y(t),

$$y(t) = \frac{1}{\pi}\int_{-\infty}^{\infty} \frac{x(\tau)}{t-\tau} d\tau, \tag{4.4}$$

The envelope A(t) and the instantaneous analytic phase θ(t) are respectively defined as

$$A(t) = \sqrt{x^2(t) + y^2(t)} \text{ and} \tag{4.5}$$

$$\theta(t) = \tan^{-1}\left(\frac{y(t)}{x(t)}\right) \tag{4.6}$$

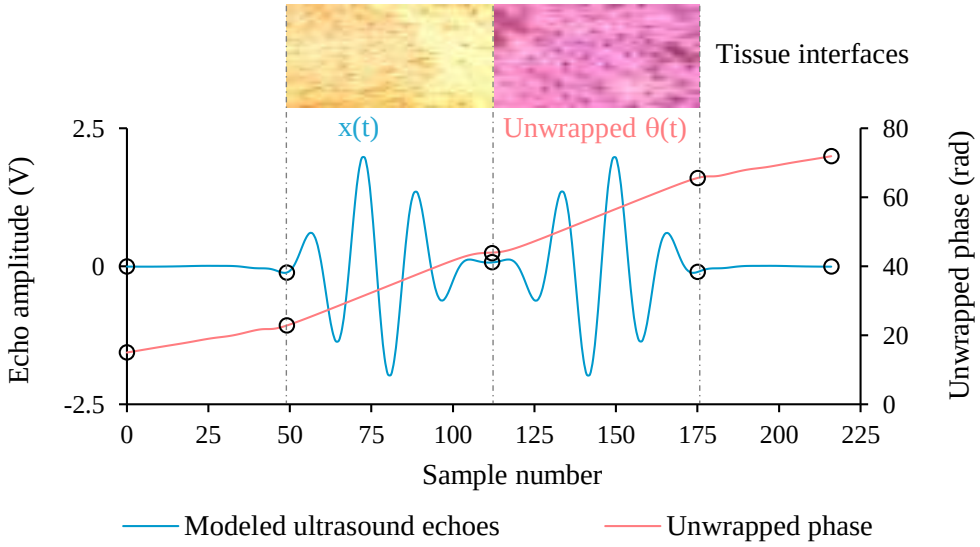

Figure 4.2 Illustration of two adjacent gaussian modulated echoes (simulated) and its unwrapped analytic phase that is piecewise linear with breakpoints at the boundaries of the echoes.

The unwrapped form this θ(t) should be linear for a sinusoidal signal without discontinuities. On the contrary, since the RF data that is acquired consists of many echoes from several areas of the tissue, the unwrapped analytic phase (UAP) will be piecewise linear with a breakpoints or knots at every boundary between two different types of tissue with distinctly different echogenicity (Figure 4.2).

4.2 PILOT METHOD OF GAUSSIAN MIXTURE MODELLING

The the first method we have proposed exploits the Gaussian modeling of the A-mode RF frames to estimate the leading and trailing edges of the intima and adventitia echoes of the NW and FW, and thereby evaluate sIMT. We have explored the method for the measurement of intima-media thickness alone, and not diameter, owing to a few limitations which are discussed later in this section.

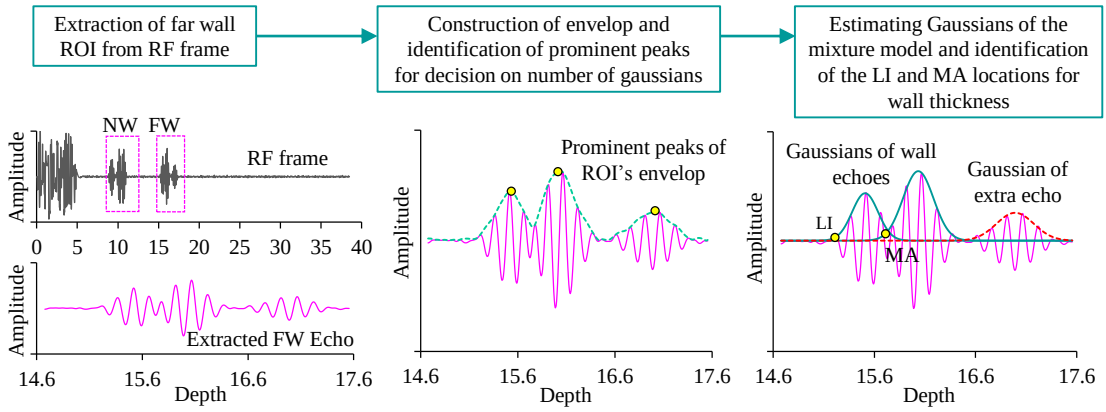

Figure 4.3 Illustration of various stages involved in the Gaussian mixture model method to estimate the wall thickness.

4.2.1 Proposed algorithm

An overall schematic of the method is shown in Figure 4.3, taking an example frame for illustrative purpose. Since the sIMT measurements are performed on the distal wall, its real-time location in each recorded A-mode frame is to be identified, and a region of interest encompassing the wall echoes is to be extracted first. For this, our robust automated DTW based recognition and tracking methods were employed, the details of which are discussed. The extracted distal wall ROI forms the input to the proposed method, and it consists of a series of gaussian modulated sinusoids. The peaks of the sinusoids were detected based on a second derivative-based peak-detector algorithm, and an envelop signal, $E_{CS}(n)$, of the ROI, is constructed by applying cubic spline interpolation on these peaks. The ROI and its envelop constructed in this manner are equal in length.

Samples in $E_{CS}(n)$ is now modeled by a function, in (4.7), that nonlinearly combines 'M' Gaussains with model parameters $\{A_m\}$, $\{b_m\}$ and $\{c_m\}$, for m = [1, M] and the independent variable 'n'.

$$\widehat{E}_{CS}(n|\psi) = \sum_{m=1}^{M} G_m(n) = \sum_{m=1}^{M} A_m e^{-0.5*\left(\frac{n-b_m}{c_m}\right)^2} \quad (4.7)$$

Here ψ is vector containing the set of model parameters $\{A_m\}$, $\{b_m\}$ and $\{c_m\}$. A curve based on this model function is fitted onto $E_{CS}(n)$ using Levenberg–Marquardt (LM) optimization scheme by iteratively updating ψ. The fit accuracy is measured by the residuals $\Delta(n)$, in (4.8), and the best-fit curve is the one that minimizes 'S', the sum of squared residuals, in (4.9).

$$\Delta(n) = E(n) - \widehat{E}(n|\psi), \quad (4.8)$$

$$\text{and } S = \sum_n \Delta(n). \quad (4.9)$$

The number of Gaussians, M, is adaptively decided in the initial stage, based on identifying the number of prominent peaks in $E_{CS}(n)$ employing a thresholding scheme. Further, approximate model parameter values are given to the LM optimization block as the initial guess. Initial guesses for $\{A_m\}$ and $\{b_m\}$ are, respectively, the amplitudes and locations of the prominent peaks of $E_{CS}(n)$. Further, the initial guess for $\{c_m\}$ is assigned as 0.23 times the full width tenth maximum (FWTM). For any ultrasound transducer, its center frequency dictates the value of spatial pulse length and, therefore, the value of FWTM.

Once the model parameters are estimated by the alluded curve fitting method, $E_{CS}(n)$ is decomposed to M individual Gaussians (G_m). Since in the ROI, the wall layer echoes possess the strongest intensity, the two Gaussians G_I and G_A with the highest amplitudes A_I and A_A, are identified. These correspond to the intima and adventitia echoes, respectively. The (b_m–2*c_m) locations of these Gaussians are evaluated as their leading

edges. Therefore, the desired interfaces are evaluated as LI = (b_I –2*c_I) and MA = (b_A –2*c_A). The wall thickness surrogate based was evaluated as,

$$\text{sIMT} = \left(\frac{c}{2f_s}\right).(\text{LI} - \text{MA}), \tag{4.10}$$

where c is the speed of the sound propagation in tissue (=1540 m/s) and f_s is the sampling frequency of the RF signal.

4.2.2 Simulation verification study

Simulation testbed, described in section 3.3.1, was employed for the initial performance assessment of the method. The tissue scattering function I(n) in this case was defined by sequence of four impulses,

$$\text{I(n)} = \begin{cases} \delta_1, & \text{n corresponds to depth } D_1 \\ \delta_2, & \text{n corresponds to depth } D_2 \\ \delta_3, & \text{n corresponds to depth } D_3 \\ \delta_4, & \text{n corresponds to depth } D_4 \\ 0, & \text{otherwise} \end{cases}. \tag{4.11}$$

In the equation D_1, D_2, D_3, and D_4 are user-defined depths for the tissue-adventitia interface of NW, intima-lumen interface of NW, intima-lumen interface of FW, and media-adventitia interface of FW, respectively. The transmitted Gaussian modulated sinusoidal pulse was modelled using (4.3). The pulse width of the simulated p(t) was chosen as 180 ns, based on the experimentally investigated 3dB width of a transmit pulse from the 10 MHz transducer employed for the current system. The pulse in discrete domain p(n) was obtained by taking the sampling rate as 80 MHz. The impulse pairs {D_1, D_2} and {D_3, D_4} were dynamically displaced out-of-phase to each other in the consecutive RF frames according to a user-programmed quasiperiodic waveform.

Likewise, the separation between the impulses of the individual pairs was updated inversely to the motion between the pairs. This allowed emulation of realistic arterial wall dynamics, wherein the thickness of the wall inversely varies with respect to the lumen diameter. While the distance between D_2 and D_3 provided the reference lumen diameter, that between D_3 and D_4 provided the reference IMT.

Different levels of white Gaussian noise were added to the simulated RF frames to vary the SNR and evaluate the algorithm's performance under the respective conditions. The purpose of the study was (i) to investigate the performance of the proposed method over a wide range of frame SNR (0 to 40 dB), and, to define the range of SNR for which accuracies are acceptable.

4.2.3 Phantom verification study

Further the method was deployed on our image-free ultrasound technology, ARTSENS®. Controlled experiments were conducted on an arterial flow-phantom setup to evaluate the accuracy and precision of the measurements performed by the developed system (see Figure 4.4). The setup consists an anthropomorphic carotid bifurcation phantom model (CNB-STXV, Shelly Medical Imaging Technologies, Canada) and a blood mimicking fluid that's driven through it in closed loop employing a flow control unit (CompuFlow1000 physiological flow pump, Shelly Medical Imaging Technologies, Canada). The carotid phantom model was arranged in a rectangular container, and the surrounding space was filled with a tissue-mimicking elastic silicon rubber (Ecoflex™ 00-20, Smooth-on, USA). Based on a user-defined pre-programmed flow pulse waveform and the relevant settings (such as pulse rate, amplitude, and the number of cycles), the control unit pumped the fluid through the

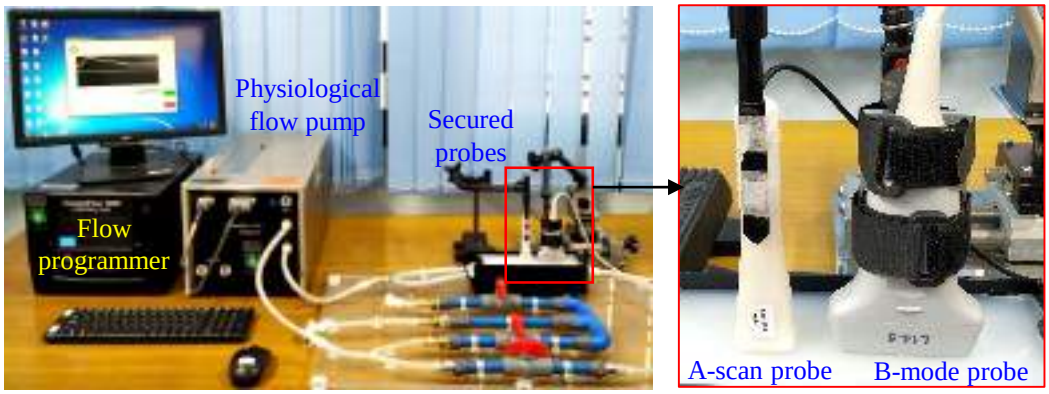

Figure 4.4 Phantom experimental setup with recording performed by the A-scan device and B-mode imaging system. The acquisition was simultaneous and the placement of the probes are illustrated.

phantom setup in a pulsatile fashion. The true measurements of D and WT of the carotid phantom model in relaxed state were referred from the manufacturer specification sheet (Shelly Medical Imaging Technologies, 2019b). Further experimentation was then performed on the dynamic phantom with controlled pulsating flow.

The setup also allows configuration of the flow parameters and thereby the amplitude of pulsations, enabling systemic assessment of measurement accuracy. As a reference for comparison, a B-mode ultrasound system (Ultrasonix SonixTouch Q+, BK Medical®, United States) was employed. To avoid excessive motion, the B-mode linear probe and the A-scan probe were secured in a stereo-tactical probe holder. To perform the D and WT measurements, they were adjusted along the longitudinal axis of the carotid phantom (Figure 4.4). The minimum and maximum values of these measurements were obtained for each pulse cycle. The respective B-mode reference measurements were obtained from the specific phantom images corresponding to the smallest and largest diameter that were selected based on manual scrutiny of the ultrasound cine buffer. The measurements using the proposed and reference systems could be compared directly since they were acquired simultaneously and also the

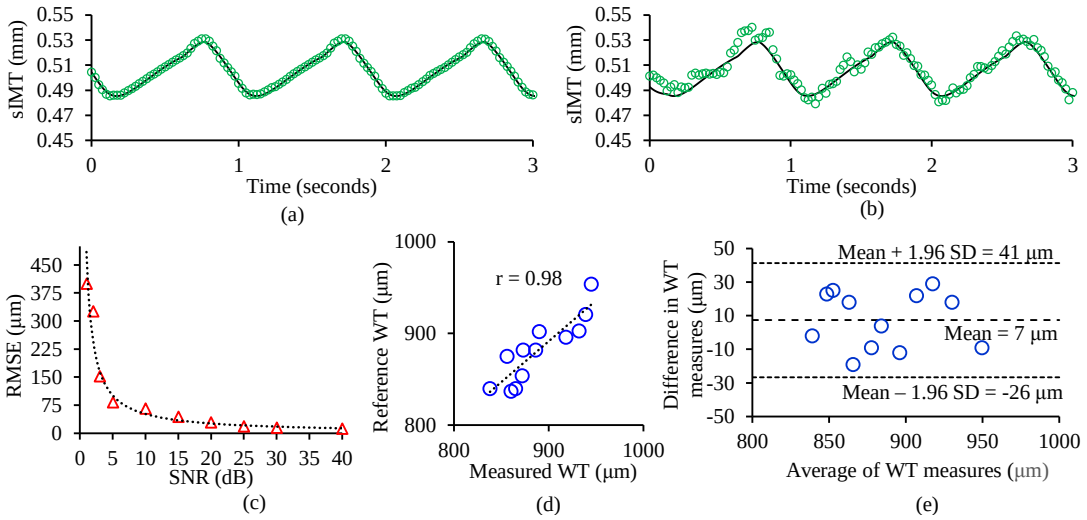

Figure 4.5 (a) and (b) Simulation versus estimated sIMT for the simulated frames with SNR 30 dB and 5 dB, respectively. (c) RMSE obtained for various SNR frames simulated. (d) Linear Regression plot indicating the correlation between the image-free and imaged based wall thickness measurements from phantom and (e) Corresponding Bland-Altman analysis.

common carotid section of the phantom offered a uniform cross-section instead of a tapper. It may be noted that, the ultrasound properties of the different media constituting the phantom model were accordingly considered for the evaluation of distance from the time-of-flight. The experimentally investigated acoustic velocity in the tissue-mimicking material was 1058 m/s. The acoustic velocities in the carotid wall mimicking material and the blood mimicking fluid were obtained from the respective data sheets, which were 1020 m/s and 1548 m/s, respectively (Shelly Medical Imaging Technologies, 2019a, 2019b).

4.2.4 Verification results

For frames with 30 dB and 5 dB SNR, the simulated reference IMT (in black line) versus the measured sIMT (green bullet markers) waveforms are shown in Figure 4.5(a) and (b), respectively. The RMSE between the reference IMT and tracked sIMT for the simulated SNR range is illustrated in Figure 4.5(c). These results indicate the ability of

the proposed method to track continuous wall thickness waveforms, with RMSE < 30 μm for SNR > 20 dB. Typically, the expected SNR of A-mode frames from human subjects is greater than 20 dB for which the method exhibited appreciable accuracy during simulations. The performance of the method for the moderate SNRs (5 to 15 dB) is also acceptable with RMSE < 80 μm.

During the phantom study, high fidelity A-mode frames with SNR > 25 dB were recorded, ensuring reliable evaluation of WT. The plots for linear regression and BA analyses for the phantom study are shown in Figure 4.5(d) and (e), respectively. A strong and statistically significant correlation was observed between the measured versus reference values ($r = 0.88$ and $p < 0.05$). Further, the BA analysis demonstrated a mean bias of 7 μm that was statistically insignificant ($p = 0.16$) and revealed that measurements are in agreement with each other within the LoA of (-26 μm, 41 μm). An absolute percentage error of (2 ± 1) % and RMSE of 19 μm, in addition to the above statistical comparisons, demonstrated the method's accuracy performance. The phantom study also demonstrated the beat-to-beat measurement repeatability of the method, with a variability smaller than 2.5 %.

4.2.5 Pitfalls and scope for improvement

Though the method has performed reliably for the simulations and in-vitro setup, there are challenges associated for applying the same for human measurements. Firstly, the NW echoes exhibited a relatively poorer A-mode counterpart of a double-line pattern when compared to the FW echoes. Concerns regarding the echogenicity of the NW due to the acoustic impedance transition, the inconsistencies in the appearance of fully defined double-line pattern across the frames, and associated difficulties in delineation

have previously been pointed out in literature (Touboul et al., 2012; Wikstrand, 2007; Zahnd et al., 2014). Further for too superficial arteries, the NW region is prone to contamination from other surrounding tissue's echoes due to exertion of hold down pressure. Factors as these directly affect the amplitude features and the visibility of distinguishable intima and adventitia echoes. Consequently, its constraints the applicability and compromises the robustness of the gaussian modelling method on the NW region making lumen diameter measurement challenging.

Another factor is ultrasound settings, which can have a direct impact on the shape and intensity of wall echoes. It is evidenced in the literature, therefore, that the thickness of these echoes does not represent any anatomical feature. Instead, their leading edges define the anatomical location of the structures or interfaces they have originated from (Pignoli et al., 1986; Wikstrand, 2007). The gaussian modelling approach, which is intrinsically dependent on the spread of each echo for detecting the echo borders, may now be affected, resulting in the incorrect identification of LI and MA interfaces on the far wall. As a result, efforts to exploit the analytic phase properties of echoes rather than merely their amplitude for delineation of wall layers were inspired.

4.3 IMPROVED METHOD EXPLOITING ANALYTIC PHASE

As seen in section 4.1.3, the locations of breakpoints or knots in the linear trend of UAP precisely correspond to the boundary locations each echo. Therefore, these breakpoints are of interest to this method, from which the LI and MA interfaces can be identified. We present a simple sinusoidal natured signal to better illustrate the signal processing scheme to locate the breakpoints. The signal is constructed by summing three shifted

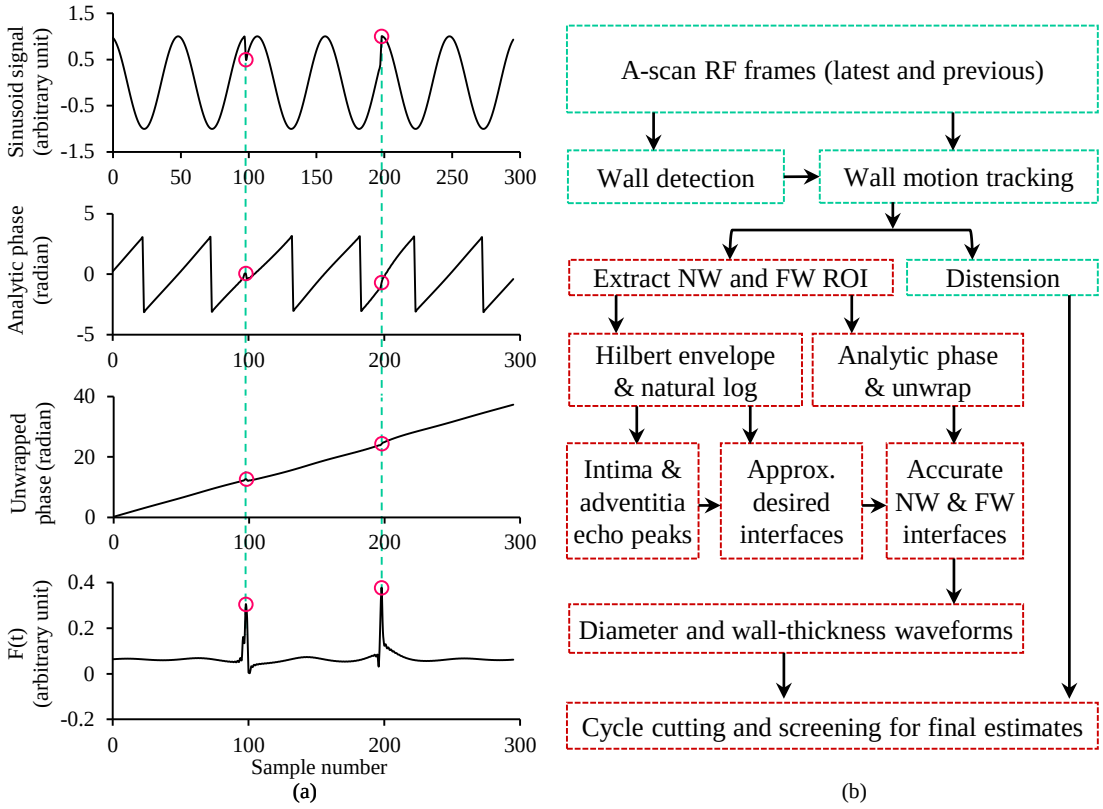

Figure 4.6 (a) Concept of using UAP to identify the phase jumps in a sinusoid signal. F(t) is the unidirectional signal obtained by subtracting the first-time derivative of the UAP with its mean and then performing a modulus operation. Prominent peaks of the F(t) provide the locations of the breakpoints. (b) Overall schematic of the computing software, with various important signal processing stages.

sinusoids with phase jumps at the interfaces (Figure 4.6(a)). A unidirectional signal F(t) obtained from the first-time derivative of the UAP, as shown in Figure 4.6(a), was used to identify the locations of these breakpoints. F(t) is obtained by subtracting the UAP's first-time derivative from its mean, followed by a modulus operation. The prominent peaks of the F(t) provide the locations of the breakpoints, which are yielded by second time derivate peak-identification method. Likewise, by adopting this concept, the interfaces between the adjacent echoes of the RF frame, characterized by jumps in the phase of the Gaussian sinusoidal pattern, can be identified. From these identified

locations, LI and MA interfaces of the arterial walls can be selected for the evaluation of the desired arterial dimensions.

4.3.1 Diameter and sIMT evaluation algorithm

Various stages of the newly proposed D and sIMT evaluation algorithm are depicted in Figure 4.6(b). Given the tracked frame-to-frame locations of NW and FW, a dynamically sized window (one-third time the distance between the NW and FW locations) was adopted for extracting two regions of interest ROI_{NW} and ROI_{FW} that encompass the echoes of the respective walls. A sample RF frame with the extracted FW and NW ROIs are illustrated in Figure 4.7, rows 1 and 2. These ROIs were used in the first phase of this algorithm in order to estimate the approximate locations of peak intensities P_LI_{NW}, $P\_ LI_{FW}$, and $P\_ MA_{FW}$ (indicated in Figure 4.7, row 3) for the echoes originating from near-wall intima-lumen (LI_{NW}), far-wall intima-lumen (LI_{FW}), and far-wall media-adventitia (MA_{FW}) interfaces, respectively. Initially, envelopes were constructed for the ROI_{NW} and ROI_{FW} using Hilbert transform, representing the intensity profiles of the encompassed echoes. The Hilbert signal was also used for evaluating the unwarpped phase of the ROIs. An over-smoothened version of this envelope $\bar{E}(t)$, was further obtained using a low-pass filter (LPF) of cut-off 1 MHz. The locations of peaks in $\bar{E}(t)$ for the respective ROIs ($P\_\bar{E}_{NW}$ and $P\_\bar{E}_{FW}$) lie in between the echoes formed at intima and adventitia of the respective walls, and therefore, these were used to find P_LI_{NW}, $P\_ LI_{FW}$, and $P\_ MA_{FW}$ using the following:

$$P\_LI_{NW} = \min\left\{L \middle| \left(L \in L_{SDV\_NW}\right) \cap \left(L > P\_\bar{E}_{NW}\right)\right\}, \tag{4.12}$$

$$P\_LI_{FW} = \max\{L | (L \in L_{SDV\_FW}) \cap (L < P\_\bar{E}_{FW})\}, \tag{4.13}$$

$$\text{and } P\_MA_{FW} = \min\{L | (L \in L_{SDV\_FW}) \cap (L > P\_\bar{E}_{FW})\}. \tag{4.14}$$

Here L_{SDV_NW} and L_{SDV_FW} are the set of locations corresponding to the second time-derivative valleys of ROI_{NW} and ROI_{FW}, respectively.

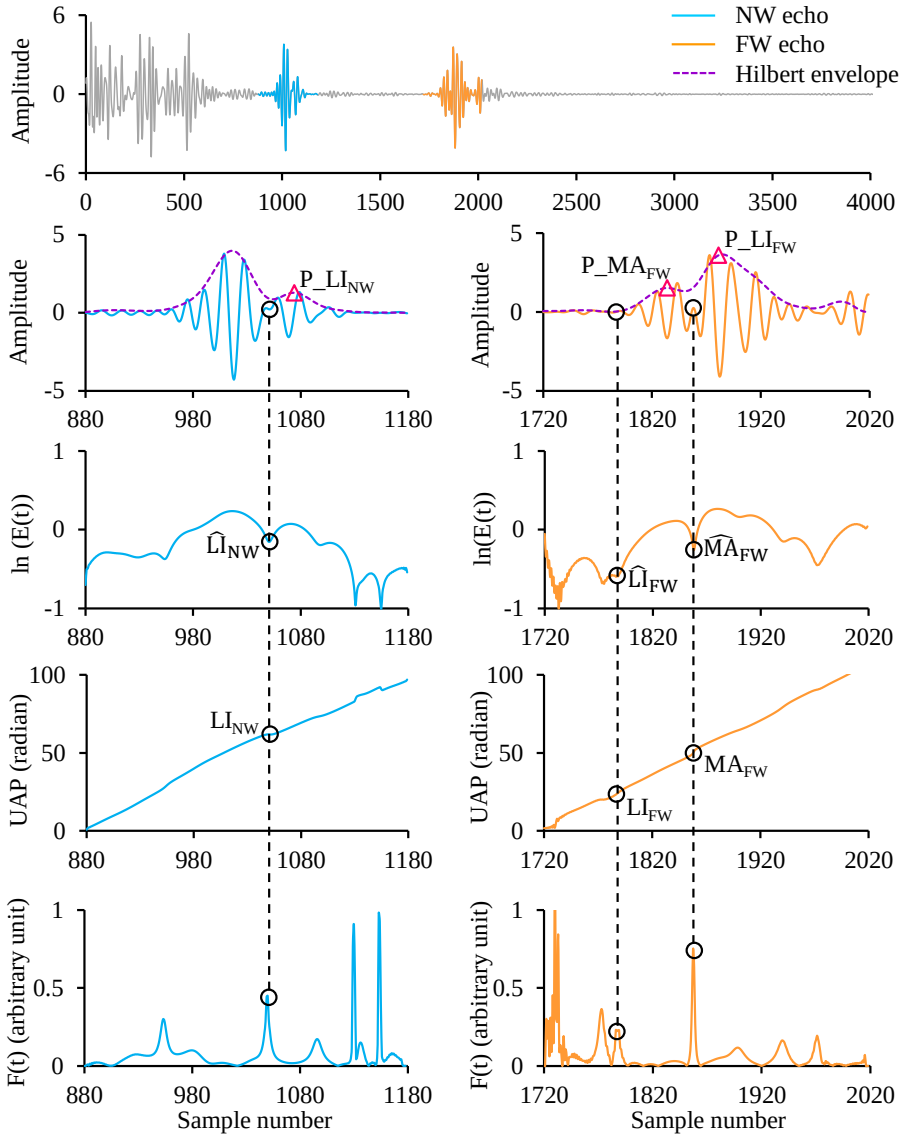

Figure 4.7 Various steps of the proposed algorithm: A-mode RF frame and the extracted wall ROIs, in first and second rows. Peak intensities identified from Hilbert envelop, in the second row. The natural logarithm of Hilbert envelops used to find approximate locations of the desired, in row three. Unwrapped analytic phase of the ROIs, in row four. Finally, the F(t) signals, shown in row five, used to identify the accurate interface locations.

Note that these locations would merely act as reference locations in the later stages of the proposed algorithm. In the second phase of the algorithm, the approximate locations of the desired interfaces $\widehat{LI}_{NW}$, $\widehat{LI}_{FW}$, and $\widehat{MA}_{FW}$ were estimated. The valley locations $\{L_{EV}\}$ of the natural logarithm of E(t) were used for this purpose. The logarithmic operation allowed the characteristic valleys corresponding to the boundaries of individual echoes to stand out. These approximate locations of the interfaces were evaluated as,

$$\widehat{LI}_{NW} = \max\{L \big| (L \in L_{EV\_NW}) \cap (L < P\_LI_{NW})\}, \quad (4.15)$$

$$\widehat{LI}_{FW} = \max\{L \big| (L \in L_{EV\_FW}) \cap (L < P\_LI_{FW})\}, \quad (4.16)$$

$$\text{and } \widehat{MA}_{FW} = \max\{L \big| (L \in L_{EV\_FW}) \cap (L < P\_MA_{FW})\}. \quad (4.17)$$

Further, the exact respective locations of the desired interfaces (LI_{NW}, LI_{FW}, and MA_{FW}) were evaluated by analyzing the analytic phase of ROI_{NW} and ROI_{FW} obtained using Eq. (4). Breakpoints (or knots) of the piecewise linear UAP of the ROIs (as alluded in sub-section 2.1.2) were identified to locate the boundaries of various echoes (row 4 of Figure 4.7). The breakpoints in the closest vicinity of the $\widehat{LI}_{NW}$, $\widehat{LI}_{FW}$, and $\widehat{MA}_{FW}$ yielded LI_{NW}, LI_{FW}, and MA_{FW}, respectively. Of note, LI_{NW}, LI_{FW}, and MA_{FW} can also have been directly evaluated as the locations of the breakpoints that were respectively closest and prior to P_LI_{NW}, P_LI_{FW}, and P_MA_{FW}, the criteria similar to that presented in Eq. (4.15) – Eq. (4.17). However, identification of $\widehat{LI}_{NW}$, $\widehat{LI}_{FW}$, and $\widehat{MA}_{FW}$ assists in a robust selection of the desired breakpoints corresponding to the interfaces of interest, avoiding selection of incorrect locations that might arise due to noisy low amplitude F(t) peaks.

Finally using the estimated interface locations, the D and sIMT corresponding to the N^{th} RF frame were respectively calculated using,

$$D(N) = k\left(LI_{FW}(N) - LI_{NW}(N)\right), \tag{4.18}$$

$$\text{and } sIMT(N) = k(MA_{FW}(N) - LI_{FW}(N)), \tag{4.19}$$

where sample to depth (or distance) conversion factor $k = c/2f_s$.

Following this approach, D and sIMT can be continuously captured with a time resolution dictated by the configured frame repetition rate. The beat-to-beat D and sIMT values at the end-diastole and peak-systole can be further evaluated using the respective continuous waveforms. A robust automatic cycle-cutting algorithm was developed, which segregated the waveforms corresponding to the individual cardiac cycles. This algorithm used the over-smoothened D(t) waveform for obtaining the cycle-to-cycle reference temporal locations of end-diastole and peak-systole. The ED and PS amplitudes for the individual cycles were extracted based on the reference temporal locations, that yielded the beat-to-beat estimates of D_{ED}, D_{PS}, $sIMT_{ED}$, and $sIMT_{PS}$. Gaussian error elimination method was incorporated to inspect the cycle-to-cycle values and filter out data points with random nature. Further, the ratio of adventitia and intima echo intensity peaks were used as a quality metric to select ten best cycles and the average of these cycles resulted in final estimates of D_{ED}, D_{PS}, $sIMT_{ED}$, and $sIMT_{PS}$. This quality metric represented how strong the intima echoes were when compared to the adventitia echoes, thereby ensuring that the data obtained from high-fidelity echoes were only used for the calculation of final values.

4.3.2 Performance of analytic phase method: simulation study

Simulations as narrated in section 4.2.2 were used for the evaluating the methods performance initially. The developed algorithm was tested for the estimation of D_2, D_3, and D_4 that are the interfaces of interest that correspond to LI_{NW}, LI_{FW}, and MA_{FW}, respectively. Different levels of white Gaussian noise were added to the simulated RF frames to vary the SNR and evaluate the algorithm's performance under the respective conditions. The SNR of the simulated dynamic RF sequences were varied between 40 to 2 dB. Sample RF frames at four different SNR levels are illustrated in Figure 4.8(a) as representative examples of the generated RF sequences. The first column of the figure represents examples of high-quality RF frames with SNRs 40 dB and 10 dB, and the second column represents low-quality RF frames with poor SNRs of 5 dB and 3 dB. The accuracy was quantitatively assessed as the RMSE between the programmed and estimated values of D_2, D_3, and D_4 that simulated the dynamic locations of the LI_{NW}, LI_{FW}, and MA_{FW} interfaces, respectively. In Figure 4.8(b), the RMSE (expressed in units of μm) for these interfaces is plotted for different SNR levels. For the RF frames

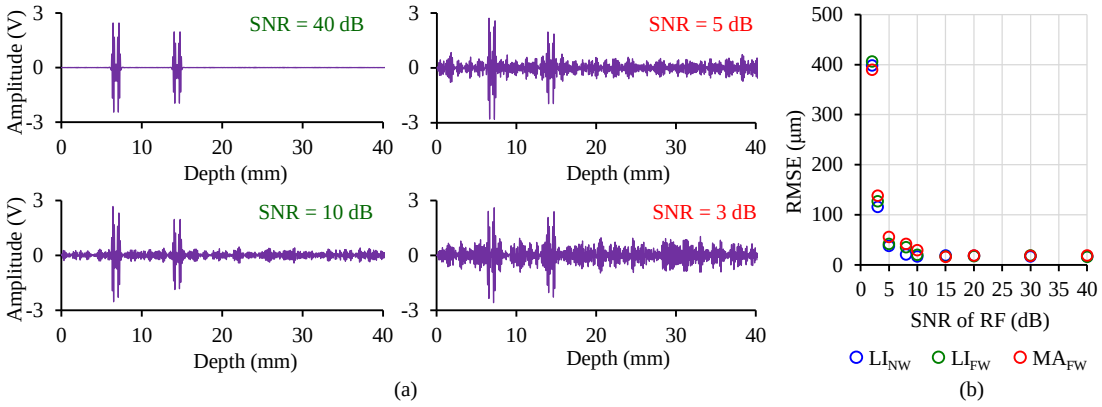

Figure 4.8 (a) Representative examples of simulated RF frames with high SNR (first column) and poor SNR (second column). (b) RMSE incurred during identification of the interface locations: LI_{NW}, LI_{FW}, and MA_{FW} for the simulated RF frames with SNRs ranging from 2 to 40 dB.

with SNR ≥ 10 dB, a RMSE < 20 μm was observed. An RMSE < 60 μm was achieved for RF frames with SNR as low as 5 dB, below which the errors elevated to > 100 μm.

4.3.3 Performance of analytic phase method: in vitro study

Post simulation experiments, the method was tested for its measurement ability on a flow phantom setup, systematically. The same arrangement that's is outlined in section 4.2.3 was employed for this purpose. As alluded, the B-mode measurements that were simultaneously collected on the flow phantom acted a reference against which the proposed method's performance was compared. The SNR of the recorded frames from the static and dynamic phantom arrangements was greater than 26 dB. The true D and WT measurements of the phantom's common carotid region, as referred from the data sheet (Shelly Medical Imaging Technologies, 2019b), were 8000 μm and 1000 μm respectively. On the static phantom the method yielded a measurement error of 111 μm (relative error = 1.39 %) and 14 μm (relative error = 1.40 %) for D and WT, respectively.

During the experimentation on the dynamic flow phantom, the peak flow rate was varied between 5 – 30 ml/s to obtain a range of controlled variation in wall dynamics. Recorded D and WT waveforms of phantom's common carotid region were of high fidelity. The beat-to-beat coefficient-of-variation (CoV) of the minimum and maximum values of the measurements were smaller than 2.3%. An average change of 7.7% and 6.5% were respectively observed in the intra-cyclic minimum-to-maximum values of D and WT of the phantom under the emulated range of flow conditions. These measurements on the dynamic phantom were further compared against manual B-mode measurements. The Pearson's correlation coefficient 'R' for measured versus reference

D was 0.94, and for WT was 0.87, with $p < 0.05$. The RMSE for D and WT measurements was 117 μm and 18 μm, corresponding to a relative error of 1.23% and 1.78%, respectively.

4.4 IN VIVO MEASUREMENT FEASIBILITY

4.4.1 Participants

The performance of the proposed analytic phase method to capture the cyclic changes in D and sIMT was further validated in-vivo. This study was performed to assess beat-to-beat repeatability, inter-operator repeatability and accuracy of D and sIMT measurements. The recruited cohort for this validation study encompassed 40 participants (normotensive), with 14 females and 26 males, with age between 18 to 40 years. An opportunistic recruitment strategy was adopted for the study, wherein the volunteers were employees of our research and development centre (Healthcare Technology Innovation Centre, IIT Madras Research Park, Chennai, India). Inclusion criteria for the study are: i) Male or female, ii) No habit of alcohol consumption or smoking, iii) Healthy with no suspected cardiac conditions, and iv) No known atherosclerotic plaque deposition. None of the subjects were offered any form of compensation for their participation. The study protocols were reviewed and approved by the internal committee of the Healthcare Technology Innovation Centre, IIT Madras, and the adopted procedures adhered to the committee guidelines. The study complied to the ethical principles of the Helsinki Declaration 1975, as revised in 2000. Written informed consent was obtained from all the participants once the study protocols and objectives were explained.

4.4.2 Data collection

Prior to the measurements, the subject-specific information such as name, date of birth, contact information, medical history, and lifestyle habits was collected from the participants through a questionnaire. The anthropometric measurements were then performed for the subjects who were qualified for the study. Initially, each subject was allowed to rest for 5-10 mins so that the BP was stabilized to a baseline level, upon which the brachial BP was measured using an automated oscillometeric device (SunTech® 247™, SunTech Medical, United States).

In this study D and sIMT were measured from the common carotid artery. All the measurements were performed in a temperature-controlled room (~23 °C). For the measurements using the proposed method, the approximate location of the left carotid artery was initially identified by palpation. The single-element ARTSENS® probe was placed near that location. The graphical user interface (GUI) of ARTSENS® Pen displayed the captured echoes in real-time as feedback to the operator to facilitate the correct positioning of the ultrasound probe and for acquiring high fidelity RF scans. For each subject, the measurements were performed by two independent operators to quantify the inter-operator variation. Procedure was repeated with the B-mode ultrasound systems. The reference data set was generated by offline processing of the acquired B-mode image sequences of the left common carotid artery (in the form of 'AVI' video clips), scanned in a longitudinal section. The offline processing of these scan data was performed on two independent tools – i) a commercial software, Carotid Studio (Cardiovascular Suite 3, Quipu, Italy) (Bianchini et al., 2010), and ii) a validated open-source tool CAROLAB (Zahnd et al., 2017b).

4.4.3 In vivo study results

4.4.3.1 Reliability of acquired signals

The proposed method was successfully applied to all the 40 recruited subjects. The recorded RF frames for the entire recruited population exhibited high fidelity, with an SNR greater than 20 dB that was sufficient for reliable measurement. The frame repetition rate was configured to 50 Hz, which yielded diameter and sIMT waveforms with a temporal resolution of 20 ms. Figure 4.9(a) illustrates the measured temporal

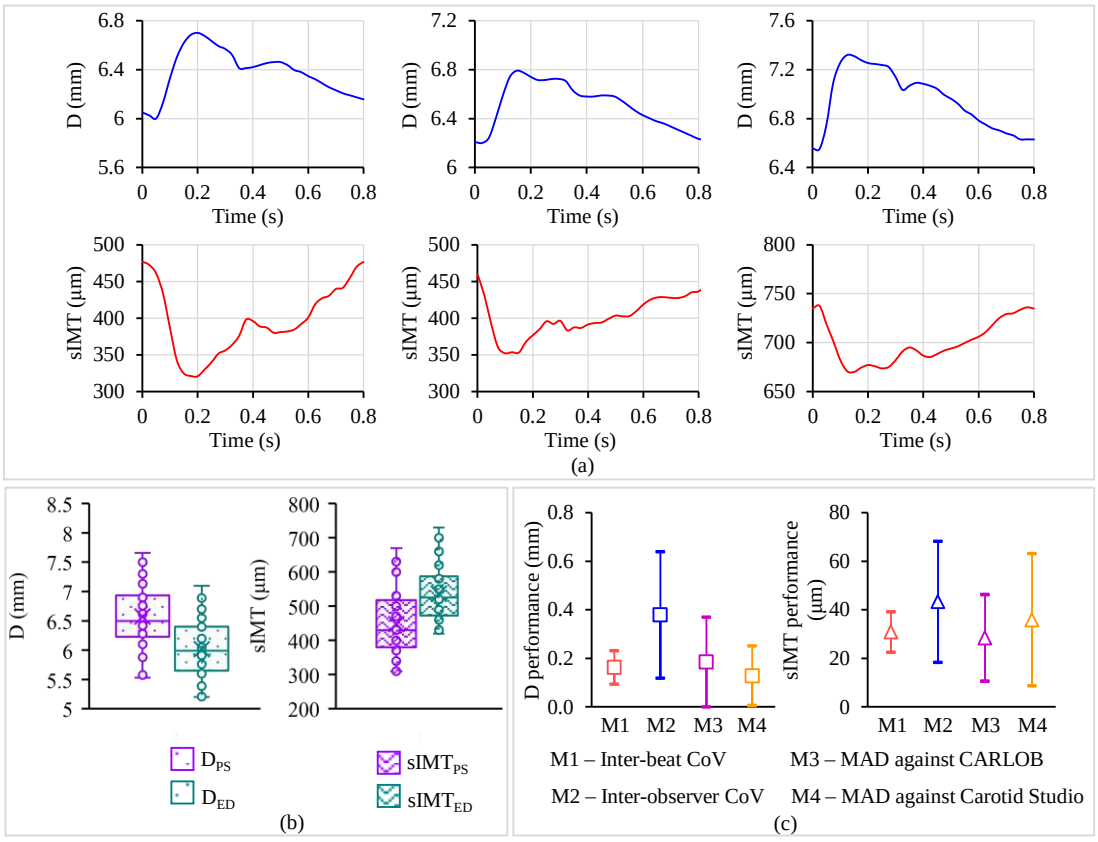

Figure 4.9 (a) Measured diameter and wall thickness waveforms over one pulsation cycle of the phantom. (b) Measured diameter and surrogate IMT waveforms for one complete cardiac cycle, from three individual subjects. (c) Box-whisker diagram illustrating a systematic difference between the peak-systolic and end-diastolic measures of D and sIMT. (d) Various performance metrics quantified for D and sIMT, indicating a better inter-beat variability, and a similarity in the ranges for the inter-observer variability and the mean absolute errors.

variations in D and sIMT within a cardiac cycle for three different individuals as representative examples of the signal fidelity. Similar high-fidelity waveforms were obtained for all the recruited subjects. The acquired B-mode image sequence clips for the reference measurements also had adequate fidelity with an image resolution of 1729×1537 pixels, and therefore none of the clips had to be discarded from the analysis.

4.4.3.2 Intra-cyclic compression-decompression in D and sIMT

As illustrated in Figure 4.9(a), the developed method reliably captured instantaneous variations in D and sIMT for individual cardiac cycles. A quasi-periodic pattern with cyclic compression-decompression was observed for the measured D and sIMT. The variations in these parameters were out-of-phase to each other. The beat-to-beat measurements of D_{ED}, D_{PS}, $sIMT_{ED}$, and $sIMT_{PS}$ for multiple cardiac cycles were automatically obtained, screened, and averaged by the developed cycle cutting algorithms. As indicated by the Box-and-Whisker diagrams in Figure 4.9(b), a significant difference ($p < 0.05$) was observed between the systolic and diastolic measures of D and sIMT, respectively. The group average D_{PS} was systematically greater than the D_{ED}, 6.57 ± 0.53 mm versus 6.02 ± 0.48 mm respectively. Likewise, the group average of $sIMT_{ED}$ was systematically greater than $sIMT_{PS}$, 537 ± 82 μm versus 448 ± 97 μm respectively. The mean of unadjusted differences between D_{PS} and D_{ED} was 0.55 mm (95% confidence interval (CI): 0.26 mm to 0.85 mm). Likewise, the mean of unadjusted differences between $sIMT_{ED}$ and $sIMT_{PS}$ was 89 μm (95% CI: 27 μm to 151 μm).

4.4.3.3 Accuracy and repeatability of in-vivo measurements

The group average CoV of the beat-to-beat measures of D and sIMT (values corresponding to both ED and PS phases) provided by the proposed method were 2.6 ± 1.1 % and 6.3 ± 1.7 %, respectively. The inter-observer CoV for these measurements was 6.03 ± 4.15 % for D and 8.84 ± 5.10 % for sIMT. For comparison, these metrics are illustrated together in Figure 4.9(c).

The measurements obtained using the proposed method were further compared against those obtained via CAROLAB and Carotid studio. Note that both the CAROLAB and Carotid studio provide D measurements corresponding to ED and PS fiduciary points. However, while the former provides IMT measurements for ED and PS fiduciary points, the later provides only an average IMT for individual cardiac cycles. Therefore, comparisons were accordingly performed against corresponding measures. First rows of Figure 4.10(a) and (b) illustrate the regression plots for the measured D and sIMT versus reference D and IMT. In the respective plots, the resulted linear regression lines are shown along the ideal regression lines (y = x) in black dotted line. These plots were obtained by pooling the systolic and diastolic measures into respective single vectors, viz. measured diameter D_{MEAS}, reference diameter D_{REF}, measured surrogate of intima-media thickness $sIMT_{MEAS}$, and reference intima-media thickness IMT_{REF}. As mentioned earlier, Carotid Studio provided only mean IMT per cardiac cycle, therefore for comparison in this case the vectors $sIMT_{MEAS}$ and IMT_{REF} include the respective mean values. The quantitative results representing the strength of correlation are also included in the respective regression plots illustrated Figure 4.10(a) and (b).

When compared with CAROLAB measurements the resulted 'R' for D_{MEAS} versus D_{REF} was 0.89 ($p < 0.05$), and for $sIMT_{MEAS}$ versus IMT_{REF} was 0.95 ($p < 0.05$). Likewise, on comparison with Carotid Studio measurements the yielded correlation coefficient

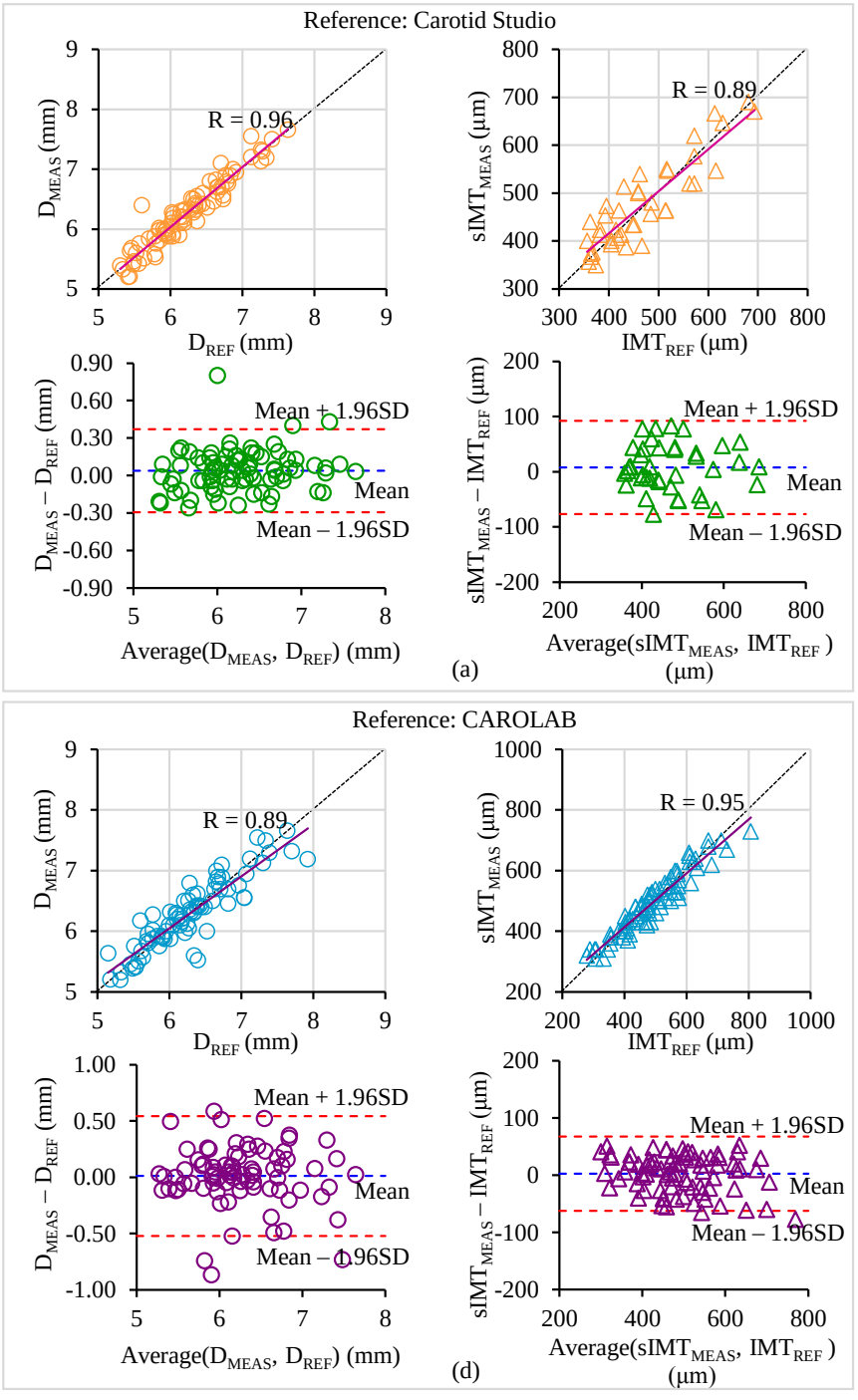

Figure 4.10 Comparison of the measured D and sIMT versus the reference D and IMT obtained from the two reference tools. Regression and BA plots against (a) Carotid studio measurements and (b) CAROLAB measurements.

for D_{MEAS} versus D_{REF} was 0.96 ($p < 0.05$), and for $sIMT_{MEAS}$ versus IMT_{REF} was 0.89 ($p < 0.05$).

The BA plots for the respective measurements are shown in second rows of Figure 4.10(a) and (b). The mean biases in diameter measurements when compared to CAROLAB and Carotid Studio was -11 μm ($p = 0.37$) and -38 μm ($p = 0.02$); likewise, in the wall thickness measurements were -2.8 μm ($p = 0.22$) and -7.7 μm ($p = 0.13$) respectively. The RMSE incurred for diameter measurements compared against the CAROLAB and Carotid Studio were 264 μm (absolute relative error = 2.94 ± 2.93 %) and 169 μm (absolute relative error = 2.04 ± 1.95 %). Similarly, the RMSE incurred for sIMT measurements compared against the CAROLAB and Carotid Studio were 33 μm (absolute relative error = 5.80 ± 3.65 %) and 42 μm (absolute relative error = 7.60 ± 5.76 %), respectively. The mean absolute differences (MAD) illustrated along with the CoV measures in Figure 4.9(c), may be referred for an intuitive comparison of these performance metrics.

4.5 DISCUSSIONS

The major contribution of this work is a fully-automated novel methods to measure the intra-cardiac variations of the arterial diameter and wall thickness simultaneously, employing an image-free ultrasound technology. A pilot initially proposed method was based on approximating the RF frames with a Gaussian mixture model, which was inherently dependent on only the amplitude features of echoes. Simulations revealed that the Gaussian-modelling method could be confidently applied to A-mode frames with above-moderate SNR (>15 dB). When applied to A-mode frames acquired from

the flow-phantom setup (SNR > 25 dB), the mean error was limited to (2 ± 1%), and RMSE was 19 μm, on comparison with B-mode measurements. The measured and reference wall thickness strongly agreed with each other (r = 0.88, insignificant mean bias = 7 μm, p = 0.16). However, the methodological challenges and its susceptibility to agents that corrupt the amplitude features of the echoes (example: ultrasound gain settings) makes it non-robust for diameter evaluation and human measurements.

This inspired an improved method that used the analytic phase signal of the RF frame. The method, by nature delineated boundaries of echoes without sole dependence on the amplitude characteristics of the echoes but the true phase discontinuities, offering adequate robustness. Hence forward the discussions in this section are pertinent to this analytic phase method. A systematic performance benchmarking of the method was carried out via simulations, phantom experiments, and in-vivo trials. While the results from the simulation experiments have demonstrated the method's capability to provide accurate locations of the desired interfaces from the simulated RF frames, they have also quantified the minimum SNR required to preserve the reliability of the method. As inference, an adequate SNR greater than 5 dB is required to perform reliable measurements from carotid artery. It should be noted that for the measurement of dimensions from much smaller vessels the required SNR may vary and should be quantified. Once the method's reliability in delineating the interfaces of interest was demonstrated through the simulation experiments, the method was applied to the phantom and human subjects. The method yielded high accuracies (with 1.38% error in diameter and 1.4% in wall thickness) for the static phantom, wherein the estimates were compared against the ground truth (provided by the manufacturer). Experiments on the dynamic phantom model with pulsatile flow also demonstrated acceptable accuracies

(relative errors < 2%). A strong significant ($p < 0.05$) correlation was observed for the measurements performed by the proposed method and the manual reference measurements ($R = 0.94$ and 0.87 for D and WT, respectively).

Further, such accuracy figures were yielded for the measured in-vivo D and sIMT measurements when compared against the independent reference tools – CAROLAB and Carotid Studio. The obtained inter-observer variabilities were comparable to the uncertainties incurred, as observed in Figure 4.9(c). It was noted that the mean absolute errors for the diameter measurements were greater than for the wall thickness measurements, 0.18 ± 0.17 mm versus 28 ± 18 μm against CAROLAB and 0.13 ± 0.12 mm versus 36 ± 27 μm against Carotid Studio as reference. A possible explanation would be based on our observation of the quality of NW echoes (from which LI_{NW} is obtained). They exhibited a relatively poorer A-mode counterpart of a double-line pattern when compared to the FW echoes. Concerns regarding the echogenicity of the NW due to the acoustic impedance transition, the inconsistencies in the appearance of fully defined double-line pattern across the frames, and associated difficulties in delineation have previously been pointed out in literature (Touboul et al., 2012; Wikstrand, 2007; Zahnd et al., 2014).

The statistical analyses on these individual measurement sets demonstrated a strong correlation (agreement) between the measured and reference values, with a mean bias that is statistically insignificant ($p > 0.05$). The measurements did not exhibit any significant under or over-estimation as indicated by the regression plots (refer to Figure 4.10) where the obtained trend line follows the ideal regression line. It was also observed by the insignificant bias values yielded from the BA analysis. As such, the

performance of the proposed method was promising in the light of the repeatability and accuracy figures reported by recent semi-automated and automated B-mode methods in the literature (Loizou, 2014; Manterola, Lo Vercio, Díaz, del Fresno, & Larrabide, 2018; Molinari et al., 2010a; Zahnd et al., 2017b, 2014).

There are a few key aspects that the proposed measurement scheme features, which allowed reliable and accurate measurements. The first is its real-time processing and the GUI feedback that displays the continuously acquired A-scan RF frames along with the processed waveforms. The average computation time taken to analyze each RF frame was 10 ms that enabled the implementation of online measurement with achievable frame repetition rates up to 100 Hz. This further allowed assessment of the recordings in real-time and gave the user a scope to re-position the ultrasound probe for improving the quality of measurements. A signal quality score (Shah, Joseph, & Sivaprakasam, 2014) representing the quality of the individual wall echoes was also displayed to notify the operator to orient the transducer probe for best signals. Therefore, this real-time feedback of the acquired RF signals and the live measurements avoided the hassle of rejection of the entire examination due to poor imaging, which other-wise is common during the post-analysis of B-mode ultrasound data. Advanced methods and even commercial tools (Example: MyLab – Genova, Italy, and ArtLab – Maastricht, the Netherlands on Esaote platform) have been introduced, emphasizing the need for such online systems with real-time feedback to ensure a high success rate for the measurements (Bianchini et al., 2010; Faita et al., 2008; Flore et al., 2015).

These signal quality scores calculated by the developed method were also used to automatically screen the measurements in real-time rejecting the ones obtained from a

poor set of RF frames. The second aspect is the employed single element ultrasound transducer that emits a focused beam (spatial half-angle < 1.3°) and has poor off-axis sensitivity. The transducer can only detect the strong specular reflections that arise out of the normal incidence of the beam on the walls. Therefore, if the transducer axis is not oriented perpendicular to both the arterial walls, the resulting echoes have considerably low amplitudes and are of drastically poor quality. As mentioned earlier, the algorithm rejects such measurements automatically based on their poor signal quality scores and only keeps the high-quality measurements.

Another major strength of the method is its ability to track reliable, continuous variations in diameter and wall thickness simultaneously in a fully automated fashion. As observed during both in-vitro and in-vivo studies, the captured diameter and wall thickness waveforms exhibited repeatable quasi-periodic and out-of-phase dynamics with notable minimum-to-maximum changes within each pulsation cycle. In the last decade, advances in automated arterial wall-tracking technologies have permitted operator-independent, non-tedious and non-time-consuming measurement of arterial stiffness (Brands et al., 1999; Palombo et al., 2012; B. M. Pannier, Avolio, Hoeks, Mancia, & Takazawa, 2002; Segers et al., 2004). These available tools majorly measured the changes in the diameter within each cardiac cycle with distending pressure. However, there are only a few works in the literature (Boutouyrie et al., 2001; Gonzalez, Wood, Dorey, Wren, & Vicente, 2008; Pascaner et al., 2015; Polak, Johnson, et al., 2012; Polak, Meisner, et al., 2012; Rueb et al., 2017; Selzer et al., 2001; Teynor, Caviezel, Dratva, Künzli, & Schmidt-Trucksäss, 2012; Zahnd et al., 2017b, 2014) that have reported on the IMT intra-cardiac cycle variations (ΔIMT). These reported studies have commented on the clinical significance of ΔIMT, presenting evidence of its

association with pulse pressure, low-density lipoprotein cholesterol, age, and cardiovascular risk factors (Boutouyrie et al., 2001; Polak, Meisner, et al., 2012; Selzer et al., 2001; Zahnd et al., 2017a). Further, another important study introduced a method to evaluate the longitudinal elongation of arteries during a cardiac cycle by measuring the corresponding changes in both diameter and wall thickness. Further, the study provided its implication on reliable measurement volumetric compliance (Pascaner et al., 2015). Now, based on the analysis for the recruited population in the current study a systematic difference, concurrent with the afore-alluded studies, was observed between the diastolic and systolic values of the measured sIMT with the former 20% greater than the later, on an average. One possible reason for the limited number of studies on the clinical utility of ΔIMT might be the complexity involved in its measurement and the scarcity of reliable commercial tools that could be easily adopted.

Further, Polak *et al.* (Polak, Johnson, et al., 2012) have also strongly emphasized on the need for reporting the IMT values labeled along with the phase of the cardiac cycle they were measured from. This would restrict the interchangeable use of normative data presented by different investigators, avoiding improper classification of patients (Polak, Johnson, et al., 2012). Also, performing measurements from the same fiduciary point reduces the inter-beat variability (Coll & Feinstein, 2008; Wikstrand, 2007). Typically, measurements corresponding to end-diastolic and/or peak systolic phases are obtained by electrocardiogram (ECG) gating or visual review of cine loops. Alternatively, we have employed an automated cycle cutting algorithm that segregates individual diameter and wall thickness pulse cycles and screens them. The scores calculated for representing the quality of RF frames and the gaussian filters efficiently screened the data obtained from multiple cycles incurring good measurement repeatability. The

maximum and minimum values of the respective measures were repeatable for multiple cycles with a variability smaller than 9%. The inter-beat variability for in-vivo measurements was relatively greater than that of the dynamic phantom as expected, owing to the beat-to-beat temporary physiological variations.

The intra-cardiac variations ΔsIMT measured during the current study was within the range of 27 – 151 μm, concurrent with the ΔIMT measurements reported in the literature previously (Boutouyrie et al., 2001; Pascaner et al., 2015; Polak, Johnson, et al., 2012; Polak, Meisner, et al., 2012; Rueb et al., 2017; Zahnd et al., 2017b). In order to track such small order variations in IMT within the cardiac cycle, high 'tracking precision' needs to be ensured. As the name suggests, this is defined as the precision with which the frame-to-frame changes of the distending arterial walls are tracked, which is perceptibly a function of the digitization resolution employed along the scan direction. B-mode systems typically decrease the pixel size of the digitized ultrasound images to improve the tracking resolution/precision (Zahnd et al., 2017b). An equivalent strategy for the proposed method was to choose a high sampling rate for digitizing the RF frames. The system was configured to sample the received RF data at 80 MHz offering a precision of 9.6 μm for the measurement of the intra-beat changes in D and sIMT. As a general caution, this may not be confused with the axial resolution of the transducer used for the study. The experimentally investigated axial resolution of the system's 10 MHz ultrasound transducer was 143 μm. Therefore, the proposed system, with its current configuration, is capable of measuring lumen diameter larger than and intima-media complex thicker than 143 μm. Employing a transducer with higher central frequency would further allow measurement of dimensions even smaller.

4.6 LIMITATIONS AND FUTURE WORK

The proposed methods were equipped to perform measurements of D and sIMT solely adopting the concept of double-line echo pair pattern, more specifically, it's A-mode analogue formed by the strongly echogenic intima and adventitia structures. This method's accuracy, therefore, is challenged by factors that disrupt this intrinsic wall echo pattern. One example is the presence of heterogenous plaques, which are likely to introduce additional dynamic echoes proximal to the wall echoes. Also, during the study, we have encountered subjects (N = 4) with dominant muscular or fat structures in the neck region, on whom measurement was challenging. This was due to the deteriorated RF signal quality and the resulting poor intima-adventitia echo pair pattern. Solutions to cope with such difficult cases and further improving the measurement reliability are under development. Incorporation of semi-automated strategies and signal quality indices to locate the intima-adventitia structures would constitute the potential improvements. Manual measurements are considered more reliable, providing end-diastolic and peak-systolic annotations by reviewing the cine-loops was laborious and time-consuming on behalf of the sonographer. Instead, in the current study, two independent rigorously validated B-mode software tools were used as the reference. As this study was conducted on a small cohort of healthy subjects with limited age diversity, a follow-up study on a larger cohort with a diverse population included healthy and diseased subjects is warranted in future. Such a study would also encompass investigations on the relationship between intra-beat temporal changes in diameter/wall thickness and vascular pathologies.

4.7 CONCLUSIONS

In conclusion, the developed automated A-scan method for diameter and IMT evaluation, as presented in this chapter, exhibited acceptable measurement accuracy and repeatability that were on a par with the recently reported image-based techniques in the literature. Of note, while the sIMT measurements that were performed in the study agree with the reference IMT measurements, it may be remembered that it is not a direct replacement for the guideline-recommended, clinically evaluated image based IMT. Nevertheless, the methods being A-scan based facilitated their deployment to affordable image-free devices as reported in the study. The methods in conjunction with the image-free technology demonstrated excellent in-vivo performance and usability. Being easily-operable, fully real-time and automated, such technology would be resourceful for field studies, settings with legal-constraints on B-mode imaging (as in India), and low-resources. Also, the real-time methods as proposed offer a platform for reliable online evaluation of functional and material properties, which will be discussed in the subsequent chapters.

CHAPTER 5.

HIGH FRAME-RATE A-SCAN ULTRASOUND FOR REAL-TIME LOCAL PULSE WAVE VELOCITY

Cardiovascular community has started clinically adopting the assessment of local stiffness, contrary to the traditionally measured cfPWV. Local PWV, a metric of the target artery's stiffness, has been emerging in its clinical value and adoption. State-of-the-art ultrasound technologies used to evaluate local PWV based on pulse waves' features are sophisticated, non-real-time, and are not amenable for field and resource-constrained settings (section 2.3). Though they offer higher reliability, ultrasound methods require advanced hardware and processing methods to perform real-time measurement of local PWV. A novel system and method to perform online PWV measurement in an automated manner are presented in this chapter, along with its characterization and validation. It is a fast image-free ultrasound technology that meets the methodological requirements necessary to measure small orders of local pulse transit time (PTT), for PWV. The method relies on recording distension waveform for which the methods presented in Chapter 3 and 4 were employed.

This chapter is partially adapted from the post-print version of:

Raj, K. V., Nabeel, P. M., & Joseph, J. (2022). Image-Free Fast Ultrasound for Measurement of Local Pulse Wave Velocity: In Vitro Validation and In Vivo Feasibility. IEEE Transactions on Ultrasonics, Ferroelectrics, and Frequency Control, 69(7), 2248–2256.

Raj, K. V., Nabeel, P. M., Joseph, J., Shah, M. I., & Sivaprakasam, M. (2018). Evaluation of local pulse wave velocity using an image free ultrasound technique. IEEE International Symposium on Medical Measurements and Applications (MeMeA), 1–6.

Raj, K. V., Nabeel, P. M., Joseph, J., & Sivaprakasam, M. (2019). Methodological and measurement concerns of local pulse wave velocity assessment. IEEE International Symposium on Medical Measurements and Applications (MeMeA), 1–6.

Raj, K. V., Nabeel, P. M., Manoj, R., Shah, M. I., & Joseph, J. (2021). Phantom Assessment of an Image - free Ultrasound Technology for Online Local Pulse Wave Velocity Measurement. 43rd Annual International Conference of the IEEE Engineering in Medicine and Biology Society (EMBC), 5610–5613.

5.1 BACKGROUND

5.1.1 Local PWV measurement principle

Direct measurement of PWV is based on pulse transit features, using the fundamental distance-time equation as in (1), relating the length of given arterial trajectory (pulse propagation length) and the time taken by a blood pulse to transit it (PTT),

$$\mathrm{PWV_{TT}} = \left(\frac{\text{Pulse propagation length}}{\text{Pulse transit time}}\right). \tag{5.1}$$

The proposed technology is equipped to measure local PWV following the transit time technique, for which it evaluates high-resolution distension waveforms from two proximally spaced locations of a target artery and measures the PTT from them (Figure 5.1(a)). The PTT is evaluated as the delay between a characteristic fiducial point located on the pair of the distension cycles (Nabeel et al., 2020). Of various fiducial points (Figure 5.1(b)), in this work is the second-derivative maxima (M_{SD}) denoting the onset of pulses' systolic phase was chosen.

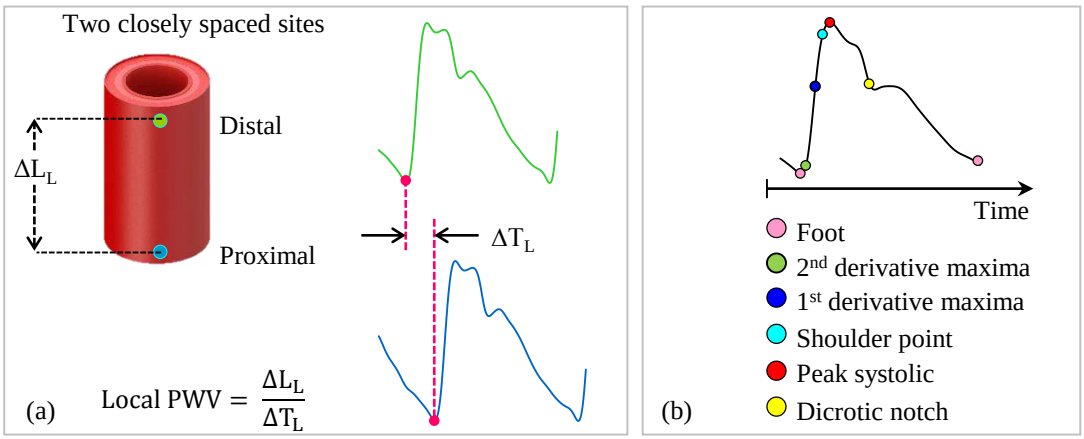

Figure 5.1 (a) Measurement principle of transit-time based PWV. (b) Popular fiducial points used for pulse transit time calculation

5.1.2 Methodological requirements

The local PTT measurements are typically of the orders smaller than 20 ms. As shown in Figure 5.2(a), the blood pulse waves therefore should have sufficient temporal resolution in-order to perform transit time measurements of such low orders. Further the general hardware requirements for accurate local PTT assessment can be broadly divided into the two – 1) the sensing modality; 2) the analog front end (AFE). The tissue transfer function of the intervening layers may potentially affect the morphology of the true transmural pulse wave (Figure 5.2(b)). Also, the non-homogenous depth of the artery at the different measurement locations introduce uneven lags (known as tissue transit time) in the captured set of blood pulse waveforms, making sensing modality an essential requirement. Lags are also introduced when the blood pulses are not conditioned or processed identically. Such may arise from non-identical AFEs and digital filters for the individual blood pulse acquisition channels. Lastly, the smoothening filters also play a critical role in the validity of the local PWV

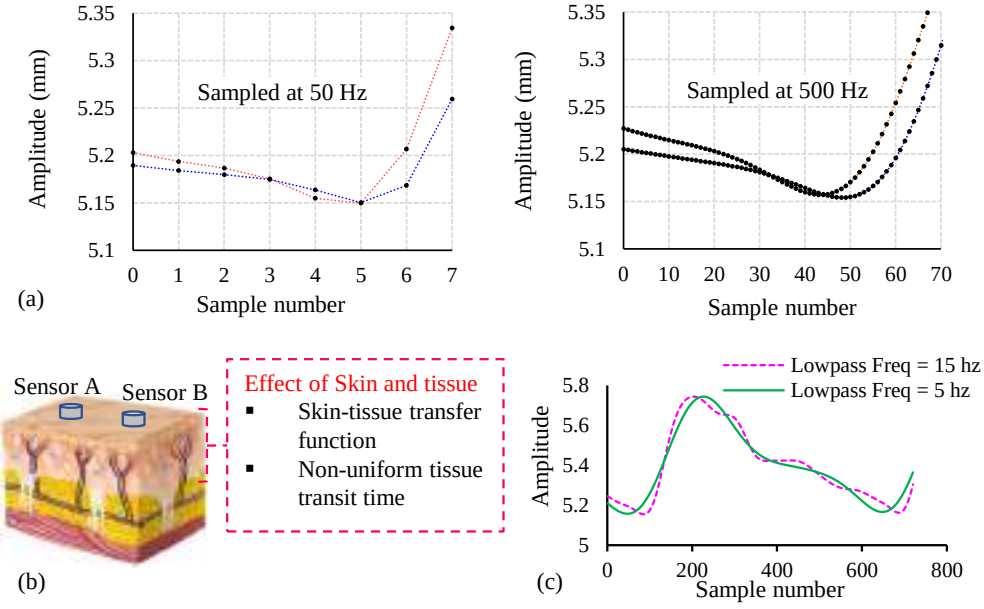

Figure 5.2 Important methodological considerations for local PWV measurement: (a) Temporal resolution of blood pulse waves, (b) sensing modality that is not susceptible to effect of skin and tissue, and (c) signal processing.

measurements. A sample example is illustrated in Figure 5.2(c), demonstrating the influence of smoothening on temporal and morphological features of the pulse.

Another methodological concern which pertains to imaging systems that employ diameter waveforms for PWV evaluation is the wall tracking method. A simulation shown in Figure 3.12, clearly demonstrates the limitation of popularly recruited cross-correlation method in providing accurate morphology of distension cycles under the influence of corrupting echoes within the ROIs. This also potentially influences PWV measurements if the such corruptions are non-uniform for the two pulses used. In addition to simulation in Figure 3.12, we have generated a second set of 150 frames in addition to the earlier one but without corruption, to illustrate such deteriorating influence. The second set is generated by providing a wall motion waveform input that is uniformly lagging the one provided for the first set by 35 ms throughout the cardiac cycle. It may be seen from Figure 5.3 that for the second set, which didn't suffer the overlap from the static echo, the distension pulses measured from both the methods were identical. Now since the proximal pulse is corrupted for the cross-correlation

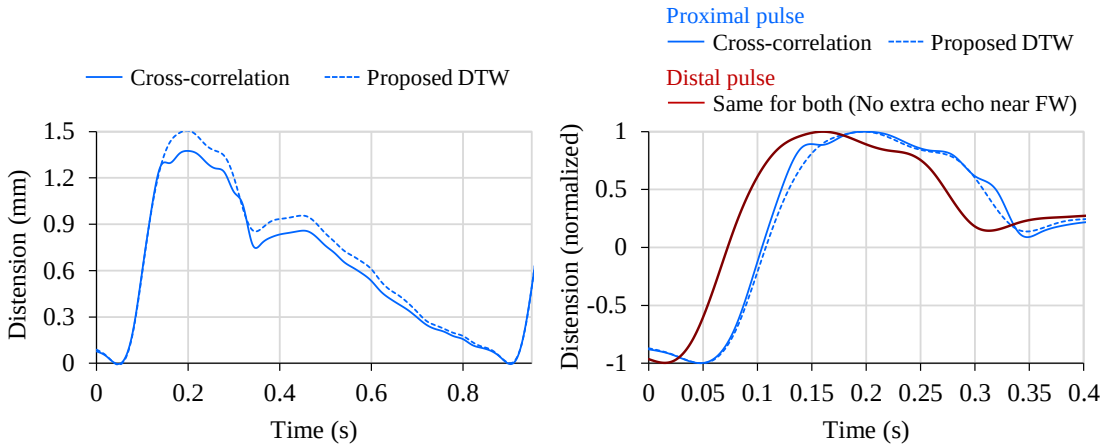

Figure 5.3 Effect of corrupting echoes within wall ROIs on the tracking efficacy. On the right, the influence of it on the lag between pulse pair is illustrated

based method, the lag as seen in Figure 5.3 appears to be decreasing when traversed from the end-diastolic point to the peak systolic point. The DTW method in this case yielded uniform lag, and this emphasizes the importance of choice of wall tracking method. These methodological aspects were addressed during the development of the proposed measurement system, which as discussed as follows.

5.2 HIGH FRAME-RATE ULTRASOUND MEASUREMENT SYSTEM

5.2.1 System Architecture

The measurement system (Figure 5.4) consists of a dual-element ultrasound probe that is interfaced to acquisition hardware via a pair of coaxial RF connectors. The transducers (diameter = 5 mm, center-frequency = 10 MHz) on the probe are separated by a center-to-center distance of 35 mm (experimentally deduced). As shown in Figure 5.4(a), the primary modules of the dual-element image-free ultrasound acquisition hardware are pulser-receiver, analog front-end, digitizer, digital logic controller, and power supply. The pulser-receiver switches the transducers' mode to act as either a 'transmitter' or as a 'receiver', operating them pulse-echo fashion. Upon excitation, the transducers are switched to the receiving mode for a fixed time period dictated by desired scan depth, and a trigger signal is generated notifying the same. The finite length RF echo signals (A-mode frame) captured by the two transducers are received by the independent channels and conditioned by identical analog front-ends constituting a high pass filter (cutoff frequency = 250 kHz) and an amplifier (gain = 40 dB). The conditioned signals are then digitized by a voltage digitizer (PXI‑5154, National Instruments, United States). As a result, a pair of A-mode frames corresponding to two scan locations are acquired whenever there is a trigger indicating the receiving mode.

The transducer is re-excited in the transmitter mode after a certain pulse repetition period, which dictates the frame-rate. The acquisition system, thus, operated in the pulse-echo mode, can provide a high frame-rate (1000 Hz). Frames acquired by utilizing this instrumentation are then transferred to a computer and processed online. Real-time processing of ultrasound data at such high frame-rates for continuous high-resolution distension waveforms would require computationally powerful systems, such as graphics processing unit (GPU)-based. Contrarily, in this work, a selective-segment processing scheme has been implemented; wherein only a portion of the high-

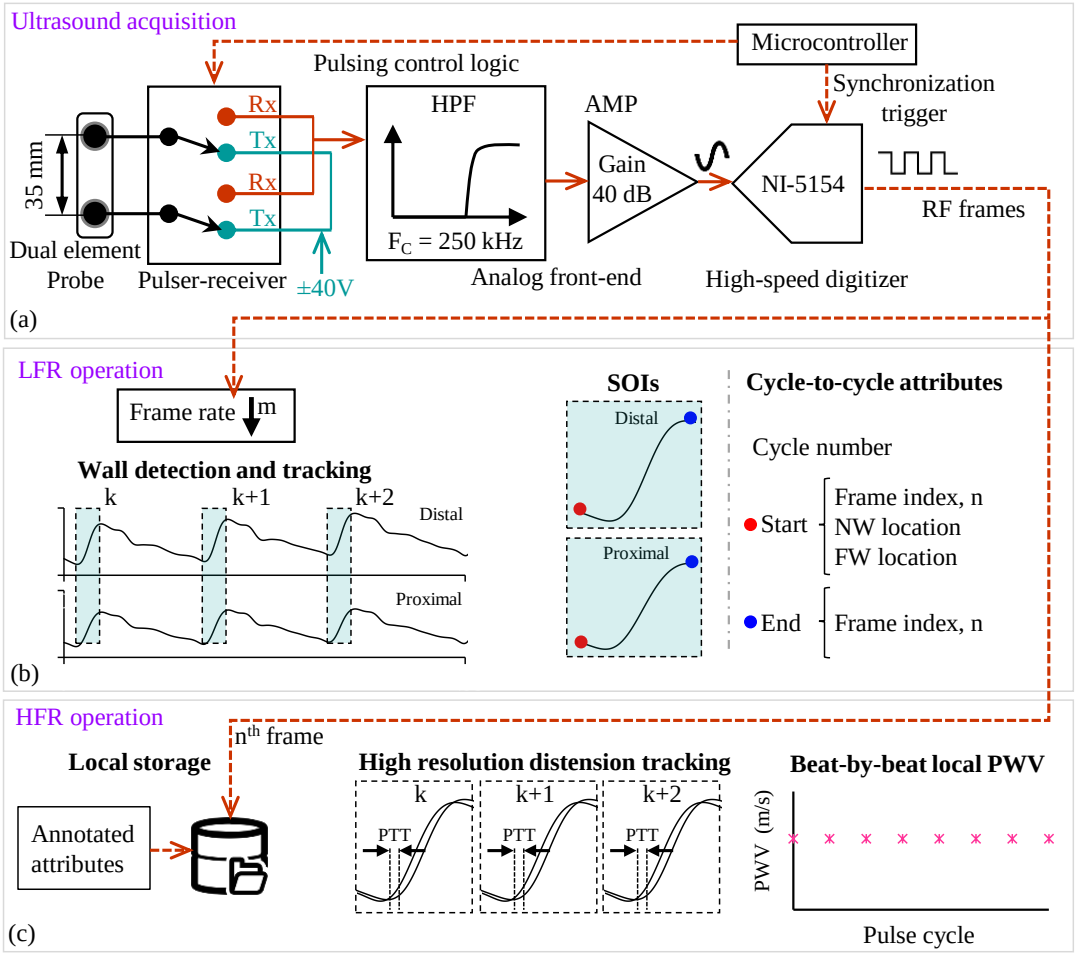

Figure 5.4 Schematic of the proposed system: (a) Acquisition hardware, and Selective-segment processing scheme for real-time local PWV evaluation comprising of two stages, (b) Low frame rate operation for yielding cycle attributes and (c) High frame rate operation for high resolution tracking and local PWV calculation.

resolution distension waveform (a segment of interest) constituting the desired characteristic fiduciary point is evaluated for each cardiac cycle. Such a scheme was realized by implementing a two-tier computation: (i) processing at low frame-rate (LFR) for cycle-to-cycle attributes and (ii) processing at high frame-rate (HFR) for local PTT evaluation.

5.2.2 Computing software: Cycle-to-cycle annotations during low frame-rate operation

For the first-tier processing, i.e., LFR operation (Figure 5.4(b)), a frame-decimator was employed for collecting every m^{th} acquired frame to obtain a sub-set with a reduced rate (m is the ratio of high frame-rate to low frame-rate configured). The objective of LFR processing is to evaluate the low-resolution distension waveforms in real-time and annotate the attributes for individual cardiac cycles that are necessary for second-tier processing (i.e., HFR selective-segment processing). Since the operations involved in obtaining each distension sample require < 5 ms, choosing an LFR of 50 Hz provides real-time distension waveform with adequate morphological features. Note that the frames at high-rate were still being acquired and temporarily stored in a local storage space along with the corresponding frame numbers and timestamps (Figure 5.4(c)), which were accessed for the second-tier processing.

Evaluation of continuous distension waveforms involves auto-recognition of arterial near-wall (NW) and far-wall (FW) locations and then auto-track their frame-to-frame motion. For these the methods proposed in Chapter 3 were employed. The latest 2.5 seconds' distension waveform samples and the frame numbers (n = 1, m+1, 2m+1...) from which they have originated are accumulated to a buffer. Once the buffer fills (an

example illustrated in Figure 5.4(b) with k^{th}, $k+1^{th}$, and $k+2^{th}$ cycles within a buffer), a cycle-cutting method extracts the individual distension cycles based on detecting the prominent valley points of oversmoothed distension waveform that is normalized between 0–1. Using the valley locations corresponding to each cycle as reference, the method annotates the following attributes: actual 'n' and arterial wall locations for the frames corresponding to the *start* and *end* of the segment-of-interest (SOI). The *start* corresponds to ($1/10^{th}$ of total cycle) samples prior to the cycle minima (valley) and *end* corresponds to the peak of the cycle, resulting in SOI that comprises the anacrotic phase.

5.2.3 Computing software: Local PWV evaluation during high frame-rate operation

With the annotated index of *starting* and *ending* frames for each cycle's SOI, the subset-of-frames were accessed from the recorded files (Figure 5.4(c)). Since the arterial wall locations were annotated for the *starting* frame of SOI, the shift in these locations is now tracked in the remaining subset-of-frames, yielding a pair of distension waveform segments corresponding to one cardiac cycle that is of high temporal resolution. To match the temporal resolution, the amplitude resolution of tracking was also improved by up-sampling the RF echo ROIs to 1 GHz using cubic-spline interpolation. In this manner, the distension segment pairs were constructed for multiple cardiac cycles by simultaneously accessing the corresponding subsets of frames. The obtained subsample-resolution (of 0.1 ms) distension segment pairs were further up-sampled to 10 kHz using a cubic-spline interpolation scheme and then were conditioned with identical zero-phase digital LPF. By obtaining M_{SD} for the distension segments, beat-by-beat local PTT was evaluated. The system also evaluates the effective pulse propagation length based on the separation distance between the transducers and the

depth difference between the NWs from the two sites. Local PWV was then calculated using the distance-time equation.

5.2.4 Computing software: Quality check, feedback, and screening

In addition to the live display of the recorded RF frames and the LFR distension waveforms, signal quality (SQ) scores (Shah et al., 2014) (0-50 for each wall) notifying the quality of vessel wall echoes from proximal and distal sites were displayed as visual feedback. These scores averaged for each frame in a cardiac cycle serve as a metric to validate the reliability of the local PWV measurement from the corresponding beat. Also, Pearson correlation coefficient was evaluated between the distension cycle pair (where cycles were trimmed to their respective leading to trailing minimum) for each beat, and cycle pairs yielding a coefficient beyond a set threshold were selected. A check as such assists in the selection of high-fidelity cycles in-vivo, avoiding the ones that have suffered severe motion or breathing artifacts. The measurements from these screened cycles are specifically used for the final local PWV calculation (averaged estimate over multiple cardiac cycles) making it robust.

5.2.5 Provision for multimodal acquisition

The developed system also accommodates acquisition from additional modalities, other than just ultrasound, example: pressure, plethysmogram, force resistor sensors, etc. It has provision for four such acquisition channels, built around data acquisition card (DAQ; NI-USB 6216, National Instruments, United States). The sensors are connected to this card via. an AFE (based on instrumentation amplifier). The needed power supplies are drawn from the primary power supply unit of the developed ultrasound

device. The microcontroller that controls the ultrasound transducers, also sends a trigger pulse to the DAQ, such that its acquisition is completely synchronized to the recording of ultrasound. Therefore, the configured frame rate of ultrasound module dictates the sampling rate of the DAQ, making both the acquisition modules frequency matched and time synchronized.

5.3 IN-HOUSE PHANTOM SETUP FOR SYSTEM CHARACTERIZATION AND ASSESSMENT

The arterial flow phantom-setup Figure 5.5(a) consisted of an in-house developed pulsatile-flow generator connected to a silicon vessel-model (diameter = 7 mm, wall thickness = 1 mm, length = 700 mm), which was used to emulate wide range of pulse wave velocities. The vessel model contained ultrasound-compatible blood mimicking fluid (BMF-US, Shelly Medical Imaging Technologies, Canada) and was sheathed by soft-grade silicon (EcoflexTM 00-20, Smooth-on, United States) to match the acoustic properties of the vessel. The in-house developed flow-generator combined an air pump, a solenoid valve, and a regulatory valve to produce a series of periodic pneumatic pulses that were further transformed into the pulsatile flow of blood mimicking fluid in the vessel. The pulse amplitude and rate were varied by controlling ON/OFF times of the solenoid valve using a microcontroller. For an assigned closing time of the valve, the pressure elevates in the system. Now, by configuring the opening time of this valve the pressure in the system could be decayed to a designated level, hence giving a control of the pulse pressure. This also has an effect on the mean pressure, i.e. when the closing time keeps increasing the pressure levels are elevated to higher amounts. Further, the mentioned second valve is a regulatory valve whose degree of orifice opening can be regulated for further degree of control on the flow conditions. This valve is placed right

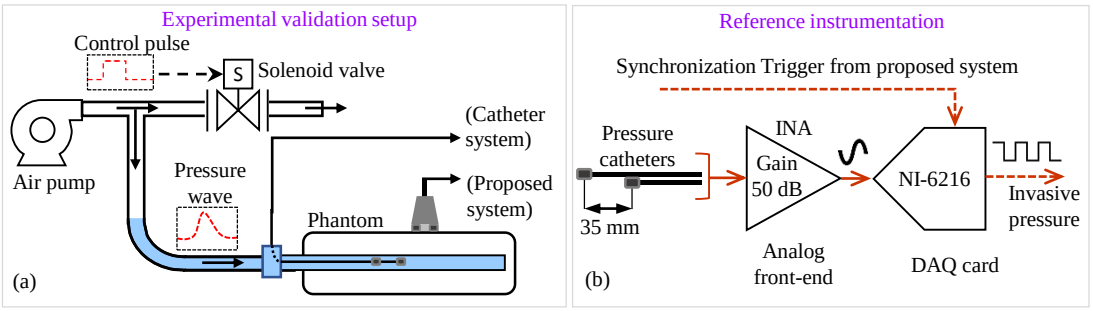

Figure 5.5 (a) Experimental arterial flow phantom setup allowing simultaneous measurement using the proposed and reference systems for validation and (b) Reference instrumentation with dual pressure catheter arrangement for invasive local PWV.

after the pump so that even when the solenoid valve is closed, the opening of the regulatory valve acts as partial vent to the air reducing the effective pneumatic pressure in the system. Hence for each set of ON/OFF timing configurations, the regulatory valve gave additional control on the pressure variations when it was changed all the way from fully closed to fully open, yielding several combinations of minimum and pulse pressures. For the in-vitro study, the minimum pressure could be varied from 21 to 42 mmHg and the pulse pressure from 12 mmHg to 45 mmHg, yielding 23 different combinations. Therefore, it is the different combinations (intuitively adjusting the solenoid valves ON/OFF times, and opening of the regulatory valve) of minimum and pulse pressures that would alter the flow conditions. These variations consequently altered the propagation velocity of the flow pulses (reflected in PWV) systematically.

5.4 SYSTEM CHARACTERIZATION

It is imperative to characterize the developed system for yielding accurate and reliable local PWV measurements. This involves studying the potential influence of the key design parameters: (i) minimum spacing between ultrasound transducers, (ii) frame-rate and (iii) sampling-rate of RF signals, (iv) cutoff frequency, and (v) order of the

LPF for the distension waveforms on the accuracy of local PWV. The characterization experiments were initially conducted on an arterial flow phantom setup and then on human subjects.

5.4.1 Preliminary investigation on sensor separation distance

Figure 5.6 shows the relationship curves between PWV and PTT for different path lengths – 10 mm, 15 mm, 25 mm, 35 mm, 50 mm, and 60 mm. To measure from carotid artery, a site of prominent interest, it's rational to keep the pathlength below 70 mm which allows a practically feasible form factor for the ultrasound probe. Now, since for the majority of arteries the local PWV was found to be within 2 – 15 m/s, these thresholds are highlighted in the Figure 5.6. It may be observed pathlengths below 25 mm make the measurement of upper end of PWV range challenging, with resultant PTTs smaller than 1 ms. Measurement of such sub-millisecond delays incur large variabilities even with high resolution blood pulses. Further higher pathlengths imply larger formfactor of the probe which may impose practical constraints for patients with shorter necks. We found 35 mm to be a suitable pathlength that offers a measurable PTT range of ~2.5 to 19 ms and physically allows measurements from wider population.

To further corroborate this inference, an in-vitro experiment was conducted on the inhouse developed phantom setup presented in section 5.3. The valves were kept to emulate high mean pressure and consequently, yield a larger PWV (> 10 m/s). Two independent single element ultrasound probes were placed on the surface of the phantom model, scanning the artery. Measurements were performed changing the separation distance between the two measurement sites while keeping the flow

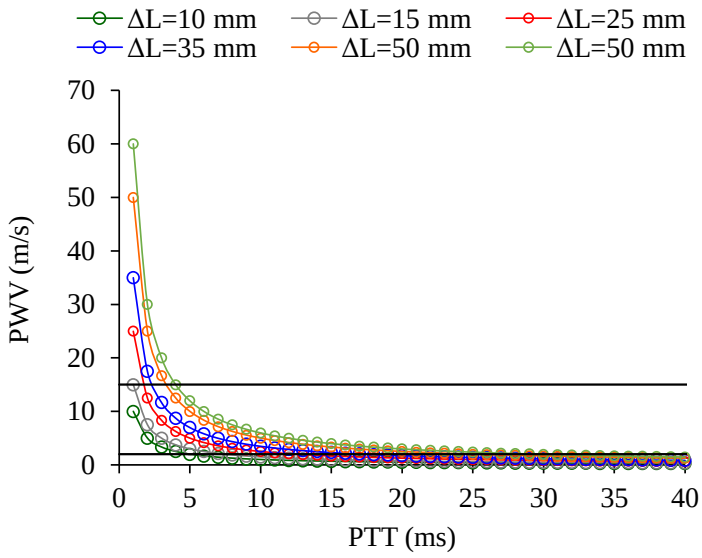

Figure 5.6 Relationship curves between PWV and PTT for different path lengths (ΔL).

conditions unaltered. These two probes were first placed 70 mm apart and the measurements were performed. Then keeping the flow settings unchanged the measurements were again performed by reducing the separation distance between the two probes to 35 mm. For both the test cases the measurement was done for a sufficient number of cardiac cycles. The PTT and PWV measurements (averaged over 15 consecutive cycles) for test case with 70 mm separation distance were 4.5 ± 0.1 ms and 15.6 ± 0.4 m/s respectively (with CoV = 2%). Similarly, the PTT and PWV measurements for test case with 35 mm separation distance were 2.2 ± 0.05 ms and 15.8 ± 0.4 m/s respectively (with CoV = 2.6%). It may be noted that the error between the PWV measurements from the two test cases was in acceptable range (percentage error = 1.3%). The results indicated that the performance of equally appreciable when the pathlength was reduced from 70 mm to 35 mm. This confirmed that reliable local PWV measurements could be performed with a shorter arterial segment of 35 mm, supporting a compact probe design for further in-vivo measurements.

5.4.2 Reference and proposed system's PWV from Phantom

For measuring the transit-time-based local PWV from the proposed system (PWV_M), the dual-element ultrasound probe was mounted on the flat surface of the silicon platform along the longitudinal axis of the vessel. The probe was secured with a stereotactic holder. Further, the instrumentation for measuring the reference (invasive) transit-time-based local PWV (PWV_R) Figure 5.5(b) consisted of a pair of pressure catheters (3.5F, Millar SPR-882, ADInstruments, Australia) with sensing tips separated by 35 mm apart. The catheters were not directly placed under the ultrasound elements' scan axis, but the distal catheter was placed very close to the ultrasound's proximal transducer, as shown in Figure 5.5(a). This was to avoid any potential echo interference from the catheter to that of one of the walls or in the lumen area. They were connected to a data acquisition card (NI-USB 6216, National Instruments, United States) via an AFE comprising of an instrumentation amplifier with gain = 50 dB and second-order LPF with cutoff frequency = 40 Hz. The sampling rate for digitizing the conditioned pressure signals was 20 kHz. A *starting* trigger signal ensured that the non-invasive and invasive recording systems were synchronized.

Given that the diameter and pressure was being measured by the ultrasound and catheter, respectively, the theoretical local PWV was also calculated using these for comparison. BH equation theoretically relates the PWV within a vessel segment to its distensibility (DC), and therefore, it has been used as a theoretical reference for local PWV in multiple studies reported in the literature (Hermeling, Reesink, Kornmann, Reneman, & Hoeks, 2009; J M Meinders et al., 2001). PWV using BH equation is expressed as

$$PWV_{BH} = \sqrt{\frac{A_D \, dP}{\rho \, dA}} \tag{5.2}$$

where dP is the instantaneous pulse pressure, dA is the instantaneous change in circumference area, and A_D is the minimum area (end-diastolic) for a vessel segment. Now, for the evaluation of PWV_{BH}, pressure, and diameter recordings are needed from a single site of the vessel which is facilitated in the arranged phantom setup. The ratio dP/dA is evaluated at M_{SD} characteristic point from the synchronously recorded pressure and diameter cycles and used for theoretical PWV calculation.

5.4.3 Reference and proposed system's PWV from Human subjects

In-vivo data collection for characterization was conducted on 20 young subjects with a mean age of 24 ± 6.5 years. This study was carried out in compliance with the Helsinki Declaration. The study objectives and procedure were explained to the recruited subjects and written informed consent was obtained prior to the trials. Anthropometric measures were recorded for each subject. They were allowed to relax for 5 minutes before the trials and the BP was recorded using a clinical grade oscillometric BP monitor (SunTech® 247™, SunTech Medical). Post obtaining the subject's BP, the measurements were performed by a single operator on the left common carotid artery while the subject was in the supine posture.

For this purpose, a custom probe (Figure 5.7(a)) was developed to host a pair focused single element ultrasound transducer (center-frequency = 5 MHz, spatial half angle < 1.3°, diameter = 5 mm) and a clinical-grade tonometer (SPT-301 – Millar Instruments). The objective was to acquire a pair of distension pulses and one pressure pulse, all from

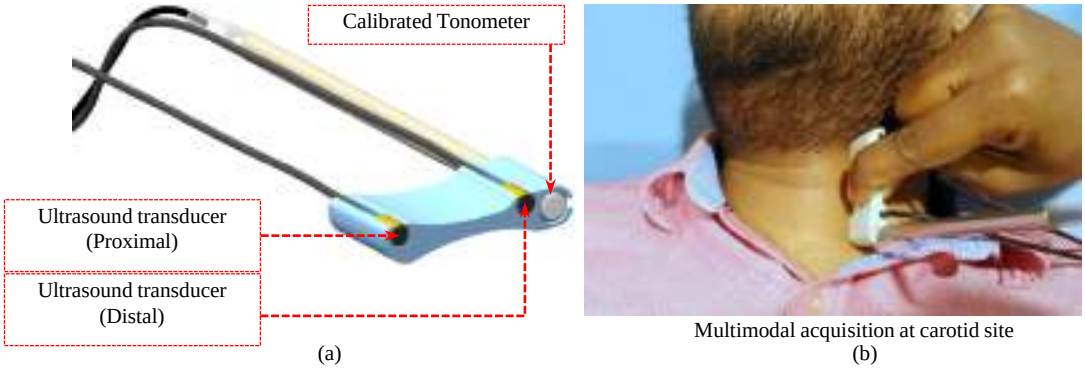

Figure 5.7 (a) The developed multimodal probe for simultaneous PTT-based PWV and BH-based PWV and (b) Positioning of probe for carotid PWV.

a small target arterial segment in simultaneous fashion, as shown in (Figure 5.7(b)). The separation distance between the ultrasound transducers was designed to have 35 mm, and between the tonometer and one of the ultrasound transducers was 2 mm. The smaller separation distance between the tonometer and the ultrasound transducers ensured nearly single site acquisition. The tonometer was interfaced to the same acquisition card and AFE which was mentioned in section 5.4.2 pertaining to catheter signal acquisition.

Once the subject relaxed in supine posture, the arteries approximate location was identified by palpation. The custom probe was placed at the identified location (Figure 5.7(b)) and aligned to obtain high fidelity pressure waveform and good quality ultrasound frames with strong and sharp arterial wall echoes. The beat-to-beat measures of local PWV were evaluated, transit-time-based for the proposed system (using equation (5.1) and BH-based (using equation (5.2)) as reference.

5.4.4 Study design for characterization

The raw A-mode frames from the two channels were sampled at 250 MHz, acquired at 1000 Hz frame-rate and were saved to local storage. For investigating the frame-rate influence, independent data sets were generated, selecting every k^{th} frame making the effective frame-rate = 1000/k. Likewise, various sampling rates were emulated by uniform down-sampling of the frames. The influence of the digital filter applied to the distension waveforms was studied for independent combinations of cutoff frequencies and orders. The influence of these parameters on the deviation between the measured versus reference local PWVs was studied by varying them over a rational range. The findings from the characterization were used for quantifying optimal design settings, post which the performance of the measurement system was validated adopting them.

5.4.5 Results from in vitro characterization experiments

High fidelity continuous reference invasive pressure waveform and non-invasive diameter waveform pairs were acquired, as illustrated in Figure 5.8. CoV of the pressure cycles (15 beats) was 0.55 ± 0.23%. The phantom setup simulated a pressure pulse rate between 40 to 115 beats per minute (BPM), a minimum pressure of 21 to 42 mmHg, and a pulse pressure of 12 to 45 mmHg. The induced variations in flow pulses' amplitude and rate resulted in PWV_R variation over a range of 2.7 to 11.4 m/s (5.6 ± 2.3 m/s). Beat-to-beat CoV in the PWV_R for individual flow conditions was less than 3.5% (1.82% for 40 BPM, 2.41% for 115 BPM, and average CoV = 1.9 ± 0.7%). The SNRs of ultrasound frames for all recordings were greater than 25 dB. For the selected phantom, the magnitude of distension varied between 0.65 – 1.75 mm for the configured

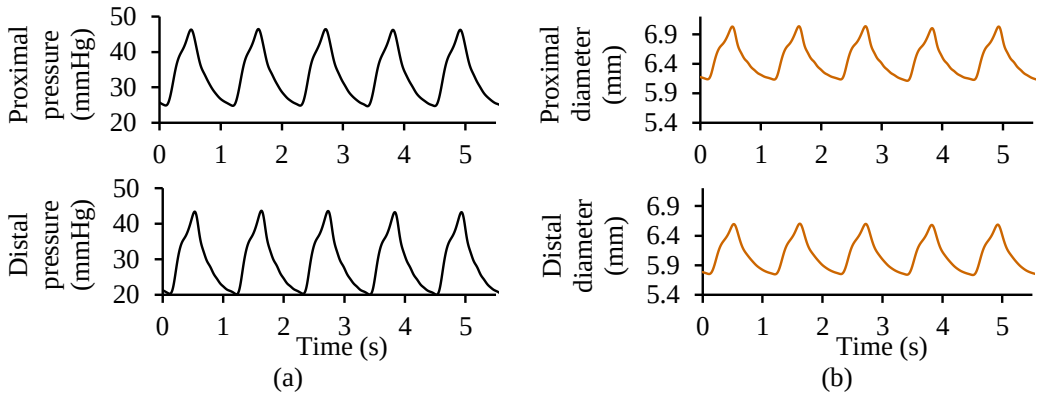

Figure 5.8 Continuous high-fidelity recording of (a) catheter pressure pair and (b) diameter pair.

flow conditions. The average CoV of distension cycles was less than 1.1% (0.34% for 40 BPM, 0.52% for 115 BPM, and average CoV = 0.44 ± 0.27%).

Keeping a constant rate (250 MHz) for sampling RF frames and LPF's cutoff (20 Hz) and order (4) for smoothening the distension, the variation in mean absolute percentage error and RMSE resulted from varying the frame-rate across 10 Hz to 1 kHz is presented in Figure 5.9(a) (The error bars in the mean absolute percentage error curve denote SDs over 1170 beat-to-beat measurements). This filter sufficiently allows up to 10 harmonics of the pulses (given the maximum pulse rate was 1.9 Hz). As the frame-rates reduced to lower than 100 Hz, errors increased steeply to unacceptable levels. However, as highlighted in the inset of Figure 5.9(a), for frame-rates ≥ 100 Hz, the absolute percentage errors and RMSE dropped below acceptable levels of 10% and 0.4 m/s, respectively, and continue to decrease at a rate of 0.5% and 0.018 m/s per 100 Hz increment in frame-rate. Best accuracies were seen above 200 Hz, where the absolute percentage error was within 3.8% to 2.2%, and RMSE was within 0.27 m/s to 0.21 m/s.

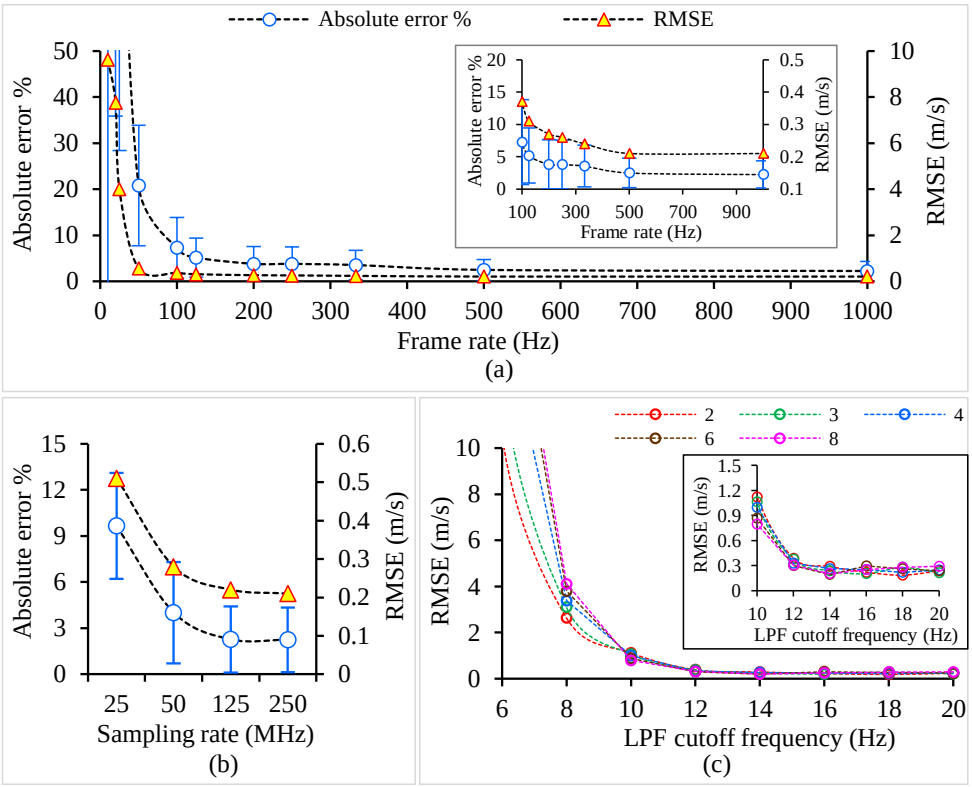

Figure 5.9 The effect of various system design parameters on accuracy of local PWV: (a) Variation in the mean absolute percentage error and RMSE across various frame rates and (b) sampling rates of RF frames. Further, (c) shows the influence of cutoff frequency low pass filter used for distension waveforms on RMSE for a frame rate of 500 Hz and sampling rate of 125 MHz, the effect of filter order (2 to 8) for each of the cutoff frequencies is indicated by different colors.

Beyond 500 Hz, there was no substantial improvement in the accuracy. Now, keeping the frame-rate constant at 500 Hz, the variations in absolute percentage error and RMSE incurred for different RF frame sampling rates (range = 25 to 250 MHz) are shown in Figure 5.9(b). The sampling rate was inversely influencing the errors; a nearly 10-times increase in the rate decreased errors at least by 3-times. An appreciable performance (absolute percentage error < 3% and RMSE < 0.25 m/s) was achieved for sampling rates > 100 MHz.

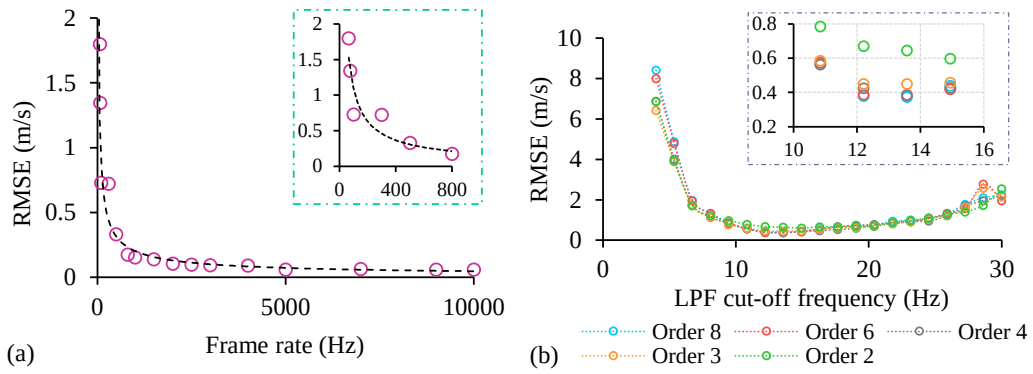

Figure 5.10 The RMSE of local PWV values evaluated for (a) various frame rates; the inset shows a closer view for the frequencies lower than 800 Hz, and (b) at various frequencies for different orders; inset shows RMSEs for the frequencies 10 to 16 Hz.

Further, the effect of zero-phase LPF design on the RMSE is illustrated in Figure 5.9(c) by varying LPF cutoff frequency from 6 Hz to 20 Hz. The errors surged to non-practically high values when cutoffs were below 6 Hz. Errors increased with over-smoothening (by lowering the cutoff frequency) the distension waveforms. An increase in cutoff-frequency decreased the RMSE at a rate of 0.76 m/s/Hz initially (for 8 to 12 Hz), and then, as shown in the inset of Fig. 3(c), RMSE was approximately constant at 0.23 m/s. The filter order was also varied from 2 to 8, in combinations with the cutoff frequencies, the influence of which is indicated by different colors in Fig. 3(c). Higher filter orders affected the accuracy performance for filter cutoffs $\leq$ 8 Hz but had an insignificant ($p > 0.05$) influence for higher cutoffs (>10 Hz) that were of interest.

5.4.6 Results from in vivo characterization experiments

The measurements performed at various frame rates for all the recruited subjects were used for evaluating the RMSE for in vivo PWV_M, taking the obtained in vivo PWV_{BH} as the reference. RMSEs evaluated at various frame rates are illustrated in Figure 5.10(a). It may be observed that a minimum sampling rate of 400 Hz is required for the

blood pulse waveforms in order to obtain accurate measurements with an RMSE smaller than 0.5 m/s. Influence of signal processing blocks was studies by varying the cutoff of pulse from 4 to 30 Hz (digital Butterworth bandpass) for different orders. RMSEs of the measurements obtained from all the subjects for different frequencies and order are illustrated in Figure 5.10(b). A RMSE smaller than 0.5 m/s was obtained for higher order filters (order greater than 2) with higher cutoff frequency ranging between 10 to 16 Hz. It was observed that the RMSE improved with the increase in filter order. Further, the results also demonstrate that over-smoothening of the blood pulse waveforms by choosing the higher cutoff frequencies of the bandpass filter smaller than 10 Hz may deteriorate the accuracy.

5.5 IN VITRO PERFORMANCE WITH OPTIMAL DESIGN SETTINGS

Based on the characterization, the optimal design parameters (frame-rate = 500 Hz, RF sampling rate = 125 MHz, LPF cutoff frequency = 14 Hz, and order = 4) were implemented in the system, and its performance was validated. The average of local PTT measurements performed by the proposed system was 7.2 ± 2.7 ms. The PWV_M evaluated from the PTTs ranged from 2.7 m/s to 11.4 m/s, with a mean of 5.7 ± 2.2 m/s. Average CoV of PWV_M (across the simulated heart rates 40 to 115 BPM) was 2.1 ± 1.1 % (range = 0.7 to 4.5 %). The distribution of relative errors (comparing PWV_M and PWV_R) did not differ significantly from the normal distribution ($p = 0.15$). The mean absolute percentage error in the measured local PWV was 2.4 ± 2.1 %, and RMSE was 0.19 m/s. Figure 5.11(a) illustrates the frequency distribution (in %) of relative errors along with an overlaid gaussian distribution trend (dashed line), indicating a normal distribution with proportional frequencies above and below the mean. Gaussian trend

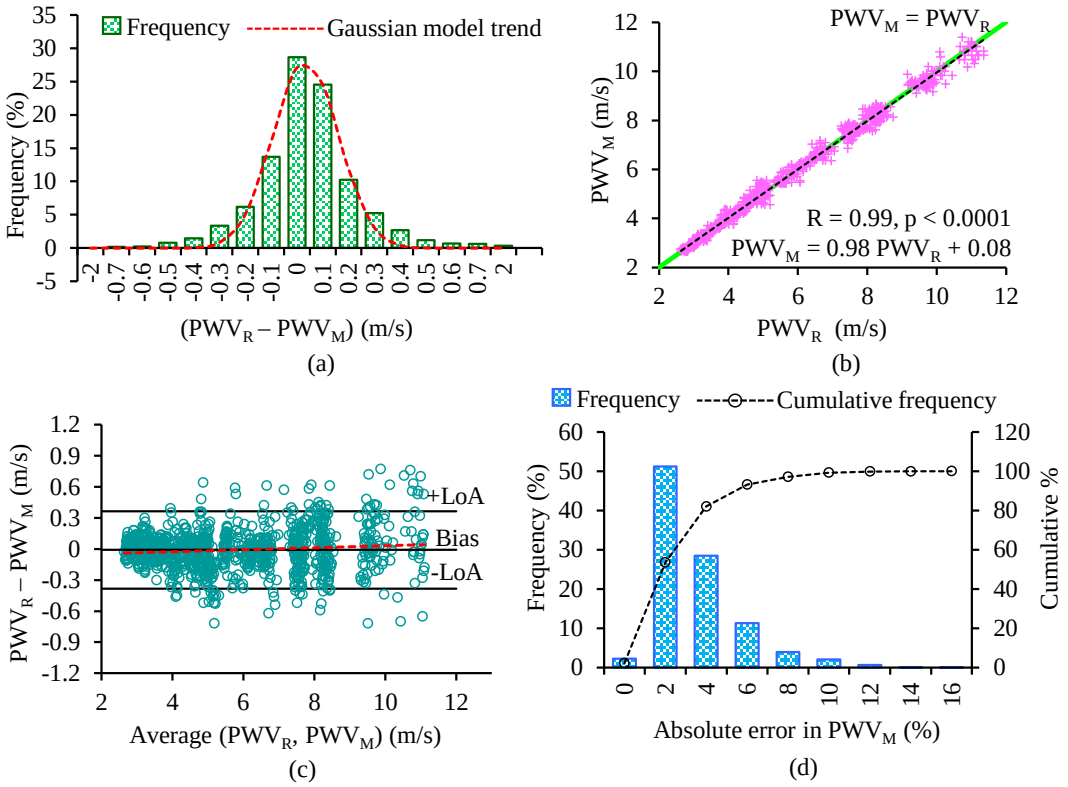

Figure 5.11 Comparing PWV_M with PWV_R, (a) illustrates the relative error distribution and actual Gaussian distribution fit (in red), (b) correlation plot along with the obtained (dashed line in black) and ideal regression line (in green), (c) Bland-Altman plot and a linear regression line (dashed line in red) of the data points and (d) frequency distribution and cumulative frequency trend of the absolute percentage errors.

fits the actual distribution with an r = 0.97 (p <0.0001) and RMSE = 1.5%, yielding peak of the curve as 28.2%, peak position at 0.03 m/s, and SD as 0.17 m/s.

The association and agreement between the PWV_M versus PWV_R measurements are illustrated by regression and BA plots in Figure 5.11(b) and (c), respectively. Linear regression analysis yielded a model as PWV_M (in m/s) = 0.98 PWV_R (in m/s) + 0.08, with r = 0.99 (p < 0.001). The predicted regression line (dashed line) was collinear with the ideal 45° line (in green) (Figure 5.11(b)). The mean bias from BA analysis was -0.01 m/s (p = 0.91), with the upper and lower LoA of 0.36 m/s and -0.38 m/s,

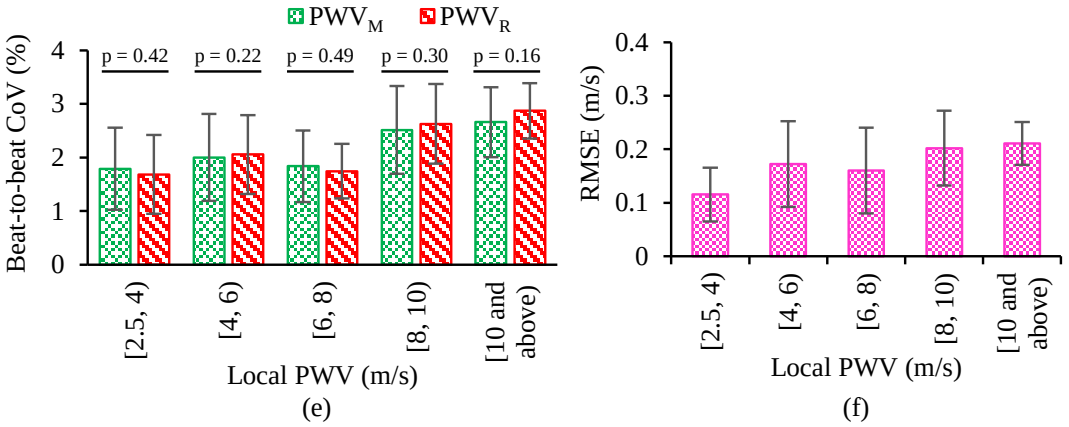

Figure 5.12 (a) and (b) are coefficient of variation for the proposed versus reference system and the RMSE, respectively, across different local PWV ranges.

respectively. There was no specific trend revealed in the BA plot (Figure 5.11(c)), as indicated by the slope of the linear regression line (in red) that was close to zero (~0.01). The frequency distribution and the corresponding cumulative frequency (in %) of absolute percentage errors are illustrated in Figure 5.11(d), demonstrating more than 90% of measurements with errors smaller than 6%. The inter-beat CoV was investigated across the measured local PWVs (grouped into bins of size 2 m/s) and compared with that of the reference in Figure 5.12(a). The discrepancy between the CoVs offered by the two systems was non-significant ($p > 0.05$) for all the groups. The RMSE is shown for these groups in Figure 5.12(b). The CoV and RMSE of the groups were below 3% and 0.25 m/s, respectively. Lastly, PWV_M values also strongly correlated (r=0.98) with theoretically evaluated PWV_{BH} from the phantom, yielding a negligible bias of -0.01 m/s, 95% CI of ± 0.55 m/s, mean error of 3.4%, and RMSE of 0.28 m/s.

5.6 IN VIVO MEASUREMENT RELIABILITY

5.6.1 Study design

A study was performed to investigate the *in vivo* measurement feasibility of the proposed system. In brief, the study investigated the repeatability and reproducibility of the local PWV assessments from the carotid artery, performed on 33 healthy subjects by two independent operators (‘A’ with experience with the image-free technology for approximately 4 months and ‘B’ for more than one year). Subjects with a history of cardiovascular diseases, habitual smoking, and alcohol consumption were excluded from the study. The protocols (adhered to the principles of Helsinki declaration) were approved by the ethics committee of the Indian Institute of Technology, Madras (IEC/2021-01/JJ/07). Participants were the employees and students of the institute’s research and development laboratory – Healthcare Technology Innovation Centre. Written informed consent was obtained from all the volunteers.

The assessments were performed in a temperature-controlled room 22 – 24 °C. Overall, four carotid PWV assessments for each subject were performed over the day, two trials by the two operators, each with a one-hour intervening gap. Subjects were not allowed to take caffeinated beverages 6 hours prior to the respective assessments. Upon reporting for each assessment, the subject was asked to relax for 10 mins in supine, followed by a brachial BP measurement. An approximate location of the left common carotid artery was identified by palpation, over which the dual-element ultrasound probe was placed. The probe was positioned and oriented to obtain sharp and strong NW and FW with the help of visual feedback – (i) the A-mode frames, (ii) the quality

score of walls, and the (iii) beat-to-beat local PWV. When measurements from 15 high-fidelity cycles are achieved, the software displays the mean local PWV result.

5.6.2 In vivo repeatability and reproducibility results

Descriptive characteristics of the study population are presented in Table 5.1. The SNR of the recorded frames from which the measurements were yielded was > 10 dB for all the subjects and > 20 dB for more than 80% of the assessments. A sample of acquired frames and a processed distension cycle pair is illustrated in Figure 5.14(a) and (b). The beat-to-beat variation in local PWV collected over 15 cardiac cycles was 3.7 ± 0.6 %. Due to the inclination of the artery with respect to the measurement probe surface, the

Table 5.1 Descriptive characteristics of population

Parameters	**Value** **Mean ± SD (Min – Max)**
Participants (N)	33
Male/Female (N)	19/14
Age (Years)	28 ± 7 (21 – 52)
Body mass index (kg/m^2)	24.3 ± 4.1 (16.3 – 35.6)
Heartrate (BPM)	68.9 ± 9.9 (46 – 94)
Brachial SBP (mmHg)	119 ± 12 (87 – 138)
Brachial DBP (mmHg)	72 ± 8 (56 – 97)
Hypertensives (N)	8
PTT (ms)	8.4 ± 2.5 (3.6 – 15.1)
PWV (m/s)	4.6 ± 1.6 (2.3 – 9.7)

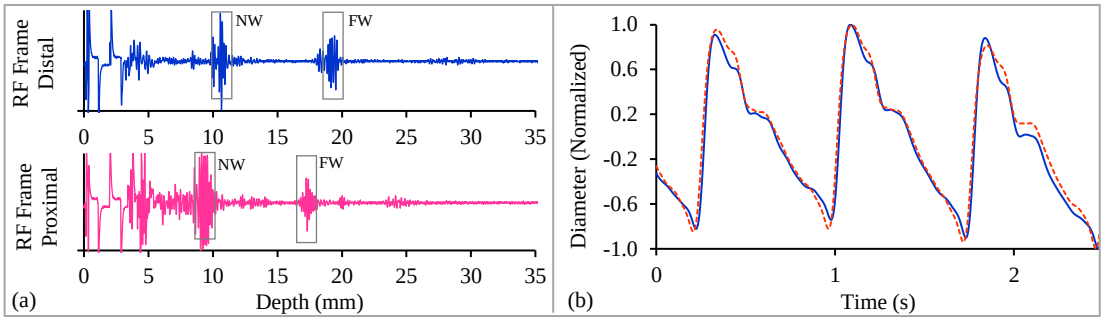

Figure 5.13 (a) and (b) are a sample of RF frames and distension cycle pairs obtained using the dual-element ultrasound probe from a subject.

NW depth between the two measurement sites differed by 1.52 ± 1.05 mm. Consequently, the corrected pulse propagation length was 35.04 ± 0.05 mm.

For the subjects (n = 28) where the probe could be held stable throughout, the 15 best cycles were yielded within the first 25 to 30 beats by the more experienced operator (B), and likewise, within 40 to 50 beats for the other (A). For the difficult subjects (substantial breathing and motion), the rejection rate of the cycles was higher owing to frequent artifacts in the distension cycles.

However, for all the subjects, the measurements could be finished within 2 to 5 minutes, which included identifying the artery's location, positioning the measurement probe, performing the recording, and promptly repositioning the probe in the event of undesirable movement. Scatter and BA plots for the intra-operator and inter-operator measurements are illustrated in Figure 5.14(c) and (d), respectively. The ICC for the intra- and inter-operator measurements were 0.95 and 0.93, respectively. For both cases, BA analysis achieved a statistically negligible bias ($p > 0.05$).

5.6.3 Feasibility of real-time PWV measurement

Estimation of each distension sample during high frame rate operation required 3-5 ms (due to cross correlation operation on RF echoes resampled at 1 GHz rate using spline interpolation), on a general-purpose computer (Processor: Intel® Core™ i5 CPU @2.36 GHz, RAM: 4 GB, Operating system: 64-bit Windows 7). The anacrotic segment being approximately $1/5^{th}$ to $1/4^{th}$ of the cycle, would ideally consist of 100-150 sample points for a frame-rate of 500 Hz. Therefore, it needed 500-800 ms, to achieve a pair of high-resolution distension cycles. This allows online estimation and display of beat-to-beat

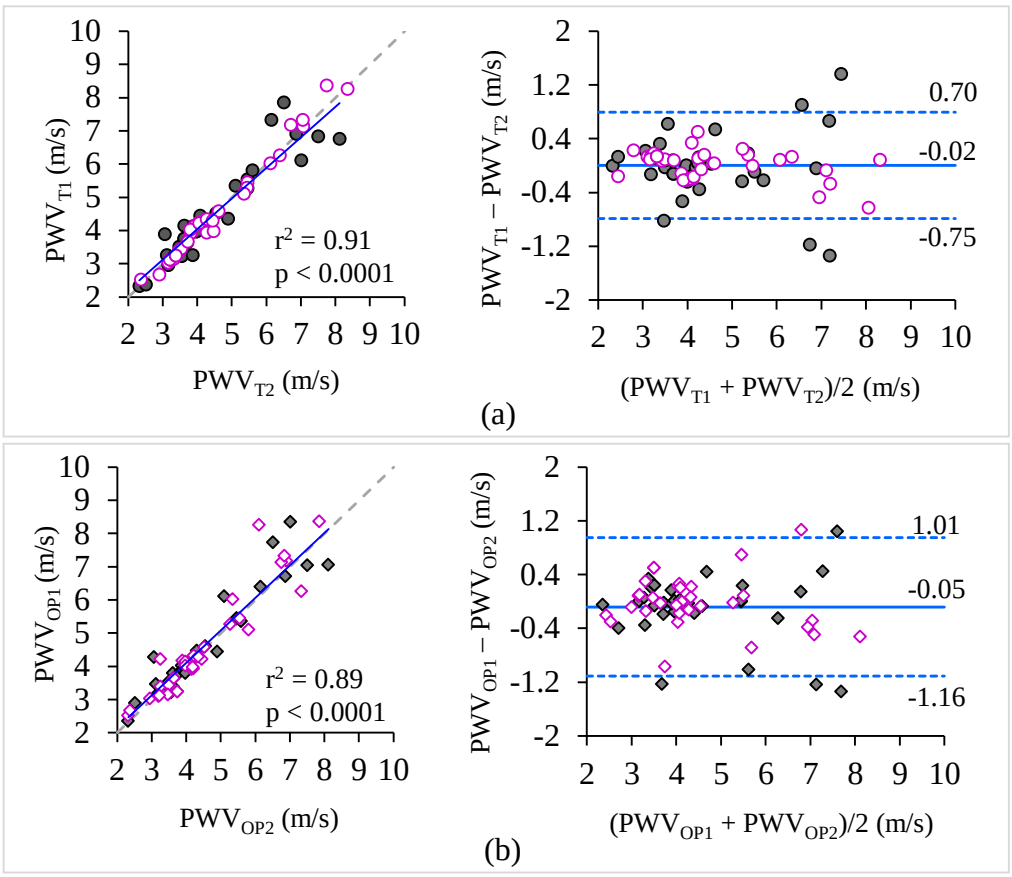

Figure 5.14 Correlation and Bland-Altman plots obtained for (b) intra-operator measurements, where the two marker types represent the measurements from individual operators, and (c) inter-operator measurements, where the two marker types represent the measurements from individual trials..

local PWV with a delay of approximately one to two beats (1-2 s). Since multiple beats were processed in parallel, it was possible to display them together, making it quasi-real-time.

5.7 DISCUSSION

We have presented an image-free ultrasound technology that performs high-speed scanning and measures local PWV in real-time. A controlled *in vitro* study characterized the measurement system, and the design specification outcomes were used to optimize the system's performance in terms of accuracy and computation

overhead. The findings from in-vitro validation study have demonstrated the ability of the proposed system to perform non-invasive local PWV measurements over a wide range with excellent accuracy (mean absolute percentage error = 2.4 ± 2.1%, RMSE = 0.19 m/s) and precision (mean CoV = 2.1 ± 1.1%). As evidenced from regression and BA analyses, both the measured and reference local PWVs (both transit time-based and BH equation based) were in strong agreement with each other having an insignificant bias and 95% of the errors within ±0.4 m/s from the bias. Such performance figures were deemed as excellent in the literature (typical variability < 4 m/s, RMSE < 0.4 m/s, mean bias within ±0.2 m/s, r > 0.8) reporting similar in-silico and *in vitro* studies (Borlotti et al., 2014; Campo et al., 2014; Hermeling et al., 2007; Hoctor, Dentinger, & Thomenius, 2007; Nauleau et al., 2018; Ruesink, Medero, Rutkowski, & Roldán-Alzate, 2018; Vardoulis, Papaioannou, & Stergiopulos, 2013; Z. Wang et al., 2015). Further, the system with the experimentally finalized design parameters performed repeatable intra- and inter-operator carotid local PWV measurements (ICC > 0.92), demonstrating its *in vivo* feasibility.

Several methods performing local PWV measurements *in vivo*, though from the same site, have reported substantially different ranges (Nabeel et al., 2020). Since there exist no analytic means to compare the methods against the true *in vivo* local PWV unless, through invasive procedures (Nabeel et al., 2020), *in-silico* and *in vitro* validations are critical. Our recent review summarizes the local PWV measurements obtained from the central arteries in various studies, ranging from 3 – 15 m/s (Nabeel et al., 2020). Ultrafast imaging methods reportedly provided similar and consistent ranges from the carotid artery, a site that is more preferred for ultrasound assessments (Hermeling et al., 2009; X. Li et al., 2017; Luo et al., 2012; Yin et al., 2021). The developed in vitro setup

reliably emulated a wide range (2.7 – 11.4 m/s) of PWV, as a result of controlling the mean and pulse pressures via. two valves – solenoid and regulatory. Also, the carotid PWV measurements yielded in this study for a population aging 21 – 52 years concur with that of recent work reporting normal reference values (Yin et al., 2021). The heart rate has an influence on PWV and on the slope of the blood pulses' anacrotic phase affecting the available number of points within it for the identification of characteristic time points. In the study, the pulse rate was varied over a wide physiologically relevant range over which the developed method demonstrated reliability.

An important methodological consideration for the transit-feature-based local PWV evaluation is the temporal resolution of the pulse waves. This translates to the frame-rate requirement for ultrasound-based methods. About 99% of the blood pulse signal's energy is concentrated in the frequency band below 8 Hz (Nichols, O'Rourke, & Vlachopoulos, 2011). For such signals, although theoretically-required sampling rate is less than 20 Hz, our findings in coherence to other ultrasound methods in literature (Hermeling et al., 2008; Arnold P G Hoeks, Willigers, & Reneman, 2000; C. Huang et al., 2014; Luo et al., 2012; Nabeel et al., 2020) underline the importance of employing fast systems with way higher frame-rates (in the order of few hundreds and thousands). Such high frame-rates are essential to tackle aperture and jitter errors during the evaluation of the arterial distension pulses, yielding reliable characteristic time points (C. Huang et al., 2014). Studies further point that such high bandwidth (much higher than the pulses' frequency range) systems inhibit phase distortions in characteristic time points and also allow visibility of certain time points, which otherwise is challenging (Arnold P G Hoeks et al., 2000).

Higher frame-rates (≥ 200 Hz) in our *in vitro* and *in vivo* studies evidently improved the accuracy of local PWV (Figure 5.9(a)). Note that the distension pulses evaluated for different frame-rates (10 – 1000 Hz) were up-sampled to 10 kHz for maintaining a uniform test condition, despite which the reduction in frame-rates manifested a detrimental effect on local PWV accuracy. Since the presented system aims to provide real-time measurements, a frame-rate of 500 Hz was sufficient in terms of the offered accuracy (Figure 5.9(a) and Figure 5.10(a)) and computational complexity. Higher frame-rates would allow the reliable measurement of local PTT with better time-resolution for smaller arterial segments or narrow vessels with higher PWV, however, at the expense of increased computational overhead. The minimum local PTT measurable with this frame-rate is 2 ms, which sets the theoretical upper limit of the measurable local PWV to ~17 m/s. However, practically errors associated with jitter and fiducial point locating will be dominant for higher PWVs that are linked to lower PTTs. This was evidenced by the increased beat-to-beat variability at higher PWVs (Figure 5.12(e)).

While the temporal resolution gets finer with high frame-rates, it is also important to correspondingly improve the amplitude tracking resolution. Subsample delay estimates were achieved by up-sampling the wall ROIs during cross-correlation, which effectively increased the tracking resolution (~0.8 μm). In spite of the interpolation, the results suggest that a sampling rate above 100 MHz achieves high accuracy (Figure 5.9(b)). With the increase in frame-rate, the actual wall motion per frame reduces, and at lower sampling rates, these shifts would be closer to the resolution offered. Consequently, the variability in shift estimation may potentially increase, adversely affecting the accumulating distension.

Smoothening filters (typically Butterworth LPF) are used to remove high-frequency perturbations in the acquired blood pulse waveforms. Their characteristics, if poorly designed, would affect fiducial time points leading to inaccurate local PTT estimates. Earlier studies have assessed the impact of filter characteristics on the pulse waves for respective local PWV measurement methods (Hermeling et al., 2007, 2008; Arnold P G Hoeks et al., 2000). In this work, smaller LPF cutoffs (below 8 Hz), even being greater than the fundamental frequencies of generated waves, yielded significant error in local PTT/PWV. Though LPF at such lower frequencies does not affect the frequency content, it over smoothens the pulses introducing phase distortions, even leading to the annihilation of characteristic points (Hermeling et al., 2008; Arnold P G Hoeks et al., 2000). When the cutoff frequency was chosen above 12 Hz, high accuracies were obtained (Figure 5.9(c) and Figure 5.10(b)). An LPF cutoff of 20 Hz was taken for the present system, which yielded high accuracy. The choice of an LPF cutoff between 12 – 20 Hz adequately encompasses the fundamental frequencies of heart rates and, in our *in vivo* study, could reliably capture the higher frequency components that exist due to the dicrotic notch, inflection/shoulder point, etcetera. Similar cutoffs were adopted by other methods in the literature measuring local PWV (Hermeling et al., 2007; J M Meinders et al., 2001; Nabeel et al., 2020).

Hermeling *et al.* have demonstrated that the filter order has an influence on the precision of local PWV measurements (Hermeling et al., 2007). From our *in vitro* investigations, the filter order did not significantly influence the measurement accuracy over the range of desired cutoffs frequencies (12 – 20 Hz). There are other potential sources that introduce additional systematic lags between the pulse signal pair and corrupt the local PTT. Primarily the tissue-transit time and the inter-channel delay introduced by

hardware and signal processing components (Nabeel et al., 2020). The developed system, unlike skin-surface sensors, measures the blood pulses directly from the arteries in the form of distension waveforms and is not prone to uncertainties caused by tissue-transit time. In addition, identical AFEs for the pair of RF signals incurred a negligible sub-microsecond inter-channel delay. The digital signal processing blocks, such as filters for digitized RF frames and distension waveforms, were also identical and zero-phase filters, ensuring zero delays between the channels.

While the *in vitro* study validated the system design, the advantage of its features was manifested through the *in vivo* study. Undoubtedly, there is an advantage with the sophisticated systems imaging systems (Hermeling et al., 2007; C. Huang et al., 2014; Luo et al., 2012; J M Meinders et al., 2001) that are capable of scanning pulses from multiple lines (as shown below), from which the transit of a particular fiducial point or phase within the cycle can be more robustly annotated. However, being image-free in nature and using only two scan lines, the device's hardware is frugal as compared to such fast ultrasound systems for local PWV, making it a viable option for resource constraint settings. For robustness, the system leverages the real-time feedback of the recording, its quality, and the beat-to-beat measurements. Such features allow the operator to improve any probe angulation-associated SNR degradation and, therefore, have been deemed necessary in the literature concerning local PWV measurements (Hermeling et al., 2009; J M Meinders et al., 2001; Nabeel et al., 2020).

The automated methods also screen the cycles that suffer severe breathing and motion artifacts with the aid of SQ scores and similarity measure between the pulse pair. It is desirable for the SQ score thresholds to be tighter (>20 out of 50 for each wall) as they

represent the quality of the wall echoes. These scores would represent SNR > 10 dB and also that the echoes are sufficiently sharp without spreading. On the other hand, the similarity measure (between the distension pulse pair) threshold should be carefully considered as the pair may differ in likeness when subject to non-uniform effects occurring due to wave-reflections and geometric inhomogeneities. In the *in vivo* reliability study, the collected cycle pairs were correlated with an r > 0.94. However, an allied study is required to assess the effect of this threshold. Aligning the two ultrasound elements parallel to the artery may be practically challenging sometimes, owing to the vessel tortuosity. However, the PWV measurements were performed by obtaining corrected propagation distances. Nevertheless, the corrected distances deviated by 0.05 mm on average from the actual 35 mm. Therefore, the local PWV values would have deviated by only 0.14% if 35 mm was directly substituted in (1). Extremely tortuous vessels pose a limitation for this system. The transducer elements are focused in nature with a spatial half-angle smaller than 1.5°, and therefore the SNR drastically deteriorates when the vessel is largely inclined from the normal.

5.8 LIMITATIONS AND FUTURE WORK

Practical challenges and limitations of the *in vitro* experiment should be underlined. One of the limitations is that the local PWV beyond 12 m/s could not be reliably emulated with the current setup. For higher amplitude pneumatic pulses, turbulence in the flow-induced substantial motion artifacts in the reference (invasive) waveforms due to the collision of catheter-tip against vessel walls, making the local PWV measurements nonreliable. The phantom arrangement emulated ideal and controlled settings to assess the accuracy performance of the system. In contrast, *in vivo*

measurements pose more complex settings such as non-uniform vessel segments, bifurcations, and inhomogeneous geometries. The reliability of the system was demonstrated *in vivo* via. intra- and inter-operator repeatability. However, lack of reference standards or analytic means to validate the accuracy in vivo constrained the studies in this regard. Studies on animal models with interventions to alter the pressure, heart rate, and PWV are underway to further validate the system. Multi-centric human study on diverse population (healthy and diseased) are also in progress to establish its clinical usability and significance.

5.9 CONCLUSION

We have demonstrated that the local PWV can be measured with high beat-to-beat precision and accuracy across a short vessel segment of 35 mm with a fast image-free ultrasound system. The system ensures reliable measurements over a wide physiologically relevant range of local PWVs. Design optimization (frame-rate = 500 Hz, RF sampling rate = 125 MHz, LPF cutoff frequency = 14 Hz, and order = 4) allowed the achievement of reliable local PWV measurements (beat-to-beat variability = 1.9%, RMSE = 0.19 m/s, absolute-percentage-error = 2.4%). The *in vivo* local PWV were repeatable and reproducible (beat-to-beat variability = 3.7%, ICC > 0.92), demonstrating the measurement feasibility. The technology offers several advantages: (i) yield online PWV and real-time measurement quality feedback, (ii) promote frugal hardware and affordable system design, and (iii) reduced demand for operator expertise. The beat-to-beat measurement feature and provision for multimodal sensing allows to capture acute changes in PWV, which will be presented in the next chapter.

CHAPTER 6.

HIGH FRAME-RATE A-SCAN ULTRASOUND FOR REGIONAL STIFFNESS MEASUREMENT

As opposed to PWV being measured locally (presented in chapter 5), it is typically measured across carotid-to-femoral sites, cfPWV, which is known is to be a gold standard stiffness metric. Tonometry based methods that are majorly recruited for this require extensive skill for ensuring reliability. To our knowledge only one study reports ultrasound measurement, employing 2D doppler for carotid and femoral recordings sequentially with ECG. Either of the methods yield only regional stiffness and don't furnish other relevant makers. In this Chapter, we have validated the use fast image-free ultrasound technology presented in Chapter 5, for the measurement of cfPWV, alongside local stiffness metrics. The system relies on capturing high resolution blood pulse signals from carotid and femoral arteries, as diameter from the former and pressure from the later. Signal processing methods presented in Chapter 3 and 4, were used for automated measurement of continuous diameter pulses. The core system was enhanced to incorporate a cuff control and pressure detection module to enable the system to record the required femoral pulses, continuously. In this chapter, the system's architecture and measurement scheme are presented, succeeded by the details of the experiments performed to validate the cfPWV measurements.

This chapter is partially adapted from the post-print version of:

Nabeel, P. M., **Raj, K. V**, & Joseph, J. (2022). Image-free ultrasound for local and regional vascular stiffness assessment: The ARTSENS Plus. Journal of Hypertension, 40(8), 1537–1544.

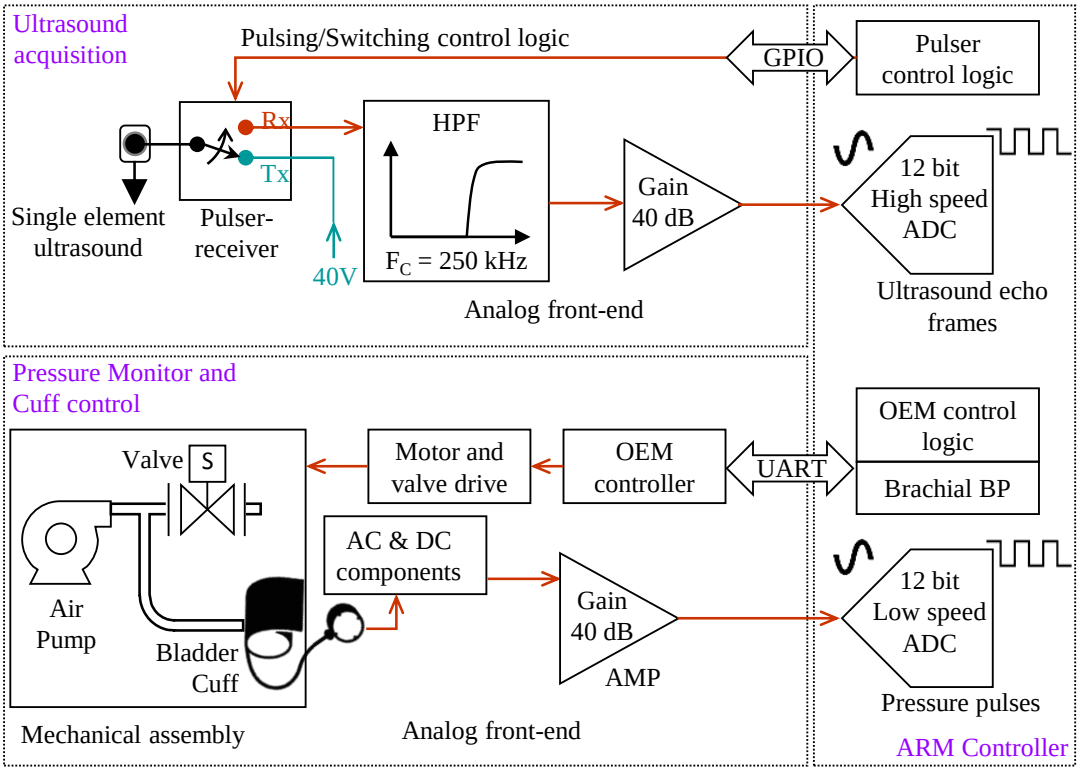

Figure 6.1 The hardware architecture of the proposed device for simultaneous regional and local stiffness measurements

6.1 MEASUREMENT SYSTEM

6.1.1 Hardware architecture

The hardware described in section 5.2 was developed as an embedded version and was constructed around 32-bit Arm Cortex M4 microcontroller. The schematic of the hardware architecture is shown in Figure 6.1. It has primarily an ultrasound section, and a cuff control and pressure detection section. The ultrasound section comprises pulser-receiver, and high voltage generation circuitry that operates a single element ultrasound transducer in pulse-echo mode for obtaining A-mode echo frames; the details can be found in section 5.2. For the cuff control and pressure detection section, an original equipment manufacturer (OEM) pressure module was employed that provided independent control to inflate a bladder type cuff and record the cuff pressure

fluctuation and also allowed Oscillometric brachial BP measurement. The module had a provision for serial communication, via UART interface, that enabled its control via the microcontroller of the device. Further, with respect to signals digitization, the microcontroller consisted of high-speed analog-to-digital-converter (ADC) channels for acquiring ultrasound A-mode frames (at scan rate of 250 frames per second) sampled at 80 MHz and low-speed ADC channels for acquiring the femoral pressure pulse signal at 250 Hz. The hardware is employed to record carotid ultrasound A-mode scans (using the ultrasound probe) and femoral pressure pulse waveforms (using the thigh cuff) simultaneously Figure 6.2.

6.1.2 Computation of regional stiffness alongside local stiffness

We have demonstrated earlier the ability of A-mode technology to furnish local stiffness indices (Joseph et al., 2020). With the technology enhancement supporting fast imaging and provision for cuff control and pressure detection, the system now is capable of performing the regional stiffness alongside in single test. A dedicated software was developed to realize this. The software communicates with the OEM pressure module to perform Oscillometric BP measurement. It further, processes the A-mode echo frames captured by the device's hardware to auto-identify and track the arterial wall locations, and evaluate the continuous carotid diameter pulses, employing

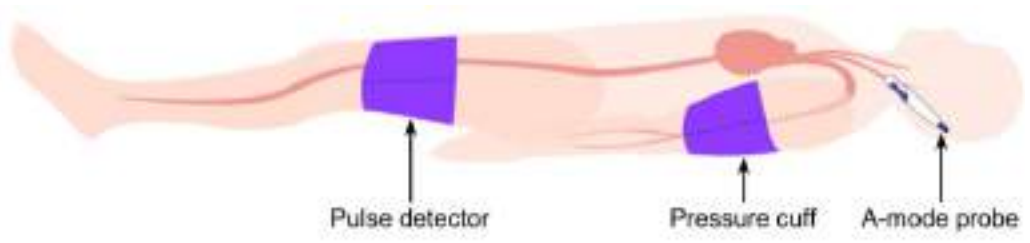

Figure 6.2 Representation of subject preparation and recordings for comprehensive regional and local stiffness assessment using the DUT

the algorithms presented in Chapter CHAPTER 3 andCHAPTER 4. As the diameter is evaluated, the software communicates with the OEM pressure module for actuating the cuff connected on the thigh and captures the femoral pressure pulsations. For each beat, the carotid and femoral pulse cycles are segregated. The diameter parameters – end-diastolic diameter and peak distension are obtained from the carotid diameter cycles. The carotid-to-femoral PTT is measured as delay between carotid and femoral pulse cycles using the intersecting tangent method. Arterial path lengths (Wilkinson et al., 2010) – distance from carotid artery site-to-sternal notch, sternal notch-to-thigh pulse detector, and femoral artery site-to-thigh pulse detector – were measured and entered in the user interface, which were used along-with carotid-to-femoral PTT for cfPWV evaluation. The measured carotid diameter parameters and estimated carotid BP were used to calculate the local stiffness indices (specific stiffness index (β), pressure-strain elastic modulus (E_P), arterial compliance (AC), and one-point pulse wave velocity (PWV_β). For these calculations, carotid BP was estimated (based on the measured diameter pulse cycle and brachial BP) using a well-established scheme proposed by Meinders and Hoeks (Jan M. Meinders & Hoeks, 2004b), with a rational assumption that end-diastolic and mean pressures are consistent across the arterial tree (Jan M. Meinders & Hoeks, 2004b; Vermeersch et al., 2008). Once measurements are recorded for sufficient cardiac cycles meeting the quality measures, the software terminates all acquisition and displays the final results and waveforms.

6.2 IN VIVO VALIDATION STUDY

The study reported herein aimed to assess the usability, accuracy, and the intra-/inter-operator variabilities of the device in healthy subjects. The locally measured arterial

dimensions and stiffness indices of the carotid artery obtained using the device under test (DUT) were compared against the ones obtained using a reference clinical-grade imaging ultrasound. Likewise, DUT's regional stiffness and central/peripheral BP were validated against a state-of-the-art reference.

6.2.1 Study participants

The study was performed in the period between May-August, 2021, in accordance with a protocol approved by the Indian Institute of Technology Madras Institutional Review Board (IEC/2021-01/JJ/07). The sample size, selection of subjects, and measurement procedures adhered to the ARTERY Society guidelines (Wilkinson et al., 2010) that lays out instructions for validating non-invasive hemodynamic measurement devices. A total of 90 asymptomatic individuals (faculty staff, employees, and students from the institution) aged $\geq$ 18 years and with BMI $\leq$ 30 kg/m^2 were opportunistically recruited for the study following a submission of their written informed consent. The participants were ~50% from each gender, distributed between the ages of 20 and 52 years. The exclusion criteria were (Wilkinson et al., 2010): age < 18 years, BMI > 30 kg/m^2, pregnancy, known carotid or femoral artery stenosis, patient dependent on a pacemaker, and/or not in sinus rhythm.

6.2.2 Study design

Two trained operators with moderate skills were involved in data collection. While the subjects rested in a supine position (~ 15 min), they were prepared by the *first* operator by attaching the DUT's upper arm pressure cuff and thigh pulse detector (Figure 6.2). The brachial BP and heart rate were obtained from the left arm. The left common carotid

was palpated to identify a suitable measurement site. Arterial path lengths (Wilkinson et al., 2010) – distance from carotid artery site-to-sternal notch, sternal notch-to-thigh pulse detector, and femoral artery site-to-thigh pulse detector – were measured and entered in the user interface along with the subject's details. As the recording started, the operator placed the carotid probe to record steady A-mode echoes which also auto-activated the pressure detector. Once a sufficient number of carotid diameter and femoral pulses (of the desired quality) were captured, the DUT performed the local and regional stiffness evaluation and displayed/saved the results.

While the subject remained in a supine posture, reference measurements were performed by the *second* operator. Firstly, aortic BP and regional stiffness were sequentially measured using the SphygmoCor XCEL (AtCor Medical, Sydney, Australia). Following this, for the reference local stiffness assessment, the brachial BP was re-measured using an oscillometric monitor (SunTech® 247™, SunTech Medical, United States). A linear-array ultrasound imaging probe was then positioned to scan the left common carotid along the longitudinal axis. B-mode image sequences were acquired and saved for a sufficient duration. The video sequences were processed offline using the Carotid Studio (Cardiovascular Suite 3, Quipu, Italy), and the diameter waveform thus obtained was used to evaluate local stiffness indices.

For quantifying the reproducibility, the procedure was repeated by interchanging the first and second operators. Measurements taken by one operator were blinded to the other and trials order was randomized.

6.2.3 Statistical analysis

All measurements and results obtained are presented as mean ± SD and categorical variables as numbers (or percentages), unless otherwise stated. Absolute percentage error and RMSE were calculated to quantify any deviation between the DUT and the reference devices. Their reproducibility (inter- and intra-operator agreement) was verified based on the CoV and regression analysis. The average of the measurements given by the operators was further analyzed. Linear regressions and BA representations were used to compare the DUT against reference devices. The significance of the observations was assessed using the paired Student's t-test. Statistical significance was inferred at $p \leq 0.05$. The mean and SD of the differences in cfPWV given by the DUT and reference device were graded according to the ARTERY Society guidelines. Analyses were performed using the SAS® University Edition.

6.3 RESULTS

Participants' demographic characteristics and baseline measurements are presented in Table 6.1. A #-symbol denotes manual input provided to the DUT. Figure 6.3 provides

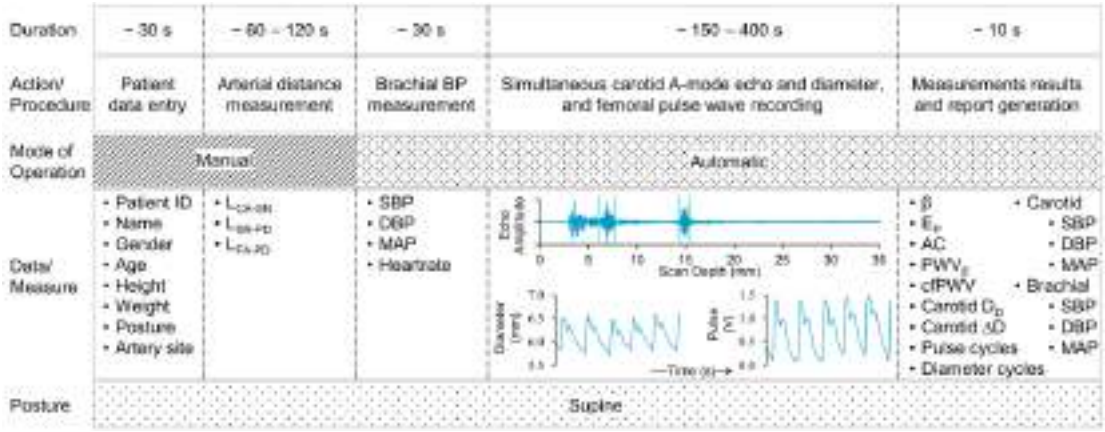

Figure 6.3 Phases of measurements procedure with DUT illustrating both manual and automated tasks along with the respective approximate time duration and input/output parameters.

Table 6.1 Baseline characteristics and vital measurements of study population

Parameter	Value (Mean ± SD)	Range (Min. – Max.)
Age (Years) #	27.4 ± 7.8	20 – 52
Height (cm) #	170 ± 8.5	150 – 195
Weight (kg) #	72.2 ± 8.9	46 – 92
Carotid-to-sternal notch (mm) #	87.7 ± 18.2	35 – 180
Sternal notch-to-thigh cuff (mm) #	661.0 ± 51.8	540 – 780
Femoral-to-thigh cuff (mm) #	109.1 ± 23.8	60 – 170
Body mass index (kg/m^2)	24.96 ± 2.81	18.15 – 29.8
Heartrate (BPM)	73.8 ± 9.9	55 – 101
Brachial SBP (mmHg)	120.36 ± 11.05	95 – 145
Brachial DBP (mmHg)	74.84 ± 7.19	59 – 95

the operation of the DUT, with examples of A-mode ultrasound frame from the carotid artery, simultaneous recording of carotid diameter and femoral pulse waveforms, and the other aforesaid measurements. The operators completed the entire procedure (from patient's data entry to report generation) within 5–10 minutes. The signal-to-noise ratio of raw A-scan frames and femoral pulse waves were greater than 25 dB and 30 dB, respectively.

6.3.1 Repeatability and Short-Term Reproducibility of DUT Measurements

A strong intra- and inter-operator reproducibility was observed for the DUT's brachial BP measurements. A CoV less than 3% was achieved for all the trial combinations conducted by the same as well as different operators ($r^2 > 0.978$, $p < 0.001$). The estimated carotid-femoral path length did not reveal significant difference ($p > 0.05$) between the operators (485.2 ± 59.9 mm versus 483.1 ± 56.1 mm), and exhibited a significant correlation with $r^2 = 0.944$ ($p < 0.001$).

In terms of the reproducibility of carotid diameter measurements with the DUT, an inter-operator agreement with $r^2 = 0.952$ ($p < 0.0001$) and $r^2 = 0.976$ ($p < 0.0001$) and

CoV equal to 6.6% and 4.4% were achieved for D_D and ΔD, respectively. The intra-operator recordings for D_D and ΔD were also in close agreement, with $r^2 = 0.966$ ($p < 0.0001$) and $r^2 = 0.978$ ($p < 0.0001$) and the CoV equal to 5.8% and 3.8%, respectively.

Reproducible local and regional stiffness values were obtained by both the operators; $r^2 > 0.946$ ($p < 0.001$). Inter-operator trials yielded a mean CoV < 7% for all the stiffness indices. Intra-operator measurement of both local and regional stiffness values were also repeatable, with $r^2 > 0.970$ ($p < 0.001$) and coefficients of variation < 5.5%. In a trend similar to that of the performance figures for intra-operator trials (although the difference was insignificant), the inter-operator reproducibility for cfPWV was also higher ($r^2 = 0.974$, $p < 0.001$).

6.3.2 Reliability of Blood Pressure and Diameter Parameters

Brachial DBP and SBP recorded by the DUT were accurate and in close agreement with the reference measurements: RMSE = 2.19 mmHg, $r^2 = 0.916$, $p < 0.0001$ for DBP and RMSE = 3.42 mmHg, $r^2 = 0.921$, $p < 0.0001$ for SBP. The carotid SBP recorded by the DUT was 108.30 ± 10.58 mmHg, i.e. 10.02% lower than the brachial SBP. Likewise, the aortic SBP given by SphygmoCor (109.14 ± 9.82 mmHg) was 10.41% lower than the corresponding brachial value. Comparable DBP values (carotid and aortic) were acquired from both the devices: 74.84 ± 7.19 mmHg (DUT) versus 75.40 ± 7.32 mmHg ($p > 0.05$) (SphygmoCor). Pulse pressure amplifications of 12.06 ± 5.01 mmHg between the carotid and brachial arteries and 12.68 ± 5.23 mmHg between the aorta and brachial artery were clearly observed in the population recruited for study.

D_D and ΔD obtained from the DUT and the imaging system revealed significant correlations (r^2 = 0.903, $p < 0.0001$ and r = 0.959, $p < 0.0001$, respectively). They exhibited close agreements, incurring CIs of –0.37 to 0.52 mm for D_D and –0.045 to 0.061 mm for ΔD. The diameter differences between the DUT and reference system were statistically insignificant: bias in D_D = 0.07 mm ($p > 0.05$) with a RMSE = 0.24 mm, and bias in ΔD = 0.008 mm ($p > 0.05$) with a RMSE = 0.03 mm.

6.3.3 Comparison of Local and Regional Arterial Stiffness Indices

In Table 6.2, simultaneously-recorded carotid (local) and carotid-femoral (regional) stiffness indices by the DUT are presented. The corresponding sequentially-obtained reference local stiffness (β, E_P, AC, PWV_β) and regional stiffness (cfPWV) from the respective devices are also summarized. The vascular health markers provided by the DUT were within an (average) absolute percentage error band ranging between 3.22% and 8.76%. Among the local stiffness indices, the average deviation from the reference was minimal in PWV_β (3.22%), followed by E_P (6.78%), β (7.81%), and AC (8.76%). The average deviation in cfPTT and cfPWV was 3.97% and 4.06%, respectively. A maximum deviation of 0.77 m/s was observed in cfPWV compared to the reference. The comparison of stiffness measurements from the DUT and the reference(s), using linear regression, is shown in Figure 6.4 and Figure 6.5.

Table 6.2 Comparison of DUT's stiffness measurements with reference values

Stiffness metrics	**DUT's measurements**	**Reference measurements**		**Deviation in measurements**	
		B-mode ultrasound	SphygmoCor	Relative error	Absolute error
β (–)	4.09 ± 1.16	4.05 ± 1.14	–	- 0.05 ± 0.46	0.32 ± 0.34
E_P (kPa)	48.96 ± 15.70	48.57 ± 15.13	–	- 0.39 ± 4.63	3.30 ± 3.25
AC (mm^2/kPa)	1.19 ± 0.33	1.24 ± 0.33	–	0.06 ± 0.14	0.11 ± 0.10
PWV_β (m/s)	4.30 ± 0.64	4.29 ± 0.63	–	- 0.01 ± 0.19	0.14 ± 0.13
cfPWV (m/s)	6.34 ± 1.05	–	6.40 ± 1.00	0.06 ± 0.31	0.26 ± 0.18

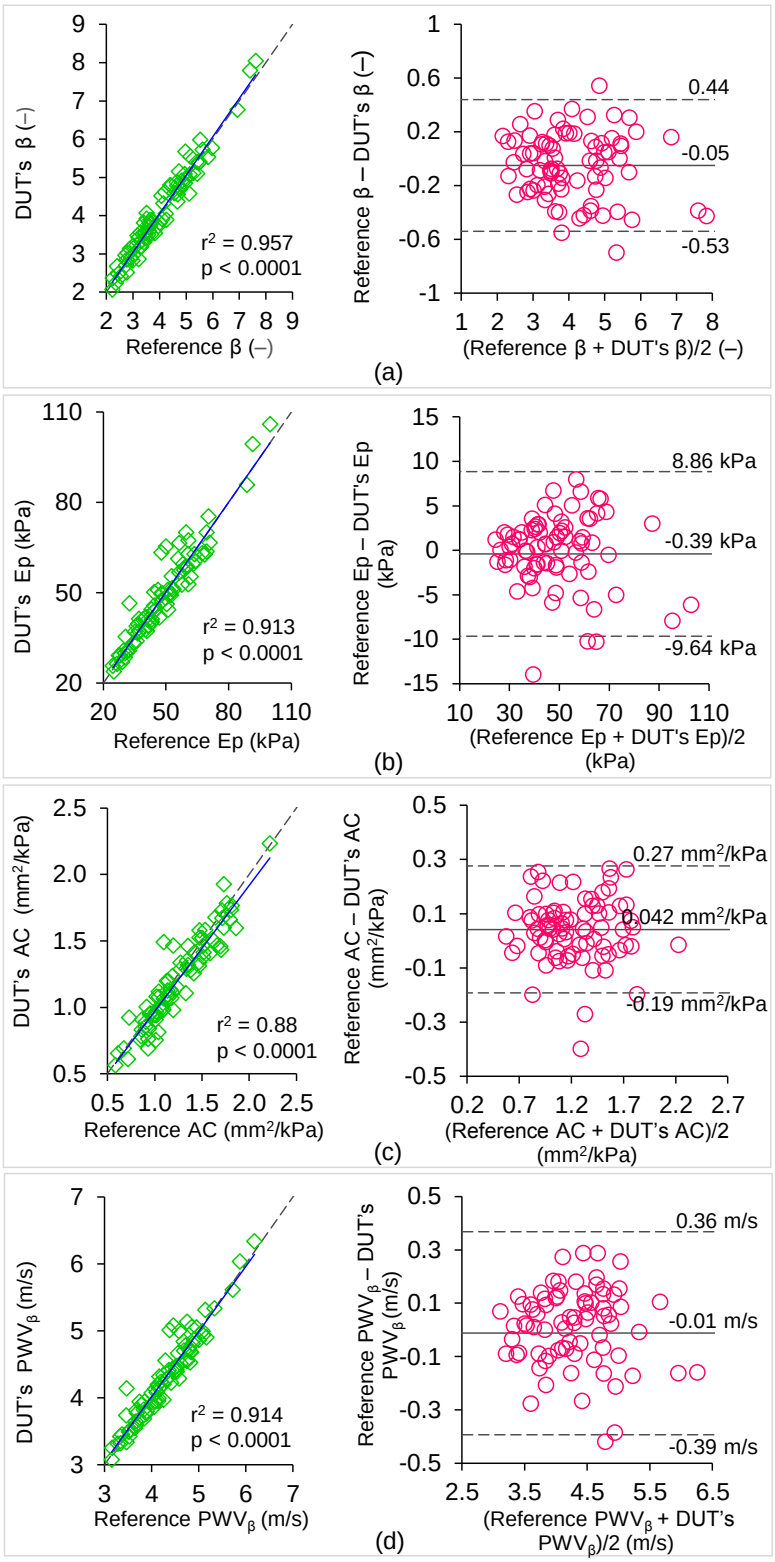

Figure 6.4 Scatter plots (showing linear correlation) and Bland-Altman plots (showing agreement) for (a) reference β versus DUT's β, (b) reference Ep versus DUT's Ep, (c) reference AC versus DUT's AC, (d) reference PWV_{β} versus DUT's PWV_{β}.

The DUT-based carotid and carotid-femoral stiffness indices were tightly correlated with the ultrasound-based carotid stiffness ($r^2 > 0.880$, $p < 0.0001$) and SphygmoCor-based carotid-femoral stiffness ($r^2 = 0.912$, $p < 0.0001$) respectively. There were no outliers, and the measured values were close to the ideal regression line. All local stiffness indices ($r^2 = 0.913$ to 0.957, $p < 0.0001$) were found to be comparably correlating with the regional one (cfPWV: $r^2 = 0.912$, $p < 0.0001$), except for AC ($r^2 = 0.880$, $p < 0.0001$). Among them, carotid β depicted a closer association with its reference counterpart ($r^2 = 0.957$, $p < 0.0001$).

The BA analysis (Figure 6.4) indicated that the CIs comparing the DUT and imaging system's carotid stiffness ranged from –0.53 to 0.44 with a mean bias of –0.05 for β; from –9.64 to 8.86 kPa with a mean bias of –0.39 kPa for E_P; from –0.19 to 0.27 mm^2/kPa with a mean bias of 0.042 mm^2/kPa for AC; and from –0.39 to 0.36 m/s with a mean bias of –0.01 m/s for PWV_β. These results showed an insignificant offset ($p > 0.001$) with good agreement among the respective local stiffness measurements.

A good agreement between the cfPWV obtained from DUT and SphygmoCor was observed, as illustrated in the BA plot (Figure 6.5(a)), with a CI ranging from –0.54 to 0.67 m/s and a bias of 0.06 m/s. Finally, when the carotid PWV_β was compared against the reference cfPWV, the former was significantly ($p < 0.001$) lower by 31.71% on average. As can also be seen from their correlation in Figure 6.5(b) with $r^2 = 0.324$, $p < 0.001$, they are not interchangeable, and possess a significant bias of 2.01 m/s with a large variation in CI (0.28 to 3.71 m/s). Likewise, the correlation of the reference cfPWV with the carotid β, E_P, and AC was moderate, with $r^2 < 0.4$ ($p < 0.001$). Analysis performed using the DUT's cfPWV also provided information of a similar nature.

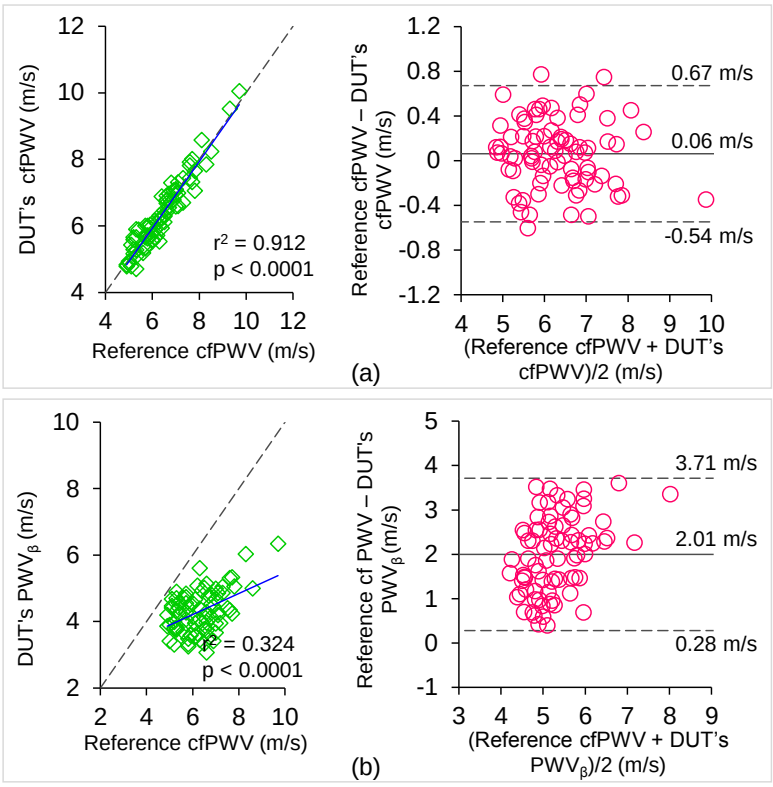

Figure 6.5 Scatter plots (showing linear correlation) and Bland-Altman plots (showing agreement) for (a) reference cfPWV versus DUT's cfPWV, and (b) reference cfPWV versus DUT's PWV_{β}.

6.4 DISCUSSION

The composition of matrix proteins, smooth muscle cells, and other matrix components in the arterial wall changes from the central aorta towards the peripheral sites (Segers et al., 2020). Consequently, the gradient of progressive stiffening of the arteries varies across the vascular bed (Fortier & Agharazii, 2015; Yu & Mceniery, 2020) and is majorly influenced by age. Since large central arteries encompass concentric elastic lamellae (which are, however, much lower in peripheral arteries), the stiffness gradient decreases from the central to peripheral sites (Fortier & Agharazii, 2015; Segers et al., 2020; Yu & Mceniery, 2020). For instance, stiffening of the aorta increases at a greater rate compared to that of the peripheral (femoral or brachial) arteries due to vascular

aging (Laina, Stellos, & Stamatelopoulos, 2018; London & Pannier, 2010). At the same time, the arteries are further susceptible to a localized stiffening (or dysfunction of a specific branch/segment), due to the large arterial wall structure heterogeneity at different sites (Nabeel et al., 2020). Therefore, it is relevant to analyze (multiple) local and regional stiffness indices as comprehensive biomarkers of vascular health for the purpose of both efficient risk stratifications early on and obtaining reliable quantification of vascular aging.

On the one hand, the regional stiffness indices (say, cfPWV) are known to provide information on an overall increase in the large artery and smooth muscle cell stiffness, vascular aging, pressure-dependency of arterial stiffness, adverse consequences for the organism, and beyond, as summarized in allied research in the domain (Nabeel et al., 2020). The 2018 ESC/ESH guidelines have, therefore, recommended cfPWV for vascular stiffness measurement (Williams et al., 2018). It is pertinent to note that, despite reliable evaluation of average stiffness distribution across a long arterial segment, the regional stiffness indices may mask the position of vascular structural abnormalities, and thereby do not endorse the evaluation of a target vessel section's biomechanical properties (Nabeel et al., 2020). On the other hand, local stiffness measures are able to provide insights into the functional stiffening and structural abnormalities of a small arterial section (Nabeel et al., 2020), even at a sub-local level (Apostolakis et al., 2016). Beyond typical stiffness-specific investigations, the potential use of central arteries' local indices for assessing (or as a surrogate marker for) the cardiac afterload (Hermeling et al., 2012), vascular Ehlers–Danlos syndrome (Mirault et al., 2015), continuous CBP parameters (Nabeel et al., 2018), and the dynamics of intra-cycle stiffness variations (Alberto Avolio, 2013; Nabeel et al., 2021) have been

demonstrated by independent researchers. Further discussion on the comparison of local versus regional stiffness indices and their unique pathophysiological implications is beyond this article's scope of research, and is summarized in allied studies (Nabeel et al., 2020). Ultimately, the simultaneous measurement of local and regional stiffness has incremental value above and beyond conventional measures, enabling comprehensive characterization of vascular conditions, assessment of stiffness levels, and quantification of the vascular age. Additionally, this type of single-examination approach would also be efficient for high-throughput and large-scale adoption at population-level screening and early-diagnosis.

The DUT evaluated herein, has thus demonstrated its potential for accurately evaluating local and regional stiffness indices simultaneously, along with the peripheral and CBP parameters, in a single test. To our knowledge, this is the first device that performs such a comprehensive vascular assessment; and is executed without the need for image feedback. The measurements obtained with the DUT (carotid local stiffness β, E_P, AC, PWV_β, and regional stiffness cfPWV) showed a good agreement with the reference standard techniques. Compared with the ultrasound imaging system, the DUT revealed an accuracy greater than 91% regarding carotid stiffness evaluation. This is an acceptable agreement between two non-invasive vascular stiffness monitors (Francesconi et al., 2021; Godia et al., 2007). Moreover, when compared to SphygmoCor, the DUT has met the criteria (mean difference = 0.06 ± 0.31 m/s) for an 'excellent' grade of accuracy for cfPWV, as stated by the ARTERY Society guidelines (Wilkinson et al., 2010). There was evidence of no systemic bias in the measured base parameters (BP and arterial dimensions) and the vascular health markers that were further evaluated. Given the combined assessment, the DUT was (approximately) twice

as fast as the cumulative time taken by the reference devices. It is important to note that the DUT's fully automated system, with real-time feedback (of the recording and its quality), enabled the device's operators to orient the probe quickly and precisely at the palpated carotid location. A bladder-type pulse detector, synchronized with the carotid probe, performed an automated capture of femoral pulses along with the carotid distension. Moreover, an online beat-by-beat evaluation of the desired parameters and their real-time quality checks considerably reduced the overall measurement time, as already stated.

An important point under discussion in this context pertains to obtaining the best possible local stiffness measurement using the diameter and BP of the target artery. Since it is impractical to noninvasively measure the central arterial pressure, even with a tonometer (O'Rourke, 2016), the common practice is to adopt the (supine) brachial BP, ignoring the pulse pressure amplification. One can then calculate only surrogates of the desired local indices, which are bound to be somewhat overestimated. The DUT particularly addresses this concern by performing an online evaluation of CBP (carotid BP in this study) while recording diameter waveforms from the common carotid artery, and using that for local stiffness evaluation. The individual diameter cycles were calibrated to carotid pressure using fundamental non-linear pressure-diameter relationship, considering consistent end-diastolic and mean pressures across the arterial tree (Jan M. Meinders & Hoeks, 2004b). Such a model, accounting for pulse pressure amplification, has been validated by on large population (Vermeersch et al., 2008).

It is also to be noted that cfPWV is most predominantly used to report vascular stiffness in research and clinical practice. It is of little doubt that it has virtually become a

synonym for aortic/arterial stiffness (Segers et al., 2020). However, it must be remembered that cfPWV is a popular and widely used reliable proxy for the overall stiffness level of the carotid-femoral segment (that is, carotid, aorta, iliac and femoral arteries), measured in terms of the propagation speed of blood pulses along the arterial wall. By definition, it is not a substitute or interchangeable measure for other markers that describe the elastic behavior of arteries (Alberto Avolio, 2013; Segers et al., 2020). As observed here, the reference/DUT's cfPWV was moderately associated with the carotid β, E_P, AC, and PWV_β, with a significant offset between both the PWVs. These findings were consistent with the results of previous studies (Simova, Katova, Santoro, & Galderisi, 2016; Vriz et al., 2013), besides corroborating the indices reported in this study. A recent study (Quinaglia et al., 2018) comparing the differential impact of local and regional stiffness has revealed that central PWV_β helps predict the hemodynamic load and age-related left ventricular remodeling when assessed together with cfPWV, thus accentuating the need for their simultaneous evaluation. The DUT would be an asset for similar studies that examine the differential or complementary impacts of local and regional arterial stiffening and the associated pathophysiological consequences.

6.5 CONCLUSION

In conclusion, this pre-clinical study has demonstrated that the DUT is efficient for the non-invasive measurement of simultaneous carotid artery dimensions, carotid local stiffness, and carotid-femoral stiffness. It offers the added advantages of rapid and reliable measurement, operator-independent assessment, small size/portability, and cost-effectiveness. Such a device would benefit any clinical application or study of vascular stiffness, and is suitable for large-scale use in population studies. Beyond its

multi-centric validation on a diverse cohort and over a wide pathophysiological range, the device's ongoing clinical studies focus on its performance in the unique role of comprehensive vascular health assessment in early vascular aging syndrome, vascular toxicity, end-organ damage, and other pre-clinical conditions.

CHAPTER 7.

MEASUREMENT OF PRESSURE-DEPENDENT LOCAL PWV VARIATIONS

As seen in Chapter 2 (section 2.4), the stiffness varies with pressure in an acute manner as-well, and therefore, being able to measure those variations will allow pressure-standardizing the stiffness measures. This acute dependence is evidenced intra-beat (diastolic-to-systolic) due to the hyper-elasticity of the artery, and also inter-beat, if there are hemodynamic variations that perturb pressure. As seen from the literature, both these measurements accompany instrumentation and methodological challenges, which the work presented in this chapter attempts to solve. We have proposed novel instrumentation and algorithms to measure both the inter- and intra-cardiac cycles changes in local PWV and demonstrated their functionality *in-vivo* over independent experimental investigations, which are discussed in this chapter.

This chapter is partially adapted from the post-print version of:

Raj, K. V., Nabeel, P. M., Chandran, D., Sivaprakasam, M., & Joseph, J. (2022). High-frame-rate A-mode ultrasound for calibration-free cuffless carotid pressure: feasibility study using lower body negative pressure intervention. Blood Pressure, 31(1), 1–11.

Raj, K. V., Nabeel, P. M., Joseph, J., & Sivaprakasam, M. (2018). Non-invasive assessment of arterial incremental elastic modulus variations within a cardiac cycle. 13th Russian-German Conference on Biomedical Engineering (RGC), 108–111.

Raj, K. V., Nabeel, P. M., Joseph, J., & Sivaprakasam, M. (2019). Incorporating Arterial Viscoelastic Modelling for the Assessment of Changes in Pulse Wave Velocity Within a Cardiac Cycle Using Bramwell-Hill Equation. Computing in Cardiology (CinC), 46, 1–4.

Raj, K. V., Nabeel, P. M., Joseph, J., Frese, H., & Sivaprakasam, M. (2019). Multimodal Image-Free Ultrasound Technique for Evaluation of Arterial Viscoelastic Properties: A Feasibility Study. 41st Annual International Conference of the IEEE Engineering in Medicine and Biology Society (EMBC), 5034–5037.

Raj, K. V., Nabeel, P. M., Joseph, J., Chandran, D., & Sivaprakasam, M. (2020). P.41 Measurement of Pressure-dependent Intra-Beat Changes in Carotid Pulse Wave Velocity using Image-Free Fast Ultrasound. Artery Research, 26(Supplement 1), S63.

Raj, K. V., Manoj, R., Ishwarya, S., Nabeel, P. M., Joseph, J. (2022). Comparison of Approximated and Actual Bramwell-Hill Equation Implementation for Local Pulse Wave Velocity: Ex-vivo Study. 44th Annual International Conference of the IEEE Engineering in Medicine and Biology Society (EMBC), 5034–5037.

7.1 PRESSURE DEPENDENT INTER-BEAT VARIATIONS IN LOCAL PWV

7.1.1 Methodological considerations

Chapter 5 has discussed direct and in-direct measurement of local PWV, where the former is based on measuring transit features and the latter is by theorical means, popularly employing BH-equation. In-direct approach has limitations for capturing the inter-beat pressure dependent variations in local PWV from central arteries. While diametric variations can be captured non-invasively from carotid artery during hemodynamic perturbations, hitherto, there lacks reliable means to measure the central arterial pressure that is required for local PWV evaluation. Therefore, direct measurement is preferable, for which the methodological considerations enlisted in the last chapter equally apply, but more stringently. From instrumentation perspective, (i) high rate acquisition, (ii) lower computation complexity, (iii) beat-to-beat online evaluation, and (iv) feedback on the quality of raw and evaluated signals are important methodological requirements for tracking the inter-beat PWV perturbations. These were thoroughly addressed for the technology developed and presented in Chapter 5. Therefore, in this chapter, more specifically in section 7.1, we aim to demonstrate the ability of the system to capture the hemodynamically induced variation in local PWV.

7.1.2 Study design

In-vivo investigations on inter-beat PWV variations were conducted on two independent cohorts, each consisting eight participants. The study on the first cohort was conducted in the premises of Healthcare Technology Innovation Centre, Chennai, India, where participants underwent a hemodynamic intervention that elevates BP. The protocols (adhered to the principles of Helsinki declaration) were approved by the ethics

committee of the Indian Institute of Technology, Madras (ethics approval: IEC/2021-01/JJ/07). Likewise, the second cohort study was at All India Institute of Medical Sciences (ethics approval: IECPG-153/28.02.2019), New Delhi, India, where the participants were subject to BP lowering intervention. The availability of the needed equipment for inducing these different pressure perturbations was the reason for study on two independent cohorts and venue. Young and healthy male subjects were selected that were devoid of cardiovascular risk symptoms (such as hyper/hypotension or autonomic nervous dysfunction) and were not on any medication known to alter autonomic nervous function. This was to ensure appropriate hemodynamic response and adequate tolerance to the BP perturbing interventions. The experimental procedure was performed in a temperature-controlled room (~23°C). Investigations were scheduled from 9 A.M. and then 2 P.M., after standard intake of a meal without any caffeinated beverages. The same operator performed all the assessments on both the cohorts and the subjects during the measurement were in supine posture. In both the studies continuous finger BP and carotid PWV were recorded beat-to-beat simultaneously and analysed. The volunteers' response to the interventions were assessed initially to verify if the intervention could yield at least a 10-mmHg perturbation in the finger DBP from baseline. This was necessary for functionality assessment, as the intervention was intended to serve as a source for dynamic pressure profile and yield a range perturbation in BP values.

A commercial NIBP system (Human NIBP Nano, ADInstruments South Asia, India) used with appropriate finger-cuff provided the measures of continuous peripheral pressure values. The equipment also employed a hydrostatic pressure sensory unit for

offset adjustment. Finger pressure cycles yielded the corresponding beat's diastolic (DBP_{FIN}), systolic (SBP_{FIN}), and mean arterial (MAP_{FIN}) pressures.

7.1.3 Measurement under pressure elevating intervention

For the experiment physical-exercise based intervention was chosen to alter the BP. Figure 7.1(a) illustrates the measurement procedure during the thread-mill exercise study. It is a well-known intervention in the literature, yielding a substantial elevation in BP acutely. The procedure involved three phases – baseline, intervention and recovery phase. The subject was asked to rest initially to measure the baseline BP and HR using an automatic BP device (HEM-8712, Omron Healthcare, Japan) and a D-ring type arm cuff. NIBP system was then instrumented onto the subject for the measurement of continuous peripheral BP from the finger. The left common carotid artery was identified by palpation, and the developed dual-element ultrasound probe was positioned at the identified site. The probe was oriented to yield the best quality RF signals with strong wall echoes from both the proximal and distal sites. Baseline

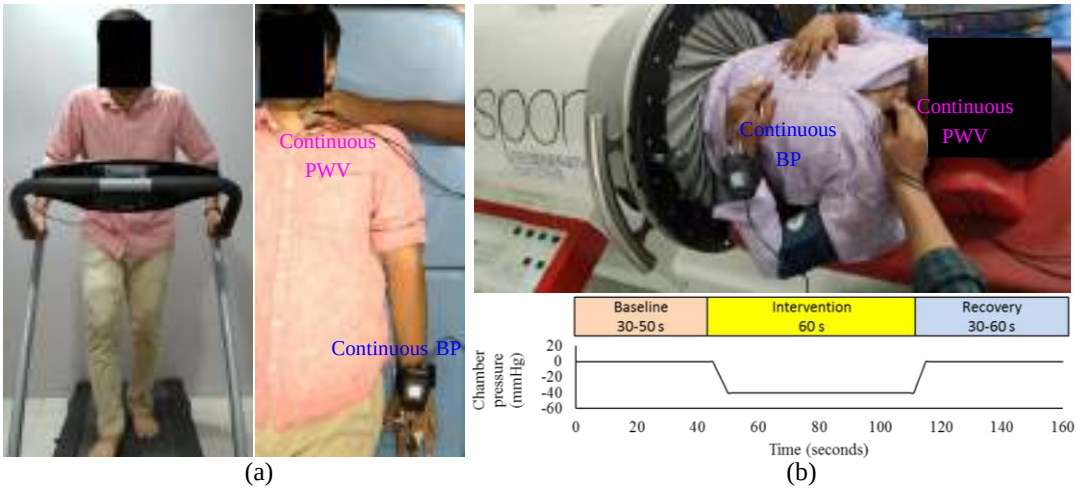

(a) (b)

Figure 7.1 Measurement of simultaneous pressure and local PWV under induced hemodynamic variations - (a) Exercise intervention for BP elevation and (b) LBNP intervention for BP lowering.

measurements from NIBP and the proposed devices were performed for sufficient duration. The subjects were then asked to perform a tread-mill exercise for 10 mins with a graded increase of speed from 3 to 9 km/hr. Post to the exercise the finger BP and local PWV was re-measured continuously until the pressure recovered to baseline.

7.1.4 Measurement under pressure lowering intervention

Even the pressure lowering intervention experiments followed the same three phases on baseline, intervention, and recovery. The measurement instrumentation and data collection were almost similar, except that in this case the recording were feasible during the intervention phase as well. The subject was positioned horizontally in supine posture in a lower-body-negative-pressure (LBNP) chamber (VACUSPORT® - Regeneration system, Weyergans High Care® Medical, Germany) up to the level of the iliac crest, as shown in Figure 7.1(b), and was allowed to rest for 10-15 minutes. Baseline measurements (finger BP and carotid PWV) were performed for 30-50 s. LBNP (–40 mmHg) was then applied for about 1 minute (intervention phase), during which all the measurements were continued. Finally, upon intervention withdrawal, the measurements were collected for another 30-50 s (recovery phase).

7.1.5 Study results: Inter-beat PWV variations

The SNR of the acquired high-speed A-mode frames were greater than 25 dB during all the phases – baseline, intervention, and recovery. Fidelity of the diameter cycles measured from both proximal and distal carotid sites was adequate for the reliable evaluation of local PWV throughout the course of measurement. The baseline local PWV measured from first and second cohorts were 3.62 ± 0.61 m/s and 3.95 ± 0.33

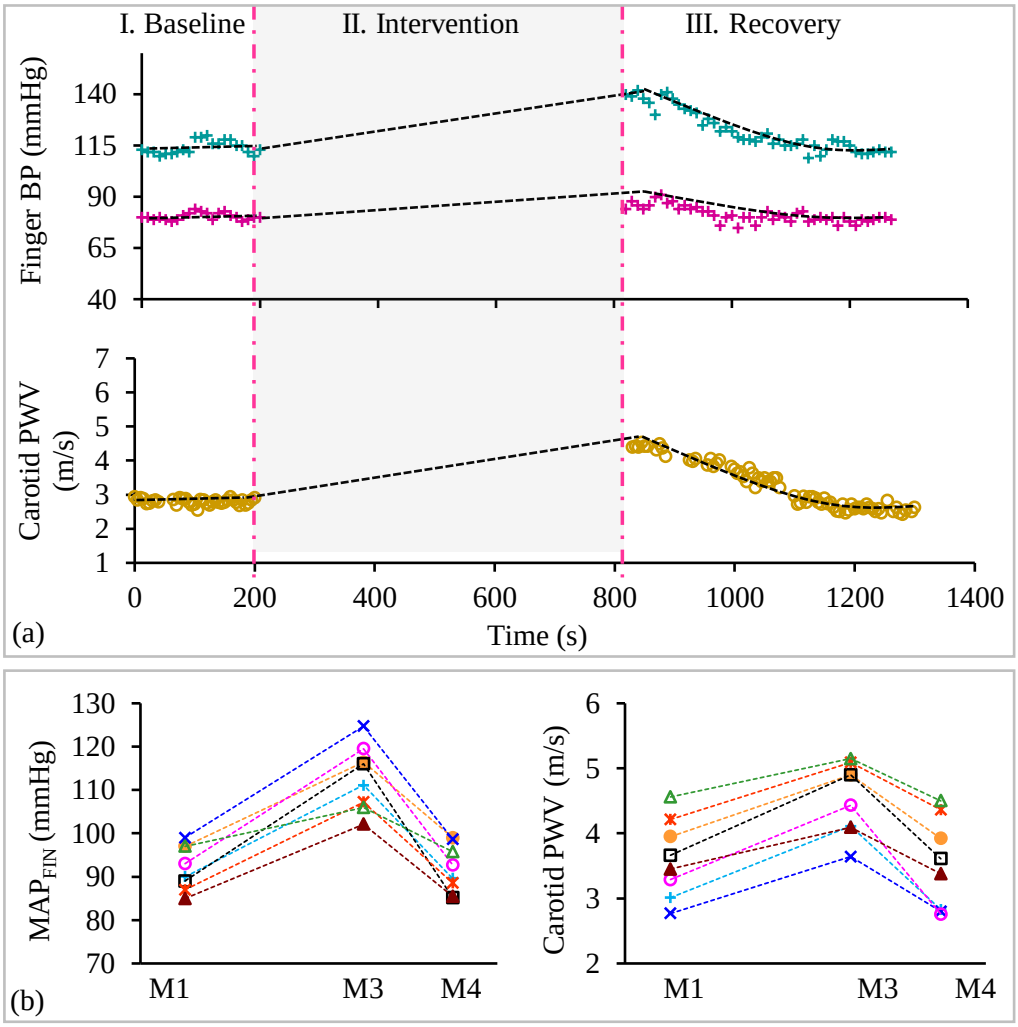

Figure 7.2 (a) Sample Beat-to-beat measurement of simultaneous BP and local PWV during exercise induced hemodynamic variation study, and (b) Subject wise measures during important phases of measurement (M1: baseline, M3: Immediately after exercise intervention, M4: end of recovery).

m/s, respectively (range = 2.77 to 4.56 m/s). The beat-to-beat variation during the baseline was smaller than 7%, for both cohorts. Figure 7.2(a) shows a representative example of beat-to-beat measurements of finger BP and carotid local PWV during the exercise intervention. It was observed that post exercise the measured BP elevated and it gradually recovered to the baseline value in 3-4 mins. The measured local PWV increased with the elevated pressure and decayed to the baseline value similar to the measured pressure. Subject-wise data points recorded for multiple important phases

during the exercise experiment are shown in Figure 7.2(b). The selected measurement instants were M1: Baseline (in average form), M2: during the intervention (extremum), M3: immediately after intervention, M4: end of recovery. During the exercise study only M1, M3, and M4 could be obtained. A ~22 % increase in finger MAP caused PWV to increase by ~25 %, both were significant ($p < 0.05$). For the cohort which underwent LBNP intervention, the pressure significantly reduced during the intervention, suffered an overshoot just after the intervention withdrawal, and finally recovered to baseline

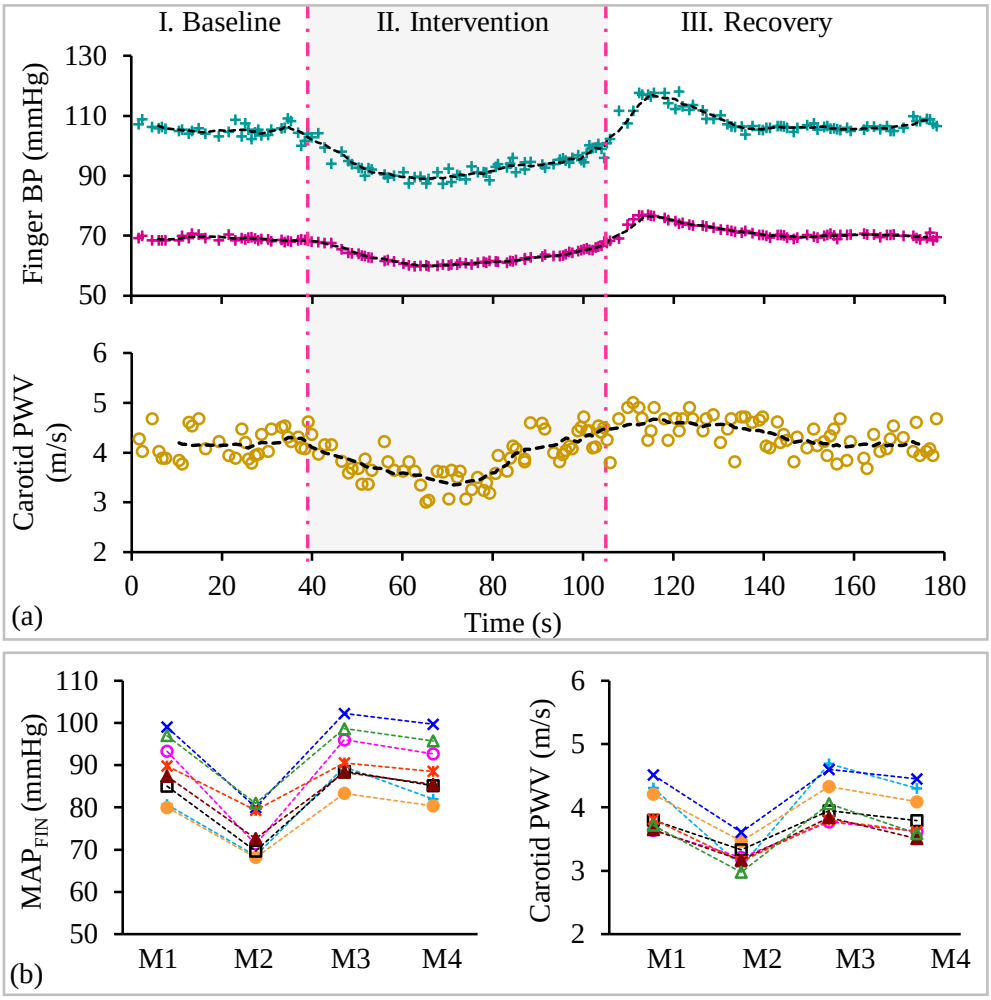

Figure 7.3 (a) Sample Beat-to-beat measurement of simultaneous BP and local PWV during LBNP induced hemodynamic variation study, and (b) Subject wise measures during important phases of measurement (M1: baseline, M3: Immediately after exercise intervention, M4: end of recovery).

value. Concurrent to the pressure Figure 7.3(a), it may be observed that the local PWV as well perturbed following similar trend. For both pressure and local PWV maximum drop during the intervention occurred at within 17 ± 5 s, and they recovered in 25 ± 7 s of withdrawal. Subject-wise data points recorded for multiple important phases during the exercise experiment are shown in Figure 7.3(b). A 17% pressure change incurred a 14 % PWV change. In both cohorts the pressure significantly correlated ($r > 0.6$, $p < 0.001$) to the local PWV, even after adjusting for heart rate.

7.2 PRESSURE DEPENDENT INTRA-BEAT VARIATIONS: INDIRECT MEASUREMENT

7.2.1 Methodological considerations

As highlighted in section 2.5, the young's modulus and hence the local PWV are incremental with distending pressure. Equation (5.2) shows the BH formula that relates the PWV to the slope of P-D curve. Measuring the changing slope (dP/dD) of the curve is the means to evaluate the changes in the local PWV. Now in-order to reliably evaluate this changing slope within the cardiac cycle high-fidelity waveforms of pressure and diameter are required and also there shouldn't be hysteresis between them. Hysteresis may arise due to uncertain lags between pressure and diameter (section 2.4). The sources of these lags majorly arise from instrumentation, signal processing, and signals recording scheme. It may be noted that even after these factors are carefully considered and addressed the viscoelastic nature of the artery poses a challenge. The BH formula is applicable on P-D curve where the assumption on the association between them is of an elastic material. Hence BH formulation also requires incorporation of viscoelastic modelling to compensate for viscous component, and yield just the elastic component.

7.2.2 Incorporating viscoelastic modelling

The arteries in the circulatory system are hyper-elastic and the circumferential stress on the arterial walls during the blood pulse propagation results in a non-linear circumferential strain (Alberto Avolio, 2013). Therefore, the elastic properties of the arterial walls are a function of the circumferential stress induced by the instantaneous blood pressure, P(t). The local PWV, being a direct function of the elastic modulus of the arterial walls (Alberto Avolio, 2013), changes with the P(t) within the cardiac cycle. The increase in the blood pulse propagation velocity with the increase in distending pressure during the systolic phase of the cardiac cycle is termed as incremental local pulse wave velocity $PWV_{(P)}$. BH equation (Bramwell & Hill, 1922; Segers et al., 2014), presented in equation (5.2) can be re-written in terms of time varying pressure and diameter D(t).

$$PWV = \sqrt{\frac{D(t)}{2\rho}\frac{dP(t)}{dD(t)}} \tag{7.1}$$

In spite of the simplicity of this local PWV evaluation method, it may be remembered that obtaining an elastic P-D relationship curve for the calculation of dP(t)/dD(t) is not trivial. The primary challenge is the intrinsic viscoelastic nature of the arteries. More clearly, if the arteries were only elastic in nature, the P(t) and D(t) would have exhibited an ideal exponential relationship (Hayashi, Handa, Nagasawa, Okumura, & Moritake, 1980), as given in (7.2). Here the P_D and D_D are diastolic pressure and diameter respectively and the exponential coefficient β is referred to as stiffness index.

$$P(t) = P_D \, e^{\beta\left(\frac{D(t)}{D_D} - 1\right)} \tag{7.2}$$

However, the viscoelastic nature of the arterial wall yields a hysteresis loop between P and D, contrary to an exponential curve. Therefore, quantifying the viscous component is essential to obtain a relationship curve between the elastic component of P(t) and D(t). For this, we have incorporated Kelvin-Voigt type arterial viscoelastic modelling. In this approach, the recorded P(t) could be expressed as the sum of elastic and viscous pressure components ($P_e(t)$ and $P_v(t)$ respectively) (Bia et al., 2005).

$$P(t) = P_e(t) + P_v(t) = P_e(t) + \eta \frac{dD(t)}{dt} \tag{7.3}$$

'η' is the viscosity index. Expression (7.3) can be re-written as (7.4).

$$P_e(t) = P(t) - \eta \frac{dD(t)}{dt} \tag{7.4}$$

The viscosity index η can be estimated by iteratively updating its value in (4), such that the area of the loop between $P_e(t)$ and D(t) is reduced to minimum; indicating hysteresis elimination. Now an exponential curve fitted on this minimal area loop can be approximated as the purely elastic relationship between P and D. This exponential curve and the η together can also furnish wall buffer function (WBF), an indicator of buffering capacity. The slope of P-D curve at mean level of the cycle yields 'E_{pd}', the elastic index, and WBF is the ratio of η and E_{pd}. Finally, the $PWV_{(P)}$ now can be evaluated using the exponential curve constructed between the $P_e(t)$ and D(t).

$$PWV_{(P)} = \sqrt{\frac{D(t)}{2\rho}\frac{dP_e(t)}{dD(t)}} = \sqrt{\frac{D(t)}{2\rho}\frac{d\left(P(t) - \eta\frac{dD(t)}{dt}\right)}{dD(t)}} \quad (7.5)$$

7.2.3 Measurement feasibility study

A pilot feasibility study was conducted in vivo on 8 human subjects. Young subjects (group average age = 25.5 ± 2.7 years, normotensive = 4, hypertensive = 4) were recruited for the study. The study conformed to the Helsinki Declaration. All the subjects were detailed about the study and written informed consent was obtained. The subjects were allowed to rest for 5 minutes upon which the baseline BP and heart rate were recorded using an automatic BP monitor (SunTech® 247TM, SunTech Medical) and then the physiological measurements were performed. All the local PWV assessments (pressure dependent intra-beat variations) during the course of study were performed by a single operator on the left common carotid artery while the subject was in the supine posture.

7.2.4 Instrumentation for the study

A multimodal probe was designed to facilitate simultaneous measurement of P and D from a small arterial segment. The probe consists of aforementioned single element ultrasound transducer (section 5.2.1) to perform continuous measurement of changes in arterial diameter and a tonometer (SPT-301, Millar Instrument) to measure the continuous arterial distending pressure. These transducers were integrated into a 3D printed enclosure that acted as a probe holder. The distance between the pressure transducer and the single element ultrasound transducer is kept minimal so that the signals are approximately recorded from a single arterial site. The schematic of the

Figure 7.4 (a) Schematic of the multimodal acquisition probe, (b) its placement at carotid site, and (c) a sample of simultaneous pressure and diameter recorded from the carotid artery.

compact probe assembly is depicted in Figure 7.4(a). The probe placement for performing the measurements is illustrated in Figure 7.4(b).

We have shown earlier that the developed high-frame rate A-scan ultrasound prototype also supports multimodal acquisition, in a synchronised fashion. The probe consisting of the ultrasound and pressure transducers was interfaced to the acquisition hardware. For the continuous evaluation of diameter using the A-scan acquired frames the automatic algorithms introduced in Chapters 3 and 4 were employed. The pressure signal was simultaneously acquired in a synchronized manner. The pressure signals were processed via LPF with cutoff frequency 15 Hz, in order to remove any high-frequency noise. For each pair of P and D cycles a P-D loop was constructed with P along the ordinate and D along the abscissa. A differential evolution optimization method was employed to estimate η for which the loop area is minimized and hysteresis is reduced. An exponential fit of the minimal area loop based on the method of least squares was obtained and was used for evaluation of the incremental local PWV using (7.5). As intermediate step, the wall viscous properties η, E_{pd}, and WBF were evaluated.

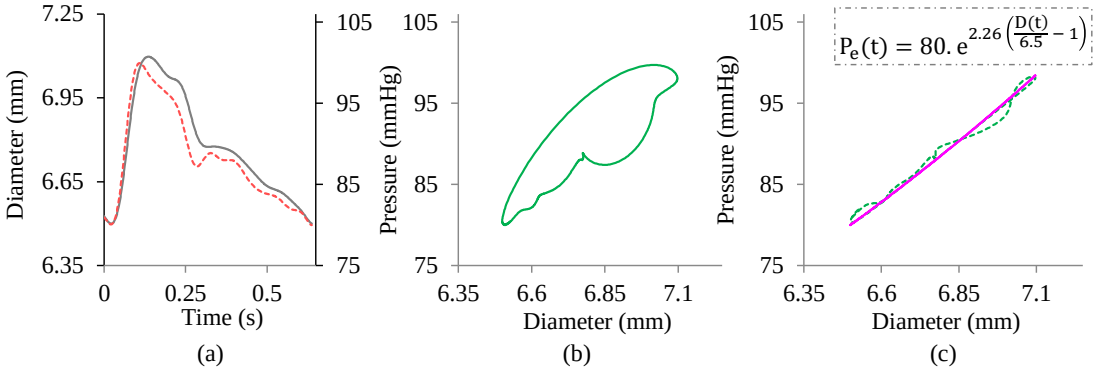

Figure 7.5 Illustration of (a) Simultaneously measured P (dotted line) and D (solid line) cycle, (b) the corresponding P-D loop, (c) Loop area minimized to obtained a P-D curve for elastic component of P; hysteresis-eliminated curve is shown in green and an exponential fit of the same is shown in pink along with its equation.

7.2.5 Study results: Indirect measurement of Intra-beat PWV changes

The recorded waveforms had a high temporal resolution of 1 ms. A sample of 5 continuous P and D cycles recorded from a particular subject is shown in Figure 7.5(a). These signals were then reliably used to construct cycle-to-cycle PD-loop. A loop constructed from one example pair of cycles Figure 7.5(a), is illustrated in Figure 7.5(b). In Figure 7.5(c), the minimal area loop and the respective exponential fit derived for the particular PD-loop shown in Figure 7.5(c), is illustrated. Similar quality loops were obtained from all the recruited subjects for continuous cardiac cycles.

For verifying the reliability of the obtained P-D fit curves the stiffness index derived from the exponential coefficient (β_{fit}) of the fit was compared against the theoretically calculated β (β_{ref}) using P_S, P_D, D_S, and D_D obtained from the measured P(t) and D(t).

$$\beta_{ref} = \frac{\ln(P_s/P_d)}{(D_s - D_d)/D_d} \tag{7.6}$$

Figure 7.5(c) shows the regression plot for the β_{fit} versus β_{ref} measures obtained from all the recruited subjects (measured for 5 cycles per subject). The β_{fit} values were strongly correlated ($r = 0.98$, $p < 0.05$) to the β_{ref} values for all the subjects with an insignificant bias (bias = -0.04, $p = 0.12$), indicating that the reliability of P-D fit curves for the measurement of $PWV_{(P)}$.

These viscoelastic parameters were obtained in a beat-to-beat manner for all the recruited subjects. To quantify the measurement repeatability, beat-to-beat estimates of η, E_{pd}, and WBF obtained for 10 consecutive cardiac cycles were used to calculate the CoV. The values were consistent with earlier reported literature that performed similar studies (Armentano et al., 1998; Bia et al., 2005; Simon & Levenson, 2001). The beat-to-beat CoV for the measurements of η, E_{pd}, and WBF was less than 4.7%, 5.6%, and 6.4% respectively. The group average of the η for hypertensive subjects was 3.46 ± 0.50 mmHg.s/mm, which was relatively higher than the normotensive subjects 1.51 ± 0.20 mmHg.s/mm. These results concur with earlier studies reported by other researchers who performed investigations on normotensive and hypertensive subjects (Armentano et al., 1998; Bia et al., 2005; Simon & Levenson, 2001). A similar trend was observed for the WBF measurements, where group average for hypertensive subjects was 5.78 ± 0.73 s and for normotensive subjects was 2.87 ± 0.66 s.

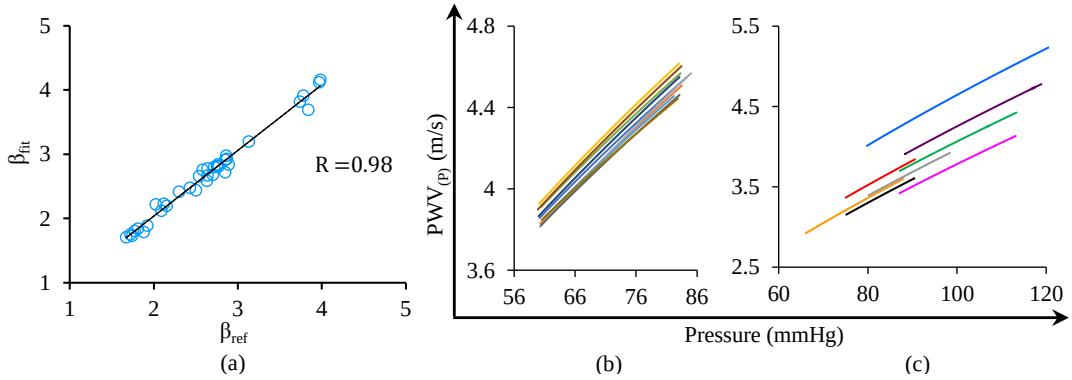

Figure 7.6 (a) A regression plot of β_{fit} versus β_{ref}, demonstrating the reliability of P-D fit curves obtained for the recruited subjects. Illustration of $PWV_{(P)}$ measured (b) Cycle-to-cycle for a particular subject and (c) From all the recruited subjects

The cycle-to-cycle exponential P-D fit curves were used to evaluate $PWV_{(P)}$ from individual cycles. Figure 7.6(a), shows the $PWV_{(P)}$ for a particular subject (age = 28 years, BMI = 18.5 kg/m^2, carotid P_S = 85 mmHg, P_D = 60 mmHg β = 3.84 ± 0.18) obtained for 10 consecutive cycles, demonstrating the measurement repeatability. The $PWV_{(P)}$ plots obtained for all the recruited subjects are shown in Figure 7.6(b). The systolic PWV (PWV_S) was on an average 20% higher than diastolic PWV (PWV_D). The group average PWV_S = (4.20±0.59) m/s and PWV_D = (3.48±0.36) m/s. The mean change in diastolic to systolic PWV (ΔPWV) was (0.71±0.26) m/s. The absolute difference in local PWV and the corresponding pressure difference (ΔP) were significantly correlated with a correlation coefficient R = 0.67 ($p < 0.001$) when the mean values were pooled over all the subjects. It was observed that the PWV was higher for hypertensive subjects with PWV_S = (4.65±0.49) m/s and PWV_D = (3.76±0.26) m/s as compared to normotensives which were (3.74±0.16) m/s and (3.20±0.21) m/s respectively. These results concur with recently reported study on $PWV_{(P)}$ (X. Li et al., 2017).

7.3 PRESSURE DEPENDENT INTRA-BEAT VARIATIONS: DIRECT MEASUREMENT

In Chapter 5, we have detailed the device development and method for measuring local PWV directly from PTT features. We have thoroughly identified the methodological design requirements and have characterised the design parameters. With that demonstrated that the measurement device reliably yielded local PWV from a single fiducial point near the foot. There are, however, a host of fiducial points within the cycle, which can be used for PWV evaluation. Figure 5.1(b) illustrates a blood pulse cycle and on it, the popularly employed fiducial points in literature. A majority of them are derived from the first- and second-time derivatives (as shown in the figure), and are situated in the anacrotic phase of the blood pulse waveform. Since these fiducial points distributed across different phases from diastole to systole, the pressure level at which they occur differ. Consequently, it is expected that the PWV also differs among these different points. More specifically, the closer the point is to the systolic peak, the higher would be the corresponding PWV value. Therefore, for measuring the intra-beat variations, PWV can be measured across multiple fiducial points starting from end-diastole to peak-systole. While the reliability of the fiducial point identification algorithms dictates the accuracy of the PTTs, the noise effecting the morphology may potentially corrupt the region of fiducial points (Hermeling et al., 2008; C. Huang et al., 2014). A pronounced concern in this regard is the influence of wave-reflections in the early systolic region of the pulse waves. As it is well-known, propagating pulses in the arterial system are not entirely free from wave reflections. But the start of the upstroke region is considered to be free from the effect of multiple wave reflection phenomena. A few experimental studies have observed to the contrary that the interference of early

reflection with the diastolic foot region (neighboring the start of the upstroke) of the arterial distension and/or diameter waveforms. These reflections are indeed more evident when the measurement site is proximal to any arterial branching location, such as carotid. Thus, some confusion exists in the literature about the 'reflection-free definition' of these well-defined, longer-established fiducial time-points.

7.3.1 Correcting for effect of wave reflection

As the proposed method intends in measuring the incremental PWV, it is at-most important that the systolic rise region should be reflection-free. Therefore, a wave-separation analysis (WSA) technique is needed to separate the forward pulse on which the measurements could be performed in a reliable manner. We propose using a technique called 'characteristic impedance method'. The separation technique is established, and it uses arterial pressure P and blood flow rate Q. We have modified the method to implement it using only diameter D and Q without requiring P, and have for the first time, used such a technique to measure incremental PTT and PWV. The method is based on analysis of the frequency dependent vascular impedance of the artery. Of note, the vascular impedance (Z) describes the spectral relationship between arterial pressure P and flow rate Q of an artery. The pressure pulse wave P(t) and Q(t) may be represented as a Fourier series.

$$P(t) = \overline{P} + \sum_{n=1}^{H} P_n \sin(n\omega t + \theta_n). \quad (7.7)$$

$$Q(t) = \bar{Q} + \sum_{n=1}^{H} Q_n \sin(n\omega t + \theta_n). \quad (7.8)$$

Now the $|Z_n|$ is defined as the ratio of $|P_n|$ and $|Q_n|$ and the phase of Z_n is defined as the $\tan^{-1}(P_n/Q_n)$. Studies argue that the higher harmonics of P and Q waves dissipate faster, and the influence of the arterial reflections on these harmonics is negligible. The impedance calculated as the averaged ratio of higher harmonics of P and Q moduli is known as characteristic impedance Z_0. Using this estimated Z_0, the forward and backward waves could be separated. The forward and backward P can be evaluated from measured P and Q as (Swillens & Segers, 2008),

$$P_{f\ or\ b} = \frac{1}{2}(P \pm Z_0 Q) \quad (7.9)$$

Modifications to these equations were incorporated by using the non-linear pressure-diameter relationship, given in (7.2). For the current implementation we have used a modelled triangular Q waveform, specific for each subject. The start of the triangle was kept at the foot of pulse, the peak at inflection point (denoting the peak flow), and the end of triangle at the dicrotic notch. The proximal and distal diameter cycles were scaled to a pseudo-pressure waveform choosing an optimal $\beta = 5$ and $P_D = 90$ mmHg. The obtained P and Q waveforms for the proximal and distal site are shown in the first column Figure 7.7(a). The separated backward and forward pulses are also shown in the same figure (second column). Once separated the forward and backward pressures cycles were back-scaled to diameter cycles with the same β and P_D. It may be observed from Figure 7.7(b), that the systolic rise segments of the normalised proximal-distal

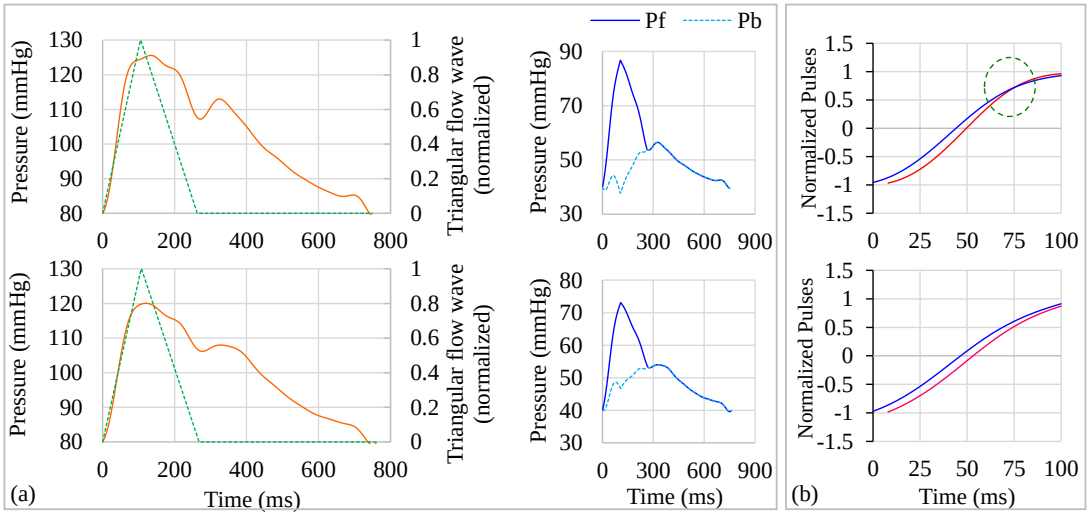

Figure 7.7 (a) Model obtained pressure (in orange) and normalized flow velocity (in green) waveforms (first column) used to separate the forward and backward pressure pulses – P_f and P_b (second column). (b) Upper row illustration showing a crossing between the proximal and distal pulses due to the influence of wave reflections and bottom row clearly manifesting that the forward separated pulses are devoid of the crossing, which makes them suitable for evaluation of the incremental PWV

diameter waveforms cross each other due the effect of reflections causing an abnormal negative PTT at systolic peak. However, post reflection elimination the effect and reflections reduce and proximal-distal diameter waveforms don't exhibit a crossing allowing for reliable PTT evaluation Figure 7.7(b).

Our earlier database of 473 subjects, (Voluntary Health Services study, proposal number: VHS-IEC/17-2016) were used to find an average value of β and P_D, which were used as the optimal values for the method. We have also tested the influence β and P_D choice for the method, by varying them over a range of (2 to 15) and (40 to 120 mmHg). As shown in Figure 7.8(a) the anacrotic phase which is region of interest for incremental PWV measurement is negligibly affected. Even in the extremes of β and P_D, the PWV was affected by only 4%. This justifies the optimal choice for these parameters in the WSA. Figure 7.8(b) and (c) show the functionality of the method,

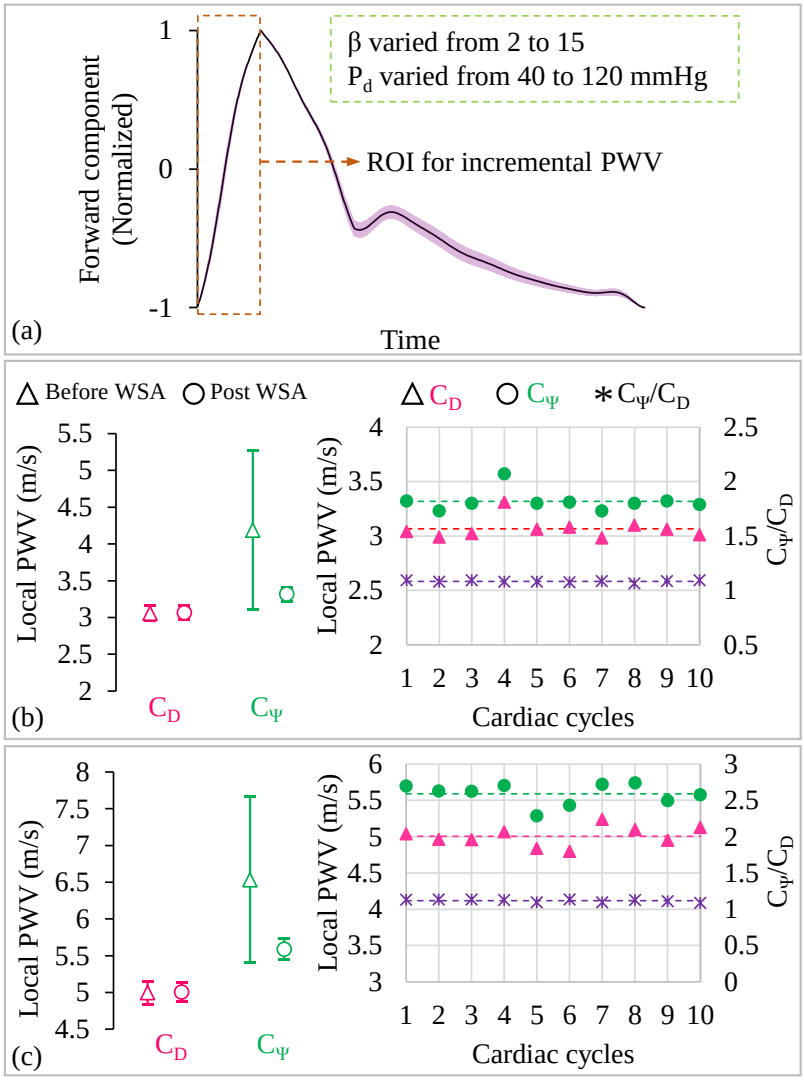

Figure 7.8 (a) Influence of β and P_D choice on the estimated forward pulse, which would also effect the estimated PWVs. The functionality of the method on (b) normotensive subject and (c) normotensive subject; the left column shows the variability in the beat-to-beat PWV measurements from diastolic and systolic phases before and after the WSA, and the right column shows the beat-to-beat repeatability of these measurement post WSA for 10 consecutive fiducial points

when applied to the data of a normal and a hypertensive subject, respectively. Variability in beat-to-beat PWV measurements (at end-diastolic and peak-systolic) before and after wave-reflection elimination are shown in the figure. For these subjects the beat-to-beat PWV (diastole and systole) is illustrated in Figure 7.8(b) and (c), indicating measurement repeatability. It is also evident that the systolic PWV is higher

than that of the diastolic, and also the differences between them is repeatable across multiple cardiac cycles. The WSA technique showcased expected functionality for the measurement of incremental PWV.

7.3.2 In-vivo pilot trials

To demonstrate the ability of the developed system for direct measurement of incremental PWV, we have used the LBNP study cohort, mentioned in section 7.1.4. It provided the opportunity to also demonstrate the feasibility of measuring the dynamics of the intra-beat PWV changes with perturbing BP. The LBNP intervention was intended only to provide a variable range of BP which could be adequately achieved within a short span of intervention with negligible motion and breathing artefacts. Therefore, the participants were not studied until the onset of pre-syncopal symptoms.

7.3.3 Study results: Direct measurement of Intra-beat PWV changes

Figure 7.9(a) shows a sample plot of incremental PWV against the arterial distension for multiple cardiac cycles measured during the baseline phase, from subject (#4). The changes in arterial distension within cardiac cycles are due to the changes in pressure, and these curves manifest the pressure dependence of local PWV within a cardiac cycle. Similar trend was evident in all subjects in each of the trials. The box and whisker plots of C_D and C_F pooled for all subjects, are shown in Figure 7.9(b). A significant ($p < 0.001$) difference existed between these measures, with group average $C_F = 4.21 \pm 1.02$ m/s versus that of $C_D = 3.92 \pm 0.82$ m/s. The mean beat-to-beat variation in the C_D and C_F measurements performed during baseline phase were 5.2 ± 1.9 %, and 6.4 ± 2.5 %, respectively. With the instantaneously perturbing BP due to the intervention, both the

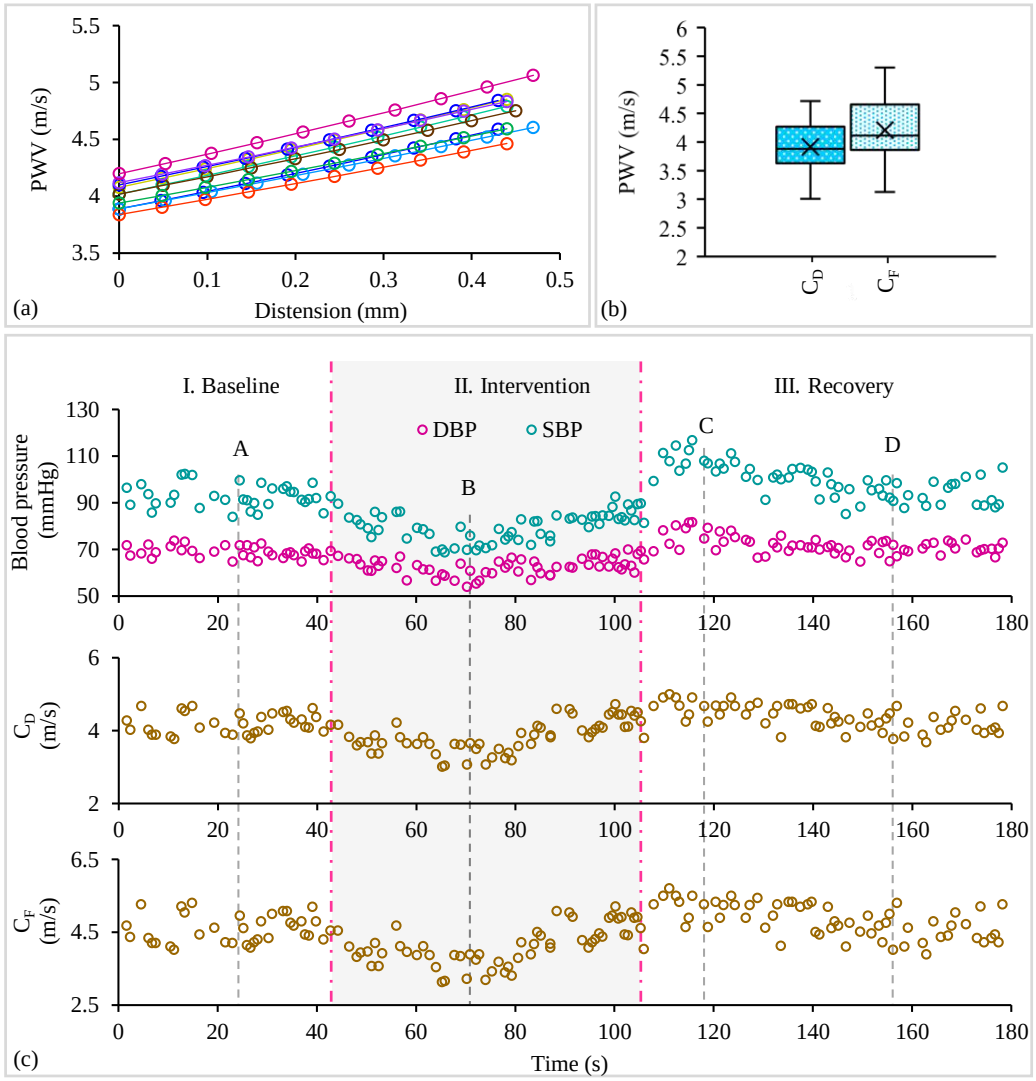

Figure 7.9 (a) Sample beat-to-beat incremental PWV curves for a subject (#4) during baseline phase. (b) Box and Whisker plot for the recruited population showing the difference in diastolic and systolic PWV. (c) Tracked beat-to-beat to variation is diastolic and systolic PWVs during the hemodynamics variations induced by LBNP, for subject #4.

systolic and diastolic PWVs varied following the BP trends, as shown in Figure 7.9(c). Also, the regression plots between the measured beat-to-beat local PWV, C_D and C_F, each with respect to reference DBP_R and SBP_R are plotted in Figure 7.10(a). The correlation coefficient was $r = 0.69$ ($p < 0.001$) for both C_D versus DBP_R and C_F versus DBP_R. Similarly, the correlation coefficients for C_D versus SBP_R and C_F versus SBP_R were $r = 0.68$ ($p < 0.001$) and $r = 0.67$ ($p < 0.001$), respectively. Further, the partial

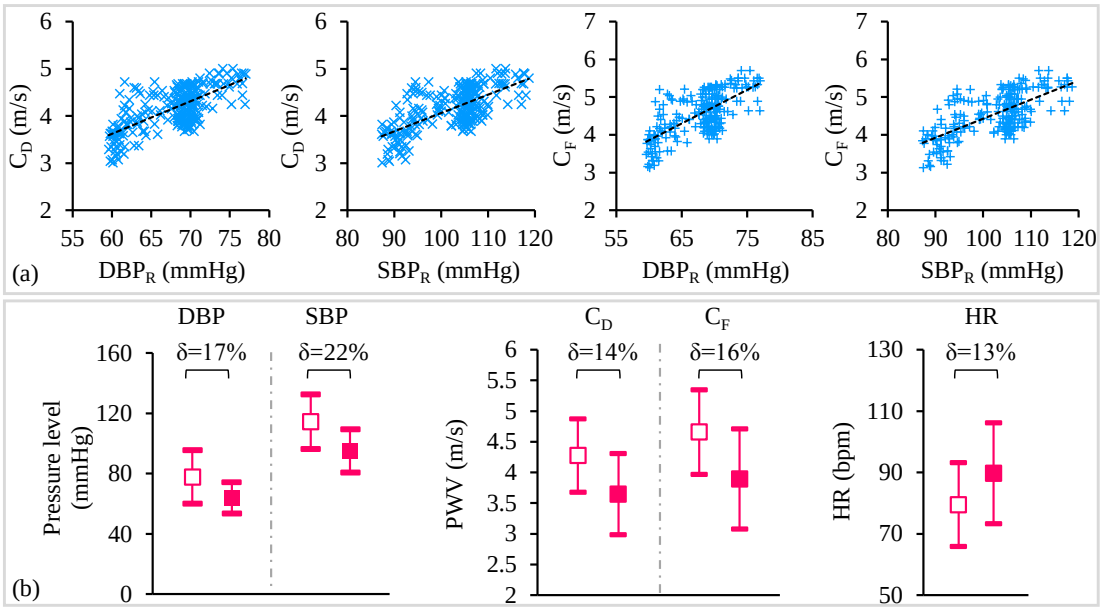

Figure 7.10 (a) Regression plots between pressure (both diastolic and systolic) and estimated local PWVs (both diastolic and systolic). (b) Baseline-to-intervention phase changes in diastolic and systolic BP and local PWV.

correlation coefficients upon controlling for HR was $r_{par} = 0.63$ ($p < 0.001$) for both C_D versus DBP_R and C_F versus DBP_R, and was $r_{par} = 0.61$ ($p < 0.001$) for both C_F versus SBP_R and C_F versus SBP_R. Similar correlations were observed for all the recruited subjects with *r*-value greater than 0.60 ($p < 0.001$). One interesting outcome was that the SBP drop due to intervention was higher than DBP, 22% versus 17%. Consequently, as shown in Figure 7.10(b), the magnitude in drop in C_F was greater relative to C_D, 16% (0.76 m/s) versus 14% (0.61 m/s). The device demonstrated its functionality and reliably measured the incremental nature of PWV. Its pressure-dependent intra-beat variations and inter-beat dynamics during the intervention concurred with literature.

7.4 DISCUSSIONS

We have presented the feasibility of capturing pressure associated changes in local PWV, both inter- and intra-beat, *in vivo*. We have identified the independent

methodological considerations and challenges pertaining to the evaluation methods for such PWV variations, and addressed them for reliable estimates. Firstly, the conducted study (section 7.1.5) on direct measurement of inter-beat local PWV variations revealed the ability of the developed system to capture them for both pressure lowering and elevating hemodynamic perturbations. The beat-to-beat variation in PWV manifested trends similar to that observed for the pressure profile, on all the subjects. More specifically, during thread-mill exercise elevated BP caused carotid PWV to elevate, and during a -40 mmHg LBNP intervention both the BP and PWV dropped concomitantly. Secondly, the measurement of intra-beat local PWV variations was demonstrated, performed by indirect means employing multimodal feature of the developed system. The importance of incorporating viscoelastic modelling into BH-equation implementation was underlined, which contributed to yielding of reliable PD-curves for incremental PWV evaluation. Finally, the feasibility of assessing the intra-beat local PWV via. direct means was presented. These measurements were performed, adopting a novel approach, on the forward moving components of the pulse waves. They were obtained using a wave separation analysis technique, which made the measurement of PWV variations possible. For both direct and indirect measurement approaches, the PWV was seen increasing from end-diastolic to peak-systolic phase within the cycle, concordant to the mechanical behavior of the hyper-elastic arterial walls. One unique aspect of the last study results was that the system demonstrated the ability of measuring both the inter- and intra-beat changes in PWV simultaneously employing direct means.

Measurement of inter-beat variations in local PWV requires the instrumentation to yield real-time. Processing ultrasound data for diameter/flow pulses, especially two-

dimensional, increases computation. So, unless specialized hardware with high processing power is employed it is challenging to perform real-time measurements. As discussed in Chapter 5 (section 5.7) real-time systems provide biggest advantage of online feedback, which is necessary to avoid operator bias and also, provides the opportunity for correcting the transducers position for high quality acquisition amidst the measurement procedure if required. Such provisions greatly improve the measurement, if beat-to-beat/continuous recordings are of interest. We have shown again in Chapter 5 that the evaluation of local PWV based on BH-formulation is popular as it theoretically related to the distensibility, however if measured from central arteries poses a challenge of reliable non-invasive central pressure recording. Such a challenge poses even of more concern when beat-to-beat PWV measurements are required. As picking up carotid pressure perturbations from tonometer is highly advised against (O'Rourke, 2016), due to the variations in hold-down pressure. In such scenarios the initial calibration doesn't hold throughout and the pressure values are compromised. Direct measurement, rather than estimation, of local PWV is hence a reliable alternative, the methodological requirements of which were already addressed by the developed system.

The measurement of instantaneous PWV changes, especially within each cardiac cycle, is challenging. In fact, the non-invasive measurement of incremental PWV has attracted the interest of investigators only in recent years, and its clinical importance is still emerging. Studies have demonstrated the pathological significance of measuring both the systolic and diastolic PWVs in diagnosing Ehlers–Danlos syndrome (Mirault et al., 2015), increased left ventricular mass index (Hermeling et al., 2012), hypertension and cardiovascular risks (X. Li et al., 2017), and microangiopathy in patients with type 2

diabetes mellitus (An et al., 2022). Our group has also developed mathematical models for calibration-free central BP evaluation using measured diastolic-to-systolic changes in local PWV (Nabeel et al., 2018), which emphasizes the scope of this measure above and beyond local PWV from a single fiducial point. Only a few studies have estimated the incremental PWV using theoretical means, and fewer have directly measured it (An et al., 2022; Hermeling et al., 2012; X. Li et al., 2017; Mirault et al., 2015; Nabeel et al., 2018; Yin et al., 2021).

Since indirect means of measuring intra-beat PWV variation adopts theoretical mechanical equations using single site pressure and diameter waveforms, their recording reliability is at most important. Using the developed multimodal probe, the measurement system was capable of recorded high-fidelity diameter and pressure signals for continuous cardiac cycles from all the recruited subjects (section 7.2.5). The real-time visual feedback provided by the GUI assisted the operator to ensure the signal fidelity. The quality of signals acquired and the PD-loops constructed were adequate for reliable calculation. Since the separation distance between the transducers was very less, the signal processing was identical and the simultaneous acquisition of P and D was synchronized using a trigger signal, the lag between the signals was observed to be negligible. The source of corrupting innate time lag can be attributed to several factors.

One potential source originates from recording the desired signal pair in a sequential manner. Traditionally, such separately recorded signals are analyzed offline, and the onset of the individual waveform cycles are aligned by visual inspection. This is typically performed by arranging the signal pair with respect to the reference ECG or adjusting the signals for the feet of cardiac cycles to coincide (Borlotti et al., 2012; Khir,

O’Brien, Gibbs, & Parker, 2001). Note that it is important to perform short-time sequential recordings of the respective hemodynamic parameter so as to assume insignificant alterations within the recording time securely. Given this, simultaneous recording of the desired signal pair is strongly recommended for online local PWV evaluation. Moreover, the use of different modalities (including transducers, recording system, and signal processing front-end) to record the pair of signals could introduce substantial time lags, primarily due to the mismatch in their frequency responses (Arnold P.G. Hoeks et al., 2000; Swalen & Khir, 2009). The measurement modalities should, therefore, be appropriately chosen to ensure a negligible difference in the frequency response. Wherever applicable, a unimodal measurement system is preferable. Simultaneous measurement of the desired hemodynamic signal pair from a single site in the target artery is always challenging due to the form-factor of commercially available transducers. Any positional offset (even in the order of few millimeters) between the measurement sites could potentially introduce further time lag. A smaller form-factor and optimized designs for the transducers, as shown in this work, can effectively minimize the position offset. Lastly, the filters required for smoothening of the signals may also shift their phase considerably; this effect is worse for the lower cutoff frequencies (Arnold P.G. Hoeks et al., 2000; Stein Inge Rabben et al., 2004). Therefore, the incorporation of efficient time synchronization algorithms is essential to compensate for the effective time lags between the signal pair. One such possible method to perform automated correction of the potential time lags in the signal pair based on the highest correlation factor between the signals was introduced (Swalen & Khir, 2009). In this work, the enlisted considerations were directly addressed, which included: (i) design of frequency matched acquisition of pressure and diameter, (ii) zero

inter-channel delay (iii) small form-factor design for probe, (iv) identical signal processing blocks, and (v) simultaneous recording.

Even with eliminating the potential sources of lags, there was a hysteresis between P and D for all the recruited subjects. The literature on BH-equation based PWV velocity methods indicate use of linear fit models on the P-D hysteresis loop assuming a linear relationship between P and D (S. Miyashita et al., 2015). Such an assumption would result in a constant PWV, that is independent of the systolic to diastolic changes variations in pressure. While attempts have also been made to fit non-linear models relating P and D on the obtained P-D loop, the key limitation was that the nonlinear model curves were fitted directly onto the hysteresis loop (Graf, Craiem, Barra, & Armentano, 2011). Further the study (Graf et al., 2011), did not report the variations in local PWV, but only the value at the minimum diastolic pressure. Our work, on the contrary, describes incorporation of Voigt type viscoelastic model for removal of the hysteresis to achieve a more reliable fit for measurement of $PWV_{(P)}$. As an added benefit, the system performed measurement of arterial viscoelastic properties as well, the ranges of which were observed to be distinguishable for normo- and hypertensives. Another important factor that concerns the uncertainties introduced by the indirect estimation is the accuracy of calibrated central pressures acquired using the tonometer. Tonometeric central BP measurements (taken from carotid site) require extensive skill and also their reliability is questioned in the literature owing to lack of an anatomical support to applanate the carotid artery (O'Rourke, 2016). This will influence the accuracy of PWV estimates as they are directly dependent on the magnitude of the pressure pulse. The challenge increase when there are acute pressure changes, where the calibration may be compromised. The beat-to-beat pressure parameters

measurement is also susceptible to the hold down pressure, which requires to be extremely stable for reliability.

Having a unimodal alternative and direct means of measuring these intra-beat PWV changes removes the above alluded hassles. As it is now recognised that indirect PWV estimation method poses a constraint on measuring the inter-beat changes in PWV as well, a direct method would then be extremely useful to assessing both inter- and intra-beat PWV changes simultaneously, or rather inter-beat changes in intra-beat PWV variations. Our group has earlier proposed a mathematical model to deduce central BP in a completely calibration free manner by measuring the incremental PWV. Therefore, for such an application it may be relevant to yield information of instantaneous perturbations in incremental PWV, by which the acute changes in central BP can be tracked. In fact, our results in the final study of this chapter have manifested that the system, by applying direct measurement approach, has reliably tracked not only the incremental PWV within the cardiac cycle, but also its acute variations across time during a -40 mmHg LBNP intervention. From Figure 7.9, as the diastolic and systolic BP were changing, carotid PWV from end-diastolic and peak-systolic phases also changed over the course of intervention. However, it is also evident that end-diastolic PWV was smaller in magnitude compared to peak-systolic measure, throughout. Wave-reflections as highlighted are a usual concern when applying transit time method for direct PWV evaluation, more if incremental PWV has be calculated as systolic phase gets corrupted. This chapter presented a scheme where triangular wave-separation technique was used to extract the forward moving components of proximal and distal distension cycles, over which the PTT and PWV calculations were performed. WSA requires pressure or diameter waveforms along with flow waveforms simultaneously.

Several techniques were employed in the literature for modelling the flow waveforms, based on contour features of the pressure wave, to deal with the practical challenges associated with realizing reliable multimodal systems. One of the simplest approaches was triangular modelling of flow waveform, which was applied to recordings obtain from aorta (B. E. Westerhof, Guelen, Westerhof, Karemaker, & Avolio, 2006). Though the method needs pressure waveform as input, we have demonstrated a technique to perform the same on diameter waveform from carotid artery. It may be remembered that in this work, the technique was only demonstrated for the reliability of incremental PWV evaluation that is dependent on the morphology of the forward moving waves. However, the method may not be generally employable for applications that are dependent on the magnitude, rather than just the morphology, of the separated pulse waves. In our investigations, it was observed that the carotid PWV obtained from the peak-systole, that is likely to be corrupted severely, improved in its repeatability after the applying WSA. This was because, before WSA the pulses had a crossing over in late systolic phase over several cardiac cycles, giving rise to anomalous peak systolic PWV for them. After application of WSA the proximal-distal diameter waveforms didn't exhibit a crossing allowing for reliable late systolic phase PTT. It was clearly evidenced that the variability in end-diastolic PWV measures were comparable before and after the WSA but a substantial improvement in peak-systolic measures were observed after applying the proposed WSA scheme.

7.5 LIMITATION AND FUTURE WORK

Though the studies in this chapter have adequately demonstrated the feasibility of performing the *in vivo* measurement of instantaneous local PWV variations, within and

across the cardiac cycles, there were a few limitations. The sample size for the studies were smaller. However, since the pressure and associated local PWV perturbations were of interest, such a size was sufficient. Even in the literature, pilot studies incurring hemodynamic perturbation reported similar cohorts. Previous chapter established the accuracy of the developed system in measuring local PWV from single fiduciary point. However, incremental PWV evaluation involves obtaining values from multiple fiducial points with the cardiac cycle. In this regard on major study limitation concerns the accuracy validation of the non-invasive incremental PWV measuring methods, both direct and indirect. This a practical limitation, as currently there lacks a gold standard non-invasive device for pertinent validation. Studies on large animal models (as porcine and ovine) and *in vitro* are underway, where such validations can be performed against invasive reference. Further, usability and reliability of the incremental PWV evaluation method and instrumentation is required to be assessed on a larger cohort in clinical settings, both controls and diseased.

7.6 CONCLUSIONS

The work in this chapter demonstrated that the developed fast A-mode ultrasound system could reliably measure the inter- and intra-beat variations in local PWV by both direct and indirect means, the latter exploiting the multimodal acquisition provision. Though BH equation theoretically related PWV and distensibility, it was challenging to apply it for measuring the inter-beat variations in local PWV. Whereas, it was possible to measure the intra-beat variations, while its applicability required addressing of viscous component elimination. Direct means, however, was more favourable alternative for measuring both the inter- and intra-beat variations simultaneously, which

was uniquely performed on forward propagating components extracted employing WSA. Such simultaneous measurement has the potential to serve several new avenues and in-fact the following chapter demonstrates one such application.

CHAPTER 8.

HIGH-FRAME-RATE A-SCAN ULTRASOUND FOR CAROTID PRESSURE: FEASIBILITY STUDY USING LBNP INTERVENTION

Existing technologies to measure central BP intrinsically depend on peripheral pressure or calibration models derived from it, as reviewed in Chapter 2 (section 2.5). Pharmacological or physiological interventions yielding different central and peripheral responses compromise the accuracy of such methods. In this chapter, we present unimodal calibration-free evaluation of BP from the carotid artery using the developed high-frame-rate ultrasound technology (refer Chapter 5). The evaluation method uses the intra-beat variations in diameter and local PWV, which are intrinsically pressure dependent, to avoid calibration of any sort, rather closed form mathematical equations. Previous chapters have concluded that system is able to directly measure these diametric and PWV variations within the cardiac reliably in a beat-to-beat manner. In this chapter, the ability of the system to capture dynamic responses of carotid pressure to LBNP was investigated and compared against the responses of peripheral pressure measured using a continuous BP monitor. The chapter discusses pertaining results in detail and emphasizes the system's advantage over the ones existing in the literature.

This chapter is partially adapted from the post-print version of:

Raj, K. V., Nabeel, P. M., Chandran, D., Sivaprakasam, M., & Joseph, J. (2022). High-frame-rate A-mode ultrasound for calibration-free cuffless carotid pressure: feasibility study using lower body negative pressure intervention. Blood Pressure, 31(1), 1–11.

8.1 CAROTID PRESSURE MEASUREMENT: THEORY

In the arteries, the transmural pressure (P) causes the changes in the lumen diameter, and the relation between them can be expressed exponentially (Hayashi et al., 1980). Further, the pressure also causes the blood pulse propagation speed to change non-linearly given the hyperplastic nature of the artery. Within each cardiac cycle, the parameters D_P and C_P increase as the pressure increases from end-diastole to peak-systole. Considering pressure estimation, known as '*P–β model*' (Nabeel et al., 2018, 2020), that combines the independent relationships of arterial pressure with diameter (Hayashi et al., 1980) and local PWV (Bramwell & Hill, 1922), respectively. This model is shown in (1), where the product of pressure P and specific stiffness of blood vessel β (Hayashi et al., 1980) is expressed in terms of pressure-dependent local PWV (C_P) and the pressure-dependent arterial diameter (D_P).

$$P\beta = 2\rho C_P^2 \frac{D_D}{D_P}. \tag{8.1}$$

Here, ρ is the blood mass density, and D_D is the end-diastolic diameter. In the equation, P, D_P, and C_P are the only parameters that vary within each cardiac cycle. Measuring D_P and C_P at two instances within one beat allows rewriting equation (1) into two with respective instant values. Hence, rearranging equation (1) in terms of PWV and diameter measures obtained from two independent phases of a cardiac cycle, i.e., from end-diastole (C_D and D_D) and neighborhood of peak-systole (C_F and D_F), β is evaluated,

$$\beta = \frac{\ln\left(\frac{C_F{}^2 D_D}{C_D{}^2 D_F}\right)}{\left(\frac{D_F}{D_D} - 1\right)}. \quad (8.2)$$

The end-diastolic point (D) is identified as the pulse cycle minimum occurring prior to the peak of the cycle. Similarly, the second derivative minimum post to D is identified as the point in the neighborhood of peak-systole (F). Using the estimated β, now DBP and SBP are evaluated as,

$$\mathrm{DBP} = \frac{2\rho C_D^2}{\beta} \quad (8.3)$$

$$\text{and } \mathrm{SBP} = \mathrm{DBP}\, e^{\beta\left(\Delta D/D_D\right)}, \quad (8.4)$$

where ΔD is the maximum distension during a cardiac cycle. The difference between the SBP and DBP yielded the PP. Further, the diameter cycles upon scaling with SBP and DBP are used for MAP. The method, therefore, uses the measured stiffness-related parameters C_D and C_F in addition to the dimensional parameters D_D, D_F, and ΔD to evaluate the pressure values in a calibration-free manner, which are directly measurable from the target central arteries using the developed system. Interested readers may find a detailed discussion on the mathematical model elsewhere (Nabeel et al., 2018, 2020).

8.2 CAROTID BP MEASUREMENT SYSTEM

The developed high-frame-rate ultrasound system incorporated two independent single-element transducers (center-frequency = 5 MHz, spatial half-angle < 1.3 degrees, diameter = 5 mm) that were operated in pulse-echo mode for the measurement of

required arterial dimensions and local PWV. The system is a portable one (dimensions = 280 mm × 200 mm × 80 mm and weight = 830 g) that could be connected to a computer via USB 2.0. The raw A-mode RF signals (acquired at frame rate = 500 Hz and sampling rate = 80 MHz) from the two transducers were processed in real-time by custom software. Processing included RF signal conditioning, automated detection and continuous tracking of arterial walls, and evaluation of high-resolution diameter waveforms. The local PWV values were measured for two independent fiducial points within each cycle, i.e., end-diastolic (point D) and 80% of peak amplitude (point F) based on transit time calculated from the diameter waveforms pair. For avoiding corruption from arterial wave reflections (Nabeel et al., 2020), PWV needed to be measured on the forward-moving pulses, and for this purpose, a frequency domain forward wave separation method was employed using a triangular blood flow velocity model (Qasem & Avolio, 2008). The diameter waveforms were further used to evaluate ΔD and to extract the corresponding diameter values from the points D and F.

The measured diameter parameters and incremental local PWV (D_D, D_F, ΔD, C_D, and C_F), were used to evaluate the carotid systolic pressure (SBP_{CAR}), diastolic pressure (DBP_{CAR}) and pulse pressure (PP_{CAR}) using the P-Beta model described in equation (1) – (4). The arterial diameter cycle waveforms were scaled between the calculated DBP_{CAR} and SBP_{CAR} to estimate the carotid pressure waveform, and the mean of the cycle was computed to yield the mean arterial pressure (MAP_{CAR}). Finally, the dynamic heart rate (HR) was also evaluated by measuring the cycle intervals. Since the measurement reliability intrinsically depended on the fidelity of diameter waveforms, or more specifically, the RF frames from which these waveforms were derived, a signal

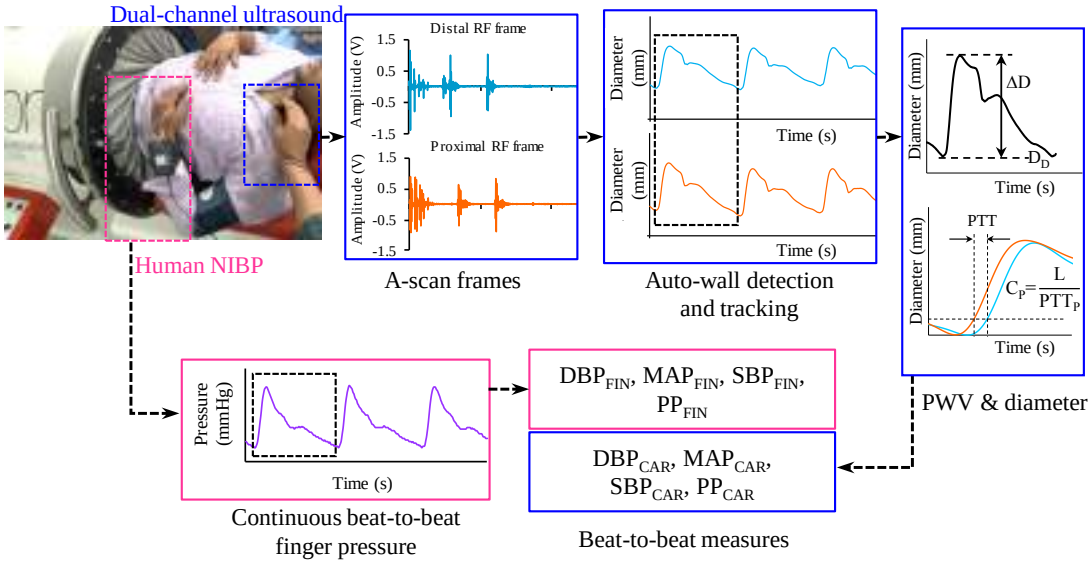

Figure 8.1 Schematic of the measurement procedure during the LBNP intervention study, illustrating the acquisition of simultaneous A-mode ultrasound data from the two proximal locations at carotid and continuous peripheral waveforms from finger employed for the evaluation or beat-to-beat pressure measurements from carotid artery and finger.

quality (SQ) check algorithm was employed (Joseph et al., 2020). The evaluated SQ scores along with the live recording of the RF frames were displayed on the screen providing the operators the opportunity to correct the orientation for achieving high-quality scans. These scores representing the quality of arterial walls were also the basis for screening the beat-to-beat measurements so that only the good quality beats were used for the final BP measurements. The automated framework for detection and tracking arterial walls, SQ quantification, cycle cutting and screening, and finally, the visual feedback on the recording quality minimizes the operator-dependent variability. The measurement scheme is present in Figure 8.1.

8.3 CONTINUOUS PERIPHERAL BP FOR COMPARATIVE STUDY

A commercial NIBP system (Human NIBP Nano, ADInstruments South Asia, India) used with appropriate finger-cuff provided the measures of continuous peripheral

pressure values. The parent technology Finapres (FMS), and its calibration algorithm 'Physiocal', have been validated and used as a reference in literature (Imholz, Wieling, Van Montfrans, & Wesseling, 1998; Rastegar et al., 2019). The equipment also employed a hydrostatic pressure sensory unit for offset adjustment. Since these measurements were from the peripheral artery (finger) and are available in beat-by-beat, they were used to compare the dynamic response of the evaluated carotid pressure to LBNP. Finger pressure cycles, aligned with the measured diameter cycles, yielded the corresponding beat's diastolic (DBP_{FIN}), systolic (SBP_{FIN}), and mean arterial (MAP_{FIN}) pressures. Only the diastolic and mean arterial pressure measurements can be directly compared for measurement uncertainty, as in the supine posture, they are found to be relatively constant across the arterial tree (H. M. Cheng et al., 2020), devoid of hydrostatic offset. On the other hand, systolic pressure varies traversing from central to peripheral arteries as a result of pulse pressure amplification (H. M. Cheng et al., 2020). This restricts a direct comparison of the SBP_{CAR} against SBP_{FIN} for the accuracy analysis.

8.4 IN-VIVO STUDY DESIGN

8.4.1 Study objectives

The preliminary study objectives were (i) to evaluate the continuous carotid pressures (DBP_{CAR}, MAP_{CAR}, and SBP_{CAR}), and investigate their dynamic response to a short-term moderate LBNP intervention, (ii) to compare and verify the LBNP response in carotid pressure against that of the continuous peripheral (finger) pressure, and (iii) to assess the accuracy of the DBP_{CAR} and MAP_{CAR}, by comparing them against the corresponding measurements obtained from the finger (DBP_{FIN} and MAP_{FIN}) in supine.

8.4.2 Subjects

Young and healthy male subjects were selected that were devoid of cardiovascular risk symptoms (such as hyper/hypotension or autonomic nervous dysfunction) and were not on any medication known to alter autonomic nervous function. This was to ensure appropriate hemodynamic response and adequate tolerance to the orthostatic interventions. The volunteers' response to the LBNP intervention was assessed initially to verify if the intervention could yield at least a 10-mmHg perturbation in the finger DBP. This was necessary for functionality assessment, as the intervention was intended to serve as a source for dynamic pressure profile and yield a range perturbation in BP values. The subjects whose data revealed modest DBP changes due to the intervention (baseline-to-intervention < 10 mmHg) were rejected. Data that formed the part of analysis was collected from 8 out of 10 normotensive subjects (mean SBP = 115.5 ± 7.1 mmHg, DBP = 77.5 ± 8.2 mmHg, and MAP = 90.1 ± 7.5 mmHg). The mean age of the subjects was 26 ± 4 years, with height = 171 ± 12 cm, weight = 73.1 ± 18.6 kg, and BMI = 24.9 ± 5.1 kg/m^2.

8.4.3 Experimental procedure

The experimental procedure was performed in a temperature-controlled room (~23°C). Investigations were scheduled from 9 A.M. and then 2 P.M., after standard intake of a meal without any caffeinated beverages. The entire measurement scheme is shown in Figure 8.1. The subject was positioned horizontally in supine posture in an LBNP chamber (VACUSPORT® - Regeneration system, Weyergans High Care® Medical, Germany) up to the level of the iliac crest and was allowed to rest for 10-15 minutes. The baseline blood pressure was measured using an automatic BP device (HEM-8712,

Omron Healthcare, Japan) and a D-ring type arm cuff. NIBP system was then instrumented onto the subject for the measurement of continuous peripheral BP from the finger. The left common carotid artery was identified by palpation, and the developed dual-element ultrasound probe was positioned at the identified site. The probe was oriented to yield the best quality RF signals with strong wall echoes from both the proximal and distal sites. Baseline measurements from NIBP and the proposed devices were performed for 30-50 seconds. LBNP (–40 mmHg) was then applied as this level of stimulus is known to incur considerable changes in the MAP (Goswami, Blaber, Hinghofer-Szalkay, & Convertino, 2019). Most of the cardiovascular events are seen occurring within 3 minutes (Goswami, Loeppky, & Hinghofer-szalkay, 2008), during which the BP perturbs in the beginning and then is corrected by compensatory reflexes. Therefore, the length of the intervention was kept as 1 minute where the instantaneous BP changes are likely to occur, and the measurement was continued. Finally, upon the withdrawal of intervention, the measurements were continually collected for another 30-50 seconds (recovery phase). In this pilot study, the LBNP intervention was intended only to provide a variable range of BP, which could be adequately achieved within a short span of intervention (Goswami et al., 2019) with negligible motion and breathing artefacts. Therefore, the participants were not studied under acute LBNP intervention, such as until the onset of pre-syncopal symptoms.

8.5 IN-VIVO STUDY RESULTS

8.5.1 Fidelity of measured signals and parameters

The SNR of the acquired high-speed A-mode frames was greater than 25 dB during all the phases – baseline, intervention, and recovery. The fidelity of the diameter cycles

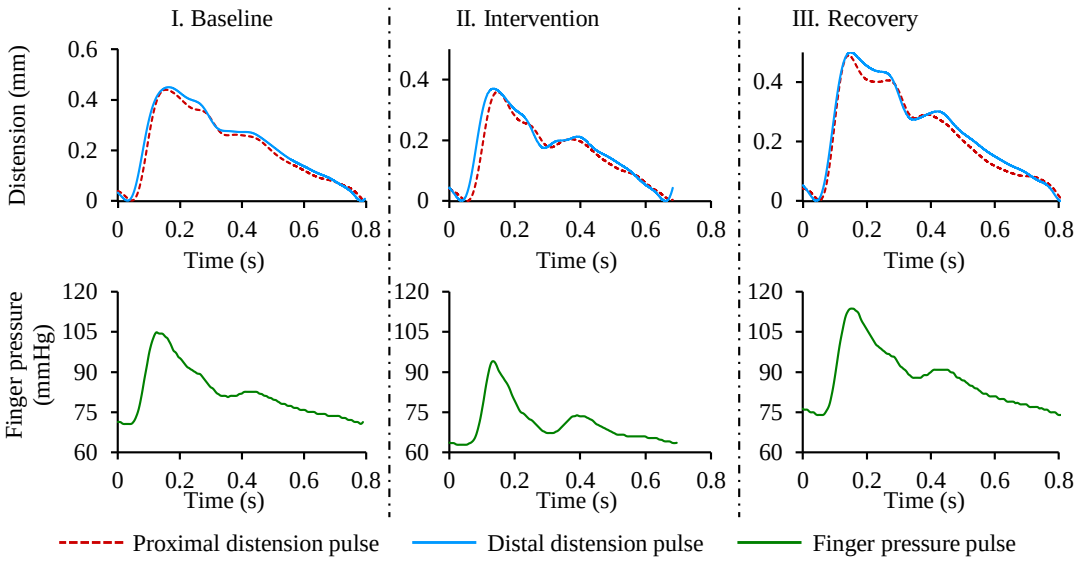

Figure 8.2 Sample proximal and distal distension pair and finger pressure pulse cycles recorded during different phases of the experiment on a subject, baseline (left column), mid of intervention (center column) and the beginning of recovery post intervention (right column).

measured from both proximal and distal carotid sites was adequate for the reliable evaluation of D_D, ΔD, C_D, and C_F. Similarly, high-quality finger BP cycles could be recorded for all the participants. In Figure 8.2, representative examples of the signals recorded from subject #4 (age = 28 years, height = 168 cm, weight = 62 kg, BMI = 22 kg/m^2) during baseline, intervention and recovery (immediate to intervention withdrawal) phases. The D_D measurements were in the range of 5.6 mm to 7.3 mm, with a mean value 6.28 ± 0.72 mm. Similarly, the measured ΔD values were within 0.30 to 0.65 mm, with a mean value 0.45 ± 0.12 mm. The measured PWV values, collectively, were within the range of 3 to 5.5 m/s. A significant ($p < 0.001$) difference existed between C_F and C_D, with group average C_F = 4.21 ± 1.02 m/s versus that of C_D = 3.92 ± 0.82 m/s. The mean variation in the D_D, ΔD, C_D and C_F measurements performed during baseline phase were 2.6 ± 0.60 %, 2.59 ± 0.62 %, 5.2 ± 1.9 %, and 6.4 ± 2.5 %, respectively.

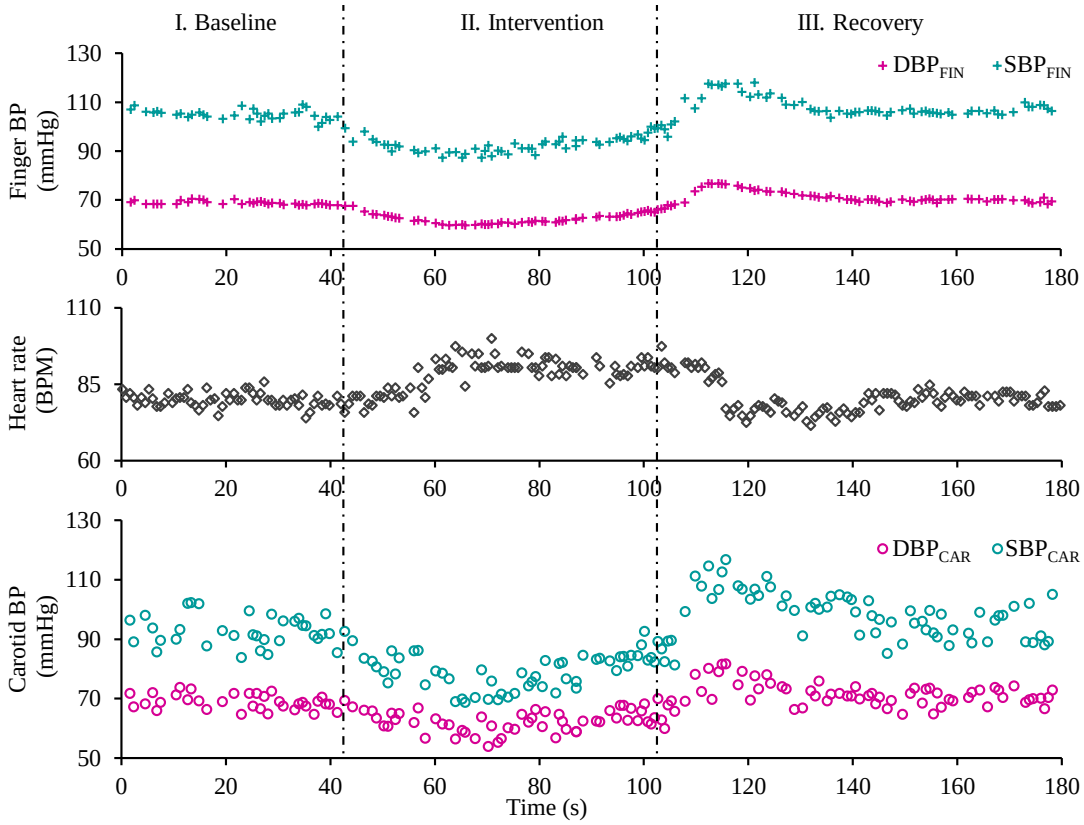

Figure 8.3 Beat-to-beat measures during the entire course of experiment on a particular subject (#4), indicating the dynamic changes (time synchronized) incurred in the finger DBP and SBP (top row), heart rate (middle row), and carotid DBP and SBP in response to the intervention.

8.5.2 Response of measured carotid BP to LBNP

Figure 8.3 illustrates the sample beat-to-beat measures of finger BP, heart rate (HR), and carotid BP measured for the subject (#4), indicating their absolute values and variations as a hemodynamic response to the LBNP intervention. The mean variation in the DBP_{CAR}, SBP_{CAR}, and MAP_{CAR} measurements performed during the baseline phase were 3.9 ± 2.1 %, 4.4 ± 2.2 %, and 4.0 ± 1.9 %, respectively. The trends in measured carotid BP followed the instantaneous variations in the finger BP, demonstrating a reliable tracking process. For all the recruited subjects, the changes in the finger and carotid pressures across various phases of the experimental time course (M1: baseline, M2: minimum value during Intervention, M3: immediate post-

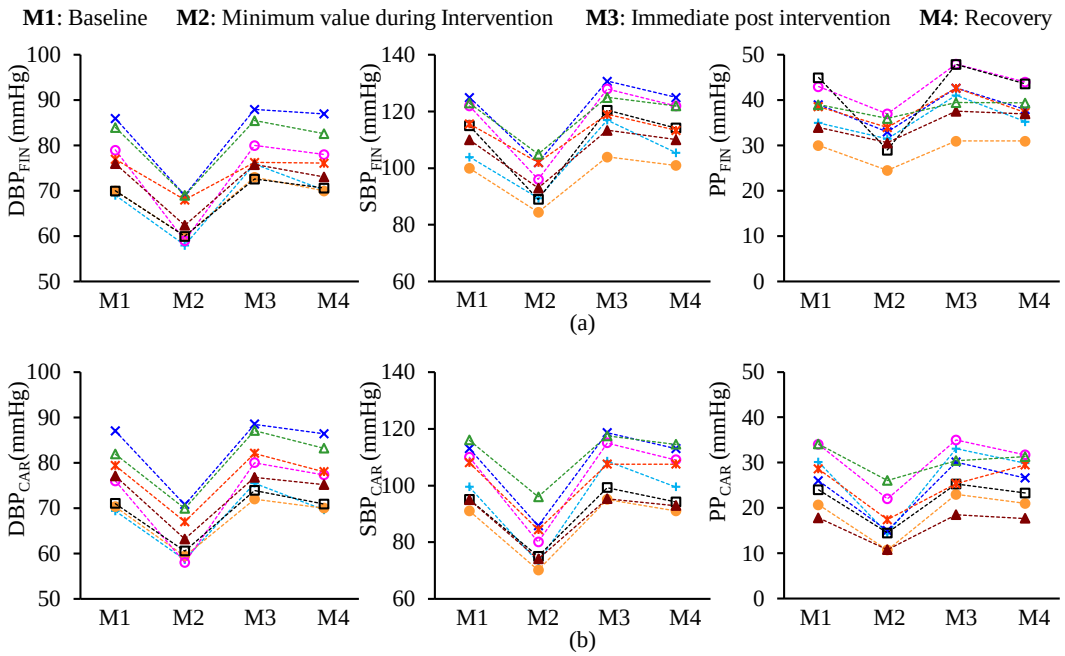

Figure 8.4 Pressure measurements (DBP, SBP, and PP) of all the 8 subjects from (a) finger and (b) carotid, corresponding to various important phases (M1, M2, M3, and M4) of the experimental time course, that include baseline, the minimum value attained during intervention, the maximum value immediately to post intervention, and the recovery. (Each subject is represented by a distinct combination of symbol and color.)

intervention, and M4: recovery) are shown in Figure 8.4(a) and (b), respectively. In the figure, each subject's data is represented with a distinct combination of color and symbol. The exhibited measurements for both finger (Figure 8.4(a)) and carotid (Figure 8.4(b)) include DBP, SBP, and PP, respectively, across the columns.

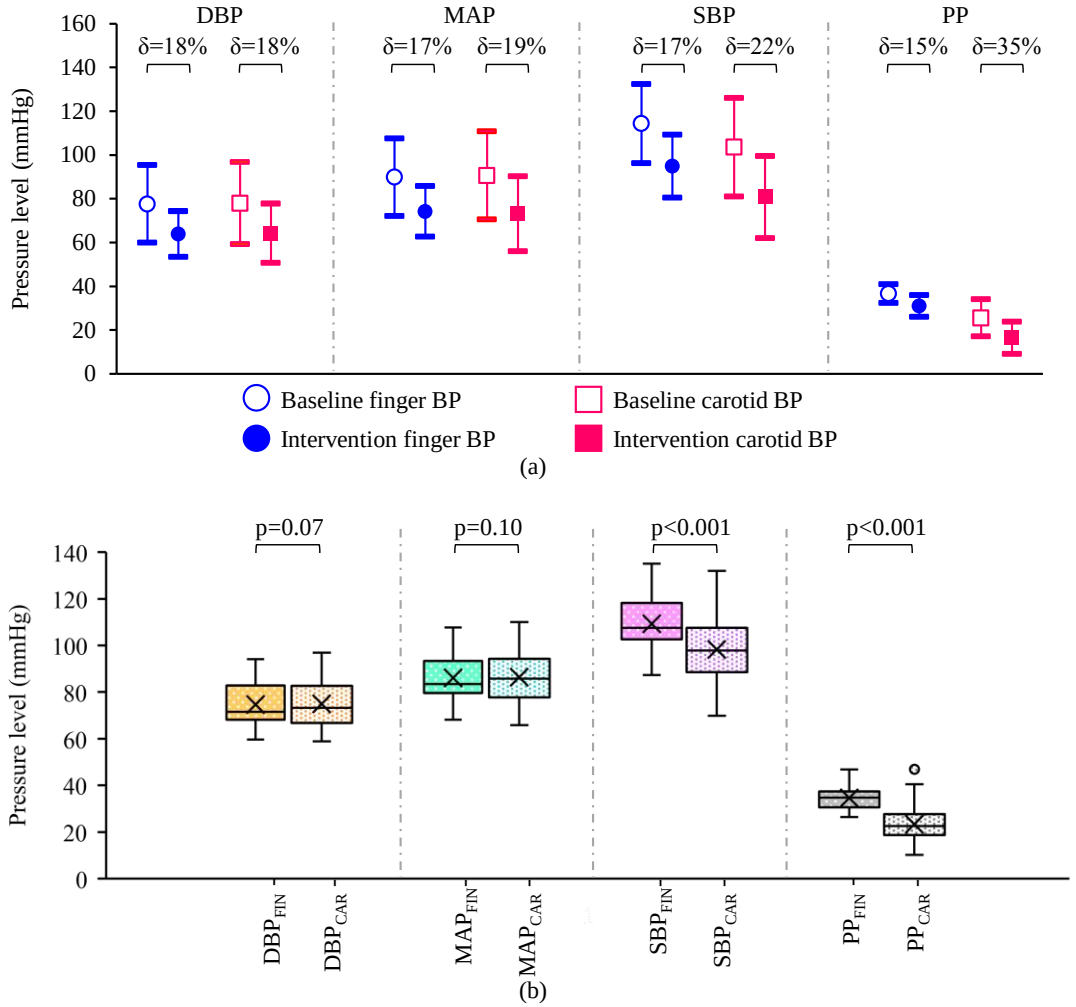

Figure 8.5 (a) Mean and deviation plot obtained for the measured and reference DBP, MAP, SBP, and PP during the baseline versus intervention phase, indicating a differential central-to-peripheral pressure response to LBNP intervention. (b) Likewise, the box and whisker diagrams (indicating median and quartile ranges) for the measured versus reference DBP, MAP, SBP, and PP for the entire measurement time course from all the subjects, show the magnitude of difference between the central and peripheral pressures measured. SBP and PP plots indicate a significant pulse pressure amplification.

The mean and deviation plots obtained for the carotid and finger DBP, MAP, SBP, and PP from all the subjects during the baseline versus intervention phase are illustrated in Figure 8.5(a) to compare the effect of the intervention on the various finger versus carotid pressure parameters. The δ values indicating the %difference between the baseline and intervention measurements are shown in the respective plots (Figure

8.5(a)). The mean bias in DBP_{FIN}, MAP_{FIN}, SBP_{FIN}, and PP_{FIN} during baseline versus intervention phases was 13.8 mmHg, 15.6 mmHg, 19.4 mmHg, and 5.6 mmHg, respectively, all of which were statistically significant ($p < 0.001$). Similarly, the mean bias in DBP_{CAR}, MAP_{CAR}, SBP_{CAR}, and PP_{CAR} during baseline versus intervention phases were 13.7 mmHg, 17.5 mmHg, 22.8 mmHg, and 9.1 mmHg, respectively, all of which were statistically significant ($p < 0.001$).

The carotid-to-peripheral BP ratios were calculated for the baseline and intervention phases using the respective beats' carotid BP and the finger BP measures. For DBP and MAP measures, the respective carotid-to-peripheral ratios were similar, with a statistically non-significant difference ($p = 0.49$ and 0.20, respectively) for the baseline versus intervention phases, (1.00 ± 0.09) versus (1.01 ± 0.13) for DBP and (1.00 ± 0.09) versus (0.99 ± 0.10) for MAP. On the other hand, these ratios significantly decreased ($p < 0.001$) during intervention from (0.91 ± 0.10) to (0.85 ± 0.13) for SBP and (0.69 ± 0.22) to (0.53 ± 0.22) for PP, respectively.

8.5.3 Reliability of calibration-free carotid BP

Figure 8.5(b) shows the box and whisker plots (representing the median and interquartile ranges) of finger versus measured carotid BP parameters for the entire measurement time course from all the subjects pooled together. The DBP and MAP values measured by the proposed system significantly agreed ($p = 0.07$ and 0.10, respectively) with that by NIBP device from the peripheral site. As expected physiologically, the SBP and PP values measured by the proposed system significantly ($p < 0.001$) differed from the corresponding measures from the finger. The mean difference between the finger and carotid SBP was 11.1 ± 9.4 mmHg, likewise for PP

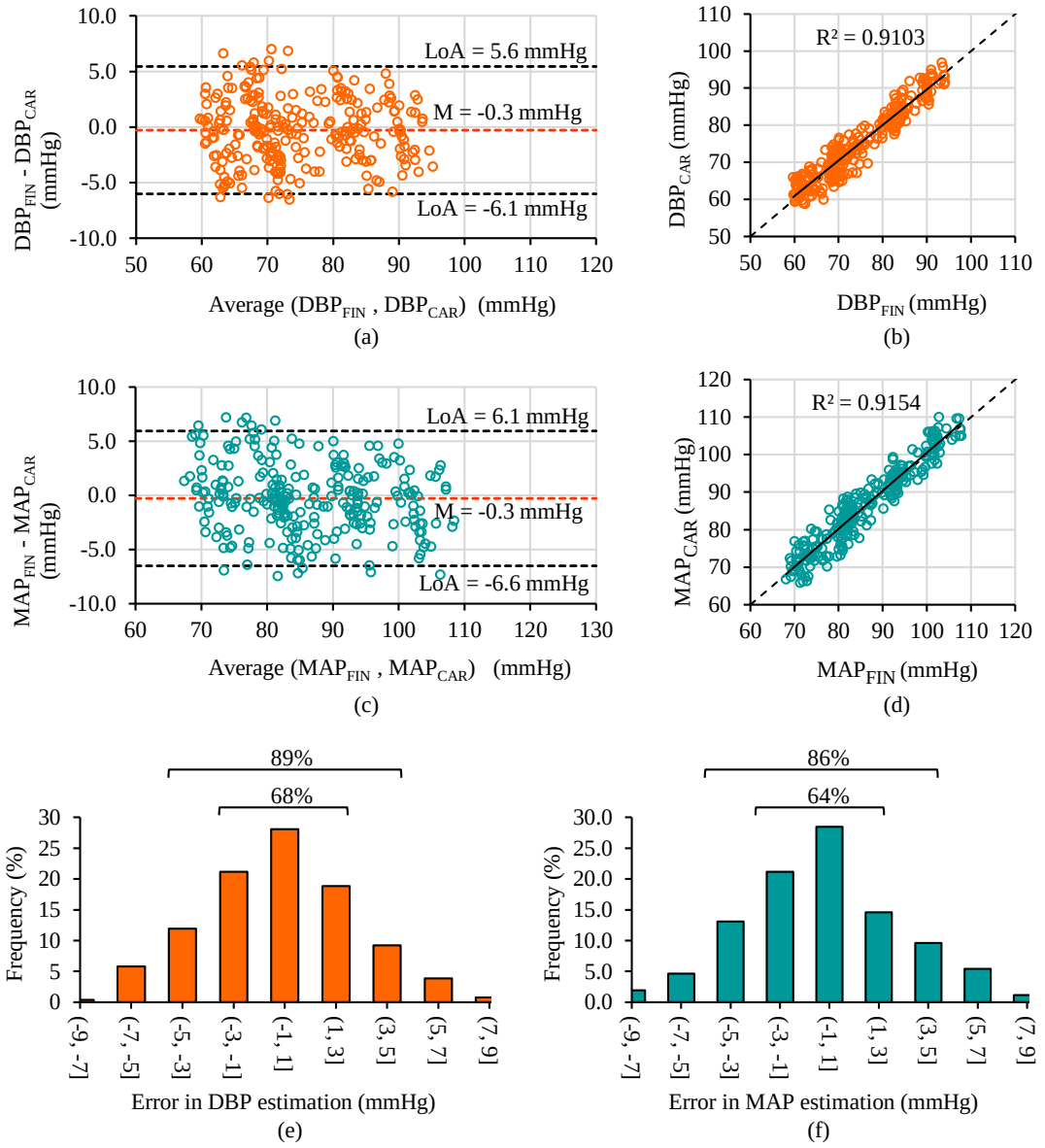

Figure 8.6 BA, regression and error histogram plots: (a), (b) and (e) respectively for the measured carotid DBP, and (c), (d) and (f) respectively for the measured carotid MAP, showing the accuracy performance of the presented method.

was 11.3 ± 8.2 mmHg. In supine posture DBP and MAP from the several arteries are consistent in magnitude, therefore, carotid and finger measures were compared for the baseline, intervention and recovery phases in Figure 8.6. The BA plots for DBP and MAP are shown in Figure 8.6(a) and (c), respectively. The bias between the finger and carotid DBP was -0.3 mmHg, and MAP was -0.3 mmHg, respectively, both of which

were statistically non-significant ($p > 0.05$). The LoA for the BA analysis on the DBP were -6.1 mmHg and 5.6 mmHg and on MAP were -6.6 mmHg and 6.1 mmHg. The correlation scatter plots for DBP and MAP are shown in Figure 8.6(b) and (d), respectively, indicating the obtained and ideal regression line along. The correlation coefficient for the finger and carotid DBP and MAP were $r = 0.91$ and 0.92 ($p < 0.001$), respectively. Their mean absolute errors were 2.4 ± 3.5 mmHg and 2.6 ± 4.0 mmHg, respectively. The error histograms for the DBP and MAP measurements are shown in Figure 8.6(e and f), respectively. The frequency of measurements (%) with errors within ±3 mmHg was greater than 60% and, likewise, within ±5 mmHg was greater than 85%. These frequencies for the DBP and MAP are indicated in the respective histogram plots (Figure 8.6(e and f)).

8.6 DISCUSSION

We have presented a cuffless and calibration-free BP measurement technique from the carotid artery using a high-frame-rate image-free ultrasound system. We have demonstrated that with the high scan rate, the system was able to simultaneously capture the changes in diameter and local PWV within each cardiac cycle. These measured parameters furnished carotid pressure estimates, which, compared with peripheral pressures, manifested accurate diastolic and mean arterial pressure values (over a range of 60 to 95 mmHg and 65 to 110 mmHg, respectively) captured the pulse pressure amplification evidenced by systolic pressures. The unique verification study based on LBNP intervention revealed that the system not only measured the instantaneous beat-to-beat perturbations reliably but also was sensitive to the difference in response of carotid pressures as opposed to the peripheral pressures to the stimulus. In this regard,

the system was able to measure the beat-to-beat changes in the pulse pressure amplification under the influence of LBNP. This demonstrated that the system measured the carotid BP and its beat-to-beat response to stimuli independent of the peripheral pressure.

Currently, the popular CBP measuring devices (H. M. Cheng et al., 2020; McEniery et al., 2014) adopt one of these techniques; (i) scaling the blood-pulse recorded using tonometer-like sensors at the carotid site by adjusting its mean and minima against the brachial MAP and DBP, respectively, (ii) calibrating peripheral pressure waveforms based on generalized or adaptive transfer function(s), (iii) N-point averaging of the peripheral pressure wave, (iv) estimation based on second systolic peak or shoulder point of peripheral pressure wave, (v) blind system identification, and (vi) learning-based techniques (Gao et al., 2016; H. Miyashita, 2012; Xiao et al., 2017; Xing et al., 2019; Yao et al., 2018). Another popular category of methods that have been employed for estimating peripheral BP, but could also be potentially adapted for CBP, is the use of models that scale PTT or PWV to the BP values (Ding et al., 2017; Douniama et al., 2009; Patzak et al., 2015; Rastegar et al., 2019; Yao et al., 2018; Yousefian et al., 2019). A common challenge associated with these non-invasive approaches that estimate CBP is their inherent dependence on peripheral pressure measurements. Their model accuracy and/or the errors of peripheral BP measurements compromise the accuracy (Kayrak et al., 2010; Stéphane Laurent et al., 2016). Machine learning approaches purport to provide a calibration-free BP as they may not require recording surrogate pressures at the time of measurement (Rastegar et al., 2019; Xiao et al., 2017; Xing et al., 2019). However, they do use prior BP information as ground truth for training the architectures on large data sets that contain inherent trends. Such approaches should be

less useful for clinical applications as they would fail to provide reliable measurements unless they have been thoroughly trained for diverse populations and pathophysiological cases (Rastegar et al., 2019). Recent evidence has shown that interventions such as pharmacological and hemodynamic modulations amplify the discrepancies between the central and peripheral pressures (H. M. Cheng et al., 2013), which poses a further challenge to aforesaid methods.

Unlike other non-invasive BP measurement methods reported so far, the novelty of the presented system is its non-dependence on any subject-specific or population-specific calibration model. More importantly, it does not require or use any prior information of neither the BP values nor the surrogate pressure waveforms recorded from peripheral arterial sites. In terms of cuffless techniques, ultrasound has been actively used, and several approaches have been reported (Rastegar et al., 2019). One advantage with ultrasound methods is they have accessibility to deeper vessels and provide true blood pulse from the arteries (either diameter or flow waveforms) that are not corrupted by the introduction of tissue or skin transfer functions. Few of the popular ultrasound methods include the ones based on the PWV-calibration (Mukkamala et al., 2015; Seo et al., 2015), diametric-calibration (Jan M. Meinders & Hoeks, 2004a; C. Wang et al., 2018) and based on active external force-vessel interaction (Rastegar et al., 2019; Zakrzewski et al., 2018). The methods again pose similar challenges (alluded earlier), such as calibration-associated issues or limited ability in tracking the beat-to-beat pressures, especially in the presence of interventions (H. M. Cheng et al., 2013; Rastegar et al., 2019).

The developed system is capable of simultaneously measuring the pressure-dependent variations of both the carotid artery diameter and local PWV within each cardiac cycle. Since the system yields PWV measure as well in addition to the pressure, it is amenable for monitoring of early vascular ageing (Peter M. Nilsson, Khalili, & Franklin, 2014). While methods in the literature rely on simultaneous pressure-diameter waveforms from a single site (Nabeel et al., 2020) for tracking PWV changes in a cardiac cycle, the unique aspect of the developed system is that it tracks them directly by measuring (varying) local PTT within each cardiac cycle. As yielded, the carotid C_F was systematically higher than C_D (by 7.27 ± 4.30%) and concord with the ones reported in the literature (Nabeel et al., 2020). The system also demonstrated repeatable baseline measurements of diameter and local PWV. The methodological considerations to perform such reliable measurements from smaller arterial segments have been addressed in our earlier works (Nabeel et al., 2020; K. V Raj, Nabeel, Joseph, & Sivaprakasam, 2019). Using simultaneously measured diameter and local PWV incremental parameters, the carotid pressure was evaluated for all the subjects during both the baseline and intervention. The baseline measurements of carotid DBP, SBP, and MAP were repeatable. The pressure obtained from the carotid artery is known to be a reliable surrogate for central aortic pressures(H. M. Cheng et al., 2020). Though employing a calibration technique, patch-based ultrasound has already been introduced for measuring BP, advancing the wearable technology (C. Wang et al., 2018). Adopting such technologies in compliment with a calibration-free technique as presented here would address the need for a continuous BP. Since the results suggest the ability of the method to track the changes in the beat-to-beat pressure, it has the potential to be

applied for monitoring short-term perturbations in clinical settings such as operative and post-operative care.

The use of the LBNP intervention provided a dynamic range of BP perturbations in a controlled manner while allowing measurement devoid of motion artifacts. The trends in carotid pressure followed that of the peripheral pressure (as depicted in Figure 8.3). From the pressure profile, it was evident that for the recruited subjects the all the pressure parameters both from finger and carotid manifested a decrement during the intervention, a moderate overshoot immediate after withdrawing the stimulus, and recovery to baseline value eventually (Figure 8.4).

Both the diastolic and systolic carotid measurements decreased significantly ($p < 0.001$), concomitant to their peripheral counterparts as a result of the intervention. One outcome of interest, however, is that the decrement for carotid DBP and MAP during the intervention was similar to that of the peripheral site (18% and 19%) versus (18% and 17%). Whereas the decrement in SBP and PP was relatively greater for the carotid artery compared to (22% and 35%) versus (17% and 15%). This inference was drawn by observing the calculated carotid-to-peripheral pressure ratios during the intervention, which were statistically similar for DBP and MAP ($p = 0.49$ and 0.20, respectively), but significantly decreased for SBP and PP ($p < 0.001$). Such a differential response of carotid versus peripheral pulsatile BP components to LBNP intervention is corroborated in an earlier work by Pannier et al. (B. Pannier, Slama, London, Safar, & Cuche, 1995). While these results have demonstrated the ability of the device to capture LBNP-induced BP perturbations, they have also captured the differential response in carotid versus peripheral pressures, especially in SBP and PP.

The carotid SBP and PP were systematically lower ($p < 0.001$) than the peripheral measures, whereas DBP and MAP from both the devices were significantly comparable ($p = 0.07$ and 0.10, respectively) for all subjects. The phenomenon of pulse pressure amplification (PPA) explains such an outcome, where the SBP and PP in peripheral arteries are usually higher than the central ones (A. P. Avolio et al., 2009; Joseph, Nabeel, Shah, & Sivaprakasam, 2018). The PPA for the recruited subjects concurs with the range reported in the literature (10 – 20 mmHg for an age group of 20 – 40 years) (A. P. Avolio et al., 2009). Likewise, studies show that DBP and MAP are reasonably constant across the arterial tree in the supine posture, where the hydrostatic offset is negligible (H. M. Cheng et al., 2020). For that matter, this has been the basis for many calibration methods in the literature that evaluate central BP (H. M. Cheng et al., 2020).

The carotid DBP and MAP measured by the system were strongly correlated with the finger pressure counterparts, and their corresponding magnitudes were in close agreement with a non-significant bias. A mean absolute error less than 3 mmHg further demonstrated the measurement accuracy. Note that the carotid DBP and MAP evaluated by the models did not utilize any calibration procedures or surrogate pressures but only are dependent on closed-form expressions relating pressure with intra-beat variations in diameter and local PWV. Therefore, the performance results obtained were encouraging, given that the system could yield reliable BP measures in spite of heart rate variability during LBNP. The potential influence of heart rate on the PWV (Lantelme, Mestre, Lievre, Gressard, & Milon, 2002) makes the BP assessment challenging, especially when based on calibration. Future invasive studies in accordance with the recommendations of ARTERY Society task force (James E.

Sharman et al., 2017) are warranted to fully establish the proposed system's accuracy over a wide physiological range.

8.7 STUDY LIMITATIONS AND FUTURE WORK

A small sample size was used to demonstrate the functionality of the developed system, which is study limitation. However, a wide range of BP changes were induced in a continuous manner through LBNP intervention (DBP: 60-95 mmHg and MAP: 65-110), and beat-to-beat measures were available for uncertainty analysis. Another limitation concerns the lack of an appropriate clinical-grade carotid BP reference device. It may be noted that, to our knowledge, no clinically established non-invasive carotid BP monitors are available as a reference standard. Thus, validation of the device against an invasive reference is essential (James E. Sharman et al., 2017) to fully establish the system's performance in terms of repeatability, reproducibility, and accuracy. Such studies on large animal models (with drug interventions to induce BP changes) are underway. Further, a large-scale study on human subjects comprising of the normal and diseased populations is in progress to investigate the system's screening capability and incremental value of the carotid pressure.

8.8 CONCLUSION

In conclusion, the system is promising in light of the current functional assessment that demonstrated reliable measurement of calibration-free, cuffless carotid pressure over continuous cardiac cycles without the need for peripheral BP. It could measure the beat-to-beat variations in the carotid pressure. Consistent with the earlier work (B. Pannier et al., 1995), the carotid measurements manifested a differential carotid-to-peripheral

pressure response during the LBNP. On comparing the peripheral and the measured carotid BP, PPA was observed with a magnitude that was concurrent with the literature (A. P. Avolio et al., 2009). The measurement accuracy was demonstrated on the directly comparable carotid versus finger measures (DBP and MAP) even in the presence of altering BP and heart rate. The system (as presented in the earlier chapters) therefore, not only yields the central BP, but has the ability to provide simultaneous diameter, IMT, and local PWV in a beat-by-beat manner.

CHAPTER 9.

CONCLUSION OF THE WORK

9.1 CONCLUSIVE SUMMARY

Chapter 1 narrated the importance and the fundamental gaps concerning clinical adoption of the VA assessment, emphasizing the need for a single, easy-to-use, affordable, field-deployable, automated device to measure a coalescence of vascular properties that can serve in the assessment of EVA syndrome. The work in this thesis involved the development of A-mode ultrasound methods and a system for multi-faceted measurement of the structural and functional properties of the artery, that were identified as important VA markers. While the entire research cumulatively attempts to address the highlighted fundamental need, the specific work pertaining to the automated measurement of each arterial property solved the challenges associated with respective state-of-the-art techniques discussed in Chapter 2.

For automated ultrasound-based vascular measurements, the perquisite is automated means to recognize and track the locations of the arterial walls, which was the first objective of the work. The developed DTW-based A-mode methods for these high-level tasks (presented in Chapter 3) performed on par and even better compared to a majority of high-performing methods in the literature, both image-processing and RF signal-processing based. In addition, the distinguishing aspects of the presented methods were the ability to discern whether the artery echoes are present or absent, to discriminate between the motion of walls and neighboring static or slow-moving echoes, and robustness towards overlapping hyperechoic regions. In fact, later in Chapter 5, as we

discuss the methodological considerations of measuring local PWV, the relevance of the developed wall motion tracking method has been underlined by comparing it to popular cross-correlation-based tracking. As the platform for automated measurement framework was laid by these wall recognition and tracking methods, the second objective was to delineate the wall layers for measurement of diameter and IMT. In Chapter 4, we presented the A-mode methods in this regard that uniquely used phase information of the wall echoes, contrary to just amplitude information. Their robustness to noise was verified via systematic simulations, the measurement accuracy and reliability were established on static and dynamic flow phantom models, and in-vivo usability was validated on human subjects. The results revealed a high performance, as good as the image-processing counterparts in the literature. A novelty of the method is that it provided continuous waveforms of both diameter and IMT, as opposed to a single value within each cardiac cycle, the significance of which has been discussed in the chapter. The work presented in Chapters 3 and 4, therefore, has demonstrated that the structural properties of the vessels can be assessed with adequate reliability using A-scan frames. This opened up the possibility of designing low-cost, high-frame-rate ultrasound systems (for fast scanning), both unimodal and multimodal, required for the measurement of local PWV and incremental stiffness.

Having automated structure measurements allows estimation of local stiffness metrics such as E_P, AC, and β using ultrasound machines with regular frame rates. But, as underlined in Chapter 2, direct measurement of local PWV requires ultrafast ultrasound systems which are inherently costly, complex, non-real-time and non-amenable to field. The work in Chapter 5 addressed this challenge, providing a dual-channel, high-frame rate A-mode system prototype which had also the provision for integrating other

sensing modalities. The system design was characterized to achieve optimal performance for online measurement of local PWV, the reliability of which was validated on flow-phantom setup against invasive and theoretically evaluated local PWV, and in-vivo trials. The experimental investigations established the accuracy, beat-to-beat variability, intra- and inter-operator repeatability. An embedded version of the high-frame rate multimodal system presented in Chapter 5 was developed to also include an OEM pressure control and detection module. The device was validated, in Chapter 6, for its ability to measure the regional stiffness (as cfPWV) alongside the local counterpart. Subsequently, in Chapter 7, it was demonstrated that the system was able to track the acute changes in local PWV, which were pressure-associated, both inter- and intra-beat changes. Such is important for several applications, most relevant of all for pressure-standardizing the stiffness. However, methodologically, measuring such changes are more challenging than measuring just an average single value of local PWV.

Indirect measurement of local PWV, which is implemented based on BH equation, requires pressure and diameter waveforms simultaneously recorded from a single site. When measuring from carotid artery, tonometry waveforms are calibrated from brachial BP for pressure which limits tracking the beat-to-beat changes, making direct measurement of local PWV more practical. In Chapter 7, initially the ability of the developed high-frame-rate ultrasound system to reliably measure the beat-to-beat variations in PWV was demonstrated during both induced BP elevating and lowering perturbations. The online measurement capability and real-time visual feedback were necessary components for tracking such changes, and the device facilitated them. Further the indirect and direct methods were presented for the measurement of intra-

beat changes, incremental PWV. A-mode modality made it possible to achieve easy integration of pressure sensing module, design of a compact pressure-ultrasound probe, and allowed frequency matched synchronized acquisition, which are demanded methodological requirements. The BH equation was also remodeled to accommodate compensation for pressure-diameter hysteresis, resulting from viscoelastic nature of the central artery walls. Similarly, for direct estimation incremental PWV, the influence of early wave-reflections on the blood pulse pair morphology is a major concern. A method was presented to account and correct for such influences. Such a method of calculating local PWV from the forward propagating component of blood pulses improved the beat-to-beat variability of PWV measures obtained from points in pulse cycle closer to peak systole. Employing this technique, the developed system could yield both inter- and intra-cardiac cycle changes in local PWV simultaneously in a reliable fashion during an LBNP intervention.

The device's ability (as shown in Chapters 4 and 7) to measure acute changes in local geometry and local PWV online using the developed A-mode algorithms demonstrated its potential to measure central BP in a continuous fashion without requiring any calibration. This was presented in Chapter 8, where the results revealed that not only is the system able to measure central BP variations due to physiological perturbation such as LBNP, but it also captured the differential response in central and peripheral vessels to the perturbation. This was a prominent advantage of the system presented over other calibration based central BP measuring methods. Conclusively, the work in this thesis clearly suggested the leverages offered by the A-mode system and the accompanying methods – (i) facilitate affordable and compact design, (ii) low processing overhead,

(iii) online measurement and visual feedback, (iv) minimal dependence on the operator, and (v) multiple markers in one examination and on a single device.

9.2 OUTLOOK

The work laid the foundation by validating the reliability of the developed device to measure several important vascular properties that are potential marker of early vascular aging. Chapter 1 has emphasized that lack of an opinion on which marker(s) are best, whether combining several marker manifest EVA more robustly, and in that case, which marker are to be combined. Hence, one of the primary future research directions includes investigations in this regard, followed by development of models that combines the markers to provide integrated VA scores. While that's the overall goal, other future directions are focused on expanding the validation of the measurement methods to specific clinical use cases. Structure measurement methods in Chapter 3 and 4 are now being enhanced to provide adequate robustness for plaque analysis. Chapter 6 presents measurement of incremental local PWV which has been very minimally explored in the literature. This is a characteristic property of the artery which is challenging to mimic as in vitro phantom models and there is no analytic means to validate the true accuracy of the measurements on human subject, otherwise through invasive procedures. Therefore, investigation on excised arteries and animal models are in progress to achieve this objective. Efforts are put into understanding the age associated trends of the incremental local PWV. Epidemiological studies on this marker are also abysmally low. So, efforts are also warranted to unveil the significance of this marker for several clinical applications. Measuring incremental PWV potentially offers a means to pressure standardize arterial stiffness to quantify the true vascular

insult and for improved patient classification. We are currently working on such methods that can standardize PWV by measuring their inter and intra-beat acute changes. The investigations in Chapter 7 were limited concerning the validation of systolic central pressure which according to ARTERY society guidelines is recommended to be performed against invasive counterpart. Validations as such in human subjects accompany risks and complications, and can be performed only in subjects that are prescribed catheterization. This limits the population diversity, owing which again, animal studies are required under infusion of drugs that can alter the BP over a wide physiological range. Overall, multicentric cross sectional and longitudinal studies are underway to establish the clinical usability of the device and method on populations diversified across age, risk factors, pathologies.

REFERENCES

1. **Aatola, H.**, **Hutri-Kähönen, N.**, **Juonala, M.**, **Laitinen, T. T.**, **Pahkala, K.**, **Mikkilä, V.**, … **Kähönen, M.** (2014). Prospective relationship of change in ideal cardiovascular health status and arterial stiffness: the Cardiovascular Risk in Young Finns Study. *Journal of the American Heart Association*, **3**(2), 1–11. https://doi.org/10.1161/JAHA.113.000532
2. **An, X.**, **Li, Y.**, **Shi, S.**, **Ge, L.**, & **Li, Y.** (2022). Clinical significance and influencing factors of carotid pulse wave velocity in patients with diabetic microangiopathy. *Journal of Clinical Ultrasound*, **50**(3), 309–316. https://doi.org/10.1002/JCU.23153
3. **Apostolakis, I. Z.**, **Nandlall, S. D.**, & **Konofagou, E. E.** (2016). Piecewise pulse wave imaging (pPWI) for detection and monitoring of focal vascular disease in murine aortas and carotids in vivo. *IEEE Transactions on Medical Imaging*, **35**(1), 13–28.
4. **Armentano, R. L.**, **Graf, S.**, **Barra, J. G.**, **Velikovsky, G.**, **Baglivo, H.**, **Sanchez, R.**, … **Levenson, J.** (1998). Carotid Wall Viscosity Increase Is Related to Intima-Media Thickening in Hypertensive Patients. *Hypertension*, **31**(1), 534–539. https://doi.org/10.1161/01.HYP.31.1.534
5. **Arndt, J. O.**, **Klauske, J.**, & **Mersch, F.** (1968). The diameter of the intact carotid artery in man and its change with pulse pressure. *Pflüger's Archiv Für Die Gesamte Physiologie Des Menschen Und Der Tiere*, **301**, 230–240.
6. **Avolio, A.** (2013). Arterial stiffness. *Pulse*, **1**(1), 14–28. https://doi.org/10.1007/s11906-004-0047-z
7. **Avolio, A. P.**, **Van Bortel, L. M.**, **Boutouyrie, P.**, **Cockcroft, J. R.**, **McEniery, C. M.**, **Protogerou, A. D.**, … **Smulyan, H.** (2009). Role of pulse pressure amplification in arterial hypertension: experts' opinion and review of the data. *Hypertension*, **54**(2), 375–383. https://doi.org/10.1161/HYPERTENSIONAHA.109.134379
8. **Avolio, Alberto**. (2013). Arterial stiffness. *Pulse*, **1**(1), 14–28.
9. **Azzopardi, C.**, **Camilleri, K. P.**, & **Hicks, Y. A.** (2020). Bimodal Automated Carotid Ultrasound Segmentation Using Geometrically Constrained Deep Neural Networks. *IEEE Journal of Biomedical and Health Informatics*, **24**(4), 1004–1015. https://doi.org/10.1109/JBHI.2020.2965088
10. **Bastida-Jumilla, M. C.**, **Menchón-Lara, R. M.**, **Morales-Sánchez, J.**, **Verdú-Monedero, R.**, **Larrey-Ruiz, J.**, & **Sancho-Gómez, J. L.** (2013). Segmentation of the common carotid artery walls based on a frequency implementation of active contours: segmentation of the common carotid artery walls. *Journal of Digital Imaging*, **26**(1), 129–139. https://doi.org/10.1007/S10278-012-9481-7
11. **Bazan, I.**, **Ramos, A.**, **Balay, G.**, & **Negreira, C.** (2018). Power spectral estimation of high-harmonics in echoes of wall resonances to improve resolution in non-invasive measurements of wall mechanical properties in rubber tube and ex-vivo artery. *Ultrasonics*, **87**, 133–144. https://doi.org/10.1016/j.ultras.2018.02.004
12. **Bercoff, J.** (2011). Ultrafast Ultrasound Imaging. In I. Minin & O. Minin (Eds.), *Ultrafast ultrasound imaging 3* (pp. 3–24). Rijeka: InTech.
13. **Bia, D.**, **Aguirre, I.**, **Zócalo, Y.**, **Devera, L.**, **Cabrera Fischer, E.**, & **Armentano,**

R. (2005). Regional differences in viscosity, elasticity, and wall buffering function in systemic arteries: pulse wave analysis of the arterial pressure-diameter relationship. *Revista Española de Cardiología*, **58**(2), 167–174. https://doi.org/10.1016/s1885-5857(06)60360-5

14. **Bianchini, E.**, **Bozec, E.**, **Gemignani, V.**, **Faita, F.**, **Giannarelli, C.**, **Ghiadoni, L.**, … **Laurent, S.** (2010). Assessment of carotid stiffness and intima-media thickness from ultrasound data: comparison between two methods. *Journal of Ultrasound in Medicine*, **29**(8), 1169–1175. https://doi.org/10.7863/jum.2010.29.8.1169
15. **Borlotti, A.**, **Khir, A. W.**, **Rietzschel, E. R.**, **De Buyzere, M. L.**, **Vermeersch, S.**, & **Segers, P.** (2012). Noninvasive determination of local pulse wave velocity and wave intensity: changes with age and gender in the carotid and femoral arteries of healthy human. *Journal of Applied Physiology*, **113**(5), 727–735.
16. **Borlotti, A.**, **Li, Y.**, **Parker, K. H.**, & **Khir, A. W.** (2014). Experimental evaluation of local wave speed in the presence of reflected waves. *Journal of Biomechanics*, **47**(1), 87–95. https://doi.org/10.1016/j.jbiomech.2013.10.007
17. **Bortolotto, L. A.**, **Hanon, O.**, **Franconi, G.**, **Boutouyrie, P.**, **Legrain, S.**, & **Girerd, X.** (1999). The aging process modifies the distensibility of elastic but not muscular arteries. *Hypertension*, **34**(4), 889–892.
18. **Boutouyrie, P.**, **Chowienczyk, P.**, **Humphrey, J. D.**, & **Mitchell, G. F.** (2021). Arterial Stiffness and Cardiovascular Risk in Hypertension. *Circulation Research*, 864–886. https://doi.org/10.1161/CIRCRESAHA.121.318061
19. **Boutouyrie, P.**, **Germain, D. P.**, **Tropeano, A. I.**, **Laloux, B.**, **Carenzi, F.**, **Zidi, M.**, … **Laurent, S.** (2001). Compressibility of the carotid artery in patients with pseudoxanthoma elasticum. *Hypertension*, **38**(5), 1181–1184. https://doi.org/10.1161/hy1101.096108
20. **Bramwell, J. C.**, & **Hill, A. V**. (1922). The velocity of the pulse wave in man. *The Royal Society Publishing*, **93**(652), 298–306.
21. **Brands, P. J.**, **Hoeks, A. P. G.**, **Ledoux, L. A. F.**, & **Reneman, R. S.** (1997). A radio frequency domain complex cross-correlation model to estimate blood flow velocity and tissue motion by means of ultrasound. *Ultrasound in Medicine and Biology*, **23**(6), 911–920. https://doi.org/10.1016/S0301-5629(97)00021-5
22. **Brands, P. J.**, **Hoeks, A. P. G.**, **Willigers, J.**, **Willekes, C.**, & **Reneman, R. S.** (1999). An integrated system for the non-invasive assessment of vessel wall and hemodynamic properties of large arteries by means of ultrasound. *European Journal of Ultrasound*, **9**(3), 257–266. https://doi.org/10.1016/S0929-8266(99)00033-6
23. **Bruno, R. M.**, **Nilsson, P. M.**, **Engström, G.**, **Wadström, B. N.**, **Empana, J. P.**, **Boutouyrie, P.**, & **Laurent, S.** (2020). Early and supernormal vascular aging: Clinical characteristics and association with incident cardiovascular events. *Hypertension*, 1616–1624. https://doi.org/10.1161/HYPERTENSIONAHA.120.14971
24. **Campo, A.**, **Segers, P.**, **Heuten, H.**, **Goovaerts, I.**, **Ennekens, G.**, **Vrints, C.**, … **Dirckx, J.** (2014). Non-invasive technique for assessment of vascular wall stiffness using laser doppler vibrometry. *Measurement Science and Technology*, **25**, 1–10.
25. **Carerj, S.**, **Nipote, C.**, & **Zimbalatti, C.** (2005). A new tool for the evaluation of stiffness vascular parameters in clinical practice : eTRACKING. *Cardiology*, **2008**(63), 1–2.

26. **Carovac, A.**, **Smajlovic, F.**, & **Junuzovic, D.** (2011). Application of Ultrasound in Medicine. *Acta Informatica Medica*, **19**(3), 168. https://doi.org/10.5455/aim.2011.19.168-171
27. **Cheng, D. C.**, **Schmidt-Trucksäss, A.**, **Liu, C. H.**, & **Liu, S. H.** (2010). Automated detection of the arterial inner walls of the common carotid artery based on dynamic B-mode signals. *Sensors (Basel, Switzerland)*, **10**(12), 10601–10619. https://doi.org/10.3390/S101210601
28. **Cheng, D. chuan**, **Schmidt-Trucksäss, A.**, **Cheng, K. sheng**, & **Burkhardt, H.** (2002). Using snakes to detect the intimal and adventitial layers of the common carotid artery wall in sonographic images. *Computer Methods and Programs in Biomedicine*, **67**(1), 27–37. https://doi.org/10.1016/S0169-2607(00)00149-8
29. **Cheng, H. M.**, **Chuang, S. Y.**, **Wang, T. D.**, **Kario, K.**, **Buranakitjaroen, P.**, **Chia, Y. C.**, … **Chen, C. H.** (2020). Central blood pressure for the management of hypertension: Is it a practical clinical tool in current practice? *Journal of Clinical Hypertension*, **22**(3), 391–406. https://doi.org/10.1111/jch.13758
30. **Cheng, H. M.**, **Lang, D.**, **Tufanaru, C.**, & **Pearson, A.** (2013). Measurement accuracy of non-invasively obtained central blood pressure by applanation tonometry: a systematic review and meta-analysis. *International Journal of Cardiology*, **167**(5), 1867–1876. https://doi.org/10.1016/j.ijcard.2012.04.155
31. **Chirinos, J. A.**, **Segers, P.**, **Hughes, T.**, & **Townsend, R.** (2019). Large-Artery Stiffness in Health and Disease: JACC State-of-the-Art Review. *Journal of the American College of Cardiology*, **74**(9), 1237–1263. https://doi.org/10.1016/j.jacc.2019.07.012
32. **Climie, Rachel E.**, **Gregory, A. T.**, **Denniss, A. R.**, **Mynard, J. P.**, & **Pepe, S.** (2021). Vascular Ageing: A Key Frontier in the Fight Against Cardiovascular Disease. *Heart Lung and Circulation*, **30**(11), 1585–1590. https://doi.org/10.1016/j.hlc.2021.09.001
33. **Climie, Rachel Emma**, **Mayer, C. C.**, **Bruno, R. M.**, & **Hametner, B.** (2020). Addressing the unmet needs of measuring vascular ageing in clinical practice-european cooperation in science and technology action vascagenet. *Artery Research*, **26**(2), 71–75. https://doi.org/10.2991/artres.k.200328.001
34. **Coll, B.**, & **Feinstein, S. B.** (2008). Carotid intima-media thickness measurements: techniques and clinical relevance. *Current Atherosclerosis Reports*, **10**(5), 444–450. https://doi.org/10.1007/s11883-008-0068-1
35. **Cooney, M. T.**, **Bc, H.**, **Dudina, A. L.**, **Graham, I. M.**, & **Bc, H.** (2009). *Value and Limitations of Existing Scores for the Assessment of Cardiovascular Risk A Review for Clinicians*. **54**(14). https://doi.org/10.1016/j.jacc.2009.07.020
36. **Crea, F.** (2022). European Society of Cardiology guidance for the management of cardiovascular disease during the pandemic and a focus on long COVID. *European Heart Journal*, **43**(11), 1017–1021. https://doi.org/10.1093/eurheartj/ehac087
37. **Criqui, M. H.**, **McClelland, R. L.**, **McDermott, M. M.**, **Allison, M. A.**, **Blumenthal, R. S.**, **Aboyans, V.**, … **Shea, S.** (2010). The ankle-brachial index and incident cardiovascular events in the MESA (Multi-Ethnic Study of Atherosclerosis). *Journal of the American College of Cardiology*, **56**(18), 1506–1512. https://doi.org/10.1016/J.JACC.2010.04.060
38. **Csiszar, A.**, **Wang, M.**, **Lakatta, E. G.**, & **Ungvari, Z.** (2008). Inflammation and endothelial dysfunction during aging: role of NF-kappaB. *Journal of Applied Physiology (Bethesda, Md. : 1985)*, **105**(4), 1333–1341.

https://doi.org/10.1152/JAPPLPHYSIOL.90470.2008
39. **Currie, G.**, & **Delles, C.** (2017). Healthy Vascular Aging. *Hypertension*, **70**(2), 229–231. https://doi.org/10.1161/HYPERTENSIONAHA.117.09122
40. **de Jong, P. G.**, **Arts, T.**, **Hoeks, A. P.**, & **Reneman, R. S.** (1990). Determination of tissue motion velocity by correlation interpolation of pulsed ultrasonic echo signals. *Ultrasonic Imaging*, **12**(2), 84–98. https://doi.org/10.1016/0161-7346(90)90152-n
41. **De Ruijter, W.**, **Westendorp, R. G. J.**, **Assendelft, W. J. J.**, **Den Elzen, W. P. J.**, **De Craen, A. J. M.**, **Le Cessie, S.**, & **Gussekloo, J.** (2009). Use of Framingham risk score and new biomarkers to predict cardiovascular mortality in older people: population based observational cohort study. *BMJ (Clinical Research Ed.)*, **338**(7688), 219–222. https://doi.org/10.1136/BMJ.A3083
42. **Delsanto, S.**, **Molinari, F.**, **Giustetto, P.**, **Liboni, W.**, **Badalamenti, S.**, & **Suri, J. S.** (2007). Characterization of a completely user-independent algorithm for carotid artery segmentation in 2-D ultrasound images. *IEEE Transactions on Instrumentation and Measurement*, **56**(4), 1265–1274. https://doi.org/10.1109/TIM.2007.900433
43. **Demirli, R.**, & **Saniie, J.** (2001). Model-based estimation of ultrasonic echoes. Part I: Analysis and algorithms. *IEEE Transactions on Ultrasonics, Ferroelectrics, and Frequency Control*, **48**(3), 787–802. https://doi.org/10.1109/58.920713
44. **Destrempes, F.**, **Meunier, J.**, **Giroux, M. F.**, **Soulez, G.**, & **Cloutier, G.** (2009). Segmentation in ultrasonic B-mode images of healthy carotid arteries using mixtures of Nakagami distributions and stochastic optimization. *IEEE Transactions on Medical Imaging*, **28**(2), 215–229. https://doi.org/10.1109/TMI.2008.929098
45. **Ding, X.**, **Yan, B. P.**, **Zhang, Y. T.**, **Liu, J.**, **Zhao, N.**, & **Tsang, H. K.** (2017). Pulse transit time based continuous cuffless blood pressure estimation: a new extension and a comprehensive evaluation. *Scientific Reports*, **7**(1), 1–11. https://doi.org/10.1038/s41598-017-11507-3
46. **Douniama, C.**, **Sauter, C. U.**, & **Couronne, R.** (2009). Blood pressure tracking capabilities of pulse transit times in different arterial segments: a clinical evaluation. *Computers in Cardiology*, 201–204. Park City.
47. **Eigenbrodt, M. L.**, **Sukhija, R.**, **Rose, K. M.**, **Tracy, R. E.**, **Couper, D. J.**, **Evans, G. W.**, … **Mehta, J. L.** (2007). Common carotid artery wall thickness and external diameter as predictors of prevalent and incident cardiac events in a large population study. *Cardiovascular Ultrasound*, **5**(11), 1–11. https://doi.org/10.1186/1476-7120-5-11
48. **Engelen, L.**, **Ferreira, I.**, **Stehouwer, C. D.**, **Boutouyrie, P.**, & **Laurent, S.** (2013). Reference intervals for common carotid intima-media thickness measured with echotracking: relation with risk factors. *European Heart Journal*, **34**(30). https://doi.org/10.1093/EURHEARTJ/EHS380
49. **Epstein, F. H.**, **Moncada, S.**, & **Higgs, A.** (1993). The L-arginine-nitric oxide pathway. *The New England Journal of Medicine*, **329**(27), 2002–2012. https://doi.org/10.1056/NEJM199312303292706
50. **Erusalimsky, J. D.**, & **Skene, C.** (2009). Mechanisms of endothelial senescence. *Experimental Physiology*, **94**(3), 299–304. https://doi.org/10.1113/EXPPHYSIOL.2008.043133
51. **Eskurza, I.**, **Myerburgh, L. A.**, **Kahn, Z. D.**, & **Seals, D. R.** (2005).

Tetrahydrobiopterin augments endothelium-dependent dilatation in sedentary but not in habitually exercising older adults. *The Journal of Physiology*, **568**(Pt 3), 1057–1065. https://doi.org/10.1113/JPHYSIOL.2005.092734

52. **Faita, F.**, **Gemignani, V.**, **Bianchini, E.**, **Giannarelli, C.**, **Ghiadoni, L.**, & **Demi, M.** (2008). Real-time measurement system for evaluation of the carotid intima-media thickness with a robust edge operator. *Journal of Ultrasound in Medicine*, **27**(9), 1353–1361.
53. **Fan, L.**, **Santago, P.**, **Jiang, H.**, & **Herrington, D. M.** (2000). Ultrasound measurement of brachial flow-mediated vasodilator response. *IEEE Transactions on Medical Imaging*, **19**(6), 621–631. https://doi.org/10.1109/42.870669
54. **Faraji, M.**, **Cheng, I.**, **Naudin, I.**, & **Basu, A.** (2018). Segmentation of arterial walls in intravascular ultrasound cross-sectional images using extremal region selection. *Ultrasonics*, **84**, 356–365. https://doi.org/10.1016/j.ultras.2017.11.020
55. **Flore, R.**, **Ponziani, F. R.**, **Tinelli, G.**, **Arena, V.**, **Fonnesu, C.**, **Nesci, A.**, … **Santoliquido, A.** (2015). New modalities of ultrasound-based intima-media thickness, arterial stiffness and non-coronary vascular calcifications detection to assess cardiovascular risk. *European Review for Medical and Pharmacological Sciences*, **19**(8), 1430–1441.
56. **Fortier, C.**, & **Agharazii, M.** (2015). Arterial Stiffness Gradient. *Pulse*, **3**(3–4), 159–166. https://doi.org/10.1159/000438852
57. **Francesconi, M.**, **Martina, M. R.**, **Armenia, S.**, **Buzzelli, A.**, **Di Franco, G.**, **Gemignani, V.**, … **Bruno, R. M.** (2021). Technical Validation and Usability of a Portable Ultrasound-Based System for Carotid Assessment of Vascular Ageing: A Pilot Study. *Heart Lung and Circulation*, **30**(11), 1734–1743. https://doi.org/10.1016/j.hlc.2021.06.530
58. **Freire, C. M. V.**, **Ribeiro, A. L. P.**, **Barbosa, F. B. L.**, **Nogueira, A. I.**, **De Almeida, M. C. C.**, **Barbosa, M. M.**, … **Ribeiro-Oliveira, A.** (2009). Comparison between automated and manual measurements of carotid intima-media thickness in clinical practice. *Vascular Health and Risk Management*, **5**, 811. Retrieved from /pmc/articles/PMC2754094/
59. **Gao, M.**, **Rose, W. C.**, **Fetics, B.**, **Kass, D. A.**, **Chen, C. H.**, & **Mukkamala, R.** (2016). A simple adaptive transfer function for deriving the central blood pressure waveform from a radial blood pressure waveform. *Scientific Reports*, **6**, 1–9. https://doi.org/10.1038/srep33230
60. **Giudici, A.**, **Khir, A. W.**, **Reesink, K. D.**, **Delhaas, T.**, & **Spronck, B.** (2021). Five years of cardio-ankle vascular index (CAVI) and CAVI0: how close are we to a pressure-independent index of arterial stiffness? *Journal of Hypertension*, **39**(11), 2128–2138. https://doi.org/10.1097/HJH.0000000000002928
61. **Giudici, A.**, **Palombo, C.**, **Morizzo, C.**, **Kozakova, M.**, **Cruickshank, J. K.**, **Wilkinson, I. B.**, & **Khir, A. W.** (2021). Transfer-function-free technique for the noninvasive determination of the human arterial pressure waveform. *Physiological Reports*, **9**(18), e15040. https://doi.org/10.14814/PHY2.15040
62. **Godia, E. C.**, **Madhok, R.**, **Pittman, J.**, **Trocio, S.**, **Ramas, R.**, **Cabral, D.**, … **Rundek, T.** (2007). Carotid artery distensibility: a reliability study. *Journal of Ultrasound in Medicine*, **26**(9), 1157–1165. https://doi.org/10.7863/jum.2007.26.9.1157
63. **Golemati, S.**, & **Cokkinos, D. D.** (2022). Recent advances in vascular ultrasound imaging technology and their clinical implications. *Ultrasonics*, **119**(January

2021), 106599. https://doi.org/10.1016/j.ultras.2021.106599
64. **Golemati, S.**, **Stoitsis, J.**, **Sifakis, E. G.**, **Balkizas, T.**, & **Nikita, K. S.** (2007). Using the Hough transform to segment ultrasound images of longitudinal and transverse sections of the carotid artery. *Ultrasound in Medicine and Biology*, **33**(12), 1918–1932. https://doi.org/10.1016/j.ultrasmedbio.2007.05.021
65. **Gonzalez, J.**, **Wood, J. C.**, **Dorey, F. J.**, **Wren, T. A. L.**, & **Vicente, G.** (2008). Reproducibility of carotid intima-media thickness measurements in young adults. *Radiology*, **247**(2), 465–471.
66. **Goswami, N.**, **Blaber, A. P.**, **Hinghofer-Szalkay, H.**, & **Convertino, V. A.** (2019). Lower body negative pressure: physiological effects, applications, and implementation. *Physiological Reviews*, **99**(1), 807–851. https://doi.org/10.1152/physrev.00006.2018
67. **Goswami, N.**, **Loeppky, J. A.**, & **Hinghofer-szalkay, H.** (2008). LBNP : Past Protocols and Technical Considerations for Experimental Design. *Aviation Space and Environmental Medicine*, **79**(5), 459–471. https://doi.org/10.3357/ASEM.2161.2008
68. **Graf, S.**, **Craiem, D.**, **Barra, J. G.**, & **Armentano, R. L.** (2011). Estimation of local pulse wave velocity using arterial diameter waveforms: experimental validation in sheep. *Journal of Physics: Conference Series*, **332**(1), 1–8. https://doi.org/10.1088/1742-6596/332/1/012010
69. **Gutierrez, M. A.**, **Pilon, P. E.**, **Lage, S. G.**, **Kopel, L.**, **Carvalho, R. T.**, & **Furuie, S. S.** (2002). Automatic measurement of carotid diameter and wall thickness in ultrasound images. *Computers in Cardiology*, **29**, 359–362. https://doi.org/10.1109/CIC.2002.1166783
70. **Hachaj, T.**, & **Piekarczyk, M.** (2019). Evaluation of pattern recognition methods for head gesture-based interface of a virtual reality helmet equipped with a single IMU sensor. *Sensors (Switzerland)*, **19**(24), 1–19. https://doi.org/10.3390/s19245408
71. **Hahn, C.**, & **Schwartz, M. A.** (2009). Mechanotransduction in vascular physiology and atherogenesis. *Nature Reviews. Molecular Cell Biology*, **10**(1), 53. https://doi.org/10.1038/NRM2596
72. **Hayashi, K.**, **Handa, H.**, **Nagasawa, S.**, **Okumura, A.**, & **Moritake, K.** (1980). Stiffness and elastic behavior of human intracranial and extracranial arteries. *Journal of Biomechanics*, **13**(2), 175–184. https://doi.org/10.1016/0021-9290(80)90191-8
73. **Hermeling, E.**, **Hoeks, A. P. G.**, **Winkens, M. H. M.**, **Waltenberger, J. L.**, **Reneman, R. S.**, **Kroon, A. A.**, & **Reesink, K. D.** (2010). Noninvasive assessment of arterial stiffness should discriminate between systolic and diastolic pressure ranges. *Hypertension*, **55**(1), 124–130. https://doi.org/10.1161/HYPERTENSIONAHA.109.143867
74. **Hermeling, E.**, **Reesink, K. D.**, **Kornmann, L. M.**, **Reneman, R. S.**, & **Hoeks, A. P. G.** (2009). The dicrotic notch as alternative time-reference point to measure local pulse wave velocity in the carotid artery by means of ultrasonography. *Journal of Hypertension*, **27**(10), 2028–2035. https://doi.org/10.1097/HJH.0b013e32832f5890
75. **Hermeling, E.**, **Reesink, K. D.**, **Reneman, R. S.**, & **Hoeks, A. P. G.** (2007). Measurement of local pulse wave velocity: effects of signal processing on precision. *Ultrasound in Medicine and Biology*, **33**(5), 774–781.

https://doi.org/10.1016/j.ultrasmedbio.2006.11.018
76. **Hermeling, E.**, **Reesink, K. D.**, **Reneman, R. S.**, & **Hoeks, A. P. G.** (2008). Confluence of incident and reflected waves interferes with systolic foot detection of the carotid artery distension waveform. *Journal of Hypertension*, **26**(12), 2374–2380.
77. **Hermeling, E.**, **Vermeersch, S. J.**, **Rietzschel, E. R.**, **de Buyzere, M. L.**, **Gillebert, T. C.**, **van de Laar, R. J.**, … **Reesink, K. D.** (2012). The change in arterial stiffness over the cardiac cycle rather than diastolic stiffness is independently associated with left ventricular mass index in healthy middle-aged individuals. *Journal of Hypertension*, **30**(2), 396–402. https://doi.org/10.1097/HJH.0b013e32834e4b75
78. **Hoctor, R. T.**, **Dentinger, A. M.**, & **Thomenius, K. E.** (2007). Array signal processing for local arterial pulse wave velocity measurement using ultrasound. *IEEE Transactions on Ultrasonics, Ferroelectrics, and Frequency Control*, **54**(5), 1018–1027. https://doi.org/10.1109/TUFFC.2007.347
79. **Hoeks, A. P.G.**, **Brands, P. J.**, **Smeets, F. A. M.**, & **Reneman, R. S.** (1990). Assessment of the distensibility of superficial arteries. *Ultrasound in Medicine and Biology*, **16**(2), 121–128. https://doi.org/10.1016/0301-5629(90)90139-4
80. **Hoeks, Arnold P.G.**, **Willekes, C.**, **Boutouyrie, P.**, **Brands, P. J.**, **Willigers, J. M.**, & **Reneman, R. S.** (1997). Automated detection of local artery wall thickness based on M-line signal processing. *Ultrasound in Medicine and Biology*, **23**(7), 1017–1023. https://doi.org/10.1016/S0301-5629(97)00119-1
81. **Hoeks, Arnold P.G.**, **Willigers, J. M.**, & **Reneman, R. S.** (2000). Effects of assessment and processing techniques on the shape of arterial pressure-distension loops. *Journal of Vascular Research*, **37**(6), 494–500. https://doi.org/10.1159/000054082
82. **Hoeks, Arnold P G**, **Willigers, J. M.**, & **Reneman, R. S.** (2000). Effects of assessment and processing techniques on the shape of arterial pressure-distension loops. *Journal of Vascular Research*, **37**(6), 494–500. https://doi.org/10.1159/000054082
83. **Hokanson, D. E.**, **Mozersky, D. J.**, **Sumner, D. S.**, & **Strandness Jr, D. E.** (1972). A phase-locked echo tracking system for recording arterial diameter changes in vivo. *Journal of Applied Physiology*, **32**(5), 728–733. https://doi.org/10.1152/jappl.1972.32.5.728
84. **Holder, S. M.**, **Bruno, R. M.**, **Shkredova, D. A.**, **Dawson, E. A.**, **Jones, H.**, **Hopkins, N. D.**, … **Thijssen, Di. H. J.** (2021). Reference Intervals for Brachial Artery Flow-Mediated Dilation and the Relation with Cardiovascular Risk Factors. *Hypertension*, **77**(5), 1469–1480. https://doi.org/10.1161/HYPERTENSIONAHA.120.15754
85. **Huang, C.**, **Ren, T. L.**, & **Luo, J.** (2014). Effects of parameters on the accuracy and precision of ultrasound-based local pulse wave velocity measurement: a simulation study. *IEEE Transactions on Ultrasonics, Ferroelectrics, and Frequency Control*, **61**(12), 2001–2018.
86. **Huang, G.**, **Zhang, D.**, **Zheng, X.**, & **Zhu, X.** (2010). An EMG-based handwriting recognition through dynamic time warping. *2010 Annual International Conference of the IEEE Engineering in Medicine and Biology Society, EMBC'10*, 4902–4905. https://doi.org/10.1109/IEMBS.2010.5627246
87. **Humphrey, J. D.** (2008). Mechanisms of Arterial Remodeling in Hypertension:

Coupled Roles of Wall Shear and Intramural Stress. *Hypertension*, **52**(2), 195. https://doi.org/10.1161/HYPERTENSIONAHA.107.103440
88. **Humphrey, J. D.**, **Harrison, D. G.**, **Figueroa, C. A.**, **Lacolley, P.**, & **Laurent, S.** (2016). Central Artery Stiffness in Hypertension and Aging: A Problem With Cause and Consequence. *Circulation Research*, **118**(3), 379–381. https://doi.org/10.1161/CIRCRESAHA.115.307722
89. **Humphrey, J. D.**, & **Schwartz, M. A.** (2021). Vascular Mechanobiology: Homeostasis, Adaptation, and Disease. *Https://Doi.Org/10.1146/Annurev-Bioeng-092419-060810*, **23**, 1–27. https://doi.org/10.1146/ANNUREV-BIOENG-092419-060810
90. **Ilea, D. E.**, **Duffy, C.**, **Kavanagh, L.**, **Stanton, A.**, & **Whelan, P. F.** (2013). Fully automated segmentation and tracking of the intima media thickness in ultrasound video sequences of the common carotid artery. *IEEE Transactions on Ultrasonics, Ferroelectrics, and Frequency Control*, **60**(1), 158–177. https://doi.org/10.1109/TUFFC.2013.2547
91. **Imholz, B. P. M.**, **Wieling, W.**, **Van Montfrans, G. A.**, & **Wesseling, K. H.** (1998). Fifteen years experience with finger arterial pressure monitoring: Assessment of the technology. *Cardiovascular Research*, **38**(3), 605–616. https://doi.org/10.1016/S0008-6363(98)00067-4
92. **Izakian, H.**, **Pedrycz, W.**, & **Jamal, I.** (2015). Fuzzy clustering of time series data using dynamic time warping distance. *Engineering Applications of Artificial Intelligence*, **39**, 235–244. https://doi.org/10.1016/j.engappai.2014.12.015
93. **Jaffe, A. T.**, **Zubajlo, R. E.**, **Daniel, L.**, & **Anthony, B. W.** (2022). Automated Force-Coupled Ultrasound Method for Calibration-Free Carotid Artery Blood Pressure Estimation. *Ultrasound in Medicine & Biology*, **48**(9), 1806–1821. https://doi.org/10.1016/J.ULTRASMEDBIO.2022.05.006
94. **Johnson, C. P.**, **Baugh, R.**, **Wilson, C. A.**, & **Burns, J.** (2001). Age related changes in the tunica media of the vertebral artery: implications for the assessment of vessels injured by trauma. *Journal of Clinical Pathology*, **54**(2), 139–145. https://doi.org/10.1136/JCP.54.2.139
95. **Joseph, J.**, **Nabeel, P. M.**, **Shah, M. I.**, & **Sivaprakasam, M.** (2018). Arterial compliance probe for cuffless evaluation of carotid pulse pressure. *PLoS ONE*, **13**(8), 1–19. https://doi.org/10.1371/journal.pone.0202480
96. **Joseph, J.**, **Radhakrishnan, R.**, **Kusmakar, S.**, **Thrivikraman, A. S.**, & **Sivaprakasam, M.** (2015). Technical validation of ARTSENS-an image free device for evaluation of vascular stiffness. *IEEE Journal of Translational Engineering in Health and Medicine*, **3**(April), 1900213. https://doi.org/10.1109/JTEHM.2015.2431471
97. **Joseph, J.**, **Raj, K. V**, **Nabeel, P. M.**, **Shah, M. I.**, **Bhaskar, A.**, **Ganesh, C.**, & **Seshadri, S.** (2020). ARTSENS® Pen — portable easy-to-use device for carotid stiffness measurement: technology validation and clinical-utility assessment. *Biomedical Physics & Engineering Express*, **6**(2), 1–12.
98. **Juonala, M.**, **Järvisalo, M. J.**, **Mäki-Torkko, N.**, **Kähönen, M.**, **Viikari, J. S. A.**, & **Raitakari, O. T.** (2005). Risk factors identified in childhood and decreased carotid artery elasticity in adulthood: the Cardiovascular Risk in Young Finns Study. *Circulation*, **112**(10), 1486–1493. https://doi.org/10.1161/CIRCULATIONAHA.104.502161
99. **Jurasic, M. J.**, **Lovrencic-Huzjan, A.**, **Bedekovic, M. R.**, & **Demarin, V.** (2007).

How to monitor vascular aging with an ultrasound. *Journal of the Neurological Sciences*, **257**(1–2), 139–142. https://doi.org/10.1016/J.JNS.2007.01.027

100. **Kanai, H.**, & **Koiwa, Y.** (2000). Real-time velocimetry for evaluation of change in thickness of arterial wall. *Ultrasonics*, **38**(1), 381–386. https://doi.org/10.1016/S0041-624X(99)00118-3
101. **Karamzadeh, N.**, **Medvedev, A.**, **Azari, A.**, **Gandjbakhche, A.**, & **Najafizadeh, L.** (2013). Capturing dynamic patterns of task-based functional connectivity with EEG. *NeuroImage*, **66**, 311–317. https://doi.org/10.1016/j.neuroimage.2012.10.032
102. **Kayrak, M.**, **Ulgen, M. S.**, **Yazici, M.**, **Yilmaz, R.**, **Demir, K.**, **Dogan, Y.**, … **Bodur, S.** (2010). A comparison of blood pressure and pulse pressure values obtained by oscillometric and central measurements in hypertensive patients. *Blood Pressure*, **19**(2), 98–103. https://doi.org/10.3109/08037050903516318
103. **Khambhati, J.**, **Allard-Ratick, M.**, **Dhindsa, D.**, **Lee, S.**, **Chen, J.**, **Sandesara, P. B.**, … **Sperling, L. S.** (2018). The art of cardiovascular risk assessment. *Clinical Cardiology*, **41**(5), 677–684. https://doi.org/10.1002/clc.22930
104. **Khir, A. W.**, **O'Brien, A.**, **Gibbs, J. S. R.**, & **Parker, K. H.** (2001). Determination of wave speed and wave separation in the arteries. *Journal of Biomechanics*, **34**(9), 1145–1155. https://doi.org/10.1016/S0021-9290(01)00076-8
105. **Koivistoinen, T.**, **Lyytikäinen, L. P.**, **Aatola, H.**, **Luukkaala, T.**, **Juonala, M.**, **Viikari, J.**, … **Hutri-Kähönen, N.** (2018). Pulse Wave Velocity Predicts the Progression of Blood Pressure and Development of Hypertension in Young Adults. *Hypertension (Dallas, Tex. : 1979)*, **71**(3), 451–456. https://doi.org/10.1161/HYPERTENSIONAHA.117.10368
106. **Kollias, A.**, **Lagou, S.**, **Zeniodi, M. E.**, **Boubouchairopoulou, N.**, & **Stergiou, G. S.** (2016). Association of central versus brachial blood pressure with target-organ damage: systematic review and meta-analysis. *Hypertension*, **67**(1), 183–190. https://doi.org/10.1161/HYPERTENSIONAHA.115.06066
107. **Kumar, P. K.**, **Araki, T.**, **Rajan, J.**, **Laird, J. R.**, **Nicolaides, A.**, & **Suri, J. S.** (2018). State-of-the-art review on automated lumen and adventitial border delineation and its measurements in carotid ultrasound. *Computer Methods and Programs in Biomedicine*, **163**, 155–168. https://doi.org/10.1016/j.cmpb.2018.05.015
108. **Laina, A.**, **Stellos, K.**, & **Stamatelopoulos, K.** (2018). Vascular ageing: Underlying mechanisms and clinical implications. *Experimental Gerontology*, **109**(2016), 16–30. https://doi.org/10.1016/j.exger.2017.06.007
109. **Lantelme, P.**, **Mestre, C.**, **Lievre, M.**, **Gressard, A.**, & **Milon, H.** (2002). Heart rate: an important confounder of pulse wave velocity assessment. *Hypertension*, **39**(6), 1083–1087. https://doi.org/10.1161/01.HYP.0000019132.41066.95
110. **Laurent, Stéphane**, & **Boutouyrie, P.** (2015). The structural factor of hypertension: large and small artery alterations. *Circulation Research*, **116**(6), 1007–1021. https://doi.org/10.1161/CIRCRESAHA.116.303596
111. **Laurent, Stephane**, **Cockcroft, J.**, **Van Bortel, L.**, **Boutouyrie, P.**, **Giannattasio, C.**, **Hayoz, D.**, … **Struijker-Boudier, H.** (2006). Expert consensus document on arterial stiffness: methodological issues and clinical applications.

European Heart Journal, **27**(21), 2588–2605. https://doi.org/10.1093/eurheartj/ehl254

112. **Laurent, Stéphane**, **Sharman, J.**, & **Boutouyrie, P.** (2016). Central versus peripheral blood pressure: finding a solution. *Journal of Hypertension*, **34**(8), 1497–1499. https://doi.org/10.1097/HJH.0000000000001000
113. **Li, F.**, **He, Q.**, **Huang, C.**, **Liu, K.**, **Shao, J.**, & **Luo, J.** (2016). High frame rate and high line density ultrasound imaging for local pulse wave velocity estimation using motion matching: A feasibility study on vessel phantoms. *Ultrasonics*, **67**, 41–54. https://doi.org/10.1016/j.ultras.2015.12.015
114. **Li, X.**, **Jiang, J.**, **Zhang, H.**, **Wang, H.**, **Han, D.**, **Zhou, Q.**, … **Qi, Y.** (2017). Measurement of carotid pulse wave velocity using ultrafast ultrasound imaging in hypertensive patients. *Journal of Medical Ultrasonics*, **44**(2), 183–190.
115. **Liang, Q.**, **Wendelhag, I.**, **Wikstrand, J.**, & **Gustavsson, T.** (2000). A multiscale dynamic programming procedure for boundary detection in ultrasonic artery images. *IEEE Transactions on Medical Imaging*, **19**(2), 127–142. https://doi.org/10.1109/42.836372
116. **Liew, S. M.**, **Doust, J.**, & **Glasziou, P.** (2011). Cardiovascular risk scores do not account for the effect of treatment: A review. *Heart*, **97**(9), 689–697. https://doi.org/10.1136/hrt.2010.220442
117. **Lloyd-Jones, D. M.**, **Braun, L. T.**, **Ndumele, C. E.**, **Smith, S. C.**, **Sperling, L. S.**, **Virani, S. S.**, & **Blumenthal, R. S.** (2019). Use of Risk Assessment Tools to Guide Decision-Making in the Primary Prevention of Atherosclerotic Cardiovascular Disease: A Special Report From the American Heart Association and American College of Cardiology. *Journal of the American College of Cardiology*, **73**(24), 3153–3167. https://doi.org/10.1016/J.JACC.2018.11.005
118. **Loizou, C. P.** (2014). A review of ultrasound common carotid artery image and video segmentation techniques. *Medical and Biological Engineering and Computing*, **52**(12), 1073–1093. https://doi.org/10.1007/s11517-014-1203-5
119. **Loizou, C. P.**, **Kasparis, T.**, **Papakyriakou, P.**, **Christodoulou, L.**, **Pantziaris, M.**, & **Pattichis, C. S.** (2012). Video segmentation of the common carotid artery intima media complex. *IEEE 12th International Conference on BioInformatics and BioEngineering, BIBE 2012*, 500–505. https://doi.org/10.1109/BIBE.2012.6399728
120. **Loizou, C. P.**, **Pattichis, C. S.**, **Nicolaides, A. N.**, & **Pantziaris, M.** (2009). Manual and automated media and intima thickness measurements of the common carotid artery. *IEEE Transactions on Ultrasonics, Ferroelectrics, and Frequency Control*, **56**(5), 983–994. https://doi.org/10.1109/TUFFC.2009.1130
121. **Loizou, C. P.**, **Pattichis, C. S.**, **Pantziaris, M.**, **Tyllis, T.**, & **Nicolaides, A.** (2007). Snakes based segmentation of the common carotid artery intima media. *Medical & Biological Engineering & Computing*, **45**(1), 35–49. https://doi.org/10.1007/S11517-006-0140-3
122. **London, G. M.**, & **Pannier, B.** (2010). Arterial functions: How to interpret the complex physiology. *Nephrology Dialysis Transplantation*, **25**(12), 3815–3823. https://doi.org/10.1093/ndt/gfq614
123. **Lopez-gonzalez, A. A.**, **Aguilo, A.**, **Frontera, M.**, **Bennasar-veny, M.**, **Campos, I.**, **Vicente-herrero, T.**, … **Tauler, P.** (2015). *Effectiveness of the Heart Age tool for improving modifiable cardiovascular risk factors in a Southern European population : a randomized trial*.

https://doi.org/10.1177/2047487313518479
124. **Luo, J.**, **Li, R. X.**, & **Konofagou, E. E.** (2012). Pulse wave imaging of the human carotid artery: an in vivo feasibility study. *IEEE Transactions on Ultrasonics, Ferroelectrics, and Frequency Control*, **59**(1), 174–181. https://doi.org/10.1109/TUFFC.2012.2170
125. **Mackenzie, I. S.**, **Wilkinson, I. B.**, & **Cockcroft, J. R.** (2002). Assessment of arterial stiffness in clinical practice. *Q J Med*, **95**(February), 67–74.
126. **Mahmood, B.**, **Ewertsen, C.**, **Carlsen, J.**, & **Nielsen, M. B.** (2016). Ultrasound Vascular Elastography as a Tool for Assessing Atherosclerotic Plaques – A Systematic Literature Review. *Ultrasound International Open*, **2**(4), E106. https://doi.org/10.1055/S-0042-115564
127. **Manterola, H. L.**, **Lo Vercio, L.**, **Díaz, A.**, **del Fresno, M.**, & **Larrabide, I.** (2018). Validation of an open-source tool for measuring carotid lumen diameter and intima–media thickness. *Ultrasound in Medicine and Biology*, **44**(8), 1873–1881. https://doi.org/10.1016/j.ultrasmedbio.2018.04.001
128. **Marín, C.**, **Yubero-Serrano, E. M.**, **López-Miranda, J.**, & **Pérez-Jiménez, F.** (2013). Endothelial aging associated with oxidative stress can be modulated by a healthy mediterranean diet. *International Journal of Molecular Sciences*, **14**(5), 8869–8889. https://doi.org/10.3390/ijms14058869
129. **Mattace-Raso, F. U. S.**, **Hofman, A.**, **Verwoert, G. C.**, **Wittemana, J. C. M.**, **Wilkinson, I.**, **Cockcroft, J.**, … **Dolejsova, M.** (2010). Determinants of pulse wave velocity in healthy people and in the presence of cardiovascular risk factors: 'establishing normal and reference values''.' *European Heart Journal*, **31**(19), 2338–2350. https://doi.org/10.1093/eurheartj/ehq165
130. **Mayer, C. C.**, **Climie, R. E.**, **Hametner, B.**, & **Bruno, R. M.** (2020). The european cost action VascAgeNet fostering innovation - When industry comes to science. *Artery Research*, **26**(3), 125–129. https://doi.org/10.2991/ARTRES.K.200430.001
131. **McEniery, C. M.**, **Cockcroft, J. R.**, **Roman, M. J.**, **Franklin, S. S.**, & **Wilkinson, I. B.** (2014). Central blood pressure: current evidence and clinical importance. *European Heart Journal*, **35**(26), 1719–1725. https://doi.org/10.1093/eurheartj/eht565
132. **McNulty, M.**, **Mahmud, A.**, & **Feely, J.** (2007). Advanced glycation end-products and arterial stiffness in hypertension. *American Journal of Hypertension*, **20**(3), 242–247. https://doi.org/10.1016/J.AMJHYPER.2006.08.009
133. **Meinders, J M**, **Kornet, L.**, **Brands, P. J.**, & **Hoeks, A. P. G.** (2001). Assessment of local pulse wave velocity in arteries using 2D distension waveforms. *Ultrasonic Imaging*, **23**(4), 199–215.
134. **Meinders, Jan M.**, & **Hoeks, A. P. G.** (2004a). Simultaneous assessment of diameter and pressure waveforms in the carotid artery. *Ultrasound in Medicine and Biology*, **30**(2), 147–154. https://doi.org/10.1016/j.ultrasmedbio.2003.10.014
135. **Meinders, Jan M.**, & **Hoeks, A. P. G.** (2004b). Simultaneous assessment of diameter and pressure waveforms in the carotid artery. *Ultrasound in Medicine and Biology*, **30**(2), 147–154. https://doi.org/10.1016/j.ultrasmedbio.2003.10.014
136. **Menchón-Lara, R. M.**, **Bastida-Jumilla, M. C.**, **Morales-Sánchez, J.**, & **Sancho-Gómez, J. L.** (2014). Automatic detection of the intima-media thickness in ultrasound images of the common carotid artery using neural networks. *Medical & Biological Engineering & Computing*, **52**(2), 169–181.

https://doi.org/10.1007/S11517-013-1128-4
137. **Mendis, S.** (2017). Global progress in prevention of cardiovascular disease. *Cardiovascular Diagnosis and Therapy*, **7**(Suppl 1), S32–S38. https://doi.org/10.21037/cdt.2017.03.06
138. **Mestanik, M.**, **Spronck, B.**, **Jurko, A.**, **Mestanikova, A.**, **Jurko, T.**, **Butlin, M.**, … **Tonhajzerova, I.** (2020). P135 Assessment of Novel Blood Pressure Corrected Cardio-ankle Vascular Index in Response to Acute Blood Pressure Changes. *Artery Research*, **25**(Supplement 1), S173–S173. https://doi.org/10.2991/ARTRES.K.191224.158
139. **Mirault, T.**, **Pernot, M.**, **Frank, M.**, **Couade, M.**, **Niarra, R.**, **Azizi, M.**, … **Messas, E.** (2015). Carotid stiffness change over the cardiac cycle by ultrafast ultrasound imaging in healthy volunteers and vascular Ehlers-Danlos syndrome. *Journal of Hypertension*, **33**(9), 1890–1896.
140. **Miyashita, H.** (2012). Clinical assessment of central blood pressure. *Current Hypertension Reviews*, **8**(2), 80–90. https://doi.org/10.2174/157340212800840708
141. **Miyashita, S.**, **Murotsuki, J.**, **Muromoto, J.**, **Ozawa, K.**, **Yaegashi, N.**, **Hasegawa, H.**, & **Kanai, H.** (2015). Measurement of internal diameter changes and pulse wave velocity in fetal descending aorta using the ultrasonic phased-tracking method in normal and growth-restricted fetuses. *Ultrasound in Medicine and Biology*, **41**(5), 1311–1319.
142. **Molinari, F.**, **Meiburger, K. M.**, **Zeng, G.**, **Acharya, U. R.**, **Liboni, W.**, **Nicolaides, A.**, & **Suri, J. S.** (2012). Carotid artery recognition system: a comparison of three automated paradigms for ultrasound images. *Medical Physics*, **39**(1), 378–391. https://doi.org/10.1118/1.3670373
143. **Molinari, F.**, **Pattichis, C. S.**, **Zeng, G.**, **Saba, L.**, **Acharya, U. R.**, **Sanfilippo, R.**, … **Suri, J. S.** (2012). Completely automated multiresolution edge snapper-A new technique for an accurate carotid ultrasound IMT measurement: Clinical validation and benchmarking on a multi-institutional database. *IEEE Transactions on Image Processing*, **21**(3), 1211–1222. https://doi.org/10.1109/TIP.2011.2169270
144. **Molinari, F.**, **Zeng, G.**, & **Suri, J. S.** (2010a). A state of the art review on intima-media thickness (IMT) measurement and wall segmentation techniques for carotid ultrasound. *Computer Methods and Programs in Biomedicine*, **100**(3), 201–221. https://doi.org/10.1016/j.cmpb.2010.04.007
145. **Molinari, F.**, **Zeng, G.**, & **Suri, J. S.** (2010b). Automatic recognition and validation of the common carotid artery wall segmentation in 100 longitudinal ultrasound images: an integrated approach using feature selection, fitting and classification. *Medical Imaging 2010: Image Processing*, **7623**, 76233W. https://doi.org/10.1117/12.843979
146. **Montero, D.**, **Pierce, G. L.**, **Stehouwer, C. D. A.**, **Padilla, J.**, & **Thijssen, D. H. J.** (2015). The impact of age on vascular smooth muscle function in humans. *Journal of Hypertension*, **33**(3), 445. https://doi.org/10.1097/HJH.0000000000000446
147. **Mukkamala, R.**, **Hahn, J. O.**, **Inan, O. T.**, **Mestha, L. K.**, **Kim, C. S.**, **Toreyin, H.**, & **Kyal, S.** (2015). Toward ubiquitous blood pressure monitoring via pulse transit time: theory and practice. *IEEE Transactions on Biomedical Engineering*, **62**(8), 1879–1901. https://doi.org/10.1109/tbme.2015.2441951
148. **Müller, M.** (2007). *Information retrieval for music and motion*. Springer.

149. **Nabeel, P. M.**, **Chandran, D. S.**, **Kaur, P.**, **Thanikachalam, S.**, **Sivaprakasam, M.**, & **Joseph, J.** (2021). Association of incremental pulse wave velocity with cardiometabolic risk factors. *Scientific Reports*, **11**(1), 1–10. https://doi.org/10.1038/s41598-021-94723-2
150. **Nabeel, P. M.**, **Joseph, J.**, **Karthik, S.**, **Sivaprakasam, M.**, & **Chenniappan, M.** (2018). Bi-Modal arterial compliance probe for calibration-free cuffless blood pressure estimation. *IEEE Transactions on Biomedical Engineering*, **65**(11), 2392–2404. https://doi.org/10.1109/TBME.2018.2866332
151. **Nabeel, P. M.**, **Raj, K. V.**, **Joseph, J.**, **Abhidev, V. V.**, & **Sivaprakasam, M.** (2019). Local pulse wave velocity: theory, methods, advancements, and clinical applications. *IEEE Reviews in Biomedical Engineering*, **13**, 74–112. https://doi.org/10.1109/RBME.2019.2931587
152. **Nabeel, P. M.**, **Raj, K. V**, **Joseph, J.**, **Abhidev, V. V.**, & **Sivaprakasam, M.** (2020). Local pulse wave velocity: theory, methods, advancements, and clinical applications. *IEEE Reviews in Biomedical Engineering*, **13**, 74–112. https://doi.org/10.1109/RBME.2019.2931587
153. **Nagaoka, R.**, **Masuno, G.**, **Kobayashi, K.**, **Yoshizawa, S.**, **Umemura, S. I.**, & **Saijo, Y.** (2015). Measurement of regional pulse-wave velocity using spatial compound imaging of the common carotid artery in vivo. *Ultrasonics*, **55**(1), 92–103.
154. **Nambi, V.**, **Chambless, L.**, **Folsom, A. R.**, **He, M.**, **Hu, Y.**, **Mosley, T.**, … **Ballantyne, C. M.** (2010). Carotid intima-media thickness and presence or absence of plaque improves prediction of coronary heart disease risk: the ARIC (Atherosclerosis Risk In Communities) study. *Journal of the American College of Cardiology*, **55**(15), 1600–1607. https://doi.org/10.1016/J.JACC.2009.11.075
155. **Nauleau, P.**, **Apostolakis, I.**, **McGarry, M.**, & **Konofagou, E.** (2018). Cross-correlation analysis of pulse wave propagation in arteries: in vitro validation and in vivo feasibility. *Physics in Medicine and Biology*, **63**(11), 1–19.
156. **Nichols, W. W.**, **O'Rourke, M. F.**, & **Vlachopoulos, C.** (2011). *Mcdonald's blood flow in ateries: theoretical, experimental and clinical principles* (6th ed.). London: Hodder Arnold.
157. **Nichols, W. W.**, **O'Rourke, M. F.**, **Vlachopoulos, C.**, **Hoeks, A. P.**, & **Reneman, R. S.** (2011). McDonald's blood flow in arteries theoretical, experimental and clinical principles. In *Hodder Arnold* (6th ed.). https://doi.org/10.1111/j.1540-8175.1991.tb01207.x
158. **Nilsson, P.M.**, **Olsen, M. H.**, & **Laurent, S.** (2015). *Early vascular aging (EVA): New directions in cardiovascular protection*. Elsevier Science.
159. **Nilsson, Peter M.** (2008). Early vascular aging (EVA): consequences and prevention. *Vascular Health and Risk Management*, **4**(3), 547–552. https://doi.org/10.2147/vhrm.s1094
160. **Nilsson, Peter M.**, **Boutouyrie, P.**, & **Laurent, S.** (2009). Vascular aging: A tale of eva and ADAM in cardiovascular risk assessment and prevention. *Hypertension*, **54**(1), 3–10. https://doi.org/10.1161/HYPERTENSIONAHA.109.129114
161. **Nilsson, Peter M.**, **Khalili, P.**, & **Franklin, S. S.** (2014). Blood pressure and pulse wave velocity as metrics for evaluating pathologic ageing of the cardiovascular system. *Blood Pressure*, **23**(1), 17–30. https://doi.org/10.3109/08037051.2013.796142

162. **O'Rourke, M. F.** (2007). Arterial aging: Pathophysiological principles. *Vascular Medicine*, **12**(4), 329–341. https://doi.org/10.1177/1358863X07083392
163. **O'Rourke, M. F.** (2016). Carotid artery tonometry: Pros and cons. *American Journal of Hypertension*, **29**(3), 296–298. https://doi.org/10.1093/ajh/hpv194
164. **Palombo, C.**, **Kozakova, M.**, **Guraschi, N.**, **Bini, G.**, **Cesana, F.**, **Castoldi, G.**, … **Giannattasio, C.** (2012). Radiofrequency-based carotid wall tracking: A comparison between two different systems. *Journal of Hypertension*, **30**(8), 1614–1619. https://doi.org/10.1097/HJH.0b013e328354dd44
165. **Pannier, B. M.**, **Avolio, A. P.**, **Hoeks, A.**, **Mancia, G.**, & **Takazawa, K.** (2002). Methods and devices for measuring arterial compliance in humans. *American Journal of Hypertension*, **15**(8), 743–753.
166. **Pannier, B.**, **Slama, M. A.**, **London, G. M.**, **Safar, M. E.**, & **Cuche, J. L.** (1995). Carotid arterial hemodynamics in response to LBNP in normal subjects: methodological aspects. *Journal of Applied Physiology*, **79**(5), 1546–1555. https://doi.org/10.1152/jappl.1995.79.5.1546
167. **Papaioannou, T. G.**, **Karageorgopoulou, T. D.**, **Sergentanis, T. N.**, **Protogerou, A. D.**, **Psaltopoulou, T.**, **Sharman, J. E.**, … **Tousoulis, D.** (2016). Accuracy of commercial devices and methods for noninvasive estimation of aortic systolic blood pressure a systematic review and meta-analysis of invasive validation studies. *Journal of Hypertension*, **34**(7), 1237–1248. https://doi.org/10.1097/HJH.0000000000000921
168. **Park, J. H.**, **Seo, E.**, **Choi, W.**, & **Lee, S. J.** (2022). Ultrasound deep learning for monitoring of flow–vessel dynamics in murine carotid artery. *Ultrasonics*, **120**(November 2021), 106636. https://doi.org/10.1016/j.ultras.2021.106636
169. **Pascaner, A. F.**, **Craiem, D.**, **Casciaro, M. E.**, **Danielo, R.**, **Graf, S.**, & **Guevara, E.** (2015). Continuous assessment of carotid intima-media thickness applied to estimate a volumetric compliance using B-mode ultrasound sequences. *Physiological Measurement*, **36**(3), 397–407. https://doi.org/10.1088/0967-3334/36/3/397
170. **Patzak, A.**, **Mendoza, Y.**, **Gesche, H.**, & **Konermann, M.** (2015). Continuous blood pressure measurement using the pulse transit time: Comparison to intra-arterial measurement. *Blood Pressure*, **24**(4), 217–221. https://doi.org/10.3109/08037051.2015.1030901
171. **Peng, X.**, **Haldar, S.**, **Deshpande, S.**, **Irani, K.**, & **Kass, D. A.** (2003). Wall stiffness suppresses Akt/eNOS and cytoprotection in pulse-perfused endothelium. *Hypertension (Dallas, Tex. : 1979)*, **41**(2), 378–381. https://doi.org/10.1161/01.HYP.0000049624.99844.3D
172. **Pernot, M.**, **Fujikura, K.**, **Fung-Kee-Fung, S. D.**, & **Konofagou, E. E.** (2007). ECG-gated, mechanical and electromechanical wave imaging of cardiovascular tissues in vivo. *Ultrasound in Medicine and Biology*, **33**(7), 1075–1085.
173. **Peters, S. A. E.**, & **Bots, M. L.** (2013). Carotid intima-media thickness studies: study design and data analysis. *Journal of Stroke*, **15**(1), 38–48. https://doi.org/10.5853/jos.2013.15.1.38
174. **Pielmus, A. G.**, **Klum, M.**, **Tigges, T.**, **Orglmeister, R.**, & **Urban, M.** (2020). Progressive Dynamic Time Warping for Noninvasive Blood Pressure Estimation. *Current Directions in Biomedical Engineering*, **6**(3), 3–6. https://doi.org/10.1515/cdbme-2020-3148
175. **Pignoli, P.**, **Tremoli, E.**, **Poli, A.**, **Oreste, P.**, & **Paoletti, R.** (1986). Intimal

plus medial thickness of the arterial wall: a direct measurement with ultrasound imaging. *Circulation*, **74**(6), 1399–1406. https://doi.org/10.1161/01.CIR.74.6.1399

176. **Polak, J. F.**, **Johnson, C.**, **Harrington, A.**, **Wong, Q.**, **O'Leary, D. H.**, **Burke, G.**, & **Yanez, N. D.** (2012). Changes in carotid intima-media thickness during the cardiac cycle: the multi-ethnic study of atherosclerosis. *Journal of the American Heart Association*, **1**(4), 1–8. https://doi.org/10.1161/jaha.112.001420
177. **Polak, J. F.**, **Meisner, A.**, **Pencina, M. J.**, **Wolf, P. A.**, & **D'Agostino, R. B.** (2012). Variations in common carotid artery intima-media thickness during the cardiac cycle: Implications for cardiovascular risk assessment. *Journal of the American Society of Echocardiography*, **25**(9), 1023–1028. https://doi.org/10.1016/j.echo.2012.05.007
178. **Qasem, A.**, & **Avolio, A.** (2008). Determination of aortic pulse wave velocity from waveform decomposition of the central aortic pressure pulse. *Hypertension*, **51**(2), 188–195. https://doi.org/10.1161/HYPERTENSIONAHA.107.092676
179. **Quinaglia, T.**, **Bensalah, M. Z.**, **Bollache, E.**, **Kachenoura, N.**, **Soulat, G.**, **Boutouyrie, P.**, … **Mousseaux, E.** (2018). Differential impact of local and regional aortic stiffness on left ventricular remodeling: a cardiovascular magnetic resonance study. *Journal of Hypertension*, **36**(3), 552–559.
180. **Rabben, S I**, **Baerum, S.**, **Sørhus, V.**, & **Torp, H.** (2002). *Ultrasound-based vessel wall tracking: an auto-correlation technique with RF center frequency estimation*. **28**(4), 507–517.
181. **Rabben, Stein Inge**, **Stergiopulos, N.**, **Hellevik, L. R.**, **Smiseth, O. A.**, **Slørdahl, S.**, **Urheim, S.**, & **Angelsen, B.** (2004). An ultrasound-based method for determining pulse wave velocity in superficial arteries. *Journal of Biomechanics*, **37**(10), 1615–1622. https://doi.org/10.1016/j.jbiomech.2003.12.031
182. **Raghavendra, B. S.**, **Bera, D.**, **Bopardikar, A. S.**, & **Narayanan, R.** (2011). Cardiac arrhythmia detection using dynamic time warping of ECG beats in e-healthcare systems. *2011 IEEE International Symposium on a World of Wireless, Mobile and Multimedia Networks, WoWMoM 2011 - Digital Proceedings*. https://doi.org/10.1109/WoWMoM.2011.5986196
183. **Raj, V. K.**, **Joseph, J.**, **Nabeel, P. M.**, & **Sivaprakasam, M.** (2020). Automated measurement of compression-decompression in arterial diameter and wall thickness by image-free ultrasound. *Computer Methods and Programs in Biomedicine*, **194**, 1–12. https://doi.org/10.1016/j.cmpb.2020.105557
184. **Raj, K. V**, **Nabeel, P. M.**, **Joseph, J.**, & **Sivaprakasam, M.** (2019). Methodological and measurement concerns of local pulse wave velocity assessment. *IEEE International Symposium on Medical Measurements and Applications (MeMeA)*, 1–6. https://doi.org/10.1109/MeMeA.2019.8802181
185. **Rastegar, S.**, **GholamHosseini, H.**, & **Lowe, A.** (2019). Non-invasive continuous blood pressure monitoring systems: current and proposed technology issues and challenges. *Australasian Physical and Engineering Sciences in Medicine*, **43**(1), 11–28. https://doi.org/10.1007/s13246-019-00813-x
186. **Reneman, R. S.**, & **Hoeks, A. P. G.** (2000). Noninvasive vascular ultrasound: an asset in vascular medicine. *Cardiovascular Research*, **45**(1), 27–35. https://doi.org/10.1016/S0008-6363(99)00282-5
187. **Reneman, R. S.**, **Meinders, J. M.**, & **Hoeks, A. P. G.** (2005). Non-invasive ultrasound in arterial wall dynamics in humans: What have we learned and what

remains to be solved. *European Heart Journal*, **26**(10), 960–966. https://doi.org/10.1093/eurheartj/ehi177

188. **Rodríguez-Mañas, L.**, **El-Assar, M.**, **Vallejo, S.**, **López-Dóriga, P.**, **Solís, J.**, **Petidier, R.**, … **Sánchez-Ferrer, C. F.** (2009). Endothelial dysfunction in aged humans is related with oxidative stress and vascular inflammation. *Aging Cell*, **8**(3), 226–238. https://doi.org/10.1111/J.1474-9726.2009.00466.X
189. **Roman, M. J.**, **Naqvi, T. Z.**, **Gardin, J. M.**, **Gerhard-Herman, M.**, **Jaff, M.**, & **Mohler, E.** (2006). Clinical application of noninvasive vascular ultrasound in cardiovascular risk stratification: a report from the American Society of Echocardiography and the Society of Vascular Medicine and Biology. *Journal of the American Society of Echocardiography : Official Publication of the American Society of Echocardiography*, **19**(8), 943–954. https://doi.org/10.1016/J.ECHO.2006.04.020
190. **Rossi, A. C.**, **Brands, P. J.**, & **Hoeks, A. P. G.** (2008). Automatic recognition of the common carotid artery in longitudinal ultrasound B-mode scans. *Medical Image Analysis*, **12**(6), 653–665. https://doi.org/10.1016/j.media.2008.03.003
191. **Rossi, A. C.**, **Brands, P. J.**, & **Hoeks, A. P. G.** (2010). Automatic localization of intimal and adventitial carotid artery layers with noninvasive ultrasound: a novel algorithm providing scan quality control. *Ultrasound in Medicine and Biology*, **36**(3), 467–479. https://doi.org/10.1016/j.ultrasmedbio.2009.12.007
192. **Roth, G. A.**, **Mensah, G. A.**, **Johnson, C. O.**, **Addolorato, G.**, **Ammirati, E.**, **Baddour, L. M.**, … **Fuster, V.** (2020). Global Burden of Cardiovascular Diseases and Risk Factors, 1990–2019: Update From the GBD 2019 Study. *Journal of the American College of Cardiology*, **76**(25), 2982–3021. https://doi.org/https://doi.org/10.1016/j.jacc.2020.11.010
193. **Rueb, K.**, **Mynard, J.**, **Liu, R.**, **Wake, M.**, **Vuillermin, P.**, **Ponsonby, A. L.**, … **Burgner, D. P.** (2017). Changes in carotid artery intima-media thickness during the cardiac cycle – a comparative study in early childhood, mid-childhood, and adulthood. *Vasa - European Journal of Vascular Medicine*, **46**(4), 275–281. https://doi.org/10.1024/0301-1526/a000630
194. **Ruesink, T.**, **Medero, R.**, **Rutkowski, D.**, & **Roldán-Alzate, A.** (2018). In vitro validation of 4D flow MRI for local pulse wave velocity estimation. *Cardiovascular Engineering and Technology*, **9**(4), 674–687.
195. **Sahani, A. K.**, **Shah, M. I.**, **Joseph, J.**, & **Sivaprakasam, M.** (2016). Carotid and jugular classification in ARTSENS. *IEEE Journal of Biomedical and Health Informatics*, **20**(2), 440–449. https://doi.org/10.1109/JBHI.2015.2403283
196. **Santhanam, L.**, **Christianson, D. W.**, **Nyhan, D.**, & **Berkowitz, D. E.** (2008). Arginase and vascular aging. *Journal of Applied Physiology (Bethesda, Md. : 1985)*, **105**(5), 1632–1642. https://doi.org/10.1152/JAPPLPHYSIOL.90627.2008
197. **Santhiyakumari, N.**, **Rajendran, P.**, **Madheswaran, M.**, & **Suresh, S.** (2011). Detection of the intima and media layer thickness of ultrasound common carotid artery image using efficient active contour segmentation technique. *Medical & Biological Engineering & Computing*, **49**(11), 1299–1310. https://doi.org/10.1007/S11517-011-0800-9
198. **Segers, P.**, **Rabben, S. I.**, **De Backer, J.**, **De Sutter, J.**, **Gillebert, T. C.**, **Van Bortel, L.**, & **Verdonck, P.** (2004). Functional analysis of the common carotid artery: Relative distension differences over the vessel wall measured in vivo. *Journal of Hypertension*, **22**(5), 973–981. https://doi.org/10.1097/00004872-

200405000-00020
199. **Segers, P.**, **Rietzschel, E. R.**, & **Chirinos, J. A.** (2020). How to Measure Arterial Stiffness in Humans. *Arteriosclerosis, Thrombosis, and Vascular Biology*, (May), 1034–1043. https://doi.org/10.1161/ATVBAHA.119.313132
200. **Segers, P.**, **Swillens, A.**, **Taelman, L.**, & **Vierendeels, J.** (2014). Wave reflection leads to over- and underestimation of local wave speed by the PU- and QA-loop methods: theoretical basis and solution to the problem. *Physiological Measurement*, **35**(5), 847–861.
201. **Selzer, R. H.**, **Mack, W. J.**, **Lee, P. L.**, **Kwong-Fu, H.**, & **Hodis, H. N.** (2001). Improved common carotid elasticity and intima-media thickness measurements from computer analysis of sequential ultrasound frames. *Atherosclerosis*, **154**(1), 185–193. https://doi.org/10.1016/S0021-9150(00)00461-5
202. **Seo, J.**, **Pietrangelo, S. J.**, **Lee, H. S.**, & **Sodini, C. G.** (2015). Noninvasive arterial blood pressure waveform monitoring using two-element ultrasound system. *IEEE Transactions on Ultrasonics, Ferroelectrics, and Frequency Control*, **62**(4), 776–784. https://doi.org/10.1109/TUFFC.2014.006904
203. **Shadwick, R. E.** (1999). Mechanical design in arteries. *Journal of Experimental Biology*, **202**(23), 3305–3313.
204. **Shah, M.**, **Joseph, J.**, & **Sivaprakasam, M.** (2014). Ultrasound signal quality parameterization for image-free evaluation of arterial stiffness. *36th Annual International Conference of the IEEE Engineering in Medicine and Biology Society*, 2326–2329. https://doi.org/10.1109/EMBC.2014.6944086
205. **Sharman, J. E.**, & **Laurent, S.** (2013). Central blood pressure in the management of hypertension: soon reaching the goal? *Journal of Human Hypertension*, **27**(7), 405–411. https://doi.org/10.1038/jhh.2013.23
206. **Sharman, James E.**, **Avolio, A. P.**, **Baulmann, J.**, **Benetos, A.**, **Blacher, J.**, **Blizzard, C. L.**, … **Vlachopoulos, C.** (2017). Validation of non-invasive central blood pressure devices: ARTERY Society task force consensus statement on protocol standardization. *European Heart Journal*, **38**(37), 2805–2812. https://doi.org/10.1093/eurheartj/ehw632
207. **Shelly Medical Imaging Technologies**. (2019a). Blood mimicking fluid for doppler ultrasound. Retrieved November 27, 2019, from http://www.simutec.com/Products/bloodmimicking.html
208. **Shelly Medical Imaging Technologies**. (2019b). Carotid bifurcation doppler flow phantoms. Retrieved November 27, 2019, from http://www.simutec.com/Products/dopplerflowphantoms.html
209. **Shi, F.**, **Yang, Q.**, **Guo, X.**, **Qureshi, T. A.**, **Tian, Z.**, **Miao, H.**, … **Fan, Z.** (2019). Intracranial Vessel Wall Segmentation Using Convolutional Neural Networks. *IEEE Transactions on Biomedical Engineering*, **66**(10), 2840–2847. https://doi.org/10.1109/TBME.2019.2896972
210. **Shirai, K.**, **Utino, J.**, **Otsuka, K.**, & **Takata, M.** (2006). A novel blood pressure-independent arterial wall stiffness parameter; cardio-ankle vascular index (CAVI). *Journal of Atherosclerosis and Thrombosis*, **13**(2), 101–107. https://doi.org/10.5551/JAT.13.101
211. **Sifakis, E. G.**, & **Golemati, S.** (2014). Robust carotid artery recognition in longitudinal B-mode ultrasound images. *IEEE Transactions on Image Processing*, **23**(9), 3762–3772. https://doi.org/10.1109/TIP.2014.2332761
212. **Sigrist, R. M. S.**, **Liau, J.**, **Kaffas, A. El**, **Chammas, M. C.**, & **Willmann, J.**

K. (2017). Ultrasound elastography: Review of techniques and clinical applications. *Theranostics*, **7**(5), 1303–1329. https://doi.org/10.7150/thno.18650

213. **Simon, A.**, & **Levenson, J.** (2001). Effect of hypertension on viscoelasticity of large arteries in humans. *Current Hypertension Reports*, **3**(1), 74–78. https://doi.org/10.1007/S11906-001-0084-9
214. **Simova, I.**, **Katova, T.**, **Santoro, C.**, & **Galderisi, M.** (2016). Comparison between regional and local pulse-wave velocity data. *Echocardiography*, **33**(1), 77–81.
215. **Spronck, B.** (2021). Disentangling Arterial Stiffness and Blood Pressure. *Heart Lung and Circulation*, **30**(11), 1599–1601. https://doi.org/10.1016/j.hlc.2021.05.086
216. **Spronck, B.**, **Avolio, A. P.**, **Tan, I.**, **Butlin, M.**, **Reesink, K. D.**, & **Delhaas, T.** (2017). Arterial stiffness index beta and cardio-ankle vascular index inherently depend on blood pressure but can be readily corrected. *Journal of Hypertension*, **35**(1), 98–104. https://doi.org/10.1097/HJH.0000000000001132
217. **Spronck, B.**, **Heusinkveld, M. H. G.**, **Vanmolkot, F. H.**, **Roodt, J. O. t.**, **Hermeling, E.**, **Delhaas, T.**, … **Reesink, K. D.** (2015). Pressure-dependence of arterial stiffness: Potential clinical implications. *Journal of Hypertension*, **33**(2), 330–338. https://doi.org/10.1097/HJH.0000000000000407
218. **Stein, J. H.**, **Korcarz, C. E.**, **Mays, M. E.**, **Douglas, P. S.**, **Palta, M.**, **Zhang, H.**, … **Fan, L.** (2005). A semiautomated ultrasound border detection program that facilitates clinical measurement of ultrasound carotid intima-media thickness. *Journal of the American Society of Echocardiography : Official Publication of the American Society of Echocardiography*, **18**(3), 244–251. https://doi.org/10.1016/J.ECHO.2004.12.002
219. **Swalen, M. J. P.**, & **Khir, A. W.** (2009). Resolving the time lag between pressure and flow for the determination of local wave speed in elastic tubes and arteries. *Journal of Biomechanics*, **42**(10), 1574–1577.
220. **Swillens, A.**, & **Segers, P.** (2008). Assessment of arterial pressure wave reflection: Methodological considerations. *Artery Research*, **2**(4), 122–131. https://doi.org/10.1016/j.artres.2008.05.001
221. **Taddei, S.**, **Virdis, A.**, **Ghiadoni, L.**, **Salvetti, G.**, **Bernini, G.**, **Magagna, A.**, & **Salvetti, A.** (2001). Age-Related Reduction of NO Availability and Oxidative Stress in Humans. *Hypertension*, **38**(2), 274–279. https://doi.org/10.1161/01.HYP.38.2.274
222. **Tang, C. J.**, **Lee, P. Y.**, **Chuang, Y. H.**, & **Huang, C. C.** (2020). Measurement of local pulse wave velocity for carotid artery by using an ultrasound-based method. *Ultrasonics*, **102**(1), 106064. https://doi.org/10.1016/j.ultras.2020.106064
223. **Teynor, A.**, **Caviezel, S.**, **Dratva, J.**, **Künzli, N.**, & **Schmidt-Trucksäss, A.** (2012). An automated, interactive analysis system for ultrasound sequences of the common carotid artery. *Ultrasound in Medicine and Biology*, **38**(8), 1440–1450. https://doi.org/10.1016/j.ultrasmedbio.2012.03.015
224. **Thijssen, D. H. J.**, **Rongen, G. A.**, **Van Dijk, A.**, **Smits, P.**, & **Hopman, M. T. E.** (2007). Enhanced endothelin-1-mediated leg vascular tone in healthy older subjects. *J Appl Physiol*, **103**, 852–857. https://doi.org/10.1152/japplphysiol.00357.2007.-Advanced
225. **Touboul, P. J.**, **Hennerici, M. G.**, **Meairs, S.**, **Adams, H.**, **Amarenco, P.**, **Bornstein, N.**, … **Woo, K. S.** (2012). Mannheim carotid intima-media thickness

and plaque consensus (2004-2006-2011). An update on behalf of the advisory board of the 3rd, 4th and 5th watching the risk symposia, at the 13th, 15th and 20th European stroke conferences, Mannheim, Germany, 2004, B. *Cerebrovascular Diseases*, **34**(4), 290–296. https://doi.org/10.1159/000343145.Mannheim

226. **Touboul, P. J.**, **Prati, P.**, **Scarabin, P. Y.**, **Adrai, V.**, **Thibout, E.**, & **Ducimetière, P.** (1992). Use of monitoring software to improve the measurement of carotid wall thickness by B-mode imaging - PubMed. *Journal of Hypertension*, **10**(5), S37–S42.
227. **Townsend, R. R.** (2019). Arterial Stiffness in CKD: A Review. *American Journal of Kidney Diseases*, **73**(2), 240–247. https://doi.org/10.1053/j.ajkd.2018.04.005
228. **Triantafyllou, A.**, **Elia, S.-A.**, **Park, C.**, **Climie, R.**, **Mayer, C. C.**, **Weber, T.**, & **Panayiotou, A. G.** (2022). Awareness and limitations of measuring vascular ageing in everyday practice: A pilot qualitative analysis from VascAgeNet (CA18216). *Journal of Hypertension*, **40**(Suppl 1), e49. https://doi.org/10.1097/01.HJH.0000835676.60261.24
229. **Tsao, C. W.**, **Himali, J. J.**, **Beiser, A. S.**, **Larson, M. G.**, **Decarli, C.**, **Vasan, R. S.**, … **Seshadri, S.** (2016). Association of arterial stiffness with progression of subclinical brain and cognitive disease. *Neurology*, **86**(7), 619. https://doi.org/10.1212/WNL.0000000000002368
230. **Udupa, J. K.**, **LeBlanc, V. R.**, **Zhuge, Y.**, **Imielinska, C.**, **Schmidt, H.**, **Currie, L. M.**, … **Woodburn, J.** (2006). A framework for evaluating image segmentation algorithms. *Computerized Medical Imaging and Graphics*, **30**(2), 75–87. https://doi.org/10.1016/j.compmedimag.2005.12.001
231. **Uejima, T.**, **Dunstan, F. D.**, **Arbustini, E.**, **Łoboz-Grudzień, K.**, **Hughes, A. D.**, **Carerj, S.**, … **Fraser, A. G.** (2019). Age-specific reference values for carotid arterial stiffness estimated by ultrasonic wall tracking. *Journal of Human Hypertension*. https://doi.org/10.1038/s41371-019-0228-5
232. **Van Bortel, L. M. A. B.**, **Struijker-Boudier, H. A. J.**, & **Safar, M. E.** (2001). Pulse pressure, arterial stiffness, and drug treatment of hypertension. *Hypertension (Dallas, Tex. : 1979)*, **38**(4), 914–921. https://doi.org/10.1161/HY1001.095773
233. **van den Munckhof, I. C. L.**, **Jones, H.**, **Hopman, M. T. E.**, **de Graaf, J.**, **Nyakayiru, J.**, **van Dijk, B.**, … **Thijssen, D. H. J.** (2018). Relation between age and carotid artery intima-medial thickness: a systematic review. *Clinical Cardiology*, **41**(5), 698–704. https://doi.org/10.1002/CLC.22934
234. **van den Munckhof, I.**, **Scholten, R.**, **Cable, N. T.**, **Hopman, M. T. E.**, **Green, D. J.**, & **Thijssen, D. H. J.** (2012). Impact of age and sex on carotid and peripheral arterial wall thickness in humans. *Acta Physiologica*, **206**(4), 220–228. https://doi.org/10.1111/J.1748-1716.2012.02457.X
235. **Vardoulis, O.**, **Papaioannou, T. G.**, & **Stergiopulos, N.** (2013). Validation of a novel and existing algorithms for the estimation of pulse transit time: advancing the accuracy in pulse wave velocity measurement. *American Journal of Physiology-Heart and Circulatory Physiology*, **304**(11), H1558--H1567.
236. **Vattikuti, R.**, & **Towler, D. A.** (2004). Osteogenic regulation of vascular calcification: an early perspective. *American Journal of Physiology. Endocrinology and Metabolism*, **286**(5). https://doi.org/10.1152/AJPENDO.00552.2003
237. **Verdecchia, P.**, **Angeli, F.**, & **Taddei, S.** (2006). At the beginning of stiffening:

Endothelial dysfunction meets "pulsology." *Hypertension*, **48**(4), 541–542. https://doi.org/10.1161/01.HYP.0000239236.12524.d3

238. **Vermeersch, S. J.**, **Rietzschel, E. R.**, **De Buyzere, M. L.**, **De Bacquer, D.**, **De Backer, G.**, **Van Bortel, L. M.**, … **Segers, P.** (2008). Determining carotid artery pressure from scaled diameter waveforms: Comparison and validation of calibration techniques in 2026 subjects. *Physiological Measurement*, **29**(11), 1267–1280. https://doi.org/10.1088/0967-3334/29/11/003
239. **Vriz, O.**, **Driussi, C.**, **La Carrubba, S.**, **Di Bello, V.**, **Zito, C.**, **Carerj, S.**, & **Antonini-Canterin, F.** (2013). Comparison of sequentially measured Aloka echo-tracking one-point pulse wave velocity with SphygmoCor carotid–femoral pulse wave velocity. *SAGE Open Medicine*, **1**, 205031211350756. https://doi.org/10.1177/2050312113507563
240. **Wagenseil, J. E.**, & **Mecham, R. P.** (2009). Vascular Extracellular Matrix and Arterial Mechanics. *Physiological Reviews*, **89**(3), 957. https://doi.org/10.1152/PHYSREV.00041.2008
241. **Waldstein, S. R.**, **Rice, S. C.**, **Thayer, J. F.**, **Najjar, S. S.**, **Scuteri, A.**, & **Zonderman, A. B.** (2008). Pulse Pressure and Pulse Wave Velocity Are Related to Cognitive Decline in the Baltimore Longitudinal Study of Aging. *Hypertension*, **51**(1), 99–104. https://doi.org/10.1161/HYPERTENSIONAHA.107.093674
242. **Wang, C.**, **Li, X.**, **Hu, H.**, **Zhang, L.**, **Huang, Z.**, **Lin, M.**, … **Xu, S.** (2018). Monitoring of the central blood pressure waveform via a conformal ultrasonic device. *Nature Biomedical Engineering*, 687–695.
243. **Wang, D. C.**, **Klatzky, R.**, **Wu, B.**, **Weller, G.**, **Sampson, A. R.**, & **Stetten, G. D.** (2009). Fully automated common carotid artery and internal jugular vein identification and tracking using B-mode ultrasound. *IEEE Transactions on Biomedical Engineering*, **56**(6), 1691–1699. https://doi.org/10.1109/TBME.2009.2015576
244. **Wang, Z.**, **Yang, Y.**, **Yuan, L. J.**, **Liu, J.**, **Duan, Y. Y.**, & **Cao, T. S.** (2015). Noninvasive method for measuring local pulse wave velocity by dual pulse wave doppler: in vitro and in vivo studies. *PLoS ONE*, **10**(3), 1–13. https://doi.org/10.1371/journal.pone.0120482
245. **Weber, T.**, & **Mayer, C. C.** (2020). "Man is as old as his arteries" Taken Literally: In search of the best metric. *Hypertension*, 1425–1427. https://doi.org/10.1161/HYPERTENSIONAHA.120.16128
246. **Wendelhag, I.**, **Liang, Q.**, **Gustavsson, T.**, & **Wikstrand, J.** (1997). A New Automated Computerized Analyzing System Simplifies Readings and Reduces the Variability in Ultrasound Measurement of Intima-Media Thickness. *Stroke*, **28**(11), 2195–2200. https://doi.org/10.1161/01.STR.28.11.2195
247. **Westerhof, B. E.**, **Guelen, I.**, **Westerhof, N.**, **Karemaker, J. M.**, & **Avolio, A.** (2006). Quantification of wave reflection in the human aorta from pressure alone: A proof of principle. *Hypertension*, **48**(4), 595–601. https://doi.org/10.1161/01.HYP.0000238330.08894.17
248. **Westerhof, N.**, & **Westerhof, B. E.** (2012). Wave transmission and reflection of waves " The myth is in their use." *Artery Research*, **6**(1), 1–6. https://doi.org/10.1016/j.artres.2012.01.004
249. **Wikstrand, J.** (2007). Methodological considerations of ultrasound measurement of carotid artery intima-media thickness and lumen diameter. *Clinical Physiology and Functional Imaging*, **27**(6), 341–345.

https://doi.org/10.1111/j.1475-097X.2007.00757.x

250. **Wilkinson, I. B.**, **McEniery, C. M.**, **Schillaci, G.**, **Boutouyrie, P.**, **Segers, P.**, **Donald, A.**, & **Chowienczyk, P. J.** (2010). ARTERY society guidelines for validation of non-invasive haemodynamic measurement devices: part 1, arterial pulse wave velocity. *Artery Research*, **4**(2), 34–40.

251. **Wilkinson, I. B.**, **Mohammad, N. H.**, **Tyrrell, S.**, **Hall, I. R.**, **Webb, D. J.**, **Paul, V. E.**, … **Cockcroft, J. R.** (2002). Heart rate dependency of pulse pressure amplification and arterial stiffness. *American Journal of Hypertension*, **15**(1 Pt 1), 24–30. https://doi.org/10.1016/S0895-7061(01)02252-X

252. **Willekes, C.**, **Hoeks, A. P. G.**, **Bots, M. L.**, **Brands, P. J.**, **Willigers, J. M.**, & **Reneman, R. S.** (1999). Evaluation of off-line automated intima-media thickness detection of the common carotid artery based on M-line signal processing. *Ultrasound in Medicine and Biology*, **25**(1), 57–64. https://doi.org/10.1016/S0301-5629(98)00138-0

253. **Williams, B.**, **Mancia, G.**, **Spiering, W.**, **Agabiti Rosei, E.**, **Azizi, M.**, **Burnier, M.**, … **Erdine, S.** (2018). 2018 ESC/ESH guidelines for the management of arterial hypertension: the task force for the management of arterial hypertension of the European Society of Hypertension (ESH) and of the European Society of Cardiology (ESC). *European Heart Journal*, **39**(33), 3021–3104. https://doi.org/10.1093/eurheartj/ehy339)(PMID:30165516)

254. **Xiao, H.**, **Qasem, A.**, **Butlin, M.**, & **Avolio, A.** (2017). Estimation of aortic systolic blood pressure from radial systolic and diastolic blood pressures alone using artificial neural networks. *Journal of Hypertension*, **35**(8), 1577–1585. https://doi.org/10.1097/HJH.0000000000001337

255. **Xing, X.**, **Ma, Z.**, **Zhang, M.**, **Zhou, Y.**, **Dong, W.**, & **Song, M.** (2019). An unobtrusive and calibration-free blood pressure estimation method using photoplethysmography and biometrics. *Scientific Reports*, **9**(1), 1–8. https://doi.org/10.1038/s41598-019-45175-2

256. **Xu, C.**, **Zarins, C. K.**, **Pannaraj, P. S.**, **Bassiouny, H. S.**, & **Glagov, S.** (2000). Hypercholesterolemia superimposed by experimental hypertension induces differential distribution of collagen and elastin. *Arteriosclerosis, Thrombosis, and Vascular Biology*, **20**(12), 2566–2572. https://doi.org/10.1161/01.ATV.20.12.2566

257. **Xu, W.**, **Yang, X.**, **Li, Y.**, **Jiang, G.**, **Jia, S.**, **Gong, Z.**, … **Zhang, N.** (2022). Deep Learning-Based Automated Detection of Arterial Vessel Wall and Plaque on Magnetic Resonance Vessel Wall Images. *Frontiers in Neuroscience*, **0**, 699. https://doi.org/10.3389/FNINS.2022.888814

258. **Xu, X.**, **Zhou, Y.**, **Cheng, X.**, **Song, E.**, & **Li, G.** (2012). Ultrasound intima–media segmentation using Hough transform and dual snake model. *Computerized Medical Imaging and Graphics*, **36**(3), 248–258. https://doi.org/10.1016/J.COMPMEDIMAG.2011.06.007

259. **Yamashita, S.**, **Dohi, Y.**, **Takase, H.**, **Sugiura, T.**, & **Ohte, N.** (2014). Central blood pressure reflects left ventricular load, while brachial blood pressure reflects arterial damage. *Blood Pressure*, **23**(6), 356–362. https://doi.org/10.3109/08037051.2014.923250

260. **Yang, J.**, **Faraji, M.**, & **Basu, A.** (2019). Robust segmentation of arterial walls in intravascular ultrasound images using Dual Path U-Net. *Ultrasonics*, **96**(February), 24–33. https://doi.org/10.1016/j.ultras.2019.03.014

261. **Yano, Y.**, **Stamler, J.**, **Garside, D. B.**, **Daviglus, M. L.**, **Franklin, S. S.**, **Carnethon, M. R.**, … **Lloyd-Jones, D. M.** (2015). Isolated Systolic Hypertension in Young and Middle-Aged Adults and 31-Year Risk for Cardiovascular Mortality: The Chicago Heart Association Detection Project in Industry Study. *Journal of the American College of Cardiology*, **65**(4), 327. https://doi.org/10.1016/J.JACC.2014.10.060
262. **Yao, Y.**, **Wang, L.**, **Hao, L.**, **Xu, L.**, **Zhou, S.**, & **Liu, W.** (2018). *Blood Pressure - From Bench to Bed* (1st ed.). https://doi.org/10.5772/intechopen.76770
263. **Yeboah, J.**, **McClelland, R. L.**, **Polonsky, T. S.**, **Burke, G. L.**, **Sibley, C. T.**, **O'Leary, D.**, … **Herrington, D. M.** (2012). Comparison of Novel Risk Markers for Improvement in Cardiovascular Risk Assessment in Intermediate-Risk Individuals. *JAMA*, **308**(8), 788–795. https://doi.org/10.1001/JAMA.2012.9624
264. **Yin, L. X.**, **Ma, C. Y.**, **Wang, S.**, **Wang, Y. H.**, **Meng, P. P.**, **Pan, X. F.**, … **Li, Y. H.** (2021). Reference Values of Carotid Ultrafast Pulse-Wave Velocity: A Prospective, Multicenter, Population-Based Study. *Journal of the American Society of Echocardiography*, **34**(6), 629–641. https://doi.org/10.1016/j.echo.2021.01.003
265. **Yousefian, P.**, **Shin, S.**, **Mousavi, A.**, **Kim, C. S.**, **Mukkamala, R.**, **Jang, D. G.**, … **Hahn, J. O.** (2019). The potential of wearable limb ballistocardiogram in blood pressure monitoring via pulse transit time. *Scientific Reports*, **9**(1), 1–11. https://doi.org/10.1038/s41598-019-46936-9
266. **Yu, S.**, & **Mceniery, C. M.** (2020). Central versus peripheral artery stiffening and cardiovascular risk. *Arteriosclerosis, Thrombosis, and Vascular Biology*, **40**(5), 1028–1033. https://doi.org/10.1161/ATVBAHA.120.313128
267. **Zahnd, G.**, **Kapellas, K.**, **van Hattem, M.**, **van Dijk, A.**, **Sérusclat, A.**, **Moulin, P.**, … **Orkisz, M.** (2017a). A fully-automatic method to segment the carotid artery layers in ultrasound imaging: application to quantify the compression-decompression pattern of the intima-media complex during the cardiac cycle. *Ultrasound in Medicine and Biology*, **43**(1), 239–257.
268. **Zahnd, G.**, **Kapellas, K.**, **van Hattem, M.**, **van Dijk, A.**, **Sérusclat, A.**, **Moulin, P.**, … **Orkisz, M.** (2017b). A fully-automatic method to segment the carotid artery layers in ultrasound imaging: application to quantify the compression-decompression pattern of the intima-media complex during the cardiac cycle. *Ultrasound in Medicine and Biology*, **43**(1), 239–257. https://doi.org/10.1016/j.ultrasmedbio.2016.08.016
269. **Zahnd, G.**, **Orkisz, M.**, **Sérusclat, A.**, **Moulin, P.**, & **Vray, D.** (2014). Simultaneous extraction of carotid artery intima-media interfaces in ultrasound images: assessment of wall thickness temporal variation during the cardiac cycle. *International Journal of Computer Assisted Radiology and Surgery*, **9**(4), 645–658. https://doi.org/10.1007/s11548-013-0945-0
270. **Zahnd, G.**, **Salles, S.**, **Liebgott, H.**, **Vray, D.**, **Sérusclat, A.**, & **Moulin, P.** (2015). Real-time ultrasound-tagging to track the 2D motion of the common carotid artery wall in vivo. *Medical Physics*, **42**(2), 820–830. https://doi.org/10.1118/1.4905376
271. **Zakrzewski, A. M.**, & **Anthony, B. W.** (2018). Noninvasive blood pressure estimation using ultrasound and simple finite element models. *IEEE Transactions on Biomedical Engineering*, **65**(9), 2011–2022. https://doi.org/10.1109/TBME.2017.2714666

272. **Zakrzewski, A. M.**, **Huang, A. Y.**, **Zubajlo, R.**, & **Anthony, B. W.** (2018). Real-time blood pressure estimation from force-measured ultrasound. *IEEE Transactions on Biomedical Engineering*, **65**(11), 2405–2416. https://doi.org/10.1109/TBME.2018.2873297
273. **Zhu, G.**, **Yuan, Q.**, **Yang, J.**, & **Yeo, J.** (2015). Experimental study of hemodynamics in the Circle of Willis. *Biomedical Engineering Online*, **14**(Suppl 1), S10. https://doi.org/10.1186/1475-925X-14-S1-S10
274. **Zieman, S. J.**, **Melenovsky, V.**, & **Kass, D. A.** (2005). Mechanisms, pathophysiology, and therapy of arterial stiffness. *Arteriosclerosis, Thrombosis, and Vascular Biology*, **25**(5), 932–943. https://doi.org/10.1161/01.ATV.0000160548.78317.29

CURRICULUM VITAE

1. **NAME** : V Raj Kiran

2. **DATE OF BIRTH** : 27 November 1990

3. **EDUCATIONAL QUALIFICATIONS**

Bachelor of Technology **2008 – 2012**

Institution	:	National Institution of Science and Technology, Berhampur, Odisha
Specialization	:	Electrical and Instrumentation Engineering
Project	:	Interactive SCADA interface for turbine monitoring systems, as part of project.

Master of Technology **2013 – 2015**

Institution	:	National Institute of Technology, Agartala
Specialization	:	Electrical Engineering, Instrumentation branch
Project	:	Non-contact vibration and flow monitoring system for nuclear plant applications.

DOCTORAL COMMITTEE

CHAIRPERSON:	Prof. K Sridharan Professor Dept. of Electrical Engineering
GUIDE(S):	Dr. Jayaraj Joseph Assistant Professor Dept. of Electrical Engineering
MEMBERS:	Prof. Boby George Professor Dept. of Electrical Engineering
	Prof. Jagadeesh Kumar V Professor Dept. of Electrical Engineering
	Dr. Raghavendra Sai V V Associate Professor Dept. of Applied Mechanics